

**PLASMA ASSISTED
DECOMPOSITION OF METHANE
AND PROPANE AND CRACKING
OF LIQUID HEXADECANE**

A thesis submitted for the degree of Doctor of Philosophy

by

Irma Aleknaviciute



School of Engineering and Design

Brunel University, Uxbridge

April, 2013

Abstract

Non-thermal plasmas are considered to be very promising for the initiation of chemical reactions and a vast amount of experimental work has been dedicated to plasma assisted hydrocarbon conversion processes, which are reviewed in the fourth chapter of the thesis. However, current knowledge and experimental data available in the literature on plasma assisted liquid hydrocarbon cracking and gaseous hydrocarbon decomposition is very limited.

The experimental methodology is introduced in the chapter that follows the literature review. It includes the scope and objectives section reflecting the information presented in the literature review and the rationale of this work. This is followed by a thorough description of the design and construction of the experimental plasma reformer and the precise experimental procedures, the set-up of hydrocarbon characterization equipment and the development of analytical methods. The methodology of uncertainty analysis is also described.

In this work we performed experiments in attempt the cracking of liquid hexadecane into smaller liquid hydrocarbons, which was not successful. The conditions tested and the problems encountered are described in detail.

In this project we performed a parametric study for methane and propane decomposition under a corona discharge for CO_x free hydrogen generation. For methane and propane a series of experiments were performed for a positive corona discharge at a fixed inter-electrode distance (15 mm) to study the effects of discharge power (range of 14 - 20 W and 19 – 35 W respectively) and residence time (60 - 240 s and 60 – 303 s respectively). A second series of experiments studied the effect of inter-electrode distance on hydrogen production, with distances of 15, 20, 25, 30 and 35 mm tested. The analysis of the results shows that both discharge power and residence time, have a positive influence on gaseous hydrocarbon conversion, hydrogen selectivity and energy conversion efficiency for methane and propane decomposition. Longer discharge gaps favour hydrogen production for methane and propane decomposition. A final series of experiments on corona polarity showed that a positive discharge was preferable for methane decomposition.

Declaration

The research presented in this thesis is the original work of the author except where otherwise specified, or where acknowledgements are made by references. This project was carried out at the School of Engineering and Design, Brunel University, under the supervision of Prof. T. G. Karayiannis and Prof. M. W. Collins.

The work has not been submitted for another degree or award to any other institution.

Acknowledgements

It is with immense gratitude that I acknowledge the support and encouragement of Professor T. G. Karayiannis. I attribute the success of this project to his close guidance and invaluable advice throughout the project. He also sacrificed his own personal time to study chemistry.

I would also like to acknowledge my second supervisor Professor M. W. Collins. His constructive suggestions and comments have greatly facilitated the writing of this thesis and the successful publications.

I am grateful to the technician Mr. C. Xanthos for his support in the installation and construction of the facility and test reactor. The success of the experimental work was facilitated by his constant help and advice.

To the School of Engineering and Design, Brunel University, for providing me the scholarship and the opportunity to complete this study. Special thanks to Professor L. Wrobel for enabling the project to continue.

My heartfelt thanks go to my partner Mr. T. Doyle for his patience, understanding, encouragement and love throughout my PhD research. In addition, his constructive suggestions and advice have greatly facilitated the writing of this thesis.

Finally I would like to express my great thanks to my dearest friend Miss. I. Desnica. It is with her encouragement and belief that I started this project, and continuous support that I completed it.

Contents

Abstract	i
Declaration	ii
Acknowledgements	iii
List of Figures	xi
List of Tables	xxii
Nomenclature	xxvii
Chapter 1: Introduction	1
1.1. Research Background	1
1.2. Project objectives	3
1.3. Overview of this thesis	4
Chapter 2: Importance and Processing of Fuels	5
2.1. Introduction: From ‘Oil Era’ to ‘Hydrogen Economy’	5
2.2. Hydrocarbons	7
2.2.1. Composition, structure and bonding	7
2.2.2. Bond dissociation energies	8
2.3. From crude oil to gasoline	9
2.3.1. Crude oil composition	9
2.3.2. Gasoline – importance and production	10
2.3.2.1. Thermal cracking	10
2.3.2.2. Catalytic cracking	12
2.3.2.3. Problems with conventional cracking technologies	13
2.4. Fuelling the future: from hydrocarbon to hydrogen	14
2.4.1. Hydrogen Economy	14
2.4.2. Applications of hydrogen	15

2.4.3.	Hydrogen sources and production	16
2.5.	Pyrolysis of methane: the Hydrogen-Carbon economy	20
2.5.1.	Thermo-catalytic methane decomposition	20
2.5.2.	The use of solid carbon	27
2.6.	Propane decomposition for hydrogen production	28
2.6.1.	Advantages of propane pyrolysis	28
2.6.2.	Catalytic propane reforming	29
2.6.3.	Pyrolysis and thermo-catalytic decomposition	30
2.7.	Summary	34
Chapter 3: The Fourth State of Matter		36
3.1.	Introduction	36
3.2.	Plasma sources and processes	37
3.3.	Thermal and non-thermal plasmas	37
3.4.	Non-thermal atmospheric pressure discharges	38
3.5.	Corona discharge	40
3.5.1.	What is corona?	40
3.5.2.	Positive pin-to-plate corona processes	41
3.5.3.	Negative pin-to-plate corona processes	43
3.5.4.	Multipoint and point-to-liquid electrode configurations	44
3.5.5.	Important parameters reported in the literature	46
3.5.6.	Corona discharge applications	48
Chapter 4: Plasma Processing of Hydrocarbons		50
4.1.	Introduction	50
4.2.	Conversion rate, selectivity and energy consumption	51
4.3.	Plasma-assisted generation of hydrogen from methane	52
4.3.1.	General theory	52
4.3.2.	Syngas production by partial oxidation of methane	54
4.3.2.1.	Atmospheric pressure glow discharge and plasma jet	54

4.3.2.2. Microwave and corona discharges	57
4.3.2.3. Arc discharges	59
4.3.2.4. Thermal plasma	62
4.3.2.5. Comparing plasma assisted partial oxidation systems	64
4.3.3. Hydrogen production by methane decomposition	66
4.3.4. Steam and autothermal reforming of methane	69
4.3.5. Comparing PO, pyrolysis and SR plasma systems	71
4.3.6. Important parameters reported in literature	73
4.3.6.1. Flow rate	73
4.3.6.2. Power input	76
4.3.6.3. Gas composition	78
4.3.6.4. Other parameters investigated	86
4.3.6.5. Summary	92
4.4. Hydrogen generation from propane	98
4.5. Plasma assisted cracking of liquid hydrocarbons	102
4.6. Plasma-catalytic systems for hydrocarbon reformation	105
4.6.1. Two stage plasma-catalyst system	106
4.6.2. Single stage plasma-catalytic system	109
4.6.3. Plasma-catalytic systems conclusions	113
4.7. Summary	113
Chapter 5: Experimental Rig	116
5.1. Introduction: rationale of this study	116
5.2. Scope and objectives	117
5.3. Plasma reactor	121
5.3.1. Overview	121
5.3.2. Top plate	122
5.3.3. Bottom plates	126
5.3.4. Temperature and pressure measure and control	127

5.4. Experimental methodology	130
5.4.1. Liquid samples	130
5.4.2. Gaseous samples	130
5.4.3. Residence time and flow	131
5.5. Sample characterization	132
5.5.1. Overview	132
5.5.2. GC-MS instrument	132
5.5.2.1. GC-MS configuration for liquid analysis	134
5.5.2.2. Liquid hydrocarbon characterization	134
5.5.2.3. GC-MS configuration for gas analysis	137
5.5.2.4. Gaseous hydrocarbon characterization	138
5.5.3. Chromopack CP9001 GC	141
5.5.3.1. GC configuration for hydrogen measurement	141
5.5.3.2. Hydrogen quantification	142
5.5.4. Energy conversion efficiency calculations	143
5.6. Calibration and uncertainty analysis	145
5.6.1. General theory	145
5.6.2. Calibration process and error analysis	146
5.7. Summary	160
Chapter 6: Experimental results for hexadecane cracking under corona discharge	161
6.1. Introduction	161
6.2. Underlying theory	161
6.3. Experimental conditions	165
6.4. Discussion	165
6.5. Conclusions	166

Chapter 7: Experimental results for methane decomposition under corona discharge	168
7.1. Introduction	168
7.2. Methane decomposition under a positive corona discharge	168
7.2.1. 15 mm inter electrode distance: Effects of discharge power and residence time	170
7.2.1.1. Methane conversion	172
7.2.1.2. Hydrogen production and selectivity	174
7.2.1.3. Energy conversion efficiency	177
7.2.1.4. Other compounds generated	181
7.2.1.5. Summary	184
7.2.2. The effects of inter-electrode distance on hydrogen production	184
7.2.3. Experimental repeatability	188
7.3. Methane decomposition under a negative corona discharge	188
7.4. Summary	190
Chapter 8: Experimental results for propane decomposition under corona discharge	192
8.1. Introduction	192
8.2. 15 mm inter electrode distance: Effects of discharge power and residence time	192
8.2.1. Plasma cut-off phenomenon	195
8.2.2. Propane conversion	196
8.2.3. Hydrogen production and selectivity	198
8.2.4. Energy conversion efficiency	200
8.2.5. Other compounds generated	202
8.3. The effects of inter-electrode distance on hydrogen production	210

8.3.1. Experimental repeatability	213
8.4. Summary	214

Chapter 9: A comparative study of hydrogen generation methods and the potential of integrated PEMFC-CHP energy system 216

9.1. Introduction	216
9.2. The domestic energy supply and CO ₂ mitigating options	217
9.2.1. Domestic energy emissions	217
9.2.2. The PEMFC-CHP system	217
9.2.3. Carbon capture and storage (CCS)	219
9.2.4. CO ₂ free hydrogen generation	220
9.3. Data inputs and methodology	221
9.3.1. National Grid energy supply, emissions and costing	221
9.3.2. Compound composition conversions	224
9.3.3. Hydrogen generation cost	225
9.3.4. Input data for hydrogen generation systems	228
9.3.5. FC-CHP system specifications	230
9.4. UK National grid 2010 conditions	231
9.5. Comparison of hydrogen generation systems	234
9.5.1. Current conditions with carbon value	234
9.5.2. Post-2020 scenario with CCS	236
9.5.3. Post-2035 scenario with renewables integration	237
9.5.4. Combination with an integrated FC-CHP system	239
9.6. Conclusions	241

Chapter 10: Conclusions and Recommendations 243

10.1. Conclusions	243
10.1.1. Hexadecane Cracking	243
10.1.2. Methane decomposition	243
10.1.3. Propane decomposition	244

10.1.4. Comparing methane and propane results	244
10.2. Recommendations	245
10.2.1. Hexadecane cracking	245
10.2.2. Methane and propane decomposition	245
10.3. Future work	246
References	248
Appendix A: Fuel cell technology and commercialization	272
Appendix B: Hexadecane cracking under corona discharge:	
Conditions tested	277
Curriculum Vitae	285
Publications from the work covered in this thesis	287

List of Figures

- Figure 2.1 Examples of different types of hydrocarbons: a) an alkane – butane, b) an isomer of butane - isobutane, c) an alkene – butene, d) an alkyne – 1-butyne, e) a cycloalkane – cyclohexane, f) aromatic compound - cyclohexa-1,3,5-triene (benzene). 7
- Figure 2.2 Structure of methane. 8
- Figure 2.3 Thermal cracking using hexane molecule as an example: a) thermal cracking at moderate temperatures proceeds symmetrically and generates two molecules containing 3 carbon atoms each – a propane and a propene; b) an example of asymmetrical thermal cracking of hexane at high temperatures, which generates one molecule with 2 carbon atoms (ethane) and one molecule with 4 carbon atoms (butene). 11
- Figure 2.4 Time on stream experiments for methane decomposition using nickel catalyst reported by Villacampa et al. (2003) at different methane to nitrogen ratios shown on the graph: a) methane conversion rate against time, shows methane conversion decrease within first hour of operation; b) carbon deposition rate with time, shows highest deposition rate within the first hour. 22
- Figure 2.5 Time on stream experiments for methane decomposition using nickel catalyst reported by Villacampa et al. (2003) (Fig. 8) at different temperatures, showing hydrogen production versus time and steep hydrogen generation rate decrease in the first hour of operation. 23
- Figure 2.6 The effects of the CH₄ flow rate on hydrogen production and methane conversion rate for methane decomposition using nickel catalyst reported by Suelves et al. (2005) (Fig. 4). Run 5 is at 20 ml/min; run 7: 50 ml/min; run 6: 100 ml/min. 24

- Figure 2.7 Time on stream effect on hydrogen generation from methane using nickel-copper catalyst at different temperatures, reported by Pinilla et al. (2010) (Fig. 4). 25
- Figure 2.8 The effect of nickel catalyst regeneration process on hydrogen production reported by Villacampa et al. (2003) (Fig. 11). Shows a much lower hydrogen generation rate within 20 min after regeneration cycle. 26
- Figure 2.9 Time on stream experimental results for propane thermo-catalytic decomposition by nickel catalyst as reported by Solovyev et al. (2009) (Fig. 3). Shows the compound concentration by volume with time: methane (CH₄) and hydrogen (H₂) production decreases with time; propane (C₃H₈) concentration increases, i.e. conversion of propane decreases with time. 31
- Figure 2.10 Time on stream experimental results for propane thermo-catalytic decomposition by nickel-copper bi-metallic catalyst as reported by Solovyev et al. (2009) (Fig. 4). Shows the compound concentration by volume with time: methane (CH₄) and hydrogen (H₂) production decreases with time; propane (C₃H₈) concentration increases, i.e. conversion of propane decreases with time. 31
- Figure 2.11 Time on stream experiments for hydrogen production from propane decomposition over different catalysts at 625 °C, reported by Wang et al. (2005) (Fig. 4). Pd-Fe = palladium-iron; Ni-Fe = nickel-iron; Mo-Fe = molybdenum-iron; Fe = iron; Al₂O₃ = catalyst alumina support. 33
- Figure 3.1 Townsend breakdown mechanism (Fridman et al., 2005, Fig. 1): d = inter electrode distance; E = electric field; e = electrons; (+) = positive ion. 39
- Figure 3.2 Examples of different corona electrode configurations: a) Point-to-plane (Benocci and Mauri, 2004 – Fig. 1); b) point-to-coaxial cylinder (Benocci and Mauri, 2004 – Fig. 1); c)

	wire-to-cylinder (Mishra et al., 2004 – Fig. 1); d) multipoint-to-plane (Thanh, 1985 – Fig. 3); e) pin-to-liquid (Bruggeman et al., 2008 – Fig. 1).	41
Figure 3.3	Schematic of types of positive corona discharge (adapted from Chang and Yamamoto, 1991, Fig.1).	42
Figure 3.4	Schematic of types of negative corona discharge (adapted from Chang and Yamamoto, 1991, Fig. 1).	43
Figure 4.1	Schematic representation of the plasma reactor with a photography of the electric discharge (Luche et al., 2009, Fig. 1).	55
Figure 4.2	Schematic diagram of cold plasma jet (Long et al., 2008, Fig. 1).	56
Figure 4.3	Microwave plasma system (Tsai et al., 2005, Fig. 1).	57
Figure 4.4	Schematic diagram of corona discharge reactor (Kado, et al., 2003, Fig. 1).	58
Figure 4.5	Multistage gliding arc reactor set-up. a) configuration of gliding arc discharge system showing the set-up of the four stages, b) configuration of each gliding arc discharge reactor (Sreethawong at al., 2007, Figs. 2 and 3).	60
Figure 4.6	Gliding arc plasma reactor, showing the diverging electrodes within a quartz-glass tube (Intardo at al., 2003, Fig. 1).	61
Figure 4.7	DC thermal plasma jet (Tao et al., 2008, Fig. 2).	62
Figure 4.8	Binode thermal plasma reactor set-up. 1, 2 and 3 are feed gases; 4, 5 and 6 are gas inlets; 7 DC power supply; 8 cathode; 9 plasma generator; 10 first anode; 11 contactor; 12 the second anode; 13 graphite tube reactor; 14 collector; 15 gas outlet (Tao et al., 2009, Fig. 1).	63
Figure 4.9	Cross-sectional view of the DC-RF plasma torch set-up (Kim at al., 2005, Fig. 1).	67
Figure 4.10	Spark discharge reactor showing pin-to-plate electrode configuration (Li et al., 2004, Fig. 1b).	68
Figure 4.11	Shows the configuration of the novel water plasma torch developed by Ni et al., 2011 (Fig. 1).	71

Figure 4.12	The effects of flow rate on methane conversion reported in the literature for a flow rate range of a) 20 – 500 ml/min; b) 360 – 6000 ml/min; c) 13,000 – 40, 000 ml/min.	74
Figure 4.13	The effects of flow rate on hydrogen selectivity reported in the literature for a flow rate range of a) 20 – 500 ml/min; b) 360 – 6000 ml/min; c) 13,000 – 40, 000 ml/min.	75
Figure 4.14	The effect of power input on methane conversion reported in literature in the power range of: a) 2 – 12 W; b) 50 – 90 W; c) 200 – 1400 W.	77
Figure 4.15	Effect of discharge power on hydrogen selectivity reported in the literature.	78
Figure 4.16	Effects of O ₂ /CH ₄ ratio reported in literature on a) methane conversion; b) hydrogen selectivity.	79
Figure 4.17	Effect of variations in CH ₄ flow ratio, a) concentration of hydrogen and H ₂ /CO ratio; b) conversion rate and energy conversion rate (Kim and Chun, 2008; Fig. 2).	80
Figure 4.18	The effect of CO ₂ /CH ₄ ratio on methane conversion reported in the literature for partial oxidation and ATR reactions.	81
Figure 4.19	The effect of CO ₂ /CH ₄ ratio on hydrogen selectivity reported in the literature.	82
Figure 4.20	The effect of CO ₂ /CH ₄ ratio on methane conversion and hydrogen selectivity reported by Huang et al., 2000.	82
Figure 4.21	The effect of CO ₂ /CH ₄ ratio on methane conversion and hydrogen selectivity in a gliding arc reactor reported by Intardo et al., 2006.	83
Figure 4.22	The effect of Ar/CH ₄ ratio on methane conversion and hydrogen selectivity for direct methane decomposition employing gliding arc, reported by Intardo et al., 2006.	83
Figure 4.23	The effects of H ₂ O/CH ₄ ratio on methane conversion and hydrogen selectivity for SMR employing a microwave discharge, reported by Wang et al., 2010.	84
Figure 4.24	The effects of the addition gasses on methane conversion and hydrogen selectivity as reported by Intardo et al., 2006. The	

	gas compositions are as follows: 100 % CH ₄ , 85 % Ar / 15 % CH ₄ , 80 % He or Ni or CO ₂ to 20 % CH ₄ .	86
Figure 4.25	The effect of pulse frequency in pulsed corona discharges on methane conversion.	87
Figure 4.26	The effect of pulse frequency in a glow discharge on methane conversion and hydrogen selectivity, data taken from Ghorbanzadeh et al., 2009.	87
Figure 4.27	The effects of AC frequency in a gliding arc discharge on methane conversion and hydrogen selectivity, data taken from Sreethawong et al., 2007.	88
Figure 4.28	The effects of AC frequency in an arc discharge on methane conversion and hydrogen selectivity, data taken from Intardo et al., 2006.	89
Figure 4.29	The effect of inter-electrode distance on methane conversion reported in the literature.	90
Figure 4.30	The effects of inter-electrode distance on hydrogen selectivity reported in the literature.	90
Figure 4.31	The effect of pressure on methane conversion and hydrogen selectivity, Tsai et al., (2005).	91
Figure 4.32	The effect of temperature on methane conversion, Yao et al., 2001a.	92
Figure 4.33	The effects of O ₂ /C ratio on hydrogen to CO _x generation ratio at different propane flow rates (Horng et al., 2009, Fig. 7).	98
Figure 4.34	The effects of temperature on hydrogen selectivity in plasma assisted catalytic propane reforming at different propane flow rates (Horng et al., 2009, Fig. 8B).	99
Figure 4.35	The effect of reaction temperature on propane conversion (Yu et al., 2011, Fig. 1a).	100
Figure 4.36	Influence of the reaction temperature on hydrogen selectivity (Yu et al., 2011, Fig. 2a).	101
Figure 4.37	Effect of a) voltage along with flow rate and (b) gas type on the conversion percentage of hexadecane (Khani et al., 2011, Fig. 5). Shows that higher voltages and gas flow rates improve	

	hexadecane cracking.	104
Figure 4.38	Schematic representation of plate-to-plate reactor for liquid hydrocarbon cracking reported by Prieto et al. (1999) (Fig. 1).	105
Figure 5.1	Picture of the plasma chamber design, showing all relevant components.	122
Figure 5.2	Shows the side view of the stainless steel top disk: glass fitting groove. The units in the diagram are in millimetres.	123
Figure 5.3	Picture of a) Top plate showing the positions of high voltage supply and the active electrode; argon and vacuum supply, gas outlet, thermocouple and pressure transducer; b) Top plate showing the addition of outlet septa and propane supply.	124
Figure 5.4	Picture of the design of the pin electrode.	125
Figure 5.5	Picture of the in-house build resistor, consisting of three 1 M Ω resistors connected in parallel. The total amount of resistors is 27 and the total resistance is 3.12 M Ω , 27 W.	125
Figure 5.6	Side view of the stainless steel bottom disk: reaction media well, glass fitting groove and inlet/outlet grooves. The units in the diagram are in millimetres.	126
Figure 5.7	Picture of the close up view of the reaction well and the pin electrode.	126
Figure 5.8	Picture of the cartridge heater installation into the copper disk	127
Figure 5.9	Picture of the cartridge heater control box showing the set up of the SSR and PID.	128
Figure 5.10	Picture of the cartridge heater and the thermocouple attached to it.	128
Figure 5.11	Picture of the USB TC-08 Thermocouple Data Logger; a) USB connection to the computer, b) type K thermocouple measuring room temperature, c) type K thermocouple measuring reactor temperature, d) terminal board for reactor pressure measurement.	129
Figure 5.12	Picture of the Gas-Chromatography- Mass Spectrometer showing, a) Inlet B for liquid sample injection; b) the overall	

	set up of the GC and the MS; c) GC oven showing the column, inlet A and inlet B for gaseous and liquid column installation respectively, and the MS inlet where the column is connected to the MS.	133
Figure 5.13	Chromatogram obtained from C7-C40 standard analysis by the GC-MS instrument; a) the chromatogram shows the peaks and the retention times of compounds with different number of carbon atoms; b) zoomed in view of the carbon 14 peak showing the area and the spectrum of the peak.	135
Figure 5.14	Mass Spectrum of the standard gas, showing the retention time for each compound.	140
Figure 5.15	Shows a table generated by the data logger used to create a chromatogram and calculate the peak area; in this example the 10 % test sample shown.	142
Figure 5.16	Pressure vs voltage calibration for the pressure transducer; shows the best fit equation.	147
Figure 5.17	Thermocouple calibration data; shows the best fit equation.	149
Figure 5.18	The best fit equation for the hydrogen measurement calibration data for the range of 0 – 30 %.	153
Figure 5.19	The best fit equation for the propane measurement calibration data.	154
Figure 5.20	The best fit equation for the methane measurement calibration data.	155
Figure 6.1	Expected plasma cracking of hexadecane in Argon at atmospheric pressure in a negative pin-to-plane electrode configuration. The mechanism is described below and the numbers in the figure represent the steps: 1) High voltage is supplied to the pin electrode; 2) Electrical breakdown of argon molecule and the generation of positive ion and an electron; 3) Electron accelerates to the positive plate electrode; 4) Ionization of hexadecane molecule at the C-C bond by an impact of an energetic electron; 5) Hexadecane molecule dissociation at the C-C bond.	162

Figure 7.1	Shows the discharge characteristic of a positive pin-to-plane corona for a) unpolished, and b) polished plane electrode.	169
Figure 7.2	Shows the carbon string growth and the shortening of the active plasma area between the active positive pin and the ground electrode with time.	169
Figure 7.3	Shows the effects of discharge power and residence time on methane conversion.	172
Figure 7.4	The effect of the flow rate on methane conversion reported in the literature and this work.	173
Figure 7.5	Shows the effects of total energy on methane conversion.	174
Figure 7.6	Hydrogen production against discharge power and residence time.	175
Figure 7.7	The effects of discharge power and residence time on hydrogen selectivity.	176
Figure 7.8	The effect of flow rate on hydrogen selectivity, results reported in the literature compared to this work.	176
Figure 7.9	The effects of discharge power and residence time on energy conversion efficiency of the plasma.	177
Figure 7.10	Energy efficiency versus hydrogen selectivity.	178
Figure 7.11	The percentages of methane and electric energy consumption.	178
Figure 7.12	Generation of ethene against the discharge power and residence time.	182
Figure 7.13	Generation of acetylene against the discharge power and residence time.	182
Figure 7.14	Generation of ethane against the discharge power and residence time.	183
Figure 7.15	Other compound generation during methane conversion to hydrogen at residence time 4 minutes.	183
Figure 7.16	The effects of discharge power and residence time on hydrogen generation at inter electrode distances of 15, 20, 25, 30 and 35 mm.	185

Figure 7.17	Shows the hydrogen production trend against the discharge current at different discharge voltages at 4 min residence time.	187
Figure 7.18	Hydrogen production repeatability at inter-electrode distance of 20 mm, residence time 2 min; the error bars for hydrogen measurement are at +/- 2.06 %.	188
Figure 8.1	Characteristics of pressure change with time during propane decomposition experiments at voltage input of a) 16 kV; b) 21.7 kV.	195
Figure 8.2	Shows the pressure of the plasma cut-off point compared to the voltage input into the system.	196
Figure 8.3	Shows the effects of discharge power and residence time on propane conversion, with combined error of ± 2.06 % of the reading value.	197
Figure 8.4	Shows the effects of total discharge energy on propane conversion, with combined error of ± 2.06 % of the reading value.	197
Figure 8.5	a) Hydrogen production compared to discharge power and residence time; b) Hydrogen production compared to the total discharge energy; with combined error of ± 2.08 % of the reading value.	198
Figure 8.6	Shows the effect of a) discharge power and residence time and b) total discharge energy on hydrogen selectivity, with combined error of ± 3.59 % of the reading value.	199
Figure 8.7	Shows the relationship of energy efficiency between the discharge power and residence time, with the combined total error of ± 5.5 % of the reading value.	200
Figure 8.8	Shows the relationship between energy efficiency and total discharge energy, with the combined total error of ± 5.5 % of the reading value.	201
Figure 8.9	Shows the relationship between energy efficiency and hydrogen selectivity, with the combined total error of ± 5.5 % of the reading value.	201
Figure 8.10	Other compound generation compared to the total discharge	

	energy.	203
Figure 8.11	Shows the pattern of ethane generation against a) discharge power and residence time; b) total discharge energy.	204
Figure 8.12	Pattern of 2,5 - cyclohexadiene generation against a) discharge power and residence time; b) total discharge energy.	204
Figure 8.13	Shows the pattern of ethane generation against a) discharge power and residence time; b) total discharge energy.	205
Figure 8.14	Shows the pattern of Cyclopropane generation against a) discharge power and residence time; b) total discharge energy.	205
Figure 8.15	Shows the pattern of 1-propyne generation against a) discharge power and residence time; b) total discharge energy.	206
Figure 8.16	Shows the pattern of 1-buten-3-yne generation against a) discharge power and residence time; b) total discharge energy.	206
Figure 8.17	Shows the pattern of 1-penten-3-yne generation against a) discharge power and residence time; b) total discharge energy.	207
Figure 8.18	Shows the pattern of 1,3-pentadiene generation against a) discharge power and residence time; b) total discharge energy.	207
Figure 8.19	Shows the pattern of benzene generation against a) discharge power and residence time; b) total discharge energy.	208
Figure 8.20	Shows the pattern of 1,3 - cyclopentadiene generation against a) discharge power and residence time; b) total discharge energy.	208
Figure 8.21	Shows the pattern of 2-butene generation against a) discharge power and residence time; b) total discharge energy.	209
Figure 8.22	Shows the pattern of 1,3-butadiyne generation against a) discharge power and residence time; b) total discharge energy.	209
Figure 8.23	Shows hydrogen generation against discharge power at different residence times and inter-electrode distances.	210
Figure 8.24	Shows hydrogen generation against total discharge energy at different residence times and inter-electrode distances.	212
Figure 8.25	Shows nearly linear hydrogen increase with the total discharge energy at all inter-electrode distances.	213

Figure 8.26	Hydrogen production repeatability at inter-electrode distance of 15 mm, residence time 2 min; the error bars for hydrogen measurement are at +/- 2.06 %.	214
Figure 9.1	Summary of domestic energy supply from the National Grid in 2010 and associated carbon dioxide emissions, <i>but excluding CCS</i> . Notes: i) the costing is for the retail price for total energy consumed. ii) the heat and electricity cost does not include the stated carbon charge.	232
Figure 9.2	Summary of domestic energy supply from the National Grid using 2010 data with future anticipated CCS. Notes: i) the costing is for the retail price for total energy consumed. ii) the heat and electricity cost does not include the stated carbon charge.	233
Figure 9.3	Summary diagrams for system analysis for hydrogen generation under current conditions, carbon charges included.	235
Figure 9.4	Summary of the system analysis for hydrogen generation post 2020 with CCS.	237
Figure 9.5	Summary of the system analysis for hydrogen generation: post 2035 with clean renewable energy integration.	238
Figure 9.6	Summary of the system analysis with integrated FC-CHP system.	240
Figure 10.1	Laboratory scale flow system design for gaseous hydrocarbon decomposition to generate CO _x free hydrogen.	247
Figure A.1	Shows an example of an SOFC fuel cell, where only negative ions can pass through the electrolyte: 1) The input of hydrogen and oxygen into the fuel cell; 2) Hydrogen is oxidised to protons and electrons at the anode, oxygen diffuses to the cathode; 3) Electrons transport through the external circuit due to charge difference from anode to cathode generating electricity; 4) Electrons reduce oxygen to negative ions; 5) Negative oxygen ions pass through the electrolyte; 6) Oxygen ions combine with protons to generate water.	273

List of Tables

Table 4.1	Comparison of SEC and SER for methane partial oxidation to syngas by different plasmas, starting with the lowest energy consumption at the top.	65
Table 4.2	Comparison of PO, Pyrolysis and SR systems for hydrogen generation from methane.	72
Table 4.3	Summary of the effects of total reactant flow and the optimal conditions if selected by authors.	93
Table 4.4	Summary of the effects of power input and the optimal conditions if selected by authors.	94
Table 4.5	Summary of the effects of gas composition and the optimal conditions if selected by authors.	96
Table 4.6	Summary of the effects of other parameters and the optimal conditions if selected by authors.	97
Table 4.7	Summary of the results on the two stage pre-processing plasma-catalyst systems.	108
Table 4.8	Summary of the results on the single stage plasma-catalyst systems.	112
Table 4.9	Summary of the results of plasma-catalytic and plasma alone systems for hydrogen generation from methane.	115
Table 5.1	Liquid C7 – C40 standard specification; shows the components and their nominal and certified concentrations.	136
Table 5.2	Standard gas specification; shows the components and their nominal and certified concentrations.	140
Table 5.3	The calibration data for the pressure transducer; including the calculated resolution error of the calibration standard.	147
Table 5.4	Combined uncertainty of the pressure measurement.	147
Table 5.5	The calibration data for the thermocouple.	148
Table 5.6	Voltage and current error (%) at different inputs.	149
Table 5.7	The calibration data for the GC Chromopack.	153
Table 5.8	Propane calibration data for the GC-MS.	154

Table 5.9	Methane calibration data for the GC-MS.	155
Table 5.10	The uncertainty value in each measured parameter and calculated power input.	159
Table 7.1	Experimental conditions and the results showing the data of methane conversion, hydrogen selectivity, hydrogen production and plasma energy efficiency for the experiments, testing the effects of discharge power and residence time at 15 mm inter-electrode distance.	171
Table 7.2	Important parameters and results for plasma decomposition of methane to generate hydrogen reported in literature.	180
Table 7.3	Data table for the effects of inter-electrode distance on hydrogen production at different residence times and discharge powers.	186
Table 7.4	Comparing the hydrogen generation ability of positive and negative corona discharge at different inter-electrode distances.	189
Table 8.1	Experimental conditions and the results showing the data of propane conversion, hydrogen selectivity, hydrogen production and energy efficiency for the experiments, testing the effects of discharge power and residence time at 15 mm inter-electrode distance.	194
Table 8.2	Experimental conditions and the results showing the data of hydrogen production for the experiments, testing the effects of inter-electrode distance.	211
Table 9.1	National grid energy supply and carbon dioxide emissions for 2010.	222
Table 9.2	Data input for cost calculations.	223
Table 9.3	Steam methane reformer input and calculated data.	228
Table 9.4	Home water electrolyser specifications and calculated data.	229
Table 9.5	Data input for the plasma jet.	229
Table 9.6	Fuel Cell CHP system.	230
Table 9.7	Summary of system analysis for hydrogen generation under	

	current conditions, where LQ C _S and HQ C _S stand for low and high quality solid carbon price respectively.	235
Table 9.8	Summary of the system analysis for hydrogen generation post 2020 with CCS.	236
Table 9.9	Summary of the system analysis for hydrogen generation: post 2035 with clean renewable energy integration.	238
Table 9.10	Summary of the system analysis with integrated FC-CHP system.	240
Table A.1	Types of fuel cells.	273
Table A.2	Summary of the state of the art of the fuel cell deployment worldwide (IPHE, 2010).	276
Table B.1	Experimental conditions for power input variation at inter-electrode distance 10 mm, sample amount 5 ml and residence time 15 min.	277
Table B.2	Experimental conditions for power input variation at inter-electrode distance 15 mm, sample amount 5 ml and residence time 15 min.	277
Table B.3	Experimental conditions for power input variation at inter-electrode distance 20 mm, sample amount 5 ml and residence time 15 min.	277
Table B.4	Experimental conditions for sample amount variation at power input of 86 W, inter-electrode distance 15 mm and residence time 15 min.	278
Table B.5	Experimental conditions for residence time variation at power input of 86 W, inter-electrode distance 15 mm and sample amount 5 ml.	278
Table B.6	Experimental conditions for power input variation at inter-electrode distance 10 mm, sample amount 5 ml and residence time 15 min.	278
Table B.7	Experimental conditions for power input variation at inter-electrode distance 15 mm, sample amount 5 ml and residence time 15 min.	279
Table B.8	Experimental conditions for power input variation at inter-	

	electrode distance 20 mm, sample amount 5 ml and residence time 15 min.	279
Table B.9	Experimental conditions for sample amount variation at power input 77 W, inter-electrode distance 15 mm and residence time 15 min.	279
Table B.10	Experimental conditions for residence time variation at power input 77 W, inter-electrode distance 15 mm and sample amount 5ml.	279
Table B.11	Experimental conditions for power input variation at inter-electrode distance 10 mm, sample amount 5 ml and residence time 15 min.	280
Table B.12	Experimental conditions for power input variation at inter-electrode distance 15 mm, sample amount 5 ml and residence time 15 min.	280
Table B.13	Experimental conditions for power input variation at inter-electrode distance 20 mm, sample amount 5 ml and residence time 15 min.	280
Table B.14	Experimental conditions for sample amount variation at power input 86 W, inter-electrode distance 15 mm and residence time 15 min.	281
Table B.15	Experimental conditions for residence time variation at power input 86 W, inter-electrode distance 15 mm and sample amount 5ml.	281
Table B.16	Experimental conditions for power input variation at inter-electrode distance 10 mm, sample amount 5 ml and residence time 15 min.	281
Table B.17	Experimental conditions for power input variation at inter-electrode distance 15 mm, sample amount 5 ml and residence time 15 min.	282
Table B.18	Experimental conditions for power input variation at inter-electrode distance 20 mm, sample amount 5 ml and residence time 15 min.	282
Table B.19	Experimental conditions for power input variation at inter-	

	electrode distance 10 mm, sample amount 5 ml and residence time 15 min.	282
Table B.20	Experimental conditions for power input variation at inter-electrode distance 15 mm, sample amount 5 ml and residence time 15 min.	283
Table B.21	Experimental conditions for power input variation at inter-electrode distance 20 mm, sample amount 5 ml and residence time 20 min.	283
Table B.22	Experimental conditions for power input variation at inter-electrode distance 10 mm, sample amount 5 ml and residence time 15 min.	283
Table B.23	Experimental conditions for power input variation at inter-electrode distance 15 mm, sample amount 5 ml and residence time 15 min.	284
Table B.24	Experimental conditions for power input variation at inter-electrode distance 20 mm, sample amount 5 ml and residence time 15 min.	284

Nomenclature

A	Area of the compound peak (arbitrary units)
\dot{c}	Consumption rate of fuel (kg/s)
C	Consumption of fuel to generate 1 kg hydrogen (kg)
\dot{C}	Consumption of fuel to generate 1 kg H ₂ (kW)
\ddot{C}	Consumption of fuel to generate 1 kg H ₂ (kWh)
Conv	Methane conversion rate (percent fraction)
Cr	Compound ratio by volume
D	Discharge
d	Distance (mm)
\check{D}	Density (kg/m ³)
E	Energy efficiency (%)
e ⁻	Electron
F	Fractional part of mole parts per total moles
f	Primary fuel input (kJ or kWh)
H ⁺	Proton
HHV	Higher heating value (kJ/kg)
h ν	Photon
I	Current (A)
<i>i</i>	Compound
LHV	Lower heating value (kJ/kg)
MW	Molecular weight of a compound
\dot{m}	Mass flow rate of a compound (kg/s)
<i>n</i>	Moles of a compound (mol)
\dot{n}	Moles of a compound converted (mol)
\ddot{n}	Moles of compound converted/generated per second (mol/s)
O	Resistance (ohms)
P	Power (kW)
Q	Thermal energy (kJ)
<i>p</i>	Pressure (kPa)
\dot{p}	Production rate of fuel (kg/s)
R	Universal gas constant (8.3145 J/mol K)

r	Experimental result
S	Selectivity of a compound (%)
S_X	The standard deviation of the sample population
T	Temperature (K)
$t_{95\%}$	Value from t distribution that achieves 95 % confidence level
u	Uncertainty
U	Overall uncertainty
u	Uncertainty
V	Voltage
v	Volume (L)
\dot{v}	Volumetric flow rate (m^3/s)
X	Measured variable
X	Conversion rate of a compound (%)
\bar{X}	Mean value
W	Catalyst
w	Electric energy generated (kJ)
Y	Product
Y-W	Transition complex of product with catalyst
Z	Reactant
Z-W	Transition complex of reactant with catalyst
£	Cost in pound
σ	Power to heat ratio

Subscripts

C	Conversion
c	Combined
CH_4	Methane
C_3H_8	Propane
CO_2	Carbon dioxide
D	Discharge
elec	Electrical
H_2	Hydrogen

<i>i</i>	Compound or fuel: methane or natural gas
<i>n</i>	A number of the denominated atoms
<i>m</i>	A number of the denominated atoms
<i>s</i>	Solid
<i>T</i>	Total
<i>Test</i>	Test sample
<i>ref</i>	reference gas
<i>x</i>	A number of the denominated atoms
<i>y</i>	A number of the denominated atoms

Superscripts

*	Radical molecule or atom
+	Positive ion
-	Negative ion

Abbreviations

AC	Alternating current
ANTP	Atmospheric non-thermal plasma
API	American Petroleum Institute
APPJ	Atmospheric pressure plasma jet
ATR	Auto-thermal reforming
CCS	Carbon Capture and Storage
CHP	Combined Heat and Power
Co	Cobalt
CPJ	Cold Plasma Jet
C _s	Solid Carbon
DBD	Dielectric barrier discharge
DC	Direct current
DC-RF	Direct current – radio frequency hybrid plasma
DOE	Department of Energy
DOECC	Department of Energy and Climate Change
DCFC	Direct Carbon Fuel Cell

e ⁻	Electron
ECE	Energy Conversion Efficiency
ECED	Energy Conversion Efficiency of the Discharge
EEDF	Electron energy distribution function
EU	European Energy
ETS	Emissions Trading Scheme
FC	Fuel Cell
FCC	Fluid catalytic cracking
Fe	Iron
EPA	Environmental protection agency
eV	Electron volt (temperature)
eV/mol	Electron volts per mole (energy)
GA	Gliding arc
GAT	Gliding arc tornado
GC-MS	Gas Chromatography Mass Spectrometer
GHG	Green House Gasses
GWh	Gigawatts hour
HAGO	Heavy atmospheric gas oil
HFPP	High frequency pulsed plasma
HHV	Higher Heating Value (kJ/kg)
HQ-C _s	High Quality Carbon solid
Ir	Iridium
kV	Kilovolts
kW	Kilowatts
kWh	Kilowatts hour
LHV	Lower Heating Value (kJ/kg)
LTE	Local thermodynamic equilibrium
LQ-C _s	Low Quality Carbon solid
mA	Milliamps
MCFCs	Molten carbonite fuel cells
MEA	Membrane Electrode Assembly
MHCD	Micro hollow cathode discharge
mm	Millimetre
MW	Megawatt

Ni	Nickel
NTC	Non-Traded Carbon
O ₂	Oxygen molecule
PAFCs	Phosphoric acid fuel cells
PEFC	Polymer electrolyte fuel cell
PEMFC	Proton Exchange Membrane Fuel Cell
PO	Partial oxidation
PSA	Pressure Swing Adsorbtion
Pt	Platinum
ppm	Parts per million
Re	Rhenium
Rh	Rhodium
RHEIN	Regional Hydrogen Energy Interchange Network
RF	Radio frequency
RSS	Root Sum Square
SEC	Specific energy consumption (kJ/mol of changed reactant)
SER	Specific energy requirement (kJ/mol of generated product)
SMR	Steam Methane Reforming
SOFCs	Solid oxide fuel cells
SR	Steam reforming
SRO	Steam reforming with oxygen
TC	Traded Carbon
TD	Transmission and Distribution
VGC	Viscosity-gravity constant
VGO	Vacuum gas oil
VOC	Volatile organic compounds
WE	Water Electrolysis

Terminology

Alkane	A molecule consisting of carbon and hydrogen atoms, all bonded by single bonds (C-C)
--------	--

Alkene	A molecule consisting hydrogen and carbon atoms, with a carbon to carbon double bond (C=C)
Alkyne	A molecule consisting of carbon and hydrogen atoms, with a carbon to carbon triple bond (C≡C)
Anode	Positive polarity electrode
Aromatics	Aromatic compound consisting of a hydrogen and carbon atoms and a cyclic molecular structure, with a closed conjugated system of double bonds
Atmospheric pressure	101.325 kPa
Bias error	Fixed, constant, systematic component of the total error: calibration error (bias in a measuring standard), data acquisition error and data reduction error
Biogas	Gas produced by the biological breakdown of organic matter in the absence of oxygen, composed of methane, carbon dioxide, hydrogen and hydrogen sulphide
Bipolar conduction	Conductive plasma extends to the plane electrode
Boltzmann equation	Describes the statistical distribution of one particle in a fluid
Carbocation	An ion with a positively charged carbon atom
Catalyst	A substance that changes the rate of a chemical reaction, at the end of the reaction it remains chemically unchanged
Cathode	Negative polarity electrode
Chain Propagation	During the chemical reactions reactive intermediate is continuously regenerated
Coking	Solid carbon deposition
Cold plasma	Non-thermal plasma
Conversion rate	A percentage of the reactants consumed during the reaction divided by the reactant input into the reaction
Cyclic paraffin	Naphthene, hydrocarbon with one or more carbon ring in the molecular structure
Discharge power	The amount of power (W) supplied between the electrodes after resistance

Elastic collision	Collision of particles: internal energies of colliding particles do not change and kinetic energy is conserved, resulting in geometric scattering
Electron avalanche	Multiplication of primary electrons in a cascade ionization
Electron density	The number of electrons per unit volume
Electronegative gas	Composed of molecules or atoms that attract electrons
Electropositive gas	Composed of molecules or atoms that donate electrons and form positive ions
eV energy	1 electron volt = 1.602×10^{-19} Joules
eV temperature	1 electron volt = 11,604.505 Kelvin
Excited atom	Atom with higher energy than ground state
Experimental error	The sum of the bias error and the precision error
Heavy particle	Any atom or molecule
Hetero-atom	Any atom that is not hydrogen or carbon
Heterogeneous catalysis	Catalyst is in a different phase than the reactants
Hydride ion	Negatively charged hydrogen ion
Hydrocarbon	A molecule with carbon and hydrogen atoms
Inelastic collision	A collision between particles resulting in energy transfer from kinetic to internal, causing ionization and dissociation
Ion	Atom or molecule with unequal total electron and total proton amounts
Ionization	Converting an atom or molecule to a positive or negative ion, by adding or removing charged particles
Ionization degree	The ratio of density of major charge species to that of neutral gas
Isomers	Compounds with the same molecular formula but different structures
Molecular Formula	Expression of atoms that constitute particular compound
Naphthene	Hydrocarbon with one or more carbon ring in the molecular structure

Negative ion	Atom or molecule with more electrons than protons
Neutral atom/molecule	Atom or molecule with no charge, in its ground state
Non-thermal plasma	Temperatures of electrons exceed that of heavy particles
Octane number	Percentage of isooctane in a blend of isooctane and heptane that exactly matches the knock behaviour of gasoline
Oxygenate	Hydrocarbon containing oxygen molecule
Ozone	A molecule consisting of three oxygen atoms
Paraffin	Term use to describe an alkane
Photo-ionization	Ionization of atom or molecule by a photon
Plasmatron	Refers to thermal or non-thermal plasma type such as gliding arc (specified in the text)
Positive ion	A molecule or atom with more protons than electron
Precision error	Random repeatability error
Proton	Positive hydrogen atom
Quasi-neutral plasma	An ionised gas in which positive and negative charges are present in approximately equal numbers
Radical	Highly chemically active atom, molecule or ion with unpaired electrons on an open shell configuration
Radio Frequency plasma	Plasma excited and sustained by high frequency electromagnetic fields, usually in the frequency range 1-100 MHz and wavelengths 3-300 m
Residence time	The amount of time reactants are subjected to chemical reactions (s)
Selectivity (product)	Percentage of the product in question compared to total conversion of the reactants
Superelastic collision	Inelastic collision with internal energy from atoms or molecules transferred back into kinetic
Syngas	Carbon monoxide and hydrogen
Thermal cracking	Bond breakage of organic molecules by applying heat
Thermal plasma	Temperatures of electrons and heavy particles are in equilibrium
Townsend breakdown	Development of independent electron avalanches

Unipolar conduction	Ionization regions stay concentrated close to the active electrode
Unipolar drift region	Boundary sheath connecting ionization region (plasma) with low field electrode
Vibrational excitation	Atoms in a molecule are in periodic vibrational motion, when a molecule absorbs a quantum of energy
Quasi-equilibrium	Presents features of both, thermal and non-thermal plasmas
Zeolite	Synthetic silica-alumina, a solid acidic catalyst

Chapter 1: Introduction

1.1. Research background

Hydrocarbon-related chemical processes play a significant role in the crude oil refining industry, especially the cracking of large hydrocarbon molecules into smaller, more valuable ones. In oil refineries thermal and catalytic cracking of large molecules are highly energy consuming processes with a considerable impact on the environment, also they are lacking in the selectivity of final products. In the oil industry, heavy hydrocarbon such as hexadecane cracking in two octanes, and possible reactions to increase branching, could be very attractive for applications to increase octane number in gasoline. At the same time, due to the excessive consumption of the finite fossil fuels, current global challenges in energy include the growing scarcity of oil, the security of supply and environmental degradation. All of these are well documented, within the drive to develop a cleaner and more sustainable energy infrastructure. Hydrogen has long been recognised as a key alternative fuel to replace carbon based fossil fuels in conjunction with fuel cell technology. At present hydrogen is produced almost exclusively through steam methane reforming (SMR), but this generates a significant amount of atmospheric CO₂ emissions. Hence, generation of environmentally friendly hydrogen is necessary if hydrogen powered fuel cells are to contribute substantially to a low global carbon economy. The most promising alternative for producing hydrogen from methane is direct pyrolysis of the methane. The process is optimally environmentally friendly as it does not produce any CO_x and it is more economical than SMR with carbon capture. Pyrolysis of methane requires high temperatures in excess of 1200 °C. Therefore, much current research is being conducted on the development of an efficient catalyst for the thermo-catalytic methane decomposition process at temperatures as low as ≥ 500 °C. However, thermo-catalytic methane decomposition is challenging from the point of view of catalyst stability. This is due to the continuous deposition of carbon on the catalyst or *coking*, which is the major cause of catalyst deactivation. The problem of catalyst deactivation in thermo-catalytic methane decomposition has been reported in most of the achievements in the literature over the period 1995 to 2012. Hence, technology development for CO₂ free hydrogen generation to utilize the abundant fuel methane, as well as the exploration

of other inexpensive fuels such as propane to generate hydrogen is beneficial in terms of the economy and the environment.

Non-thermal plasmas especially are considered to be very promising for the above applications, and a vast amount of experimental work has been dedicated to plasma assisted hydrocarbon conversion processes. Plasma is a term used to describe an ionized gas, consisting of positively and negatively charged particles with approximately equal charge densities. Sir Williams Crookes was the first one to identify plasma in 1879 in what is referred as a Crookes tube and called it 'radiant matter', he also referred to it as a 'fourth state of matter'. Non-thermal plasmas offer significant intensification of traditional chemical processes, essential increases in their efficiency and often successful stimulation of chemical reactions impossible in conventional chemistry. Cracking of large hydrocarbon molecules can be achieved by plasma ionization of a hydrocarbon molecule by an impact of an energetic electron. The use of non-thermal plasmas could provide better control and more selectivity of the fuel products compared to conventional methods. Whereas the use of plasmas for gaseous hydrocarbon decomposition would provide a more environmentally friendly hydrogen production technology, eliminating problems associated with catalysts. Corona discharge is a non-thermal plasma, formed on sharp points, edges or thin wires where the electric field is sufficiently large. Corona discharges, in particular, have been recognised to be very efficient in transferring source power into promoting chemical reactions.

To date, the knowledge and data present in the literature for plasma-assisted cracking of liquid hydrocarbons and decomposition of gaseous hydrocarbons is very limited. Therefore, the present project is an experimental study of hydrocarbon cracking and decomposition using a non-thermal plasma method.

1.2. Project objectives

The purpose of this research is to design, construct and test a non-thermal plasma reactor for liquid and gaseous hydrocarbon reformation. Only very few cases have been reported to have achieved liquid hydrocarbon cracking using plasma in the literature, all with high energy penalties due to the system configurations chosen. Hence, in this research, the key for hexadecane experiments is to achieve the cracking in a liquid state. To this day, the literature available on the experimental results for plasma assisted decomposition of gaseous hydrocarbons for CO_x free hydrogen generation is very scarce. To our knowledge, direct current corona discharge plasma has not been reported for the mentioned above. Compared to the current state of research in plasma chemical conversion of hydrocarbons, the work includes and adds novel experimental data for gaseous hydrocarbon decomposition to hydrogen and solid carbon using a corona discharge reactor.

In particular, the objectives of this study include:

1. Review crude oil and hydrogen production technologies, and identify unsolved problems within current and developing chemical processes for energy generation. Review the plasma chemistry and the past work on liquid and gaseous hydrocarbon reformation using non-thermal plasmas. Summarize the existing findings and identify unsolved problems.
2. Design and construct the experimental rig to satisfy the need for current study. This includes the design and construction of the non-thermal plasma reactor to processes gaseous and liquid samples, together with the set up of the precise experimental procedures.
3. Configure and validate the analysis system for liquid and gaseous hydrocarbon classification and quantification. Set-up the Gas Chromatography Mass Spectrometer (GC-MS) by installing correct column and sample inlets, and develop methods for liquid and gaseous hydrocarbon classification and quantification. The instrument is validated by calibration with certified liquid and gaseous hydrocarbon mixtures. Configure and validate the GC Chromopack for hydrogen measurement. This includes analysis method development and calibration using certified gaseous hydrogen mixtures.

4. Calibrate the measuring instruments for temperature and pressure and perform uncertainty analysis for other parameters such as discharge power.
5. Perform experiments for liquid hexadecane cracking.
6. Perform a parametric study for the decomposition of methane and propane. The parameters include residence time, discharge power, inter-electrode distance and corona polarity.

1.3. Overview of this thesis

This thesis is organised as follows. Chapter 2 presents the importance of fuels, together with the fundamentals of hydrocarbon chemistry. The chapter contains a review of crude oil refining and hydrogen generation processes and the problems encountered. Chapter 3 introduces the reader to the fundamentals of plasma, its uses and importance. In Chapter 4, a detailed state of the art review on plasma assisted hydrocarbon reformation is provided. It describes the plasma systems reported in the literature for hydrogen production from methane, including the different plasmas and reaction pathways, the key parameters and achievements. Work reported on propane decomposition and liquid hydrocarbon cracking is also presented here. The experimental facility used in this study is described in Chapter 5. Chapter 6 presents the experimental results for hexadecane cracking. In Chapter 7, the results for methane decomposition experiments are presented. In this chapter, the experimental results are compared to those reported in the literature for different plasma configurations and reaction pathways. Chapter 8 gives novel experimental results for propane decomposition. In Chapter 9, a comparative study of hydrogen generation methods, commercialised and at Research and Development (R&D) stage, is presented. The economical viability of non-thermal plasma CO_x free hydrogen generation technology combined with the fuel cell combined heat and power system (FC-CHP) is assessed here. Finally, conclusions of the current study and the recommendations for future work are given in Chapter 10.

Chapter 2: Importance and Processing of Fuels

2.1. Introduction: From ‘Oil Era’ to ‘Hydrogen Economy’

Throughout history energy has played a major role in industrial development and economic growth. To this day crude oil (also referred to as petroleum) plays a major role in meeting the world’s energy requirements (Swaty, 2005), and will remain so until a new technology is fully integrated. In the UK, 48% of the fuels used by final consumers in 2011 were products derived from crude oil (DOECC, 2012a). Although crude oil contains a relatively small amount of fuel in the gasoline range (10-25%) (DOE, 2007), the demand for such high value products is high. For example in 2011 gasoline contributed to 33 % of the key crude oil products in UK (DOECC, 2012a). Hence, to increase the yields of gasoline and other light fuels, refineries have adapted methods to break large hydrocarbon molecules to smaller ones by thermal or catalytic cracking (DOE, 2007). The key problems, in both these processes are environmental contamination and the lack of precise control of products (selectivity). The latter is particularly significant, as the detailed refinery processes and hence the design of a refinery, is so fuel specific. Overall, the problems point to the desirability of finding alternatives to thermal and catalytic cracking. An approach with considerable potential is the use of plasmas.

At the same time, concerns have arisen for energy security as continuing economic growth in China, India and Brazil presents a higher global energy demand (Dorian et al., 2006; Neef, 2009). If the world’s economy grows as expected, oil demand is projected to rise by 40 million barrels/day by 2030, and oil prices will continue to rise (Dorian et al., 2006). Growth rates for primary energy worldwide of 1.8 % (EC, 2003) and 1.5 % (IEA, 2009) per annum have been projected for the period of 2007 – 2030, with speculations that the global energy demand could triple by 2050 (Edwards et al., 2007). The oil crisis is clearly only at an initial stage and is going to take dramatic dimensions. Overall, all forecasts point to the end of the great ‘oil era’ in the period 2030 – 2040, with an accompanying severe increase in the cost of oil, leading to energy insecurity for many nations (Mierlo et al., 2006). A further problem is that the widespread use of fossil fuels (not just oil) within the current infrastructure is now considered to be the largest source of anthropogenic emissions of carbon dioxide, which is a major contributor to the effects of global warming and

climate change (Balat, 2008). The OECD reported that 4 billion tons of CO₂ in 1990 were released into the atmosphere from vehicle operations alone, with a figure of 8 billion tons forecasted for 2020 globally (Mierlo et al., 2006). The second largest CO₂ emissions source is the use of fossil fuels for domestic energy supply, amounting to 135 million tonnes in 2011 in UK alone (DOECC, 2011). Ambitious targets set to reduce CO₂, however, can only be achieved through major efficiency and conservation gains (Dorian et al., 2006). Hence, global drivers for a sustainable energy future include: reducing global CO₂ emissions, ensuring the security of energy supply and creating a new industrial and technological base for energy (Dorian et al., 2006; Edwards et al., 2008). The factors of finite fossil fuel resources and pollution both define the necessity of developing cleaner and more sustainable energy (Veziroglu and Macario, 2011) and act as catalysts for an eventually revolutionary-like transition to a non-carbon based global economy (Dorian et al., 2006).

Alternative fuels must be technically feasible, economically competitive, environmentally acceptable, and readily available. Fuels proposed and investigated for the purpose include biodiesel, methanol, ethanol, hydrogen, boron, natural gas, liquefied petroleum gas, Fisher-Tropsch fuel, electricity and solar fuels (Balat, 2008). Of these, hydrogen is the most attractive alternative to carbon-based fuels as it can be produced from diverse sources, namely: (i) *renewable*, including hydro, wind, solar and biomass, and (ii) *non-renewable*, including methane, coal and nuclear. Hydrogen can be utilized in high efficiency technologies, e.g. fuel cells for both vehicular transportation and distributed electricity generation (Edwards et al., 2008; Neef, 2009; Veziroglu and Macario, 2011). Environmentally, its use avoids all of the major emissions (Abbas, 2010).

In this chapter, a brief introduction to hydrocarbon chemistry will be given in section 2.2. Crude oil and cracking processes will be presented in section 2.3. Even though many experts agree that crude oil will play an important role in the energy sector for more than a decade, it is necessary to prepare the transition to alternative fuels. Hence, in section 2.4 an overview of the current and alternative methods of producing hydrogen, together with chemical reactions involved are presented. Section 2.5 and 2.6 addresses the importance of the hydrogen-carbon economy with methane and propane as primary energy feedstock respectively.

2.2. Hydrocarbons

2.2.1. Composition, structure and bonding

Hydrocarbons are organic compounds consisting entirely of carbon and hydrogen atoms. The molecules are composed of either single, double or triple carbon to carbon (C-C) bonds, and single carbon to hydrogen (C-H) bonds. In 1916, G. N. Lewis was the first person to propose an idea that chemical bonding could result from sharing electron pairs between two atoms. In modern chemistry this type of bonding is referred to as covalent bonding and is represented by a line between the two molecules, e.g. C-C (Carey and Sundberg, 1937). Various molecules can accommodate a characteristic amount of bonds, called the valence number, where the valence number of carbon is 4 and hydrogen is 1 (Fieser and Fieser, 1961). The structure and C-C bonding in hydrocarbons determines the type of hydrocarbon, see Figure 2.1:

- Alkanes (paraffins) are hydrocarbons with only single C-C bonds;
- Alkenes contain one or more double C=C bonds;
- Alkynes have at least one triple C≡C bond in their structure;
- Cycloalkanes (also referred to as naphthenes) contain one or more carbon ring;
- Aromatic compounds have at least one aromatic ring.

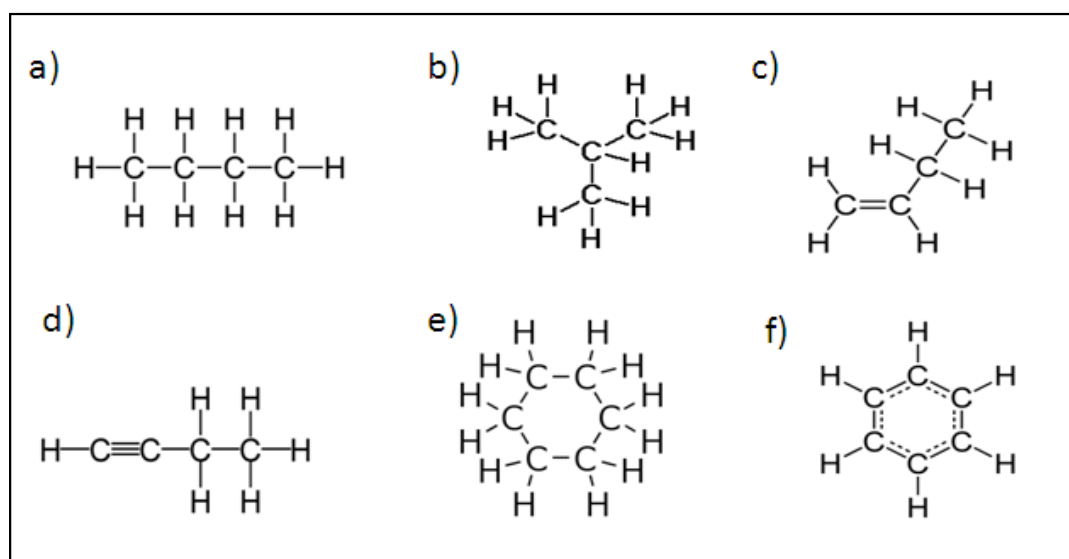
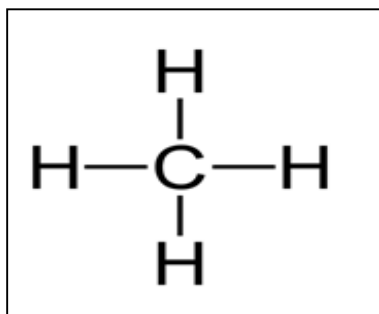


Figure 2.1: Examples of different types of hydrocarbons: a) an alkane – butane, b) an isomer of butane - isobutane, c) an alkene – butene, d) an alkyne – 1-butyne, e) a cycloalkane – cyclohexane, f) aromatic compound - cyclohexa-1,3,5-triene (benzene).

As seen in Figure 2.1, due to the different amounts of carbon and hydrogen atoms present, and the different C-C bond arrangements in different molecules, the structure of hydrocarbons may vary vastly.



Methane is the principal component of natural gas. It is the simplest alkane consisting of one carbon atom and four hydrogen atoms (CH_4). Hence, methane contains four C-H covalent bonds, refer to Figure 2.2. Hydrogen generation from methane is essentially breaking the C-H bonds.

Figure 2.2: Structure of methane.

2.2.2. Bond dissociation energies

Bond dissociation energy, as defined by Knox and Palmer (1961), is ‘the difference in energy between the parent molecule and the two fragments after bond breaking’. The dissociation energy of a bond depends on three main factors (Knox and Palmer, 1961):

- i. *The bonded atoms*: the energy requirement for C-C bond breakage in hydrocarbons is always lower than that for the C-H bonds (Simanzhenkov and Idem, 2003). For example, the dissociation energy for the middle C-C bond in butane ($\text{C}_2\text{H}_5\text{-C}_2\text{H}_5$) is 335 kJ/mol, whereas the energy required to break the C-H bond ($\text{C}_4\text{H}_9\text{-H}$) is 394 kJ/mol.
- ii. *Other atoms attached to the two bonded atoms*: for example the energy requirement to break the C-C bond in $\text{CH}_3\text{-CH}_3$ is 360 kJ/mol, whereas the energy requirement for $\text{C}_2\text{H}_5\text{-C}_2\text{H}_5$ bond is only 335 kJ/mol (Raseev, 2003).
- iii. *The configuration* (the structure) of the molecule as a whole: for example the bond dissociation energy of C-H in butane $\text{C}_4\text{H}_9\text{-H}$ is 394 kJ/mol, whereas in iso-butane $i\text{-C}_4\text{H}_9\text{-H}$ is 390 kJ/mol (Raseev, 2003).

2.3. From crude oil to gasoline

2.3.1. Crude oil composition

Crude oil is a mixture of hydrocarbon compounds ranging from the smallest with only one carbon atom to the largest containing 300 and more carbon atoms. Crude oil also contains small amounts of impurities such as sulphur, nitrogen and metals, with sulphur being the most common. Organic compounds containing sulphur are similar in structure to hydrocarbons themselves, but with the addition of one or more sulphur atoms. These compounds that contain an atom other than hydrogen or carbon in their structure are referred to as hetero-atomic compounds. The most common metal impurities found in crude oil are vanadium, nickel and sodium (Jones and Pujado, 2006).

The composition of crude oil varies between the different geographic areas of origin, the age of the oil and the depth of the individual well (Speight, 2006). In terms of the proceeding discussion, the main constituents of crude oil vary only slightly, with approximately 83 – 87 % carbon atoms, 11.5 – 14 % hydrogen and 1 – 5.5 % hetero-atoms. For example, crude oil originating from Russia consists of approximately 85 – 86 % carbon and 11 – 12.9 % hydrogen, whereas oil from the USA has a wider range of constituents with approximately 83 – 86% carbon and 11– 14 % hydrogen. However, a more significant method of describing different crudes is the fractional composition of crude oil. Each fraction is characterised by the temperatures at which boiling begins and ends. The light fractions obtained from atmospheric distillation include the gasoline range (from the start of boiling to 140 °C), the heavy naphtha (140 – 180 °C), the kerosene fraction (180 – 240 °C), and the diesel fraction (240 – 350 °C). Heavy fractions are those with boiling points above 350 °C, after further separation by vacuum distillation they undergo more processing to various fuel fractions including the vacuum gas oil (350 – 500 °C) and vacuum residue (> 500 °C); or to lubricating oils. The amount of light fractions can vary widely between the crude oils of different origins, for example, some of the oils from western Siberia (Russia) may contain over 60 % of light fractions, whereas the heavier oils from Alberta, Canada may contain as little as 20 % of the light fractions (Simanzhenkov and Idem, 2003).

2.3.2. Gasoline – importance and production

Every refinery is uniquely designed to process given crude into selected products, with an increasing demand for high value products such as gasoline (Rana et al., 2007). Separating crude oil into its various boiling fractions is one of the first and most critical operations in the refinery, and is commonly accomplished through fractional distillation (Simanzhenkov and Idem, 2003). These fractions are then chemically converted into more desirable products, which are purified by removing unwanted elements and compounds (Jones and Pujado, 2006). Typical final products of crude oil refinery in the order of lightness include gasses for chemical synthesis and fuel, aviation and automotive gasoline, aviation and lighting kerosene, diesel fuel, distillate and residual fuel oils, lubricating oil base grades, paraffin oils and waxes (Simanzhenkov and Idem, 2003). The global refinery industry is mainly driven by the demand for transportation fuels, with gasoline being the most desirable (Swaty, 2005).

Gasoline contains over 500 different types of hydrocarbons in a range of 3 – 12 carbon atoms, the main groups being: alkanes, alkenes, aromatics, oxygenates, naphthenes and other hetero-atom compounds (Simanzhenkov and Idem, 2003). As discussed in the introduction, the demand for gasoline is higher than contained within crude oil. To increase the yields of gasoline and other light fuels, refineries have adapted methods to break large hydrocarbon molecules to smaller ones by thermal or catalytic cracking, addressed in the next two sections.

2.3.2.1. Thermal Cracking

The thermal cracking process was originally developed in 1913 specifically to increase the production of gasoline (Brame and King, 1967). Thermal processes for hydrocarbon cracking such as visbreaking, delayed and fluid coking are achieved by the application of intense heat and in some cases pressure. The principle of thermal cracking is the breaking of C-C bonds in hydrocarbon molecules. Cracking proceeds at C-C bonds first, because the energy requirement for C-C bond breakage in hydrocarbons is always lower than that for the C-H bonds, as described in Section 2.2.2. The chain starts with cracking at the weakest hydrocarbon bond, which in the long chain is the C-C bond at the centre of the molecule. At moderate temperatures breaking of C-C bonds occurs symmetrically. However, at high temperatures

cracking may precede with the same probability at all C-C bonds, see Figure 2.3. This is due to the difference in energy of the C-C bonds at different locations in the molecule being smaller at high temperatures. Since thermal cracking occurs at high temperatures it may occur with the same or similar probability at all C-C bonds. Hence, it is difficult to achieve high control of desired product selectivity (Simanzhenkov and Idem, 2003).

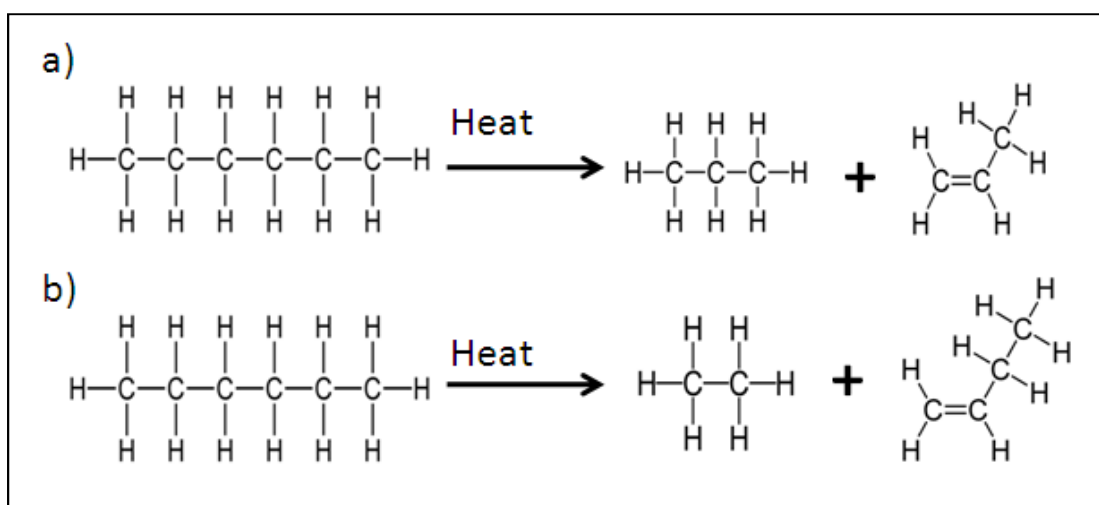


Figure 2.3: Thermal cracking using hexane molecule as an example: a) thermal cracking at moderate temperatures proceeds symmetrically and generates two molecules containing 3 carbon atoms each – a propane and a propene; b) an example of asymmetrical thermal cracking of hexane at high temperatures, which generates one molecule with 2 carbon atoms (ethane) and one molecule with 4 carbon atoms (butene).

A modern refinery uses the visbreaking thermal cracking method to convert heavy oil feed-stocks to lighter products such as fuel gas and gasoline (DOE, 2007). In general, heavy oil feed (vacuum distillation or atmospheric distillation residual) is heated in the furnace at the temperature of approximately 480 °C and then passed through a pressurised soaking zone (a reaction vessel) at pressures of approximately 690 kPa (Speight, 2006). Two designs of the visbreaking process are used in a modern refinery: coil and soaker. In the coil design, cracking is achieved within the dedicated soaking coil in the furnace. In the soaker design, some of the cracking occurs within the heater and the feed is passed to a soaker where cracking is achieved (DOE, 2007).

2.3.2.2. Catalytic cracking

Catalysis was first applied to thermal cracking of oil in 1931 to increase the yield and quality of products using less severe conditions than in thermal cracking (Brame and King, 1967). A catalyst is a substance that changes the rate of a chemical reaction, however, at the end of the reaction it remains chemically unchanged (Simanzhenkov and Idem, 2003). In catalytic cracking the active species are carbocations (an ion with a positively charged carbon atom) formed on the active sites of the catalyst (Raseev, 2003). Hence, the catalytic cracking of long hydrocarbons into lighter products can be explained by carbonium ion theory, where catalysts are classified as two groups: catalysis on metals and catalysis on acid catalysts. Typical metal catalysts are: Fe, Co, Ni, Re, Rh, Ir and Pt. During the catalytic cracking a metal catalyst promotes the removal of a negatively charged hydrogen ion from an alkane. This results in the formation of two unstable and very reactive surface compounds. Catalytic cracking on the acid catalyst proceeds via the addition of a positively charged proton (positive hydrogen atom) to an alkene, resulting in the formation of a carbonium ion. The active sites of the catalyst promote continued addition of protons or removal of hydride ions, resulting in the weakening of C-C bonds in hydrocarbon molecules and a consequent cracking into smaller compounds (Simanzhenkov and Idem, 2003). In modern refineries solid acidic catalysts such as synthetic silica-alumina (referred to as zeolites) and amorphous synthetic silica-alumina are mainly used (DOE, 2007). In heterogeneous catalysis (catalyst is in a different phase than the reactants) all reactions take place on the surface of the catalyst: reactants are adsorbed to the catalyst, chemical reactions take place on the surface of the catalyst and finally the products are desorbed. These three stages each require less energy than the corresponding total activation energy of the non-catalytic reaction. Therefore, catalytic reactions are much faster than non-catalytic reactions (Simanzhenkov and Idem, 2003).

There are three types of catalytic cracking processes used in modern oil refineries: fluid catalytic cracking (FCC), moving-bed catalytic cracking and thermofor catalytic cracking. FCC is the most widely used process, with a capacity of approximately 9.9×10^{18} litres per calendar day in the USA refineries (DOE, 1998). 'It was the commercialization of the fluid catalytic cracking process in 1942 that really established the foundation for modern crude oil refining', as recognized by

Simanzhenkov and Idem (2003). The FCC process involves the use of finely powdered catalyst, which behaves as a fluid when mixed with the vaporised feed. The most significant parts of the FCC system are the reactor and the regenerator. Pre-heated feed is mixed with the hot catalyst and introduced to the riser, where most of the catalytic reactions take place, the rest occurring in the reactor. Catalytic cracking is normally performed at temperatures ranging from 482 to 537 °C and pressures of 152 to 304 kPa. Fluidised catalyst particles are mechanically separated from cracked hydrocarbon vapour using cyclones, the spent catalyst is sent to the regenerator and the cracked hydrocarbons are separated into fractions by distillation (DOE, 2007).

2.3.2.3. Problems with conventional cracking technologies

Both thermal and catalytic cracking processes generate airborne contaminants. Catalytic cracking is one of the largest sources of air emissions in a refinery, including SO_x, CO, hydrocarbons, NO₂, aldehydes and ammonia. Thermal cracking also generates some wastewater, whereas catalytic cracking produces not only large amounts of wastewater but also spent catalyst material. The latter involves the added costs of disposal and recycling (DOE, 1998).

Conventional cracking methods use high temperatures and as noted cracking may occur with the same probability at all C-C bonds, this reduces the control of product selectivity. Problems may also occur when reactions involve aromatics, as aromatic compounds have a high tendency to undergo polycondensation reactions and form coke, which decreases the yields of desirable fractions. In catalytic cracking, compounds resistant to cracking can block the active sites of the catalyst, and coke deposition may cause catalyst deactivation, both resulting in impaired catalyst efficiency and the need for regeneration (Simanzhenkov and Idem, 2003).

2.4. Fuelling the future: from hydrocarbon to hydrogen

2.4.1. Hydrogen Economy

The hydrogen economy is generally viewed as the replacement of the overwhelming majority of petroleum fuels with hydrogen. The hydrogen can be burned in IC engines, external-combustion (jet) engines, or preferably, used in fuel cells to generate power in transportation and stationary sectors more efficiently (Bockris, 2002; Balat, 2008). The major future markets for hydrogen depend primarily upon 4 factors: (i) the future cost of hydrogen; (ii) the rate of advances of various technologies that use hydrogen; (iii) the potential long term restrictions on greenhouse gases (GHGs); (iv) the cost of competing energy systems (Balat, 2008; Bartels et al., 2010). The future of the hydrogen economy is highly dependent on the availability of low cost and environmentally friendly sources of hydrogen (Bartels et al., 2010).

‘In a world where petroleum will become increasingly scarcer, hydrogen technology could significantly and quickly reduce energy system costs, improve GHG intensity, and help achieve sustainable economic development’ (Tseng et al., 2005). Limitations of fossil fuel resources and concerns about climate changes associated with global warming led to the first World Hydrogen conference in 1976, which identified hydrogen as a clean energy carrier for the future (Utgikar et al., 2011). Hydrogen and fuel cells are ‘considered in many countries as an important alternative energy vector and a key technology for future sustainable energy systems in the stationary power, transportation, industrial and residential areas’, as recognised by the Department of Energy (DOE) in 2004 and the European Commission (Edwards et al., 2008). A study commissioned by the UK Department of Trade and Industry found that hydrogen energy offers the prospect of meeting key UK policy goals for a sustainable energy future (Edwards et al., 2008). It is quite apparent that the majority of experts consider hydrogen technology to be a long term solution for energy and environmental concerns (Bockris, 2002; EC, 2003; Dorian et al., 2006; Mierlo et al., 2006; Balat, 2008; Edwards et al., 2008). Therefore, countries globally are developing roadmaps to a future hydrogen economy and fuel cell deployment, and the global mentality as regards to transition to a hydrogen economy is at the stage of *when* and *how*, not *if* (Edwards et al., 2008).

2.4.2. Applications of hydrogen

Current uses of hydrogen include synthesis of ammonia and other nitrogenated fertilizers; refining and desulphurization (hydrogenation reactions, hydrodesulphurization); chemical plants and food preparation; synthesis of methanol, ethanol and dimethyl ether; rocket fuel; IC engine fuel; high temperature industrial furnaces fuel (Balat, 2008); alternative metallurgical processes, for example recovery of nickel and lead from their ores by means of hydrogen reduction; obtaining organic chemicals from coal (Bockris, 2002). Hydrogen gas is also being explored for use in fuel cell electric vehicles, fuel cells are in the early stages of commercialization and offer a more efficient use of hydrogen (Balat, 2008). Besides their application in transportation – cars, buses, delivery vehicles, and ships – fuel cells can also provide electricity to a wide range of other products, ranging from small portable items such as mobile phones and laptops, to domestic and industrial energy (EC, 2003). The advantages of hydrogen powered fuel cells include:

- i. **High efficiency:** fuel cells convert fuel to electricity at more than twice the efficiency of internal combustion engines (IPHE, 2010). In transportation, fuel cells can achieve 65 % electrical efficiency, compared to the internal combustion engine's 25.8 % (petrol driven). If heat generated by fuel cell is utilized in a combined heat and power systems for stationary applications, 85% efficiency can be achieved (Edwards et al., 2008).
- ii. **Low or zero emissions:** hydrogen fuel cells emit only water and have virtually no pollutant emissions due to their low operating temperature (Edwards et al., 2008; Synnogy Ltd., 2009).
- iii. **Comfort:** fuel cells are silent, vibration-free and very little or no maintenance is required (Synnogy Ltd., 2009; IPHE, 2010).
- iv. **Providing energy at all scales:** from micro power sources to multi-MW power plants (IPHE, 2010).

Hence, fuel cells can contribute substantially to a low global carbon economy, improve urban air quality and human health and enhance energy security by allowing

a wider choice of fuels (Synnogy Ltd., 2009). Hydrogen and fuel cells are increasingly considered to be a key technology for a sustainable and environmentally friendly energy supply for the future (Balat, 2008). For more information about fuel cell technology and commercialisation see Appendix A.

2.4.3. Hydrogen sources and production

Hydrogen can be produced from renewable sources such as biomass by processes, which include: steam gasification (of bio-nut shell, black liquor), pyrolysis (of olive husk, crop straw), and microbial fermentation (of pulp and paper waste, manure slurry) (Balat, 2008). However, more research and development is necessary as the yields are low for all of the above processes. Hydrogen can also be produced from water by using a variety of energy sources such as wind, solar, geothermal, hydropower, and nuclear energy (Balat, 2008). Currently the primary method of hydrogen production is the conversion of natural gas by the steam reforming process (Muradov et al., 2005; Balat, 2008; Neef, 2009). Approximately 96 % of hydrogen produced to date comes from fossil fuel conversion. Natural gas reforming contributes 48 %, oil 30 %, coal 18 % and water electrolysis 4 % to the total global hydrogen production (Balat, 2008). In the near to medium-term fossil fuels will play a major role in hydrogen production due to their availability, relatively low cost and the existing infrastructure for delivery and distribution (Muradov et al., 2005).

In 2007 global natural gas reserves (177.36 Tm^3) were estimated to last for a further 60 years at the current consumption rate (Bartels et al., 2010). It could be argued that this timescale will be less if more natural gas is utilized for hydrogen production. However, according to Balat (2008) natural gas resources will be sufficient to accommodate the expansion of supply for several decades to support the FreedomCar and Hydrogen Fuel initiatives. It is anticipated that by 2040 the use of hydrogen in fuel cell powered cars and light trucks could replace consumption of petroleum by 18.3 million barrels per day. The above initiatives are two complementary US government-industry R&D policies that promote the development of hydrogen fuel and fuel cell vehicles. Coordinated by the DOE, the initiatives aim, from the time of their launch, to mass-market fuel cell and hydrogen combustion vehicles at an affordable cost within 10 to 15 years. Assuming that hydrogen powered vehicles have 2.5 times the energy efficiency of improved

gasoline vehicles, the anticipated reduction in petroleum use would require an annual production of approximately 150 million tons of hydrogen by 2040 (Balat, 2008).

According to an EC report (EC, 2003) the wide variety of hydrogen sources will enable Europe to exploit those sources in ways that are best adapted to regional circumstances, and so provide security of energy supply that is environmentally friendly and sustainable. This key assessment that hydrogen production from methane can be classed as sustainable has been confirmed by Muradov et al (2005). The assessment is on essentially the same grounds: future methane can be obtained from a variety of currently unused and extremely large sources such as landfill gas and biogas (50 – 70 % of methane). Both of these sources are vast and unused: for example in Florida 59 landfill sites produce 1.6 m³/day of methane. Another source, rated as inexhaustible, is the methane hydrates present as the ice-like material occurring in marine sediments. However, Muradov et al, (2005) also point out that more research is needed to be able to incorporate this source.

Hydrogen can not only be produced from a variety of sources, but also by a number of quite different processes. These include: steam reforming of methane (SMR), partial oxidation (PO) of hydrocarbon fuels, coal gasification, reformation of biomass and water electrolysis (Balat, 2008). They are described in detail below, and the fundamental chemical reaction is specified for each process. The pyrolysis approach is a key to this study and will be considered in a separate section.

i. Steam reforming of methane

As previously mentioned, at present hydrogen is produced almost exclusively from fossil fuels, through steam reforming of methane (SMR). The process comprises 48 % of global hydrogen production (Balat, 2008) and 95 % of the commercialized hydrogen production in the US (Muradov et al., 2005). SMR is a well developed method and, at 83 %, has the highest system efficiency of all methods (Abbas, 2010). SMR, whether of natural gas or methane from other sources, produces a hydrogen rich gas with typical hydrogen content in the order of 70 – 75 % on a dry basis, together with smaller amounts of CH₄ (2 – 6 %), CO (7 – 10 %), and CO₂ (6 – 14 %). The SMR process consists of 3 main steps (Balat, 2008; Amin et al., 2011):

1. Methane is catalytically reformed at an elevated temperature and pressure to produce a syngas mixture of hydrogen and carbon monoxide;
2. A catalytic water gas shift reaction is then carried out to combine carbon monoxide and water to produce further hydrogen;
3. The hydrogen product is then purified by adsorption.

For SMR the reforming reaction for syngas generation (step 1 above) is:



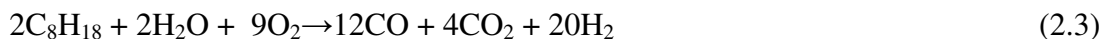
A catalytic water shift reaction is then carried out (step 2 above) to increase the yield of hydrogen. However, with the penalty of carbon dioxide generation:



SMR is currently both the most popular and the most economical method among the current commercial processes (Balat, 2008; Bartels et al., 2010; Veziroglu and Macario, 2011). According to Bartels et al. (2010) the approximate cost of hydrogen production using SMR was 2.48 – 3.17 US \$/kg of hydrogen in 2007. Since 1 kg of hydrogen is equivalent to approximately 1 gallon of gasoline in terms of energy use and the price of gasoline is 2 - 4 US \$/gallon, SMR for hydrogen production is economically competitive with conventional fuels (Bartels et al., 2010). The variation in the cost of hydrogen production by SMR is mainly due to the variable price of natural gas (Schoots et al., 2008; Bartels et al., 2010), which as feedstock contributes 52 – 68 % to the final hydrogen cost for larger plants, or 40 % if they are smaller (Balat, 2008).

ii. Partial oxidation of hydrocarbon fuels

Partial oxidation of hydrocarbons (PO) is an exothermic reaction with oxygen and steam. For example PO reaction using octane (Balat, 2008):

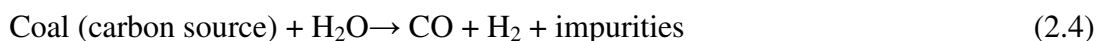


The amounts of oxygen and water vapour are controlled so that once established the reaction proceeds without the need for external energy (Balat, 2008). The overall system efficiency is 70 – 80 %, comparable with SMR (Abbas, 2010). Similar to

SMR process, Bromberg et al. (2000) have concluded that the price of hydrogen in plasma-catalytic PO of methane is most sensitive to the cost of natural gas.

iii. Coal gasification

Hydrogen production from coal is a well established commercial technology with a reported system efficiency of 63 % (Abbas, 2010). The reaction for the process can be presented as (Balat, 2008):



As for SMR process, a water shift reaction (shown in formulae (2.2)) is applied to increase hydrogen yield at the penalty of generating CO₂. The method is little used, except in areas where oil and gas are expensive, e.g. South Africa and China. Coal gasification accounts for 18 % of the world's hydrogen production (Balat, 2008). The cost of hydrogen production from coal is much lower than from methane, at 1.15 – 1.56 \$/kg hydrogen. However, the process has major drawbacks such as the generation of very high CO₂ levels and intrusive coal mining (Bartels et al., 2010).

iv. Reformation of biomass

Biomass reformation defines a range of processes, including pyrolysis, gasification, steam gasification, steam reforming of bio-oils, enzymatic decomposition of sugars and catalytic steam reforming (Balat, 2008). Thermochemical gasification and pyrolysis of biomass are the more developed processes, with system efficiencies reaching up to 50 % (Abbas, 2010), and the cost of hydrogen as low as 1.44 – 2.83 \$/kg hydrogen (Bartels et al., 2010). Biomass-based hydrogen production constitutes one of the more promising options for a long-term non-carbon and sustainable hydrogen supply system. However, no processes for hydrogen production from biomass are currently available commercially and it is not capable of meeting the demand for hydrogen, at least in the near future (Edwards et al., 2008). The use of edible biomass for hydrogen production competes with food production in terms of land use. Recent studies suggest that sourcing biofuels from energy crops increases GHG emissions due to the increased use of land which would otherwise be devoted to agriculture (Bartels et al., 2010).

v. Electrolysis of water or steam

Electrolysis means splitting water or steam into hydrogen and oxygen (Balat, 2008), giving the reaction:



The system efficiency achieved is 45 – 55 % (Abbas, 2010), with the hydrogen price typically in excess of 8 US \$/kg (Balat, 2008). The process requires large amounts of electricity, which is the major cost factor (Balat, 2008). However, if low cost nuclear generated electricity is used the hydrogen price can be lowered to 4.36 - 7.36 \$/kg (Bartels et al., 2010). Hydrogen production from water using renewable sources of electricity, such as wind, hydro and solar has also been proposed. All things considered, however, the price of hydrogen using electrolysis is still higher than that from pyrolysis (Bockris, 2002) and SMR (Edwards et al., 2008).

2.5. Pyrolysis of methane – The Hydrogen-Carbon economy

2.5.1. Thermo-catalytic methane decomposition

The SMR process generates a significant amount of CO₂ atmospheric emissions which has a global warming potential of 13.7 kg/CO₂ equivalent per kg of net hydrogen produced. For example, an SMR plant with a capacity of 1 million m³ hydrogen production generates 0.3 – 0.4 million m³ CO₂/day, which is normally vented to the atmosphere (Muradov et al., 2005). However, the decomposition of methane and the production of carbon without its oxides could be greatly beneficial. Pyrolysis of methane is a direct decomposition of methane into hydrogen and carbon black (Fridman, 2008):



Methane pyrolysis is the most promising alternative for producing hydrogen from methane (Edwards et al., 2008). The process is most environmentally friendly as it does not produce any CO_x (Fulcheri and Schwob, 1995; Muradov et al., 2005; Ahmed et al., 2009; Abbas, 2010), and is the most economical option when compared to SMR with carbon capture (Bockris, 2002; Muradov et al., 2005; Dufour et al., 2009; Besser and Lindner, 2010; Dufour et al., 2010). Pyrolysis of methane requires high temperatures in excess of 1200 °C (Muradov et al., 2005; Li et al.,

2011). Therefore, much research is conducted on the development of the efficient catalyst for the thermo-catalytic methane decomposition process (Muradov et al., 2005a) at temperatures as low as 500 °C (Li et al., 2011). Majority of the research has been focused on metal based catalysts, with nickel being at the top of the list due to its high activity at lower temperatures and low cost (Suelves et al., 2005; Li et al., 2011). However, thermo-catalytic methane decomposition is challenging from the catalyst stability point of view (Suelves et al., 2005; Li et al., 2006a; Pinilla et al., 2010). In thermo-catalytic methane decomposition, carbon deposits continuously on the catalyst forming graphite-like structures, also referred to as coking. Coking is the major cause of catalyst deactivation and damage to metal based catalyst granulate structure due to volume expansion. For example, nickel catalyst only needs 10 – 250 mg of carbon to deactivate 1 g of catalyst (Li et al., 2011). For methane pyrolysis, the solid carbon to hydrogen ratio generated is 3:1. Hence, putting the above in a commercial perspective, the maximum hydrogen generation from 1 g of nickel catalyst is 83.3 mg (250 mg carbon divided by the ratio of 3). Li et al. (2011) reported an extensive review on thermo-catalytic methane decomposition achievements in the literature from 1995 to 2010, catalyst deactivation problem has been reported in all of the systems reviewed.

In general, higher methane conversion and hydrogen production rates can be achieved at higher temperatures for methane thermo-catalytic decomposition on metal catalysts. However, low catalyst lifetime has been shown due to higher carbon deposition, some examples are described in this section. Villacampa et al. (2003) reported that for a nickel catalyst the first induction period of fast carbon growth at 0 – 1 h results in drastic methane conversion as well as hydrogen generation decrease, where higher methane conversion rates increase the deactivation rate, see Figures 2.4 and 2.5.

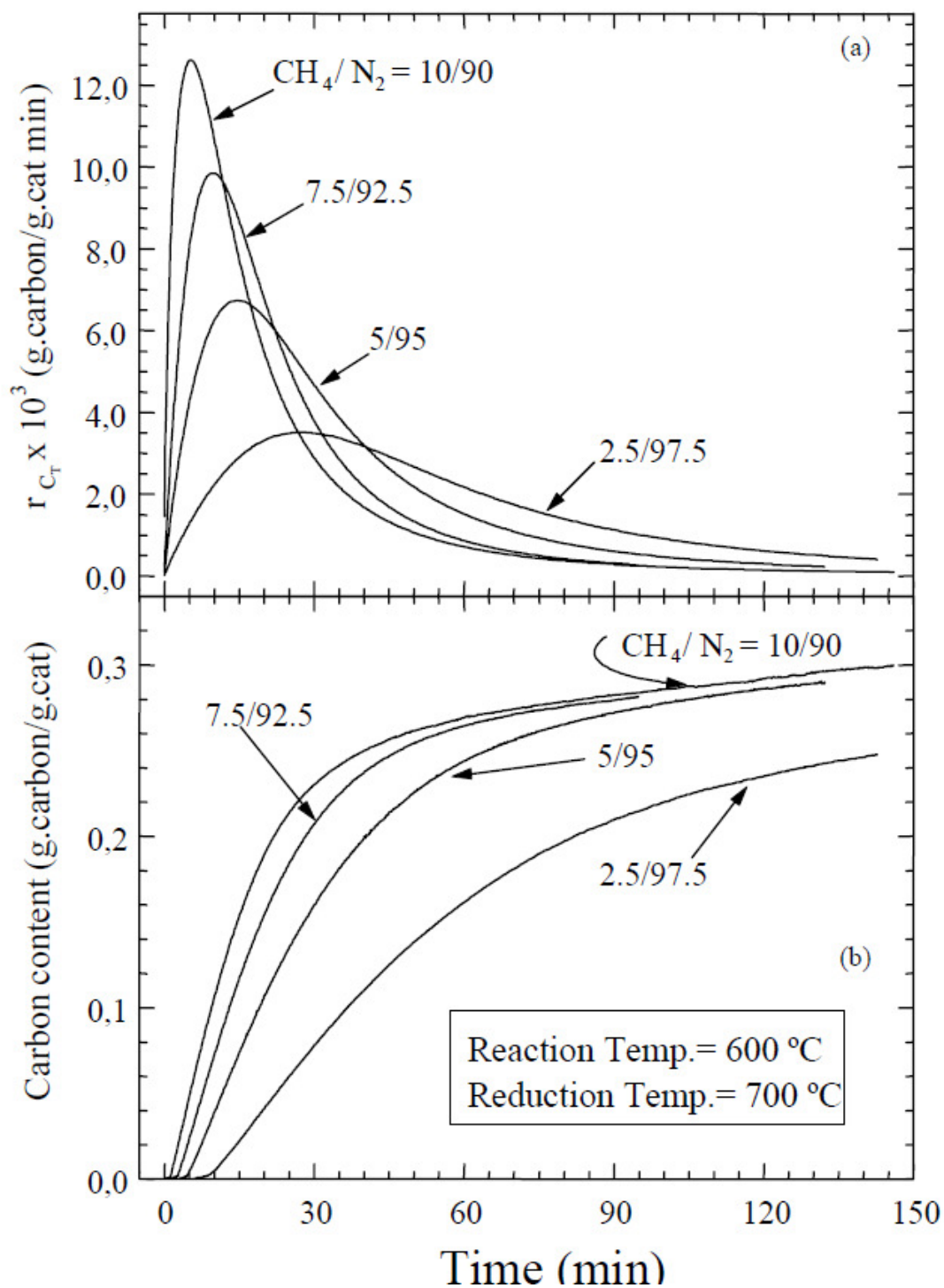


Figure 2.4: Time on stream experiments for methane decomposition using nickel catalyst reported by Villacampa et al. (2003) (Fig. 3) at different methane to nitrogen ratios shown on the graph: a) methane conversion rate against time, shows methane conversion decrease within first hour of operation; b) carbon deposition rate with time, shows highest deposition rate within the first hour.

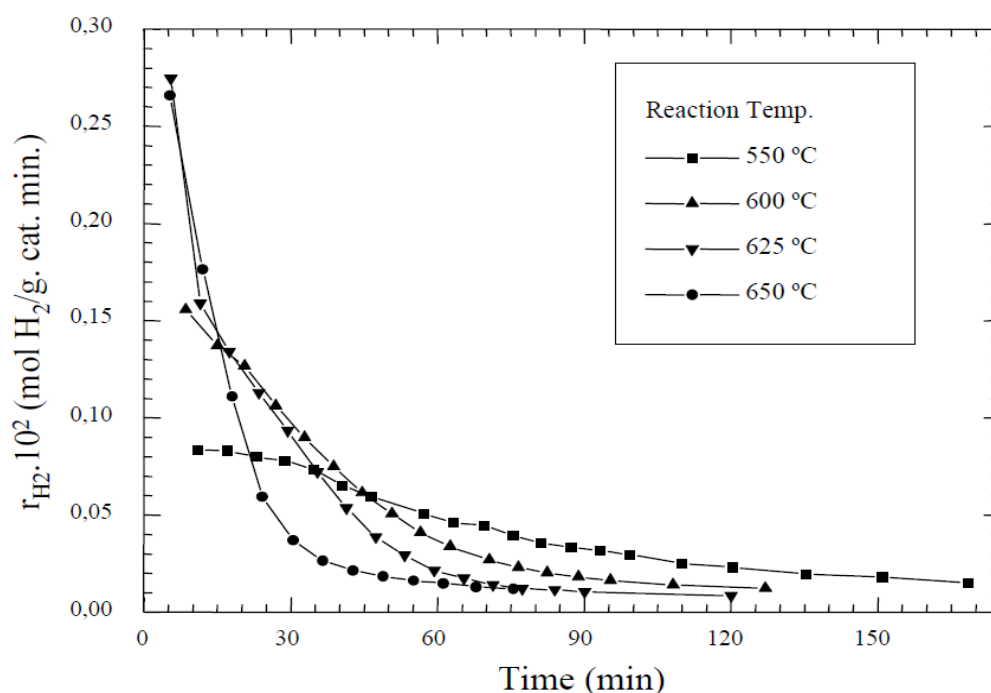


Figure 2.5: Time on stream experiments for methane decomposition using nickel catalyst reported by Villacampa et al. (2003) (Fig. 8) at different temperatures, showing hydrogen production versus time and steep hydrogen generation rate decrease in the first hour of operation.

Suelves et al. (2005) used a commercial nickel catalyst supported by silica alumina, either as fine particles ($< 100 \mu\text{m}$) or pellets (2 mm) for thermo-catalytic decomposition of methane. At lower temperatures of $650 \text{ }^\circ\text{C}$ methane conversion and hydrogen production by volume of 55 % and 70 % respectively has been achieved, and the catalytic activity was sustained for an 8 hour operation period at flow rates between 20 – 100 ml/min (Suelves et al., 2005). At higher temperatures of $700 \text{ }^\circ\text{C}$ methane conversion and hydrogen production increased to 65 % and 80 % respectively. However, increasing the flow rate of methane to 50 and 100 ml/min resulted in a full deactivation of catalyst at 1 and 3.3 h respectively, see Figure 2.6 (Suelves et al., 2005). According to the authors, nickel catalyst recovery is not feasible. Therefore, the catalyst material has to be cheaper than the generated carbon value to counteract the cost.

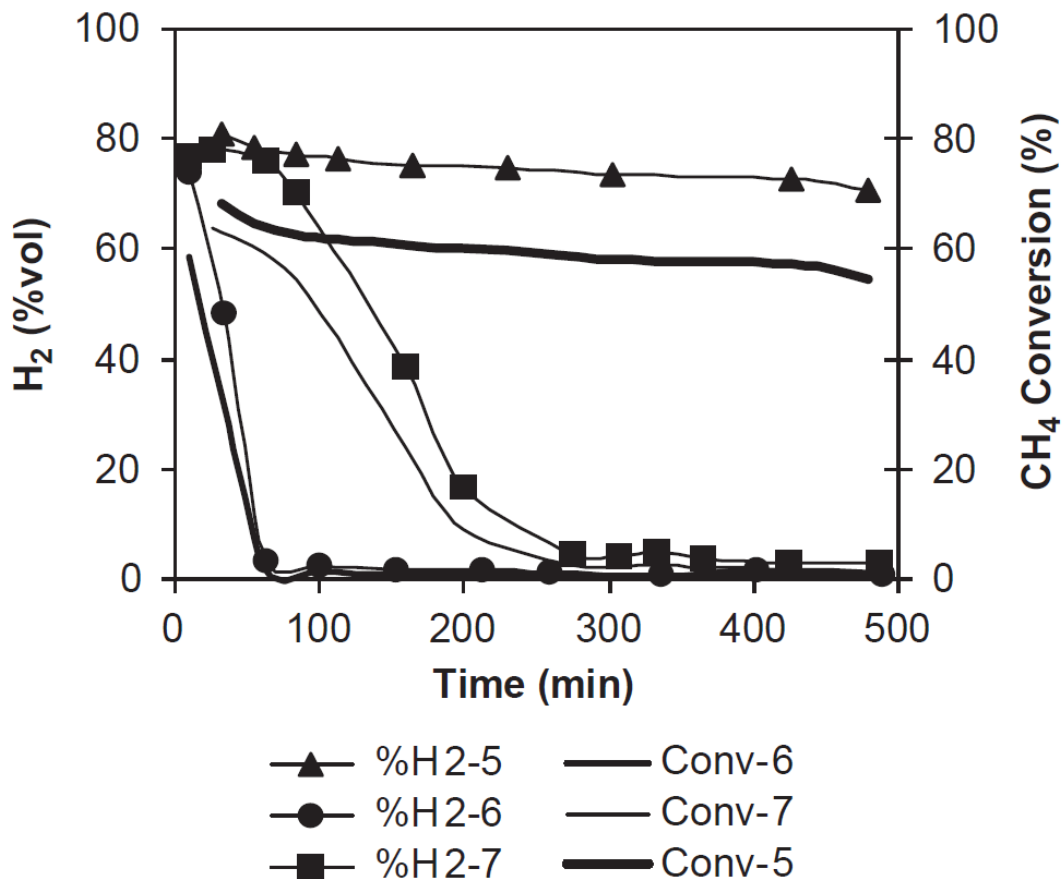


Figure 2.6: The effects of the CH₄ flow rate on hydrogen production and methane conversion rate for methane decomposition using nickel catalyst reported by Suelves et al. (2005) (Fig. 4). Run 5 is at 20 ml/min; run 7: 50 ml/min; run 6: 100 ml/min.

Pinilla et al. (2010) reported the use of nickel-copper bi-metallic catalyst in a fluidised bed reactor. At 750 °C the initial production of hydrogen reported at 78 % by volume, a sharp decrease is noted within one hour, then a gradual decrease to 30 % at 6.7 h of operation. At lower temperatures of 700 °C catalyst shows slightly higher stability with initial hydrogen production rate of 70 %, decreasing to 45 % at 6.7 h (Pinilla et al., 2010), see Figure 2.7. Similar effects have been shown with cobalt catalyst by Italiano et al. (2010), where initial methane conversion increased from 66.2 to 90 %, but catalyst lifetime decreased from 19.3 to 11.6 h, with temperature increase from 600 to 700 °C.

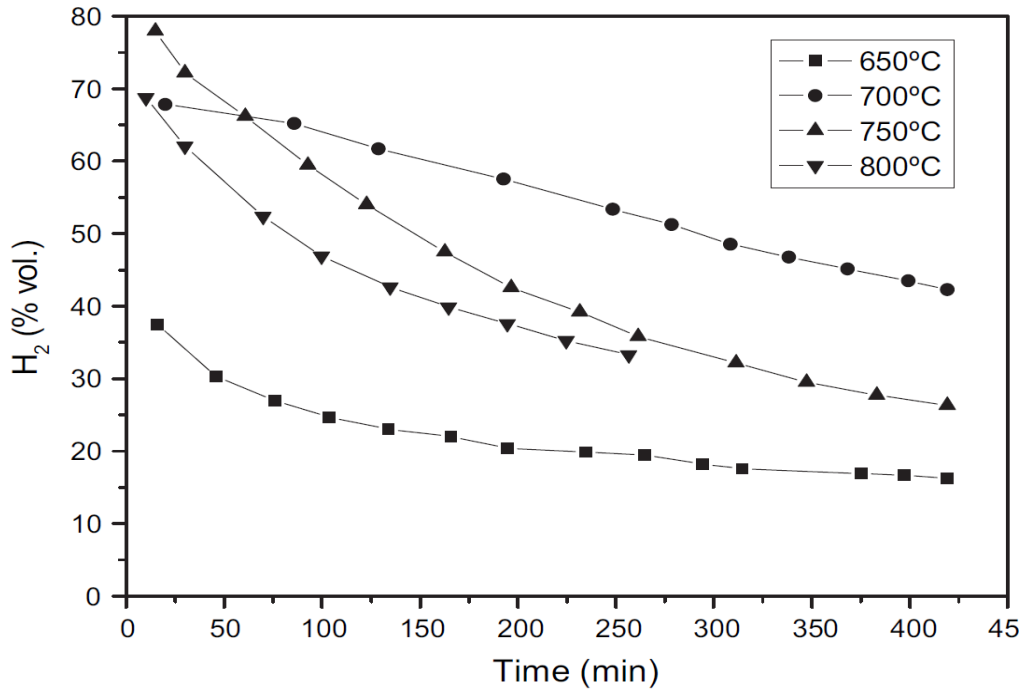


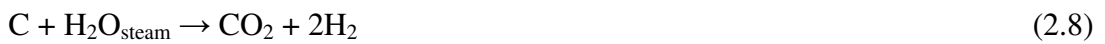
Figure 2.7: Time on stream effect on hydrogen generation from methane using nickel-copper catalyst at different temperatures, reported by Pinilla et al. (2010) (Fig. 4).

According to Li et al. (2011) for thermo-catalytic methane decomposition to be industrially viable, two processes are necessary:

1. Catalytic methane decomposition reaction



2. Catalyst regeneration



or



or



The catalytic regeneration process requires high temperatures (> 900 °C) and as seen above the process leads to the generation of CO_x compounds, amounts of which can be nearly comparable to the quantity of the CO_x emitted by the SMR processes

(Muradov et al., 2005a). A further problem is that catalyst regeneration and carbon separation has not yet been shown to be viable (Suelves et al., 2005). Villacampa et al. (2003) reported after nickel catalyst regeneration hydrogen production rate was initially recovered. However, deactivation rate of the catalyst that has been regenerated is much higher than that shown by the fresh catalyst. Repeated regeneration results in a drastic loss of catalytic activity, see Figure 2.8. Villacampa et al. (2003) suggest that this is due to an increase in size of nickel crystallites during the regeneration stage and the possibility that not all of the coke is removed.

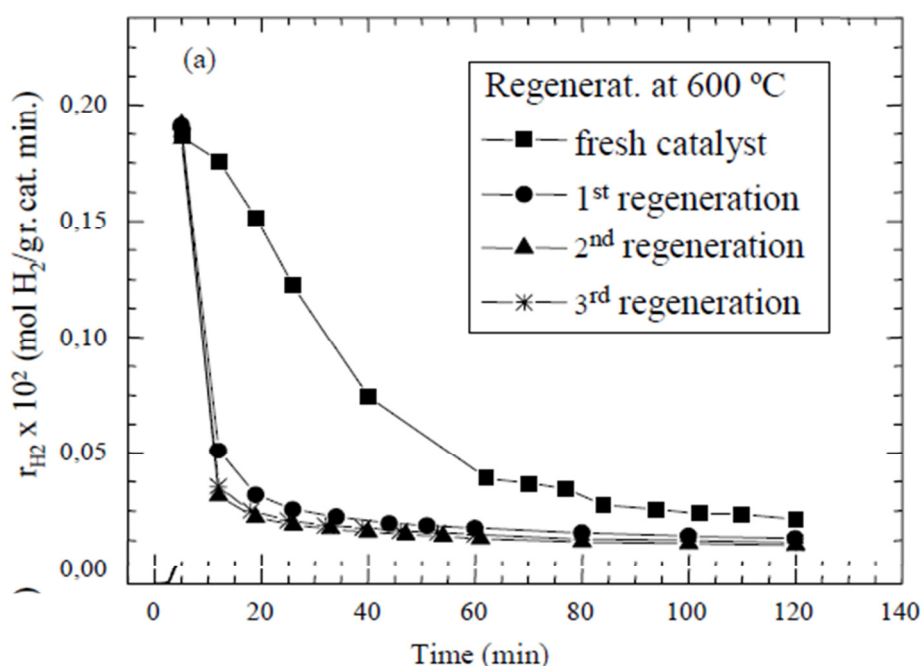


Figure 2.8: The effect of nickel catalyst regeneration process on hydrogen production reported by Villacampa et al. (2003) (Fig. 11). Shows a much lower hydrogen generation rate within 20 min after regeneration cycle.

Carbon catalysts for thermo-catalytic methane decomposition have also received some attention in the last decade. According to Muradov et al. (2005), the advantages of carbon based catalysts include low cost, tolerance to impurities such as sulphur and the production of marketable solid carbon. Abbas and Daud (2009) employed activated carbon as catalyst for methane decomposition at working temperatures of 850 – 950 °C and reported nearly complete deactivation of carbon catalyst at 0.5 h and 1 h for the experiments at 950 °C and 850 °C respectively. The authors claim that long term stability of the catalyst could be achieved via catalyst

regeneration at 1000 °C with carbon dioxide. However, as mentioned above, generation of CO_x compounds during the regeneration process counteracts the efforts of methane decomposition to generate CO_x free hydrogen. Similar to metal catalysts, carbon catalysts are also deactivated at faster rates when methane conversion is higher, due to faster carbon deposition rate (Abbas and Daud, 2009a). Ling et al. (2011) reported the use of char as a catalyst, where initial methane conversion at 850 °C reached 86 % and hydrogen yield of 90 %. However, catalyst deactivation occurred within 2 h of operation with methane conversion and hydrogen yield dipping to 30 and 40 % respectively. Hence, it is clear that as for the metal catalysts described above, carbon deposition is the reason for the deactivation of the carbon catalysts. According to Abbas and Daud (2010) the explanation for this is that the deposited carbon has a lower surface area and activity when compared to the original carbon catalyst.

2.5.2. The use of solid carbon

The decomposition of methane produces solid carbon such as graphite or carbon black (Ahmed et al., 2009; Amin et al., 2011) which is much easier to sequester than carbon compounds in gaseous form (Abbas, 2010), whilst also adding further value to the process. In the US, approximately 5 million tons/year of carbon is used in the production of electrolytes for aluminium (this takes 0.4 – 0.5 kg per kg of aluminium) and by the ferroalloy industries. If the production of carbon were to increase, there are further potential applications as described in this section.

Solid carbon can be used as a building and construction material. Carbon to carbon composites are better than other building materials such as steel, as they do not corrode, are 5 times lighter than steel, and can be installed without the use of heavy construction equipment. For example a 40 story building has already been designed completely in carbon to carbon material. Another industrial application is that of manufactured graphites, for example, graphite pipes find extensive application in various branches of industry due to their anticorrosive and thermostable properties (Muradov et al., 2005).

Studies have shown that the application of carbon products (e.g. charcoal) to soils increases germination, plant growth and hence crop yield (Glaser et al., 2002). Carbon applied to soil increases its nutrient and water retention capacities, supports

microbial communities and activates root activity, thereby promoting biomass growth (Glaser et al., 2002). The stimulation of plant growth has been shown to result from a wide range of carbonaceous materials, such as coke, graphite, black carbon, soot, and coal. Carbon products from methane pyrolysis (particularly disordered carbon with relatively high surface area) are similar to carbon materials currently used for soil fertilization. Finally, by using these carbon products the amount of fertiliser needed could be reduced (Muradov et al., 2005).

Carbon can be used to produce electricity via Direct Carbon Fuel Cells (DCFC), conversion efficiencies of up to 80 % have been achieved for this system (Giddey et al., 2012). Carbon is a good adsorbent for gasses due to its high surface area and abundant pore volume, studies have shown carbon nano-tubes are viable for hydrogen storage (Cheng et al., 2001; Orinakova and Orinak, 2011). Carbon nano-tubes can also be used in the Gas Chromatography column preparation for hydrocarbon determination and liquid chromatography (Herrera et al., 2012).

2.6. Propane decomposition for hydrogen production

2.6.1. Advantages of propane pyrolysis

As mentioned in section 2.5, pyrolysis yields two valuable products, hydrogen and carbon, without any harmful emissions. The production of hydrogen from gaseous hydrocarbons, such as propane, would especially benefit the operation of oil refineries. The demand for hydrocarbon feedstock and products vary over time, so using propane in this way gains the industry more flexibility of feedstock choice (Rakib et al., 2010). Propane is attracting considerable attention in hydrogen production studies primarily because it is a major constituent of liquefied petroleum gas (Faria et al., 2008; Wang et al., 2010a; Rafiq and Hustad, 2011; Wang et al., 2011). In addition, propane is produced in relatively high amounts from natural gas and in the refining of crude oil (Ostermark, 1995; Faria et al., 2008; Wang et al., 2010a; Rafiq and Hustad, 2011; Wang et al., 2011). Propane is also attractive for on-board hydrogen generation, because it is liquefiable and easy to store and transport (Zeng et al., 2010; Wang et al., 2011). Lastly, propane is an inexpensive fuel of high energy density, so offers a new alternative for more economical hydrogen production (Ledjeff-Hey et al., 2004). Overall, propane is a widely available and inexpensive fuel which can be stored and transported easily, for example, in the European Union

and Russian Federation, propane is delivered in cylinders as domestic fuel and for vehicles at gas filling stations (Solovyev et al., 2009). Hence, in the next two sections catalytic propane reformation reported in the literature will be described.

2.6.2. Catalytic propane reforming

There are four main approaches for propane reformation to generate hydrogen (Rakib et al., 2010):

1. Pyrolysis - direct decomposition:



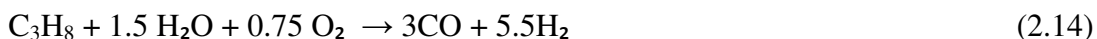
2. Partial oxidation:



3. Steam reforming :



4. Auto-thermal reforming:



For steam reforming of propane, industrial operations use excess of steam to minimize catalyst deactivation by carbon deposition and increase the hydrogen yield by water gas shift. However, excess steam results in higher CO₂ emissions (Rakib et al., 2010). Nickel based catalysts are preferred for steam reforming due to its activity and the low cost (Rakib et al., 2010). The use of precious metal catalysts such as ruthenium for steam propane reforming (Mitchell and Kenis, 2006; Schadel et al., 2009) and autothermal reforming (Lee et al., 2009), and rhodium for partial oxidation (Silberova et al., 2005) and steam reforming (Kusakabe et al., 2009) can achieve nearly 100 % propane conversion and impressive hydrogen selectivities. However, the use of high temperatures and precious metals are not favourable from the cost and feasibility point of view. Also, all of the catalytic systems above generate CO₂ due to the addition of oxygen species in the system to avoid carbon deposition and, hence, catalyst deactivation.

2.6.3. Pyrolysis and thermo-catalytic decomposition

As previously stressed – the decomposition pathway to produce hydrogen is the most environmentally beneficial approach for hydrogen production. However, this reaction is challenging in terms of catalyst stability, as described for methane thermo-catalytic decomposition in section 2.5.1. Catalysts including nickel and bi-metallic nickel-copper (Solovyev et al., 2009), iron and bimetallic iron-palladium, iron-molybdenum and iron-nickel (Wang et al., 2005), activated carbon based metal catalysts (TM-AC), where TM is manganese, iron, cobalt, vanadium or nickel (Jibril and Atta, 2011) have been reported in the literature for propane decomposition. Some of the main achievements in these systems will be addressed in this section.

Solovyev et al. (2009) performed experiments for non-catalytic propane pyrolysis, and nickel and nickel-copper catalytic propane decomposition for CO_x free hydrogen and carbon nanofiber generation. Pyrolysis experiments at 700 °C resulted to almost 90 % propane conversion, but only 11 % hydrogen was achieved, with methane being the main by- product. The authors believe this is mainly due to the C-C bond breaking rather than higher energy C-H bond. In the experiments with nickel catalyst, 95 % of propane conversion was achieved with the only gaseous products being 35 % hydrogen and 65 % methane, at 550 °C in the first 1.5 hour of the reaction. However, as the processing exceeds 1.5 hours, propane conversion and reactant concentrations decreased until nearly no effect observed at 4 hours due to catalyst deactivation, see Figure 2.9. The addition of copper to nickel to generate bi-metallic catalyst has increased the lifetime of the catalyst and hydrogen selectivity. When 50 % nickel – 40 % copper bi-metallic catalyst was used at 600 °C, highest propane conversion and hydrogen concentration of 80 and 60 % respectively was achieved. Propane conversion gradually decreased together with hydrogen concentration in the stream equalling to 35 and 25 % respectively after 12 hours of operation, further decrease is noted by the authors as the operation time reaches 45 hours, see Figure 2.10. (Solovyev et al., 2009). Even though the propane decomposition system proposed by Solovyev et al. (2009) yields pure and CO_x free hydrogen and valuable carbon nanofibres, the main problem of catalyst deactivation in the case of nickel, or partial deactivation in the case of nickel-copper still remains.

This could be a major issue if the process was to be adapted for industrial or commercial hydrogen generation applications.

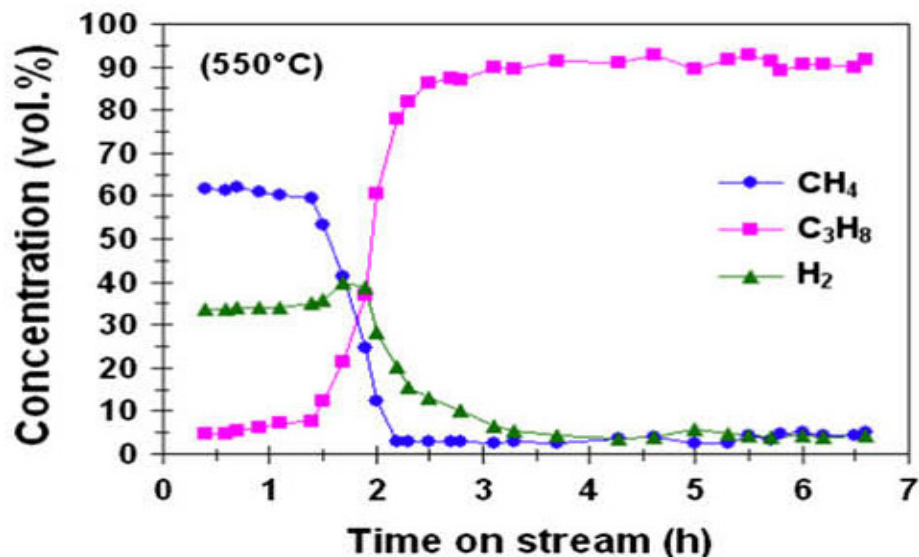


Figure 2.9: Time on stream experimental results for propane thermo-catalytic decomposition by nickel catalyst as reported by Solovyev et al. (2009) (Fig. 3). Shows the compound concentration by volume with time: methane (CH₄) and hydrogen (H₂) production decreases with time; propane (C₃H₈) concentration increases, i.e. conversion of propane decreases with time.

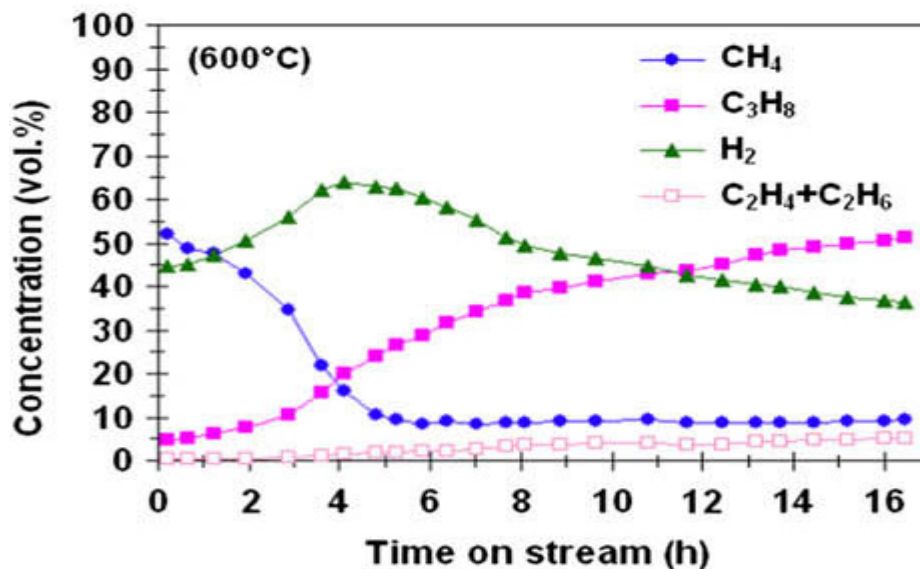


Figure 2.10: Time on stream experimental results for propane thermo-catalytic decomposition by nickel-copper bi-metallic catalyst as reported by Solovyev et al. (2009) (Fig. 4). Shows the compound concentration by volume with time: methane (CH₄) and hydrogen (H₂) production decreases with time; propane (C₃H₈) concentration increases, i.e. conversion of propane decreases with time.

Wang et al. (2005) performed experiments for non-catalytic propane pyrolysis, as well as catalytic decomposition employing iron catalyst and bimetallic catalysts iron-palladium, iron-molybdenum and iron-nickel for CO_x free hydrogen and solid carbon generation. Under non-catalytic pyrolysis conditions at 750 °C, Wang et al. (2005) reported a high propane conversion of 100 %. The gaseous products were 45 % methane, 25 % hydrogen and 15 % acetylene. Similarly to Solovyev et al. (2009), Wang et al. (2005) concluded that C-C bond breakage dominates under the pyrolysis conditions of propane. For all catalysts employed by Wang et al. (2005), methane selectivity dominated the process at temperatures of 450 – 500 °C. Highest hydrogen generation of just over 80 % by volume was achieved at 625 °C by employing bimetallic catalysts nickel-iron and molybdenum-iron in the first 30 minutes of operation. Hydrogen concentration only decreased slightly to approximately 60 % after prolonged operation of six hours. For both iron and palladium-iron catalyst, hydrogen generation decreased sharply after only two hours of operation, see Figure 2.11. Hence, as in the case of nickel-copper catalyst employed by Solovyev et al. (2009), carbon deposition and catalyst deactivation problems occurred in the catalytic systems proposed by Wang et al. (2005) and could be a major culprit. Solovyev et al. (2009) reported 50 % hydrogen concentration for nickel-copper catalyst after 6 hours of operation. Hence, nickel-iron and molybdenum-iron catalysts show only slightly better carbon deposition resistance than nickel-copper catalyst. The results for nickel-iron and molybdenum-iron were only reported for six hour operation showing a gradual hydrogen concentration decrease, see Figure 2.11. (Wang et al., 2005). Longer than six hour time-on-stream might give more insight to the effects of prolonged operation on hydrogen generation and catalyst resistance to carbon deposition.

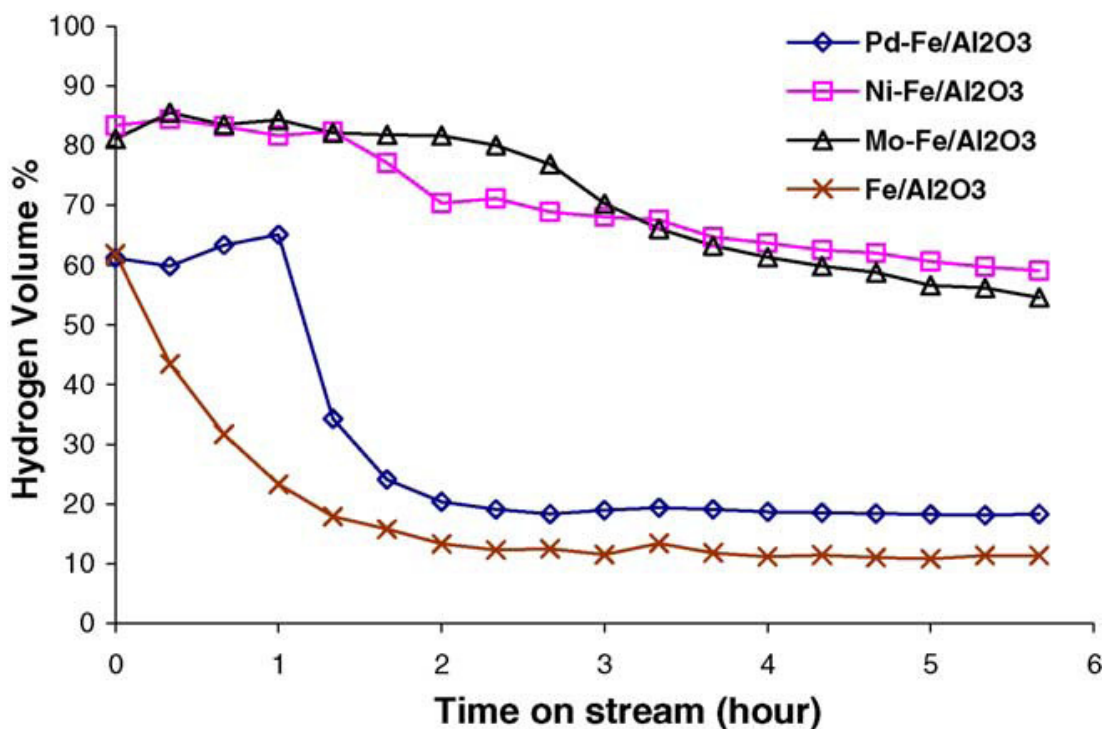


Figure 2.11: Time on stream experiments for hydrogen production from propane decomposition over different catalysts at 625 °C, reported by Wang et al. (2005) (Fig. 4). Pd-Fe = palladium-iron; Ni-Fe = nickel-iron; Mo-Fe = molybdenum-iron; Fe = iron; Al₂O₃ = catalyst alumina support.

Jibril and Atta (2011) performed experiments with 5 wt% metal catalyst vanadium (V), manganese (Mn), iron (Fe), cobalt (Co) or nickel (Ni) incorporated in activated carbon (AC), at temperature ranges of 450 – 550 °C for propane decomposition with argon in the feed. According to the authors, activated carbon has been chosen due to positive catalytic effects on hydrocarbon activation and it could also serve as a template upon which carbon based products are deposited. This system achieved a low propane conversion of 19 % and hydrogen selectivity of 40 % with nickel-AC and iron-AC catalysts at temperature of 550 °C, with an argon/propane flow rate of 70 cm³/min. The selectivity towards hydrogen at the same conditions was equal to approximately 40 % for all of the catalysts tested. However, propane conversion differed slightly, with nickel and iron showing the highest at 19 %, vanadium and cobalt were all at approximately 15 % and manganese at the lowest of 11 %. At temperatures below 550 °C, all of the catalyst exhibited a much lower propane conversion with slightly higher hydrogen selectivity of 46 – 49 % (Jibril and Atta, 2011). Time-on-stream experiments to test the effects of carbon deposition on the nickel-AC catalyst of up to 7 hours show no effect on propane conversion for up to 4

hours and a decrease of approximately 2 – 3 % thereafter. A slight decrease in hydrogen selectivity of approximately 5 % was also observed (Jibril and Atta, 2011).

Reasonable propane conversions and hydrogen selectivities were achieved for catalytic propane decomposition systems. However, time on stream experiments revealed that carbon deposition and catalyst deactivation problems occurred, drastically reducing propane conversion ability and hydrogen selectivity. Non-catalytic pyrolysis of propane has been achieved at high temperatures above 700 °C with high propane conversion of above 90 %. However, the main product generated was methane, with very low yields of hydrogen.

2.7. Summary

Thermal cracking generates air emissions (CO₂, SO_x, NO_x, hydrocarbons and particulates) through the combustion of fuels in process heaters and boilers, equipment leaks of volatile constituents and decoking. Catalytic cracking is one of the largest sources of air emissions in refineries. Contaminants CO₂, SO_x, NO_x, hydrocarbons and particulates are released in process heater flue gas, as fugitive emissions from leaking valves and pipes, and during regeneration of the cracking catalyst. FCC produces large amounts of fine catalyst dust (aluminium silicate and metals), which results from the constant movement of catalyst grains against each other. FCC generates considerable amounts of sour water (high levels of oil, suspended solids, phenols, cyanides, hydrogen sulphate, and ammonia) from the fractionation and steam strippers to separate catalyst from the product. Typical wastewater generation from FCC is 36 L of wastewater per 100 L of feed, representing the second largest source of wastewater in the refinery. FCC also generates considerable amounts of spent catalyst (metals from crude oil and hydrocarbons). While steam stripping is used to regenerate the spent catalyst, in addition fresh catalyst material is needed for each cycle to maintain an appropriate volume of active catalyst.

Hydrogen is a secondary form of energy and needs to be manufactured, just as electricity requires generation. The majority of experts agree that hydrogen has a great role to play in the future energy sector as an important energy carrier. Hydrogen production is currently achieved using well developed conventional

methods, such as steam reforming. Hydrocarbon decomposition to hydrogen and carbon in solid form has been recognized as the most efficient method for hydrogen generation from the perspective of environmental pollution and is cheaper than SMR with carbon capture. However, the necessity for catalysts in current processes results in the major disadvantage of catalyst deactivation.

Chapter 3: The Fourth State of Matter

3.1. Introduction

Plasma is a term used to describe an ionized gas, consisting of positively and negatively charged particles with approximately equal charge densities. It is estimated that approximately 99 % of the visible universe material is plasma (Gurnett and Bhattacharjee, 2005). Sir Williams Crookes was the first one to identify plasma in 1879 in what is referred as a Crookes tube and called it 'radiant matter', he also referred to it as a 'fourth state of matter' (Fridman, 2008). The nature of this 'radiant matter' was further characterized by J. J. Thomson in 1897 and Irving Langmuir was the first person to introduce the name plasma in 1928, perhaps because it reminded him of blood plasma. Langmuir wrote: 'Except near the electrodes, where there are sheaths containing very few electrons, the ionized gas contains ions and electrons in about equal numbers so that the resultant space charge is very small. We shall use the name plasma to describe this region containing balanced charges of ions and electrons' (Thomson, 1897; Langmuir, 1928)

Plasmas can occur in a wide range of pressures, electron temperatures and electron densities, where most man-made plasmas of practical significance have electron temperatures of 1 – 20 eV (11604 – 23280 K) and electron densities in the range of $10^6 - 10^{18}$ per cm^3 (electron density is the number of electrons per unit volume), (Fridman, 2008). Plasmas also vary in ionization degree (the ratio of density of major charge species to that of neutral gas) from completely to weakly ionized. In most conventional plasma-chemical systems the ionization degree is in the range of $10^{-7} - 10^{-4}$ (partially ionized), (Fridman, 2008; Bogaerts et al., 2002).

Plasma-assisted cracking can offer a more selective hydrocarbon cracking method compared to catalytic and thermal cracking, due to the low bulk temperature. The use of plasmas would also provide a more environmentally friendly hydrocarbon decomposition technology, eliminating problems associated with catalysts. Hence, in this chapter, the reader will be introduced to the plasma sources in section 3.2, the types of plasma will be described in sections 3.3 and 3.4, followed by a thorough description of the plasma type of interest for this research, the corona discharge, in section 3.5.

3.2. Plasma sources and processes

The first step in any plasma process is the creation of primary plasma (Schram, 2002). Plasmas can be generated by supplying energy to a neutral gas either in a form of thermal energy, magnetic fields or electric fields (Hollahan and Bell, 1974; Conrads and Schmidt, 2000). The most common approach of plasma generation is the use of an external electric field, which causes electrical break down of the neutral gas (Hollahan and Bell, 1974; Conrads and Schmidt, 2000). This leads to the formation of a variety of new species such as electrons and ions, excited atoms and molecules, radicals and UV photons. Electrons gain the energy from the electric field first, due to their low mass and high mobility and then transfer the energy to other plasma components via collisions. At this stage, electrons are completely detached from their ions forming an electron gas (gas containing a number of electrons). Electrons are the key players providing energy for ionization, and vibrational, rotational and electronic excitations. Ionization is the key process in plasma, as ions are highly energetic molecules and can suppress activation energy barriers of chemical reactions. Therefore, they make a significant contribution to plasma-kinetics. There are five major groups of ionization processes to generate ions which may occur in plasma: direct ionization by electron impact, stepwise ionization by electron impact, ionization by collision of heavy particles, photo-ionization and surface ionization (Fridman, 2008). The reactions of positive ions are usually highly exothermic, making their contribution to plasma processes very significant. Electron-ion recombination of positive ions release energy related to the dissociation of molecules or generation of radicals or radiation. Positive ion-molecular reactions contribute to the balance of charged particles and provide further plasma-chemical processes (Fridman, 2008).

3.3. Thermal and non-thermal plasmas

Plasmas can be classified as ‘thermal’ or ‘non-thermal’ based on the relative temperatures of electrons and heavy particles (ions and neutrals). In electric discharges electrons are first to gain energy and then transfer it to heavy particles during collisions, losing only a small fraction of their energy. At this stage electron temperatures are higher than that of heavy particles. However, if sufficient time and energy is provided, subsequent collisions of electrons with heavier particles can

equilibrate their temperatures (Fridman, 2008). High pressure and power density is required to reach this local thermodynamic equilibrium (LTE), (Tendero et al., 2006). This type of plasma is called thermal plasma and may be characterized by a single temperature at each point in space. In contrast, non-thermal plasmas are characterized by multiple different temperatures related to different particles. Heavy particles are heated only by few elastic collisions, therefore electron energy remains very high and temperature significantly exceeding that of heavy particles (Fridman, 2008).

In this study we are going to use non-thermal atmospheric pressure discharge, because we aim to develop a low-cost plasma-chemical process with high selectivity, control and energy efficiency. Thermal plasmas are more powerful and can achieve high specific productivity mainly due to their high temperature. However, the main drawbacks are high electrical energy consumption, exceeding that of the conventional catalysis systems and overheating of the reaction media (Deminsky et al., 2002). Non-thermal plasmas present some advantages for organic synthesis due to non-equilibrium properties, low power requirements and capacity to induce physical and chemical reactions at low temperatures (Petipas et al., 2007). Fridman et al. (2005) have recognised the potential of non-thermal plasmas as a relatively low energy cost technology due to high selectivity and relatively low maintenance requirements. Paulmer and Fulcheri (2005) have compared the efficiency of several plasma reactors for hydrogen production from hydrocarbons. Non-thermal gliding arc plasma has been determined to be more efficient than thermal gliding arc plasma by the authors. Since the efficiency equation used by the authors considers both energy consumption and energy generation in the form of hydrogen, it can be concluded that non-thermal plasmas can achieve high specific productivity at lower cost. Hence, in the next section we will look into atmospheric non-thermal plasmas (ANTP).

3.4. Non-thermal atmospheric pressure discharges

Gas discharge plasmas offer a wide variety of chemical non-equilibrium conditions because external parameters such as chemical input, pressure, electromagnetic field structure, discharge configuration and temporal behaviour can be easily modified (Bogaerts et al., 2002). As mentioned in section 3.2, the most common way of

plasma generation is an external electric field causing electrical break down of the neutral gas (Hollahan and Bell, 1974; Conrads and Schmidt, 2000). Electrical break down occurs when the electric field exceeds a certain value characterizing a specific set of conditions and a conductive gas channel is formed (Raizer, 1991). In non-thermal plasmas, most of the breakdown mechanisms start with an electron avalanche, which is a multiplication of primary electrons in cascade ionization (Fridman et al., 2005). The ignition potential, also referred to as the breakdown voltage and the corresponding breakdown field, depend on the gas, the material of the cathode, the pressure, and the discharge gap width (Raizer, 1991). The breakdown voltage depends only on the product pressure and distance, manifesting the similarity law or Paschen's law (Raizer, 1991). The experimental breakdown Paschen curves also show that the minimal breakdown voltage for a discharge gap exists (Raizer, 1991).

At atmospheric pressure and inter-electrode distance < 5 cm (the pressure/distance relationship of 533 kPa/cm), a mechanism of ignition of self-sustained plasma occurs, called Townsend breakdown mechanism, see Figure 3.1. This mechanism is moderately homogenous, includes the development of independent avalanches and is controlled by secondary electron emissions from the cathode. When the gaps are relatively large (≥ 1 cm at atmospheric pressure), the Townsend breakdown electric fields in electronegative gasses (atoms or molecules that attract electrons) become almost constant (Fridman, 2008).

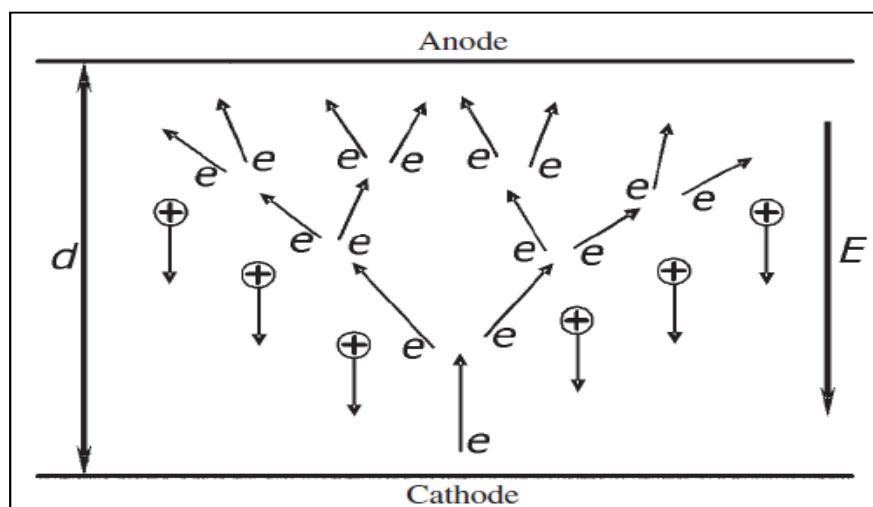


Figure 3.1: Townsend breakdown mechanism (Fridman et al., 2005, Fig. 1): d = inter electrode distance; E = electric field; e = electrons; $(+)$ = positive ion.

There are various configurations to generate ANTPs, where corona, dielectric barrier, spark and gliding arc (GA) discharges are considered to be the most important in modern technologies by Fridman et al. (2005). At this point we will look into a type of plasma called corona discharge to examine the present application. We will describe what is corona and some of the important parameters concerning the discharge.

3.5. Corona Discharge

3.5.1. What is corona?

Corona discharge is non-thermal plasma formed on sharp points, edges or thin wires where the electric field is sufficiently large (Antano et al., 2009), see Figure 3.2 for different corona discharge configurations. Power supply is in a form of electricity and can be either DC with or without pulses, or AC. Corona discharge is always non-uniform, as the geometry of electrodes confines the gas ionizing process to high-field ionization region(s) around the active electrode(s) (Goldman et al., 1985). The type of the corona discharge depends on the geometry of the electrodes, the type of gas, polarity of the active electrode and the voltage applied (Akishev et al., 2001b). Corona discharges can be either positive or negative, depending on the polarity of the active electrode (wire, pin, needle).

In the presence of a strong electric field, a neutral atom or a molecule is ionized to create a positive ion and a free electron. The electric field separates charged particles and prevents them from recombining, accelerating them to the opposite charge electrode. Electrons accelerate at much higher velocity due to lower charge to mass ratio and therefore induce more electron and ion formation by collisions, creating electron avalanches. This also creates other active species of the plasma, such as radicals (Antano et al., 2009). In corona discharges, ionization and electron attachment (to generate negative ions) are initiated by electrons. Hence, electron density is the main determinant in plasma behaviour (Uhm, 1998). This is a general mechanism for both positive and negative coronas. A more detailed process description will be addressed in the next two sections separately due to some differences between the processes.

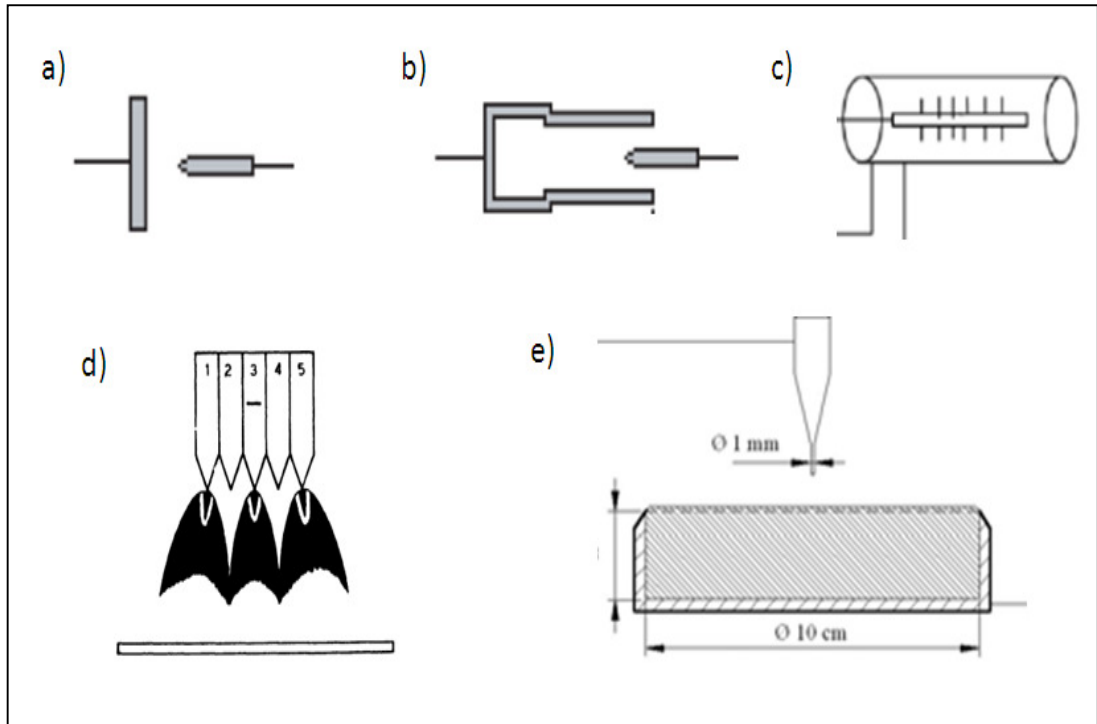


Figure 3.2: Examples of different corona electrode configurations: a) Point-to-plane (Benocci and Mauri, 2004, Fig. 1); b) point-to-coaxial cylinder (Benocci and Mauri, 2004, Fig. 1); c) wire-to-cylinder (Mishra et al., 2004, Fig. 1); d) multipoint-to-plane (Thanh, 1985, Fig. 3); e) pin-to-liquid (Bruggeman et al., 2008, Fig. 1).

3.5.2. Positive pin-to-plate corona processes

In positive coronas the point electrode is positive and for each ion-electron pair created in the ionization region an electron will impinge on the anode point whereas the positive ion will reach the plane cathode (Goldman et al., 1985). In the positive point-to-plane corona electrode configuration a discharge starts with a burst pulse corona, then proceeds to streamer corona, then to glow corona and finally spark discharge as the voltage increases or inter-electrode distance decrease (Chang et al., 1991; Lowke and Morrow, 1994), see Figure 3.3.

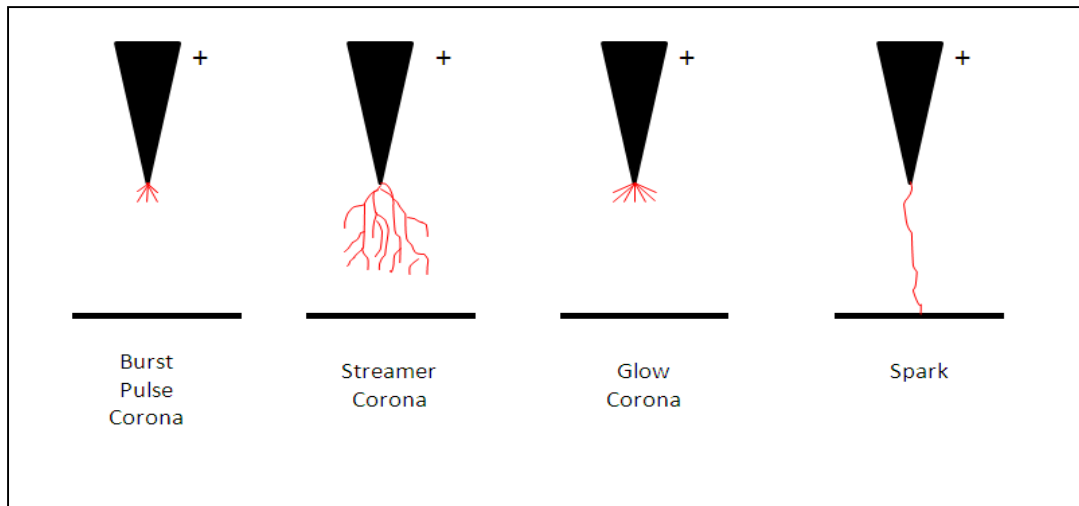


Figure 3.3: Schematic of types of positive corona discharge (adapted from Chang and Yamamoto, 1991, Fig.1).

Burst pulse positive corona current is made up of imperfectly resolved current impulses of extremely high frequency. However, once a stable corona is established the fluctuations decrease (Trichel, 1939; Akishev et al., 1999; Merbahi et al., 2007). If the field strength at the point electrode is increased, then the bursts propagate and form streamers (Trichel, 1939). Positive streamer corona forms when positive ion density is large enough to extend the region for corona initiation into the electrode gap (Chang et al., 1991). In the experimental results for positive point-to-plate configuration, the transition of the streamers straight to the spark is mostly reported. Streamer repetition rate increases with the applied voltage. However, only until a crucial voltage is reached and streamers transition into sparks (Akishev et al., 2003). Spark discharge propagates ions more intensely, and contains a dense spark core occupying a smaller total volume than streamer corona (Chang et al., 1991). Streamer channel conductivity is higher, and, therefore, the transition into sparks is faster in electropositive gasses (argon, nitrogen), when compared to electronegative gases (oxygen, carbon dioxide), due to the absence of electron attachment and slower electron ion recombination. Electropositive gases are composed of molecules or atoms that have an ability to donate electrons and become positive. In contrast, electronegative atoms or molecules attract electrons. For example, the average electric field required for streamer breakdown in air (and in other electronegative

molecular gasses) is $> 20 - 25$ kV/cm, which is $30 - 40$ times smaller for argon at > 600 V/cm (Aleksandrov et al., 1999).

3.5.3. Negative pin-to-plate corona processes

In negative coronas the point electrode is negative and for each ion-electron pair created in the ionization region (close to the cathode where the electric field is strong) positive ions will accelerate towards the cathode. High energy electrons (approx 10 eV) will accelerate towards the anode, followed by lower energy electrons (approx 1 eV); the process is called streamer (Tendero et al., 2006). Negative coronas are triggered by a short duration of burst-like emission of electrons (Laan et al., 1997). Negative corona has three modes: Trichel pulse corona (also referred to as corona mode), pulseless corona (also referred to as glow discharge) and spark discharge, occurring in the order as the voltage applied increases (Chang et al., 1991; Lowke and Morrow, 1994; Akishev et al., 2001a), see Figure 3.4. Interestingly, Diguang and Dexuan (1990) have observed streamers in negative corona. However, these could only be detected at the voltage close to breakdown.

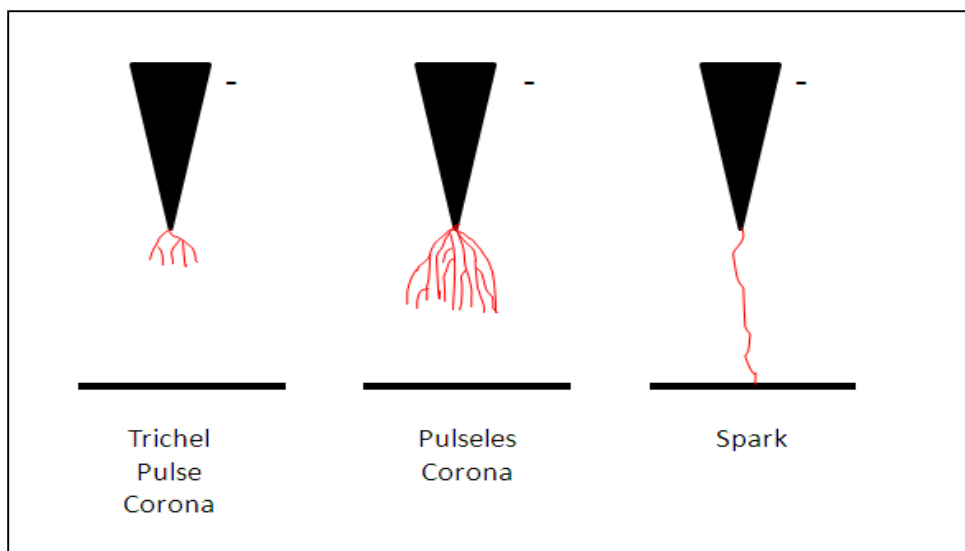


Figure 3.4: Schematic of types of negative corona discharge (adapted from Chang and Yamamoto, 1991, Fig. 1).

In the Trichel pulsing mode, the discharge propagates radially and is then cached off by accumulated space charges, giving rise to discrete pulses (Antano et al., 2009). In the experimental work with electropositive gasses, such as nitrogen and helium, Trichel pulses occur only at certain conditions, where many authors conclude that the pulsing mode does not exist in electropositive gases. The critical current (separates the pulse mode from the steady mode) in nitrogen is substantially lower than that in air, so the current range in which regular pulses exist is narrower for nitrogen (Akishev et al., 2001b). Akishev et al. (2001b) were the first to observe and report Trichel pulses in negative corona in nitrogen. In the experiments with point-to-plane negative corona discharge in air (inter-electrode distance 10 cm, pin radius 0.5 mm), regular Trichel pulses were observed at voltage 8 – 55 kV (triggering electric field 0.8 kV/cm), pulseless mode has been observed at voltages 55 – 100 kV (triggering electric field 5.5 kV/cm), and the spark breakdown observed at 120 kV (triggering electric field 12 kV/cm) (Diguang and Dexuang, 1990).

When high overvoltage is applied between the electrodes, the electric field is high across the whole inter-electrode gap and the drift region with increasing current gradually fills with quasi-neutral plasma. At this stage the discharge shows many features typical to glow discharge, however with high sparking potential (Akishev et al., 2001a). Glow to spark transition has two modes: (i) the formation of an unstable subnormal anode layer that constricts into one or more high current density spots; (ii) local development of ionization instability, driven by an ionization increase caused by energy deposition into the anode spot (Akishev et al., 2001a). Ultimate breakdown of diffuse glow discharge into non-stationary and non-homogenous spark can occur as a result of the negative space charge accumulation at high current densities (Akishev et al., 2001a).

3.5.4. Multipoint and point-to-liquid electrode configurations

In negative multipoint to plane electrode configuration the same 3 modes as in point-to-plane configuration have been observed: Trichel pulses, pulseless and sparkover (Thanh, 1985). Thanh, 1985 concluded, using the experimental results, that the sparkover voltage is independent of cathode configuration, i.e. the critical charge per unit length for sparkover is the same for multi and single points. However, Thanh (1985) also observed higher currents using a multipoint electrode. Thanh (1985) in

his discussion concluded that the presence of extra electrodes in the neighbourhood of one discharge point caused the electric field distribution surrounding that point to alter, due to the shielding effect exerted by the other points. Similarly, Jaworek and Krupa (1995a, 1996) concluded that the space charges generated by adjacent points affect the discharge current from the other points. The authors have also observed that as the inter-pin distance decreases, the corona onset voltage increases and the corona current decreases, for both positive and negative coronas.

Liquid electrodes can serve as resistive barriers, stabilizing corona discharge as they prevent the discharge from localizing and therefore, arcing or sparking (Bruggeman et al., 2008b). Negative multipoint-to-liquid (Suarasan et al., 2002) and point-to-liquid (Bruggeman et al., 2008a, and 2008b) corona discharges have been experimentally studied, mainly for ozonation of water. However, to this day plasma-liquid interaction is still not well understood (Bruggeman et al., 2008a). Bruggeman et al. (2008a) have observed liquid elevation due to Coulomb force. Once corona occurs, depression is formed under the metal pin electrode due to the ionic wind that accompanies corona discharge. The authors have noted that, at higher currents, swirl-like behaviour of the liquid is observed. In the case of the positive pin, Bruggeman et al. (2008a) have reported that corona proceeds from streamer mode straight to the spark transition; in the case of negative corona, glow to spark transition is observed.

Positive pin-to-liquid systems have been experimentally investigated for liquid ozonation (Lukeš et al., 2004), contaminant removal from liquids (Hoeben et al., 1999; Hayashi et al., 2000) and for characterization purposes (Nikiforov et al., 2006; Bruggeman et al., 2008c). Lukeš et al. (2004) wrote that corona initiates a variety of chemical and physical effects in water, including intense ultraviolet radiation, overpressure shock waves and formation of chemically active species, such as OH, H and O radicals. Bruggeman et al. (2008c) have observed a substantial change in liquid (acidification) in the positive pin-to-water corona discharge system, which can be explained by the presence of the mentioned radicals. They concluded that plasma has constricted contact at the liquid cathode and hence, is filamentary in nature near the water surface. Nikiforov and Leys (2006) have put forth the idea that the breakdown process between liquid and metal electrodes is aroused by photoionization of gases. The authors came to these conclusions due to the observations

that the spark voltage does not depend on polarity of metal electrode. Therefore, the cathode spot and second emissions of electrons from cathode do not play essential role in the breakdown process. The mechanism of phenol (contaminant) removal from liquids using corona discharge has been explained by Hayashi et al. (2000) that, strongly oxidative agents, such as OH radicals, O atoms and their reaction products are produced in the corona discharge in the gaseous phase; these then dissolve in water and degrade phenol via oxidation process.

3.5.5. Important parameters reported in the literature

Corona discharges depend on 5 main parameters: inter-electrode distance, gas composition, polarity, electrode geometry and material, and voltage applied (Akishev et al., 2001b). Inter-electrode distance affects the total electric field per unit volume of the discharge. Hence, it will have a substantial effect on the transitions between the different modes in positive and negative corona discharges. The transition to spark breakdown has been shown to be largely dependent on inter-electrode distance for both positive and negative discharges (Lowke and Morrow, 1994).

The main difference in the effects of gas composition on corona discharge can be distinguished between the electronegative and electropositive gases. Evolution of the negative corona after ignition highly depends on the type of gas used. In electronegative gases, such as air, negative diffuse corona in Trichel pulse mode occurs. As the voltage is increased, the discharge proceeds straight to the spark with the streamer mode absent. Intermediate mode (glow corona) between the diffuse corona and the spark can occur, if the discharge is stabilized. In electropositive gases, such as nitrogen and argon, the ignition voltage is much higher than the sustaining voltage. After the ignition, corona jumps straight to the non-pulsating glow discharge. However, hysteresis occurs as the voltage can be reduced after the ignition voltage without quenching corona discharge and achieve pulsating corona (Akishev et al., 2001b; 2003). For example, critical current is much lower in nitrogen corona than in air. Hence, the current range in which regular pulses exists is narrower for nitrogen (Akishev et al., 2001b). However, the mechanism for current pulse generation in negative coronas is the same in nitrogen and air, where negative ions play a major role in the pulse generation (Akishev et al., 2001c). Atrazhev et al.

(2003) concluded that the onset voltage of the corona discharge also depends on the medium density and Bonifaci et al. (1997) have experimentally shown that onset corona voltage is higher for a denser gas. In positive coronas, the streamers observed in air are always branched, whereas in argon single streamers can be observed (Aleksandrov et al., 1999). Also, in air streamer bridging the gap does not transform into a spark as easily as in argon (Aleksandrov et al., 2001a).

Polarity has substantial effects on the corona discharge development as seen in sections 3.5.2 and 3.5.3. The main difference between the positive and negative discharges is seen by the occurring different modes, i.e. as the electric field applied increases, positive corona transitions from burst pulse, to streamer, to glow, to spark, whereas negative corona discharges proceed from Trichel pulse, to glow to spark. These differences are mainly due to the mechanisms of corona development: in positive corona for each ion-electron pair created in the ionization region an electron will impinge on the anode point whereas the positive ion will reach the plain cathode. Whereas in negative corona for each ion-electron pair created in the ionization it is the positive ions that will accelerate towards the plate electrode.

Electrode geometry, material and configuration, all have substantial effects on both positive and negative corona discharges. In negative corona discharges, shaping anode surface, resistive anode material and cathode pin design, all effect corona current characteristics (Akishev et al., 2001a). Jarzebski and Chojnowski (1974) have concluded that emission currents of corona are affected by the electrode shapes. Atrazhev et al. (2003) determined experimentally that the onset voltage of the corona discharge depends on the cathode radius. Anode geometry (needle, massive pin, hollow pin) influences the transition between Trichel, glow and spark modes (Akishev et al., 2001a). Whereas resistive anode stabilizes nitrogen corona in the glow mode (Akishev et al., 2001b). Also, for negative coronas it has been shown that corona current is higher in the multipoint electrode configuration (Thanh, 1985). In positive corona discharges, resistive coating discharge electrode forces a uniform corona, prohibits formation of discrete corona sites and results in a highly uniform current distribution (Bush and Snyder, 1987). Resistive coating at the plate electrode result in higher currents than in usual pin-to-plate electrode configuration and the transition to spark requires higher currents; hence, showing the stabilization effect

(Akishev et al., 2003). In wire-to-cylinder positive corona discharges spark breakdown is largely dependent on inter wire diameter (Lowke and Morrow, 1994). It has been noted that for both, positive and negative, coronas uniformity of corona increases at a given total current as the diameter of the corona electrode (active electrode) wire decreases and the wire is smooth (Bush and Snyder, 1987).

The effect of voltage on corona evolution (i.e. the transition between the different modes) has already been described in sections 3.5.2 and 3.5.3. To summarize, as the applied electric field increases, positive corona transitions from burst pulse, to streamer, to glow, to spark, whereas negative corona discharges proceed from Trichel pulse, to glow to spark. In positive corona discharges, applied voltage also has a substantial effect on the current pulse shape and size. At lower voltages, the current peak is smaller and the second current peak vanishes (Merbahi et al., 2007; Eichwald et al., 2008) also mean stream velocity is lower (Merbahi et al., 2007). Higher voltages in positive coronas also increase streamer repetition rate (Akishev et al., 2003).

Higher gas flows in both positive and negative coronas have been reported to result in a lower discharge current, due to pressure increase in the gap. Hence, reducing the ionization processes in the ionization region and ion mobility. Glow mode can be stabilized by introducing gas flow in negative corona (Akishev et al., 2001a). According to Uhm (1998) critical voltage required for the corona discharge breakdown is inversely proportional to the chamber temperature and the voltage decreases as the temperature increases. The author concluded that overall 'plasma generation by corona discharge in a hot chamber is much more efficient than that in a cold chamber' (Uhm, 1998).

3.5.6. Corona discharge applications

Corona discharges are highly non-thermal, and have been recognised by Uhm (1998) to be very efficient in transferring source power into promoting chemical reactions. In many applications, the efficiency of a corona reactor is correlated with the radical production rate during the discharge period (Eichwald et al., 2008). Both pulsed and continuous corona discharges have been used in a wide range of applications such as flue gas cleaning (Veldhuizen et al., 1998; Dinelli et al., 1990; Hammer, 1999),

destruction of volatile organic compounds (Hartmann et al., 2007), water purification (Bogaerts et al., 2002), surface treatment (Takahashi et al., 2000) and ozone production (Peyrous and Millot, 1981; Chen and Davidson, 2003). Laboratory scale experimental work has been carried out with pulsed corona discharges for methane reformation to hydrogen and hydrogen rich gas (Li et. al., 2004; Istadi and Amin, 2006; Da Silva et al., 2006; Yao et al., 2001), methane reformation to higher hydrocarbons such as acetylene (Kado et al., 2003; Zhang et al., 2002; Zha et al., 2006; Dai et al., 2000; Kado et al., 2004) and biofuel reformation to hydrogen rich gas (Zhu et al., 2010; Chun et al., 2004).

Chapter 4: Plasma Processing of Hydrocarbons

4.1. Introduction

The importance and global challenges in energy production and supply have been addressed in Chapter 2. To draw back to the key points, conventional thermo-catalytic technology for hydrogen and syngas (carbon monoxide and hydrogen) production has certain drawbacks such as high economical investment cost, catalyst poisoning, decrease in catalyst efficiency or deactivation of catalyst by carbon deposition, high temperature requirement to activate catalytic sites, low flow rate of inlet gas injected (Luche et al., 2009) and equipment size (Fridman, 2008; Deminsky et al., 2002). The regeneration of catalyst has been recognised as a major challenge of a continuous process for hydrogen production using thermo-catalytic methane decomposition (Amin et al., 2011). The application of plasma in the production of hydrogen and syngas can eliminate or decrease problems associated with catalyst sensitivity and deterioration, achieve higher conversion efficiencies and increase specific productivity. Plasma technology offers fast response time, compactness and low weight, and can be operated over a broad range of fuels; all of which are very attractive for automotive applications (Fridman, 2008; Bromberg et al., 2000; Holladay et al., 2009). Non-thermal plasmas especially are considered to very promising for organic synthesis applications. However, the present understanding of plasma chemistry is limited and most of the present achievements are based on experimental data (Petipas et al., 2007).

In this chapter, a brief description of general terminology and calculations used for the plasma systems compared in this work is presented in section 4.2. Followed by experimental work reported in the literature on plasma assisted methane and propane conversion to hydrogen will be reviewed in section 4.3 and 4.4 respectively. Section 4.5 provides a detailed description of the experimental work reported in the literature on plasma assisted heavy liquid hydrocarbon conversion to lighter liquid hydrocarbons. In the last two sections, plasma-catalytic systems will be reviewed (4.7) and compared with plasma systems (4.8) for hydrogen generation from methane without the use of catalyst.

4.2. Conversion rate, selectivity and energy consumption

Product selectivity, conversion rate of the reactants and the efficiency of the system are three main factors used to determine viability of the process to produce hydrogen or syngas from hydrocarbons. Explanation and the formulae for these are presented below and are well used and accepted in literature (for example see: Supat et al., 2003; Intardo et al., 2003; Li et al., 2004; Long et al., 2008; Tao et al., 2008; Tao et al., 2009; Xu et al., 2009; Lee et al., 2010; Li et al., 2010). The conversion rate of the reactants, given by equation (4.1), is the amount of the reactants converted compared to the original amount of the reactants input to the system. Normally expressed as percentage, calculated by dividing the amount of the reactants consumed in the reaction by the amount of the total reactants input to the system:

$$X_i(\%) = \frac{n_{in} - n_{out}}{n_{in}} \times 100 \quad (4.1)$$

where

X_i conversion rate of the compound i

n_{in} compound input (mol)

n_{out} compound output (mol)

The selectivity towards a product refers to the ability of the system to convert the reactants to the desired product. Again expressed as a percentage, and can be calculated by dividing the generated amount of the product in question (H_2 in this case) by the total conversion of the reactants (CH_4):

$$S_{H_2}(\%) = \frac{n_{H_2}}{2 \times \dot{n}_{CH_4}} \times 100 \quad (4.2)$$

where

S_{H_2} hydrogen selectivity

n_{H_2} moles of H_2

\dot{n}_{CH_4} moles of CH_4 converted

Specific energy is a good indicator to describe and compare reforming processes. Hence, in this review the energy efficiency of a system will be compared in the form of the specific energy consumption (SEC) for methane conversion (kJ/mol of CH_4

converted) and specific energy requirement (SER) for hydrogen generation (kJ/mol H₂ generated):

$$SEC = \frac{P_{elec}}{\dot{n}_{CH_4}} \quad (4.3)$$

$$SER = \frac{P_{elec}}{\dot{n}_{H_2}} \quad (4.4)$$

where

P_{elec} power supplied to the process in kW

\dot{n}_{CH_4} moles of CH_4 converted per second

\dot{n}_i moles of product i generated per second

4.3. Plasma-assisted generation of hydrogen from methane

4.3.1. General theory

Methane is the principal component of natural gas, used as a fuel for industrial and residential heating. However, more methane is produced than required for this purpose (Patino et al., 2005). Hydrogen and hydrogen rich gas generation has a significant role in fuel cell development, as well as in industrial processes such as natural gas liquefaction. A significant amount of research has been directed towards hydrogen generation from methane employing the plasma approach. Hence, in the next section experimental work and results will be reviewed for plasma assisted methane conversion to hydrogen rich gas. To compare the viability of different systems values of SEC for methane conversion and SER for hydrogen generation will be calculated using formulae (4.3) and (4.4) respectively (refer to section 4.2).

There are three potentially different pathways that contribute to plasma reforming of methane, (Lee et al., 2010):

- i. Pure plasma effect - decomposition by collision of electrons and methane gas molecules:



9 eV or more of energy is required for this process and the main products include C₂H₆, C₂H₂ and H₂, of which C₂H₆ is dominant due to dimerization of CH₃ radicals.

ii. Thermal decomposition process:



Activation energy for this process is 443.09 kJ/mol and the main product is H₂.

iii. Hydrogen abstraction - both plasma and thermal process are sources of H radicals:



Activation energy for this process is 36.61 kJ/mol and C₂H₂ is the main product due to dehydrogenation via hydrogen interaction with C₁ and C₂ species.

Mishra et al. (2007) proposed possible methane activation and conversion mechanisms under pyrolysis conditions in a pulse discharge to be via collisions of methane molecules with energetic electrons and hence radical H and CH₃ formation, i.e. pure plasma effect (pathway 1 above):



Radical H may further react with another methane molecule to form H₂ molecule and CH₃ radical:



With the addition of argon to the system as a working gas, two extra processes may occur (Mishra et al., 2004):

Release of extra electrons:



Or production of excited Ar* by reverse processes:



Accompanied by the emission of photon, hv:



Or direct capture of an electron by Ar* and emission of photon:



Then the photo-ionic decomposition of methane may also occur (Mishra et al., 2007).

In non-thermal plasmas the rate of all discharge reactions depends on electron energy, electron density, gas temperature, gas pressure and the properties of gases. The present understanding of plasma chemistry is limited. Hence, it is difficult to predict reactions mechanisms and final products. To this day, most achievements are based on experimental data (Petipas et al., 2007).

4.3.2. Syngas production by partial oxidation of methane

Partial oxidation of methane is a slightly exothermic process. Therefore, plasma catalysis can be well suited for the purpose by providing reactive species to initiate chemical reactions. Non-thermal plasmas such as microwave (Tsai et al., 2005), corona (Mutaf-Yardimici, 1998; Yang, 2002; Supat et al., 2003; Kado et al., 2001a; Kado et al., 2003), dielectric barrier (Sentek et al., 2010), atmospheric pressure glow discharges (Luche et al., 2009; Ghorbanzadeh et al., 2009), cold plasma jet (Long et al., 2008) and gliding arc (Huang et al., 2000; Intardo et al., 2006; Sreethawong et al., 2007), as well as thermal plasma (Kim and Chun, 2008; Tao et al., 2008; Tao et al., 2009), have been reported in the literature for partial oxidation of methane to generate syngas and will be reviewed in the following sections.

4.3.2.1. Atmospheric pressure glow discharge and plasma jet

Luche et al. (2009) have reported a very low SER of 324 kJ/mol achieved by partial oxidation of methane to syngas, employing atmospheric pressure glow-like discharge. The reactor consists of a quartz tube 400 mm in length and 30 mm inner diameter, containing two conical electrodes made of graphite with an inter-electrode distance of 10 mm, see Figure 4.1 for reactor configuration. Selected optimal conditions were 10.5 ml/min flow rate with 25 % CH₄ in air and the input power of 155 W (Luche et al., 2009). Ghorbanzadeh et al. (2009) achieved a reasonable methane conversion of 61 % and high hydrogen selectivity of 77 % by employing

pulsed glow discharge with very impressive SEC of 845 kJ/mol and SER of 548 kJ/mol. The authors classified the plasma system as a combination of arc and glow, more lenient towards the glow-like discharge. The optimal conditions selected were 120 ml/min flow rate, $\text{CH}_4 / \text{CO}_2$ ratio 1/1 and the input power of 23 W. However, the SER for this system is higher by a factor of 1.69 than that reported by Luche et al. (2009).

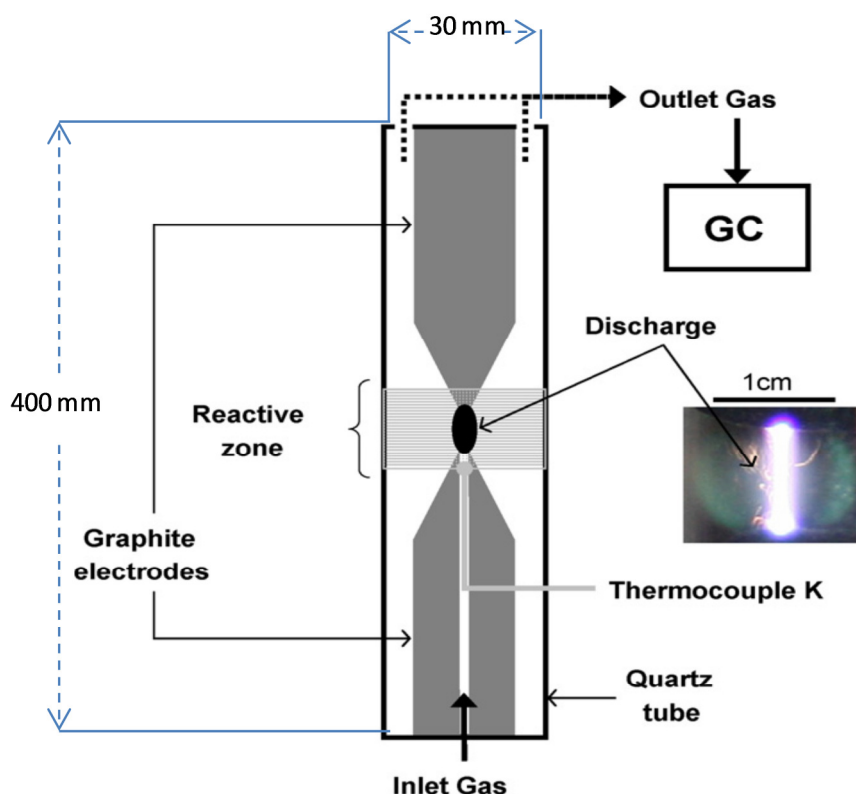


Figure 4.1: Schematic representation of the plasma reactor with a photography of the electric discharge (Luche et al., 2009, Fig.1).

Long et al. (2008) achieved a rather low methane conversion of 45.68 %, but a high hydrogen selectivity of 78.11 % by employing a cold plasma jet. The plasma apparatus consists of an inside cylindrical copper tube connected to an AC high voltage supply and the coaxial stainless steel crust serving as a ground electrode, see Figure 4.2. Optimal conditions selected were: 8300 ml/min flow rate, $\text{CH}_4 / \text{CO}_2$ ratio 4/6 and the input power of 770 W. The SEC and SER values achieved by this system, 682 kJ/mol and 437 kJ/mol respectively, are lower than for the glow

discharge system presented by Ghorbanzadeh et al. (2009) but still higher than the SER achieved by Luche et al. (2009).

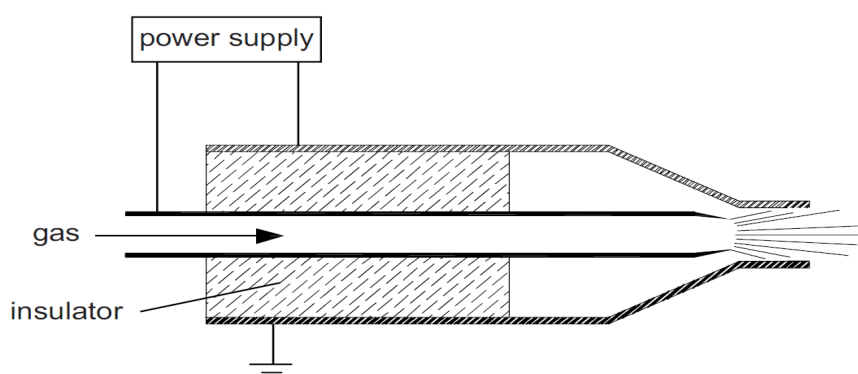


Figure 4.2: Schematic diagram of cold plasma jet (Long et al., 2008, Fig. 1).

Li et al. (2009a) have achieved a very low SEC and SER values of 174 and 97.8 kJ/mol respectively by employing an atmospheric plasma jet. The plasma reactor consists of a powered cylindrical inner electrode (8 mm OD) and a grounding outer electrode (converging nozzle with 30 mm ID upstream and 10 mm ID at the jet exit), the configuration is the same as shown in Figure 4.2. At the optimal conditions selected by the authors of 2200 ml/min flow rate, 4/6 CH_4 / CO_2 ratio and power input of 69.85 W, the conversion of methane and selectivity for hydrogen were at 60.97 and 89.3 % respectively. Using the same reactor configuration, Li et al. (2010) achieved a very high methane conversion of 97.99 % and high hydrogen selectivity of 79 % by decreasing the flow rate to 1000 ml/min and increasing the power input to 88.4 W (CH_4 / CO_2 ratio 4/6). However, this was at the expense of an increase to the SEC and SER values equalling to 312 kJ/mol and 197.9 kJ/mol respectively. In both cases described above, Li and the team have achieved much lower SEC and SER values than the glow discharge system presented by Ghorbanzadeh et al. (2009) and SER achieved by Luche et al. (2009).

4.3.2.2. Microwave and corona discharges

Tsai et al. (2005) used a near-atmospheric pressure and room temperature microwave plasma system for partial oxidation of methane. The plasma reactor consists of a magnetron (2.45 GHz, max stationary power 2 kW) feeding the microwave into the waveguide, a stainless steel tube reactor (5 cm internal diameter and 50 cm length) with a quartz tube (4 cm internal diameter and 7 cm length) and an antenna (1.6 cm diameter and approx 35 cm length) intersected perpendicularly by the waveguide and the resonator, see Figure 4.3. The optimal operating conditions as defined by the authors were at a pressure of 93.3 kPa, 7000 ml/min flow rate, O_2/CH_4 ratio of 0.5 and power input of 600 W. Under these conditions, 98 % hydrogen selectivity and 48 % methane conversion with SEC of 4800 kJ/mol and SER of 2448 kJ/mol were achieved. The authors have pointed out that the energy efficiency of the process is only moderate and needs further improvement.

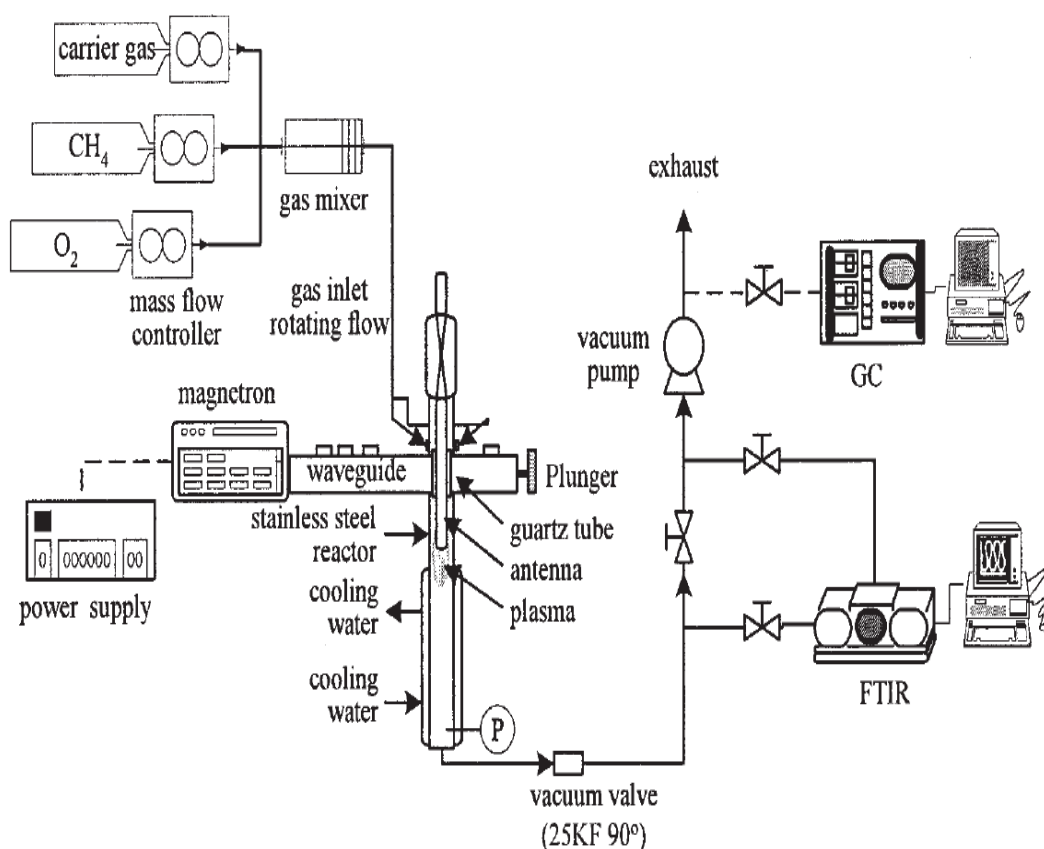


Figure 4.3: Microwave plasma system (Tsai et al., 2005, Fig. 1).

Kado et al. (2003) performed experiments using a non-equilibrium pulsed discharge with planed-tip-to-pin electrode configuration, see Figure 4.4. The authors have demonstrated partial oxidation of methane into syngas and acetylene, as well as partial oxidation approach being the most effective way to suppress carbon deposition (Kado et. al., 2003). AC corona discharge has been shown to achieve methane conversion at low input power of 11 W (42 mA), with a decent SEC of 1638 kJ/mol by Supat et al. (2003). The plasma system consisted of a circular plate as a plane electrode (6.0 mm diameter) and a perpendicular wire as a pin electrode within a quartz tube (7.0 mm internal diameter). However, a rather low methane conversion of 26 % and hydrogen selectivity of 59 % were reported by the authors. Yang (2002) has shown that corona discharges can achieve a high hydrogen selectivity of 70 % and a good methane conversion of 62.4 % at a power input of 46.3 W, flow rate of 43 ml/min and CH₄ /CO₂ ratio 1/1. However, the cost of methane conversion and hydrogen production is rather high compared to AC corona discharge, with SEC of 4638 kJ/mol and SER equalling to 3313 kJ/mol.

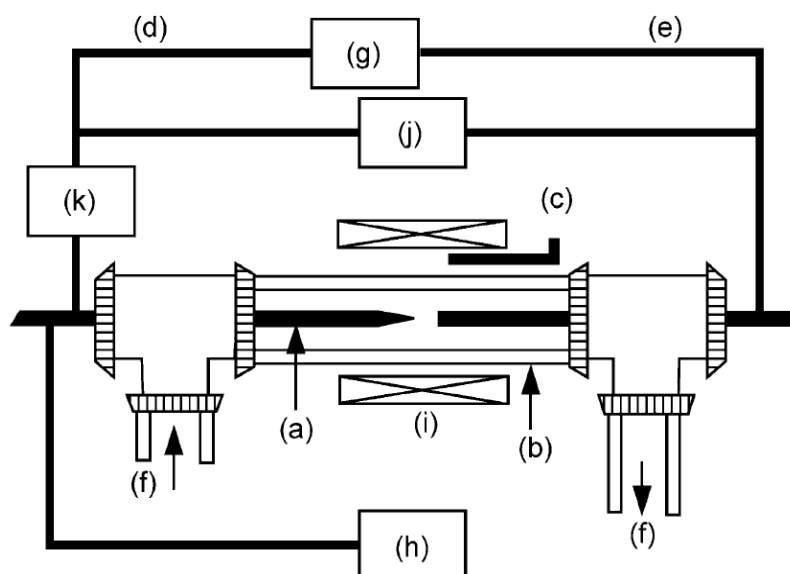


Figure 4.4: Schematic diagram of corona discharge reactor: (a) 1.0 mm diameter stainless steel electrode, (b) 4.0 mm internal diameter pyrex tube, (c) thermocouple, (d) high voltage, (e) ground, (f) direction of the flow gas, (g) direct current high voltage supply, (h) digital oscilloscope, (i) furnace, (j) voltage probe, (k) current transformer (Kado, et al., 2003, Fig. 1).

4.3.2.3. Arc discharges

A study of partial oxidative reactions of methane using carbon dioxide as an oxidative agent in an atmospheric pressure arc discharge reactor has been undertaken by Huang et al. (2000). The average root mean square voltage and current used in the experiments were 1.19kV and 17.4 mA respectively, and the main product gasses were hydrogen and carbon monoxide. Huang et al. (2000) have achieved 70 % methane conversion with 66 % hydrogen selectivity rate.

A multistage gliding arc discharge has been developed by Sreethawong et al. (2007) for partial oxidation of methane with air for syngas production. The system was operated at atmospheric pressure and room temperature, consisting of four reactors (referred to as stages 1 to 4), each containing two diverging knife shaped stainless steel electrodes, see Figure 4.5. The main experimental products were hydrogen and carbon monoxide, with other hydrocarbons present. The authors have concluded from the experimental results that increasing the stages in the process from 1 to 4 results in the increase of methane conversion due to increased residence time, as well as a decrease in power consumption. Under optimum conditions selected by Sreethawong et al. (2007), (CH_4 / O_2 ratio 3/1, flow rate of 150 ml/min, frequency of 300 Hz and voltage of 14.5 kV), the lowest SEC and SER achieved are 1475 kJ/mol and 1603 kJ/mol respectively, at very low methane conversion rate of 12 % and hydrogen selectivity of 46 %. Rueangjitt et al. (2009a) have reported an improved methane conversion and hydrogen selectivity both equalling to 50 % using the same multistage gliding arc reactor, flow rate (150 ml/min) and frequency (300 Hz) as described above, at a slightly higher voltage input of 17 kV and a different gaseous composition consisting of 49 % CH_4 , 21 % CO_2 and 30 % O_2 in the feed or a $\text{CH}_4, / \text{CO}_2 / \text{O}_2$ ratio of 4.9/2.1/3.

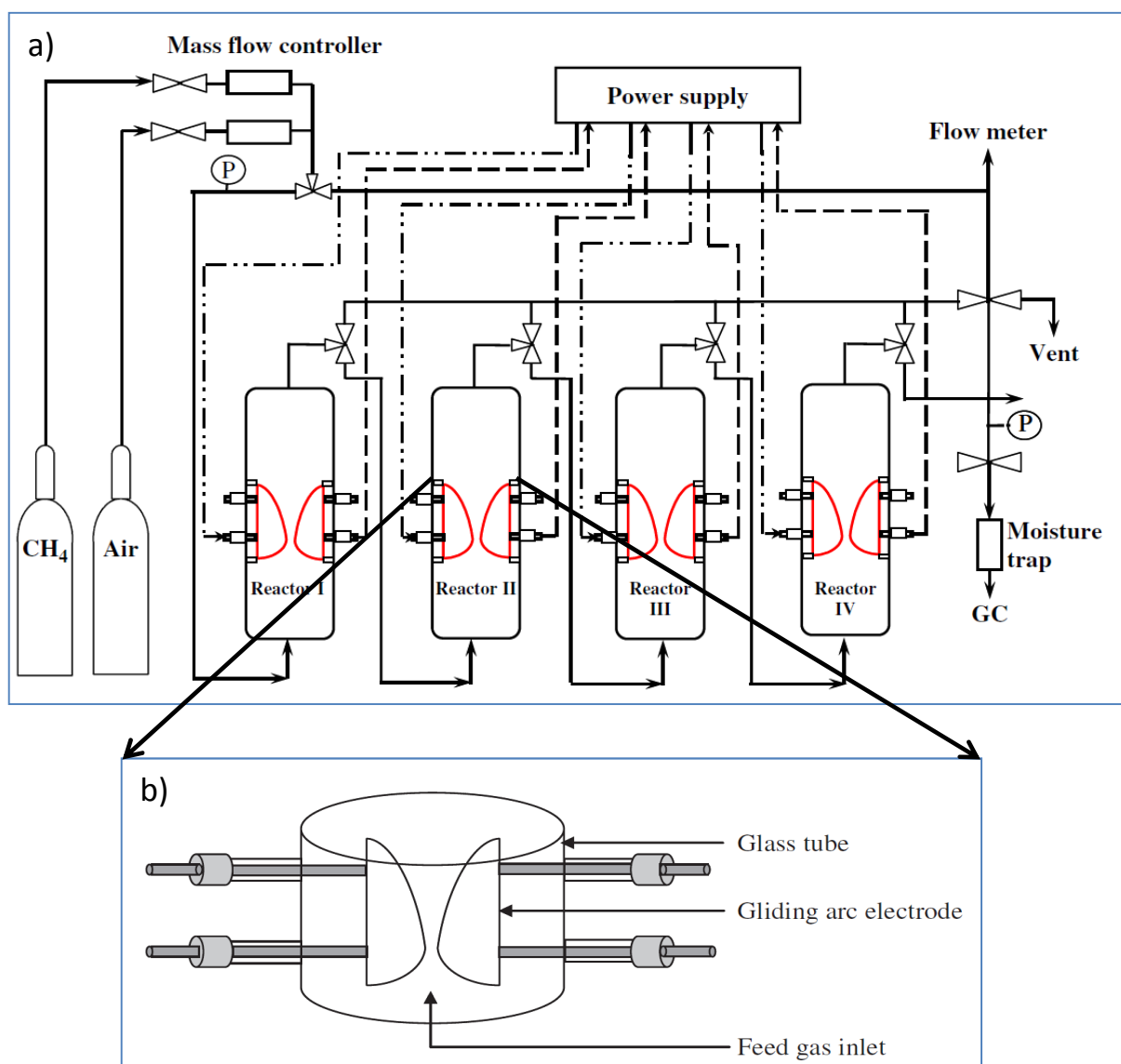


Figure 4.5: Multistage gliding arc reactor set-up. a) configuration of gliding arc discharge system showing the set-up of the four stages, b) configuration of each gliding arc discharge reactor (Sreethawong et al., 2007, Figs. 2 and 3).

Intardo et al. (2006) have achieved a lower SEC and SER (both at 1283 kJ/mol) and higher methane conversion and hydrogen selectivity of 40 % and 50 % respectively, also employing the gliding arc discharge, at the input power of 190 W, flow rate of 1000 ml/min and CH₄ /CO₂ ratio 1/1. The plasma reactor consist of two stainless steel diverging electrodes (150 mm in length, shortest separation distance of 1 mm) within a quartz-glass tube (inner diameter 450 mm, total volume 0.5 L), see Figure

4.6. Plasma was generated using a high frequency (10 – 20 kHz) AC power supply (max voltage 10 kV, max current 100 mA).

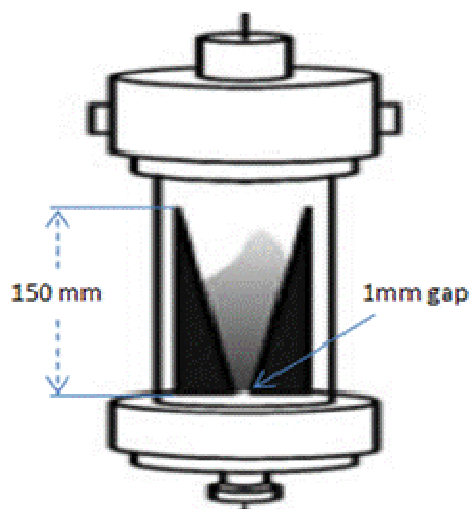


Figure 4.6: Gliding arc plasma reactor, showing the diverging electrodes within a quartz-glass tube (Intardo et al., 2003, Fig. 1).

Non-thermal plasma systems provide high selectivity and energy efficiency for plasma chemical reactions, where thermal plasmas can provide high electron density and temperature. An intermediate plasma system called gliding arc tornado (GAT) has been proposed by Kalra et al. (2005a) to combine the advantages of both thermal and non-thermal plasma features and provide simultaneously high level of chemical reaction selectivity, high electron temperature and high electron density. The main feature in GAT, as recognised by the authors is the reverse vortex flow in a cylindrical volume, which provides high gas velocity and enhances intermediate plasma parameters for gliding arc. As described by Kalra et al. (2005) an experimental unit consisting of a GAT reactor, heat exchanger, power supply and data acquisition has been developed in the Drexel Plasma Institute for partial oxidation of methane to syngas using intermediate plasma. The authors reported that 200 W of electric power is required for stable plasma formation and no soot formation, electrode erosion or corrosion was observed in the process. Maximum conversion of methane to syngas achieved, as reported by Kalra et al. (2005) is 80 - 85 %, with the highest hydrogen production of approx 35 % of total products. The GAT system has been recognised as ‘The most practically attractive yield and energy

efficiency characteristics of methane partial oxidation process and syngas production' by Fridman (2008).

4.3.2.4. Thermal plasma

Tao et al. (2008) have achieved a high methane conversion and reasonable hydrogen selectivity, 89.2 % and 65.6 % respectively, using a DC thermal plasma jet. The

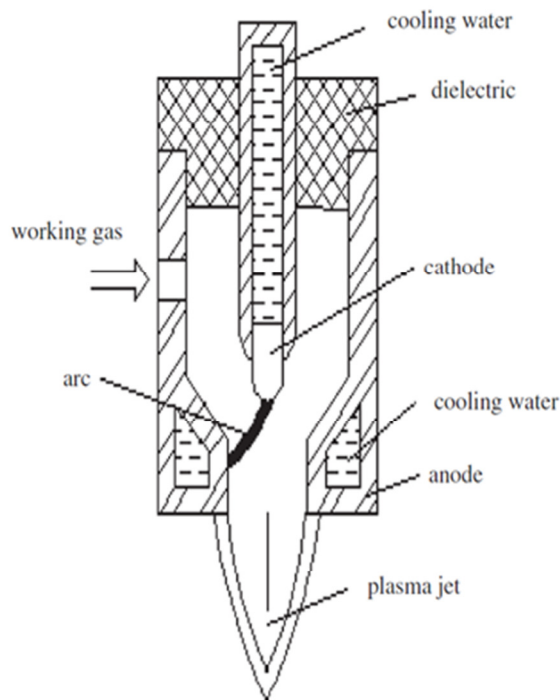


Figure 4.7: DC thermal plasma jet (Tao et al., 2008, Fig. 2).

plasma generation system is composed of a club-shaped cathode and a columnar anode, the tube reactor is composed of a metal interlining with cooling water outside, a graphite pipe inside, and heat preservation materials between the two, see Figure 4.7. Selected optimal conditions were: flow rate of 30000 ml/min, $\text{CH}_4 / \text{CO}_2$ ratio 4/6 and input power of 9.6 kW. The SEC and SER for this system are 1198 kJ/mol and 873 kJ/mol respectively, which are much higher than those of some non-thermal plasmas, such as cold plasma jet and glow discharges.

Tao and the team have reported results for an improved reactor in 2009, called the binode thermal plasma. In this configuration, the reactor consisted of a club-shaped cathode and two columnar anodes, separated by insulating materials, see Figure 4.8. To start the discharge, high voltage is triggered between cathode and the first anode, then a DC voltage is applied to the second anode, and a stable arc is maintained between the cathode and the second anode when the electric circuit of the first anode is turned off. The longer distance between cathode and the second anode results in a larger discharge power of the plasma generator than that of a single anode plasma generator (Tao et al., 2009). Under selected optimal conditions by the authors

(73300 ml/min flow rate, CH₄/CO₂ ratio 4/6 and the input power of 18 kW) methane conversion was 78.71 %, which is lower than for the thermal plasma torch reported by Tao et al. in 2008. However, hydrogen selectivity, SEC and SER were significantly improved equalling to 82.85 %, 1048 kJ/mol and 642 kJ/mol respectively.

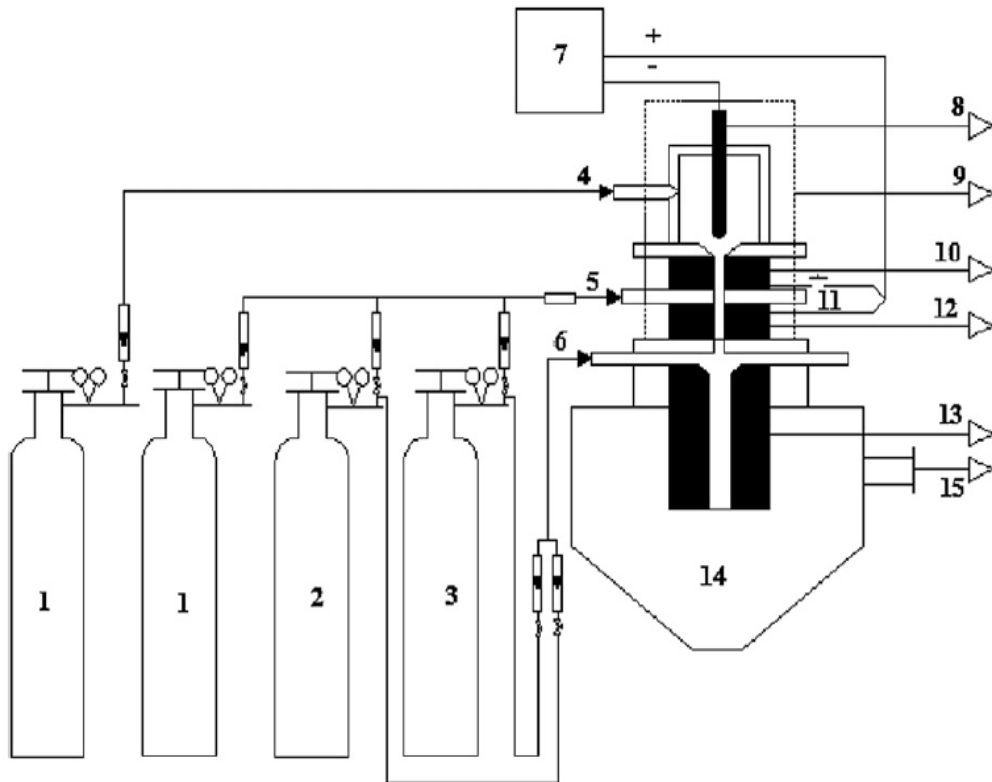


Figure 4.8: Binode thermal plasma reactor set-up. 1, 2 and 3 are feed gases; 4, 5 and 6 are gas inlets; 7 DC power supply; 8 cathode; 9 plasma generator; 10 first anode; 11 contactor; 12 the second anode; 13 graphite tube reactor; 14 collector; 15 gas outlet (Tao et al., 2009, Fig. 1).

Kim and Chun (2008) have achieved a very high methane conversion, as well as hydrogen selectivity of 99.2 % and 78.8 % respectively, by employing plasmatron applied to thermal plasma. This was achieved under the following conditions: flow rate of 5100 ml/min, 38.5 % CH₄ concentration in air and the input power of 6.4 kW. However, the SEC and SER are very high for this system, equalling to 4416 kJ/mol and 2807 kJ/mol respectively, and over 3 times higher compared to thermal plasma systems reported by Tao et al. (2008 and 2009).

4.3.2.5. Comparing plasma assisted partial oxidation systems

Table 4.1 lists the summary of conditions and experimental results obtained by the different plasmas employed for the partial oxidation of methane starting with the lowest SEC and SER. It can be seen from Table 4.1 that the lowest energy consumption for methane conversion and hydrogen generation has been achieved by employing cold plasma jet by Li et al. (2009, 2010). The cold plasma jet presented in 2009 exhibits the lowest SEC and SER values achieved of 174 and 97.8 kJ/mol respectively. Li et al. (2010) achieved a very high methane conversion of 97.99 % and high hydrogen selectivity of 79 % at the expense of an increase to the SEC and SER values equalling to 312 kJ/mol and 197.9 kJ/mol respectively (Li et al., 2009). In both cases the reactant flow was equal or above 1 L/min, another advantage for industrial applications. Very high methane conversion rate and hydrogen selectivity has been achieved by DC thermal plasmatron. However, at much higher cost of methane conversion and hydrogen production, see Table 4.1. Both single-anode and binode thermal plasmas exhibit a high potential for industrial applications, with large treatment capacity, high conversion and selectivity rates and decent SECs and SERs.

Table 4.1: Comparison of SEC and SER for methane partial oxidation to syngas by different plasmas, starting with the lowest energy consumption at the top.

Plasma form	Feed flux (ml/min)	CH ₄ to other reactants ratio	Input power (W)	CH ₄ conversion (%)	Hydrogen selectivity (%)	SEC (kJ/mol CH ₄ converted)	SER (kJ/mol H ₂ produced)	Reference
Plasma jet	2200	4/6 CH ₄ /CO ₂	69.85	60.97	89.30	174	98	Li et al., 2009a
Plasma jet	1000	4/6 CH ₄ /CO ₂	88.4	94.99	79	312	198	Li et al., 2010
Glow-like	10.5	25% CH ₄	155	-----	-----	-----	324	Luche et al., 2009*
AC Cold plasma jet	16.67 X 10 ³	4/6/11 CH ₄ /CO ₂ /N ₂	770	45.68	78.11	682	437	Long et al., 2008
Pulsed glow discharge	120	1/1 CH ₄ /CO ₂	23	61	77	845	548	Ghorbanzadeh et al., 2009
AC corona discharge	100	3/1 CH ₄ /O ₂	11	26	59	1638	-----	Supat et al., 2003**
Binode thermal plasma	7.33 X 10 ⁴	4/6 CH ₄ /CO ₂	1.8 X 10 ⁴	78.71	82.85	1048	642	Tao et al., 2009
Single-anode thermal plasma	3 X 10 ⁴	4/6 CH ₄ /CO ₂	9.6 X 10 ³	89.82	68.60	1198	873	Tao et al., 2008
GA discharge	1 X 10 ³	1/1 CH ₄ /CO ₂	190	40	50	1283	1283	Intardo et al., 2006
Gliding arc	150	3/1 CH ₄ /O ₂	14.8	12	46	1475	1603	Sreethawong et al. 2007
Plasmatron	5.1 X 10 ³	CH ₄ conc 38.5% in air	6.4 X 10 ³	99.2	78.8	4416	2807	Kim and Chun, 2008
Microwave discharge	7 X 10 ³	CH ₄ conc 5%	600	48	98	4800	2448	Tsai et al. 2005

* Use the value of kWh/kg H₂ provided by the authors. 1 kWh/kg H₂ = 7.2 kJ/mol.

** Use the value of eV/molecule provided by the authors. 1 eV/molecule = 96.4 kJ/mol (Larkin, et al., 2001).

4.3.3. Hydrogen production by methane decomposition

Pyrolysis of methane is a direct decomposition of methane into hydrogen and carbon black, described in detail in Chapter 2, section 2.5. As reported by Fridman (2008) arc plasma jets (thermal plasma) have been investigated for methane pyrolysis, reaching hydrogen concentration in products of 76 %, however used a high power input of 30 kW. Kim et al. (2005) have investigated DC-RF (direct current – radio frequency) hybrid thermal plasma for hydrogen and carbon black production, see Figure 4.9. In this configuration, plasma jets are ejected from the DC torch at very high speed and then are expanded more broadly inside an inductively coupled RF torch. This plasma reactor set-up can achieve larger hot thermal plasma volume, more stable jet flame and higher parameter control flexibility when compared to individual DC or RF torches. Radio frequency plasma is excited and sustained by high frequency electromagnetic fields usually in the frequency range 1 – 100 MHz and wavelengths 3 – 300 m (Conrads and Schmidt, 2000). Kim et al. (2005) used RF power of 14.76 kW and a DC power of 7.60 kW for the experiments, and the results showed that the main gaseous product was hydrogen with some acetylene and residual methane present. Carbon black was produced in solid form and exhibited high degree of crystallization. Therefore, the authors indicated that it might have a potential for conductive applications. This system could be very attractive as it produces two useful products, namely hydrogen and carbon black, without carbon dioxide or other emissions. However, energy consumption is considerably high as recognised by the authors.

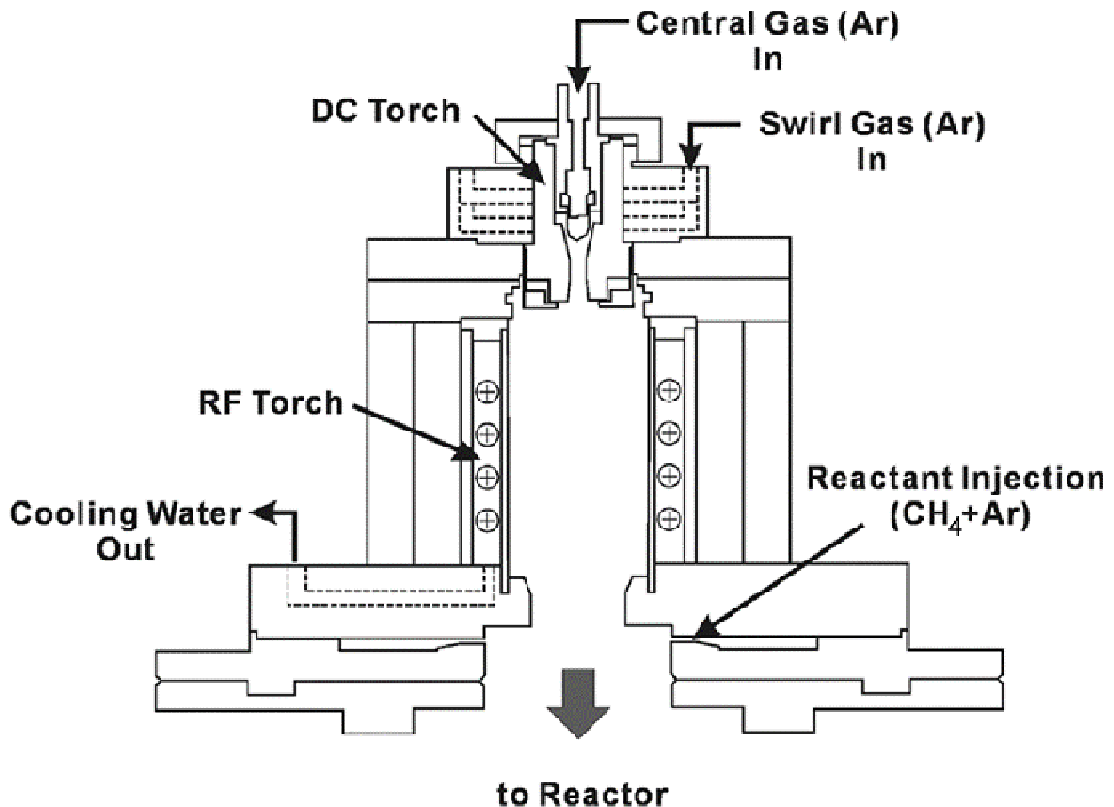


Figure 4.9: Cross-sectional view of the DC-RF plasma torch set-up (Kim et al., 2005, Fig. 1).

Slovetskii (2006) has recognized three main advantages of using non-thermal plasma in hydrocarbon decomposition: the elimination of power consumption for gas heating, possible reduction of specific power consumption and elimination of product quenching due to low gas temperature. Non-thermal plasmas including atmospheric-pressure microwave discharges (Fridman, 2008; Tsai and Chen, 2009), pulsed plasma discharges (Yao et al., 2001; Yao et al., 2002; Li et al., 2004; Da Silva et al., 2006), DBD reactors (Wang et al., 2009) and AC gliding arc (Rueangjitt et al., 2007) have been investigated for direct methane pyrolysis.

Li et al. (2004) have experimentally demonstrated that pulsed spark discharges with needle-to-plate electrode configuration, feed flow of CH₄ 10 ml/min and 12 W power input, can achieve a 69 % methane conversion, with 51 % hydrogen and 54 % acetylene yields. In this set up tungsten needle (1 mm diameter) was used as a high-voltage pin electrode and an iron plate (9 mm diameter) as the ground electrode, with the distance between the two set at 6 mm, see Figure 4.10. Low electricity consumption in this method might be attractive for process commercialization. However, low hydrogen yields and low treatment capacity, both

indicate that improvement is needed. Li et al. (2004) have also recognized that the increase in methane conversion from 18 to 69 % has led to the increase in specific energy consumption for both methane conversion (from 1349.6 to 2410 kJ/mol) and hydrogen production (from 964 to 1638.8 kJ/mol).

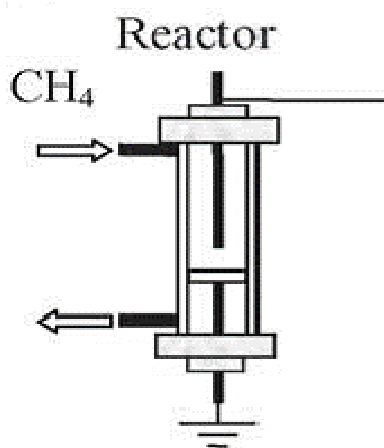


Figure 4.10: Spark discharge reactor showing pin-to-plate electrode configuration (Li et al., 2004, Fig. 1b).

High hydrogen selectivity and reasonable methane conversion, 86 % and 61.8 % respectively, has been achieved in single stage, non-catalytic, dry methane pyrolysis with atmospheric pressure microwave reactor at 0.8 kW input power and 1200 ml/min flow rate with 20 % CH₄, by Tsai and Chen (2009). The system shows a higher commercialization potential than the pulse discharge, with reasonably low SEC and SER values of 1022 kJ/mol and 646 kJ/mol respectively, decent treatment capacity and reasonable methane conversion. Synthesized

carbon powders were also examined, and the authors suggested their possible use as a support for platinum catalysts in proton exchange membrane fuel cells. Rueangjitt et al. (2007) employed AC gliding arc discharge for methane pyrolysis, at flow rate of 150 ml/min, 15.5 kV and 200 Hz. However, the authors have reported very low methane conversion and low hydrogen selectivity, 4 % and 40 % respectively, which in turn results in very high SEC and SER of 4215 kJ/mol and 4817 kJ/mol. It is very clear that the system needs major improvements in methane conversion efficiency as well as energy consumption. Interestingly, Rueangjitt et al. (2007) reported even higher specific energies for methane conversion and hydrogen production when helium was added as a dilution gas to methane. The authors suggested that, since helium is an inert gas, it absorbs some input energy leading to higher energy consumption.

Very interesting work worth mentioning has been done by Da Silva et al. (2006) on methane plasmalysis using high frequency pulsed plasma (HFPP) and simultaneous storage of hydrogen in titanium sheet. The authors recognised difficulties of hydrogen storage due to its low density and boiling point, and therefore were aiming

to achieve hydrogen storage in solid solutions, which could be easily transported and then hydrogen recovered. Metallic hydrates such as titanium depict the highest volumetric density for hydrogen and therefore were used in this study. HFPP reactor contained titanium plates set in parallel on top of the cathode and > 900ppm of hydrogen production and storage in the titanium plates have been achieved. The method was proven to be successful for simultaneous hydrogen production and storage, Da Silva et al. (2006) have also indicated that the reactor configuration and titanium electrodes can be optimized to produce large amounts of hydrogen for large scale storage.

4.3.4. Steam and auto-thermal reforming of methane

Steam reforming of methane is an endothermic process of methane oxidation by water vapour. Wang et al. (2010) have achieved a rather high methane conversion and hydrogen selectivity, 91.6 % and 92.7 % respectively, using atmospheric-pressure microwave reactor at 1 kW power input and 12000 ml/min flow rate, with 5 % CH₄ concentration in the feed. SEC and SER for this system are reasonable at 2450 kJ/mol and 1329 kJ/mol respectively. The authors themselves recognise the need for process improvement. Xu et al. (2009) have employed dielectric barrier discharge (DBD) system for steam reforming of methane. At 4 ml/min CH₄ flow and 49 W of input power methane conversion and hydrogen selectivity reported are both very low, 22 % and 42 % respectively. Hence, the cost of methane conversion and hydrogen production is very high, with SEC and SER at 7492 kJ/mol and 8909 kJ/mol respectively.

Auto-thermal reforming (ATR) of methane (also called steam reforming with oxygen - SRO) is a combination of partial oxidation and steam reforming developed by Haldor Topsøe in the late 1950s in order to perform reforming in a single reactor (Pena et al., 1996). Cormier and Rusu (2001), in their comparison of plasma reactors versus chemical reactors, have mentioned that the advantages of SRO include lower energy requirements (due to exothermic nature of partial oxidation combined with endothermic process of steam reforming), lower process temperature than partial oxidation and possible control of hydrogen/carbon monoxide ratio of the syngas produced by controlling inlet gas ratio. Experiments to investigate auto-thermal methane reforming have been successfully carried out using thermal plasma referred

to as plasmatron. Bromberg et al. (1999b) wrote that thermal plasma can be used to accelerate thermodynamically favourable chemical reactions without catalyst use or to provide the energy required for endothermic reforming reactions. The authors have reported the achievement of 70 % methane conversion and hydrogen yield of 40 % using a plasmatron at 3.5 kW power input with no additional catalyst use. The experimental data presented shows that at lower values of power input ranging between 2 – 2.5 kW, methane conversion was only 40 – 50 % and hydrogen yields were below 20 %. Bromberg et al. (1999b) have concluded that methane conversion in plasmatron strongly depends on power input. Experiments performed at plasmatron power input of 6.4 kW have shown a considerable increase of methane conversion to 97.8 % with hydrogen yield of 94.8 %, when no additional catalyst used (Kim and Chun, 2008). These experimental results support the findings of Bromberg et al. (1999b), that auto-thermal reforming of methane strongly depends on power input.

A novel DC water plasma (thermal) torch has been developed by Ni et al. (2011) for methane reformation with carbon dioxide. The water plasma torch is a DC thermal plasma generator, of coaxial design with a cathode of zirconium with 2 mm diameter embedded into a copper rod in the centre and copper nozzle anode, see Figure 4.11. Unlike the systems described above, the plasma created is from dissociating steam into H, OH and O radicals before methane and carbon dioxide are introduced into the system. Water is injected into the reservoir at a constant rate of 2 ml/min. The plasma arc is initiated (DC power supply, max 3.5 kW, 0 – 350 V, 0 – 10 A) and the water is evaporated by the evaporator, the steam then passes through the swirl hole in the evaporator and enters the discharge chamber as a vortex gas, then it is heated to high temperature due to the arc discharge and forms a plasma jet at the nozzle. Methane and carbon dioxide mixture is then introduced into the water plasma torch reactor (Ni et al., 2011). Under the optimal conditions selected by the authors, CH₄/CO₂ ratio of 1/1, feed flow of 4 L/min and power input of 1.05 kW (150 V, 7 A), methane conversion and hydrogen selectivity was at 62.2 % and 81.2 % respectively, with SEC and SER equalling to 1135 kJ/mol and 700 kJ/mol respectively. Interestingly, Nair et al. (2007) concluded that in the presence of oxygen, steam conversion is almost negligible under the experimental conditions studied (DBD, 3 W power input, CH₄ fed with 10 % N₂, ATR). The authors have

pointed out that the main role of steam is to quench the reaction, i.e. to separate stable intermediates formed during the course of the reaction.

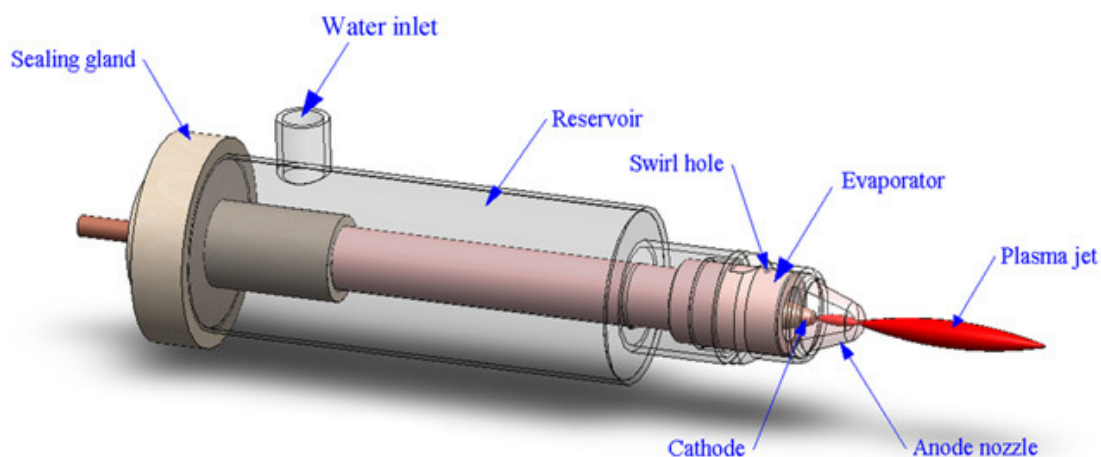


Figure 4.11: Shows the configuration of the novel water plasma torch developed by Ni et al., 2011, (Fig 1).

4.3.5. Comparing PO, pyrolysis and SR plasma systems

Table 4.2 shows the comparison of different methane reformation methods to generate hydrogen. It is clear that partial oxidation mechanism is at the top of the race. Cold plasma jets and certain types of thermal plasmas show the highest potential for industrial applications, both with high treatment capacities and reasonable SEC and SER values. Li et al. (2009, 2010) have presented the most successful system for plasma processing of methane to hydrogen yet. The SEC and the SER values are the lowest when compared to other systems, with high methane conversion and hydrogen selectivity.

Table 4.2: Comparison of PO, Pyrolysis and SR systems for hydrogen generation from methane.

Plasma form	Reaction type	Feed flux (ml/min)	CH ₄ to other reactants ratio	Discharge power (W)	CH ₄ conversion rate (%)	Hydrogen selectivity (%)	SEC kJ/mol CH ₄ converted	SER kJ/mol H ₂ produced	Reference
Plasma jet	PO	2200	4/6 CH ₄ /CO ₂	69.85	60.97	89.30	174	98	Li et al., 2009a
Plasma jet	PO	1000	4/6 CH ₄ /CO ₂	88.4	94.99	79	312	198	Li et al., 2010
NTP – glow	PO	10.5	25% CH ₄ in air	155	-----	-----	-----	324	Luche et al., 2009
Cold plasma jet	PO	8.3 X 10 ³	4/6 CH ₄ /CO ₂	770	45.68	78.11	682	437	Long et al., 2008
Glow discharge	PO	120	1/1 CH ₄ /CO ₂	23	61	77	845	548	Ghorbanzadeh et al., 2009
Microwave discharge	Pyrolysis	1.2 X 10 ⁴	20% CH ₄	800	40	86	1022	646	Tsai and Chen, 2009
Binode thermal plasma	PO	7.33 X 10 ⁴	4/6 CH ₄ /CO ₂	1.8 X 10 ⁴	78.71	82.85	1048	642	Tao et al., 2009
Thermal water plasma torch	ATR	2 X 10 ³	1/1 CH ₄ /CO ₂	1.05 X 10 ³	62.2	81.2	1135	700	Ni et al., 2011
Thermal plasma	PO	3 X 10 ⁴	4/6 CH ₄ /CO ₂	9.6 X 10 ³	89.82	68.60	1198	873	Tao et al., 2008
Gliding arc	PO	1 X 10 ³	1/1 CH ₄ /CO ₂	190	40	50	1283	1283	Intardo et al., 2006
AC corona discharge	PO	100	3/1 CH ₄ /O ₂	11	26	59	1638	-----	Supat et al., 2003
Gliding arc	PO	150	3/1 CH ₄ /O ₂	76.85	45	37	2043	2764	Sreethawong et al. 2007

PO: partial oxidation; SR: steam reforming; ATR: autothermal reforming.

4.3.6. Important parameters reported in literature

In sections 4.3.2 to 4.3.4 descriptions of plasma assisted methane conversion systems with optimal parameters chosen by the authors and the resultant methane conversion and hydrogen selectivity were described. In this section, the main parameters and their affects reported will be discussed. At the end of this section a summary with tables containing key information for each parameter are presented.

4.3.6.1. Flow rate

Flow rate is a very important factor as it resembles the residence time of the reaction and the higher the flow rate the lower the residence time. Experimental results reported show that an increase in flow rate results in a decrease in methane conversion for methane partial oxidation by: AC arc (Huang et al., 2000), multistage gliding arc (Sreethawong et al., 2007), cold plasma jet (Long et al., 2008; Li et al., 2010), glow discharge (Chen et al., 2006; Luche et al., 2009), thermal plasmatron (Tao et al., 2008), and for pyrolysis method by a microwave discharge (Tsai and Chen, 2009), see Figure 4.12. The effects of flow rate on hydrogen selectivity differ between the different methods and systems. A decrease of hydrogen selectivity with increased flow rate has been experimentally shown for methane partial oxidation by a multistage gliding arc (Sreethawong et al., 2007), cold plasma jet (Long et al., 2008) and glow discharge (Luche et al., 2009), see Figure 4.13 a) and c). Huang et al., (2000) reported that the flow rate had no effect on product distribution in methane conversion for methane partial oxidation by AC arc. Interestingly, Li et al., (2010) and Chen et al. (2006) reported hydrogen selectivity increased with the flow for cold plasma jet and glow discharge PO of methane respectively, see Figure 4.13 a) and b). Ni et al. (2011) have reported that a flow increase from 2000 ml/min to 6000 ml/min in thermal water plasma jet ATR of methane drastically decreased the conversion of methane from above 90 % to 50 %, see Figure 4.12 b). Interestingly, the selectivity of hydrogen increased from 55 to 75 % with the flow increase from 2000 /min to 5000 ml/min, then decreased to 65 % as the flow was further increased to 6000 ml/min, see Figure 4.13 b). Initial increase in hydrogen selectivity followed by a decrease with the increasing flow rate has also been reported for PO method employing thermal plasmatron by Tao et al. (2008), see Figure 4.13 c).

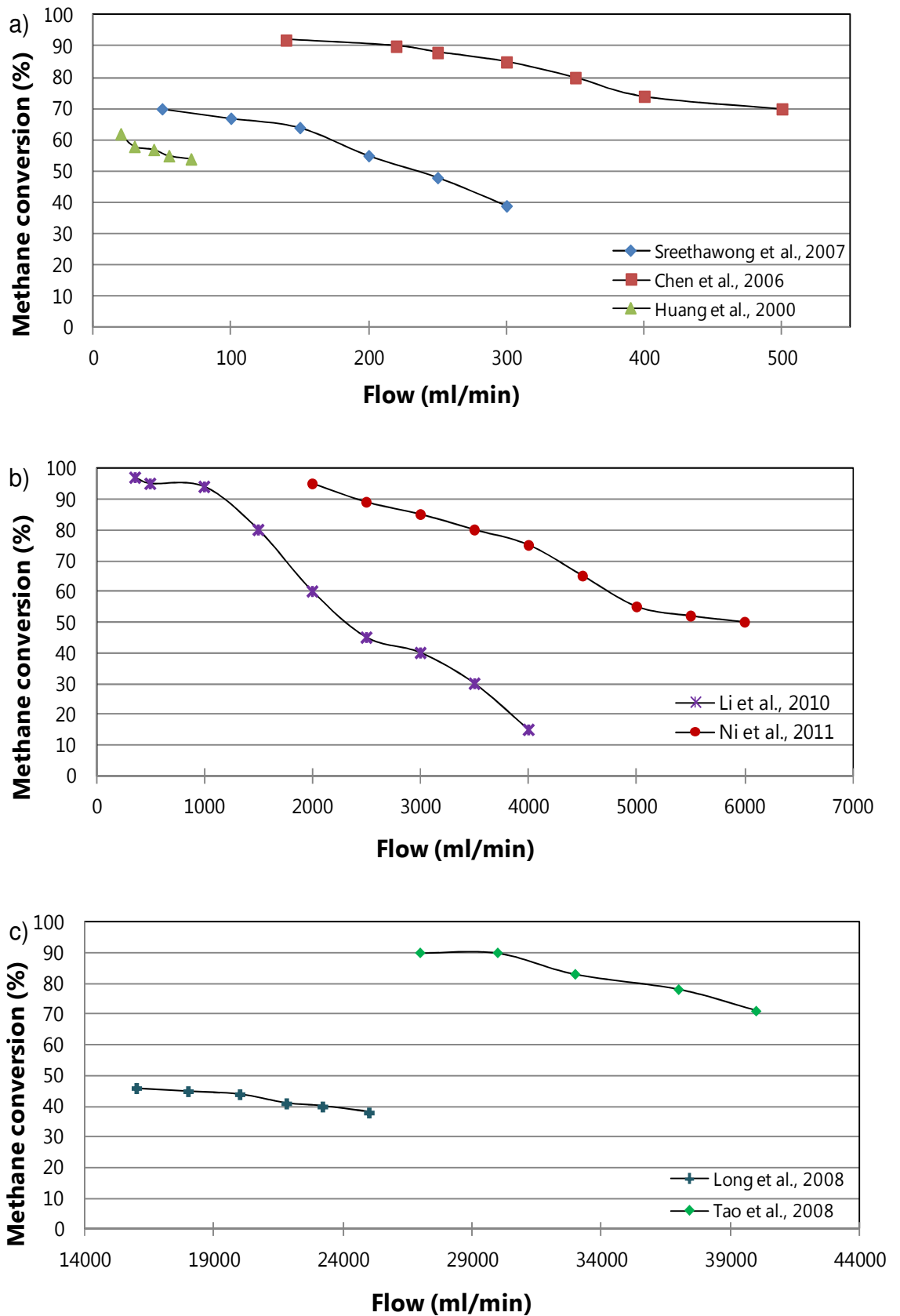


Figure 4.12: The effects of flow rate on methane conversion reported in the literature for a flow rate range of a) 20 – 500 ml/min; b) 360 – 6000 ml/min; c) 13,000 – 40, 000 ml/min.

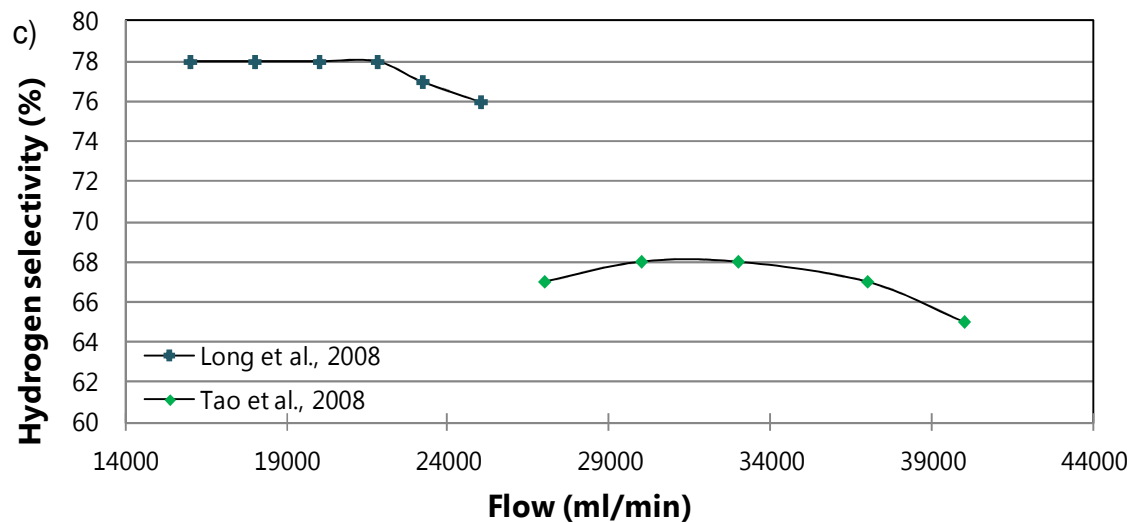
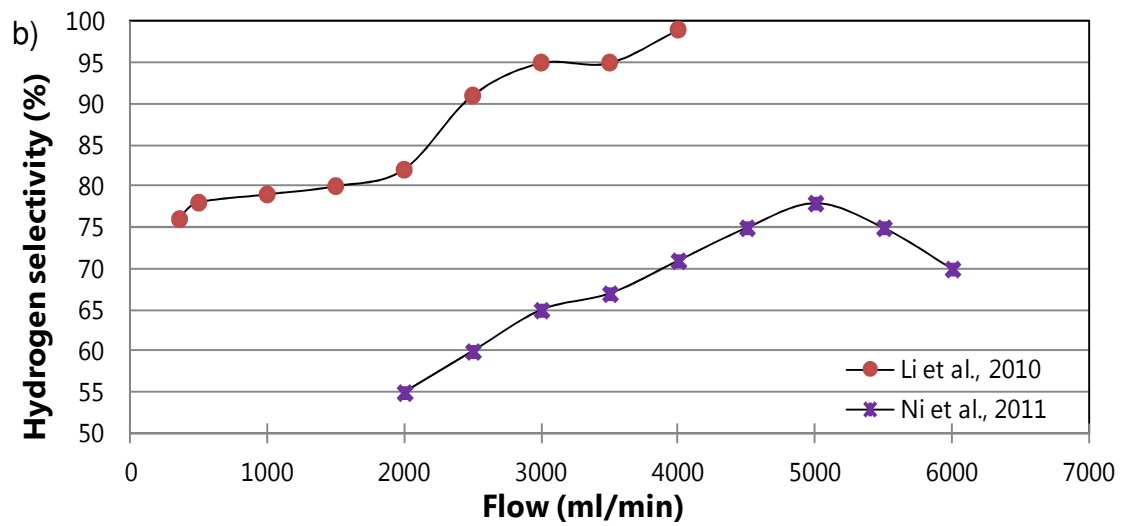
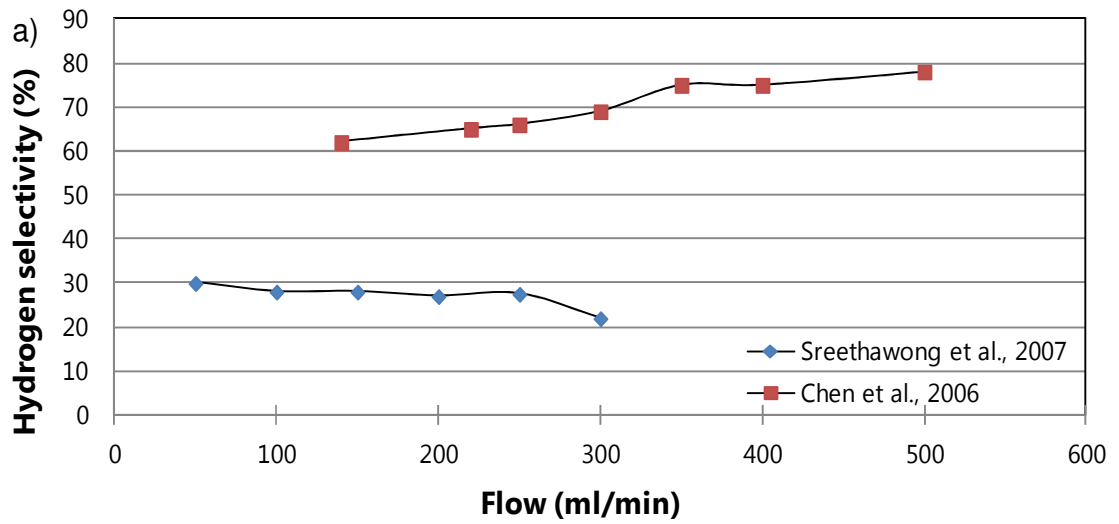


Figure 4.13: The effects of flow rate on hydrogen selectivity reported in the literature for a flow rate range of a) 20 – 500 ml/min; b) 360 – 6000 ml/min; c) 13,000 – 40, 000 ml/min.

Capezzuto et al. (1978) concluded that for plasma assisted partial oxidation and steam reforming of methane higher flow rates led to higher total yields and lower power inputs. The reported lower cost of hydrogen production at high flow rates can be explained by the fact that higher flow rates result in a higher total volume of methane converted, due to more reactant flowing in a system per second. However, this is only true if the conversion of methane is not too low to diminish the effect of the flow, as increasing the flow decreases methane conversion. Therefore, a conclusion can be drawn, that total flow of reactants is a crucial parameter for an efficient plasma assisted hydrogen generation from methane. Hence, for each system a balance between high methane conversion and the low cost of hydrogen production must be selected.

4.3.6.2. Power input

Power input is technically regarded as a key parameter in operating plasma chemical processing and in sustaining plasma stability (Rueangjitt et al., 2009). An increase in power input has been experimentally determined to result in an increase in methane conversion in autothermal reactions employing thermal plasmatron (Bromberg et al., 1999b), partial oxidation of methane in gliding arc discharges (Huang et al., 2000; Sreethawong et al., 2007), plasma jet (Li et al., 2010), microwave discharges (Tsai et al., 2005; Tsai and Chen, 2009) and glow discharge (Chen et al., 2006), and methane pyrolysis reactions in corona discharge (Li et al., 2004) and gliding arc discharge (Rueangjitt et al., 2009). An increase in methane conversion, followed by a decrease and then further increase with the power input has been observed in methane pyrolysis reactions using corona and gliding arc discharges, see Figure 4.14 a) and b). For PO reactions in microwave and glow discharges a straight forward methane conversion rate increase with the power input has been experimentally shown, see Figure 4.14 c).

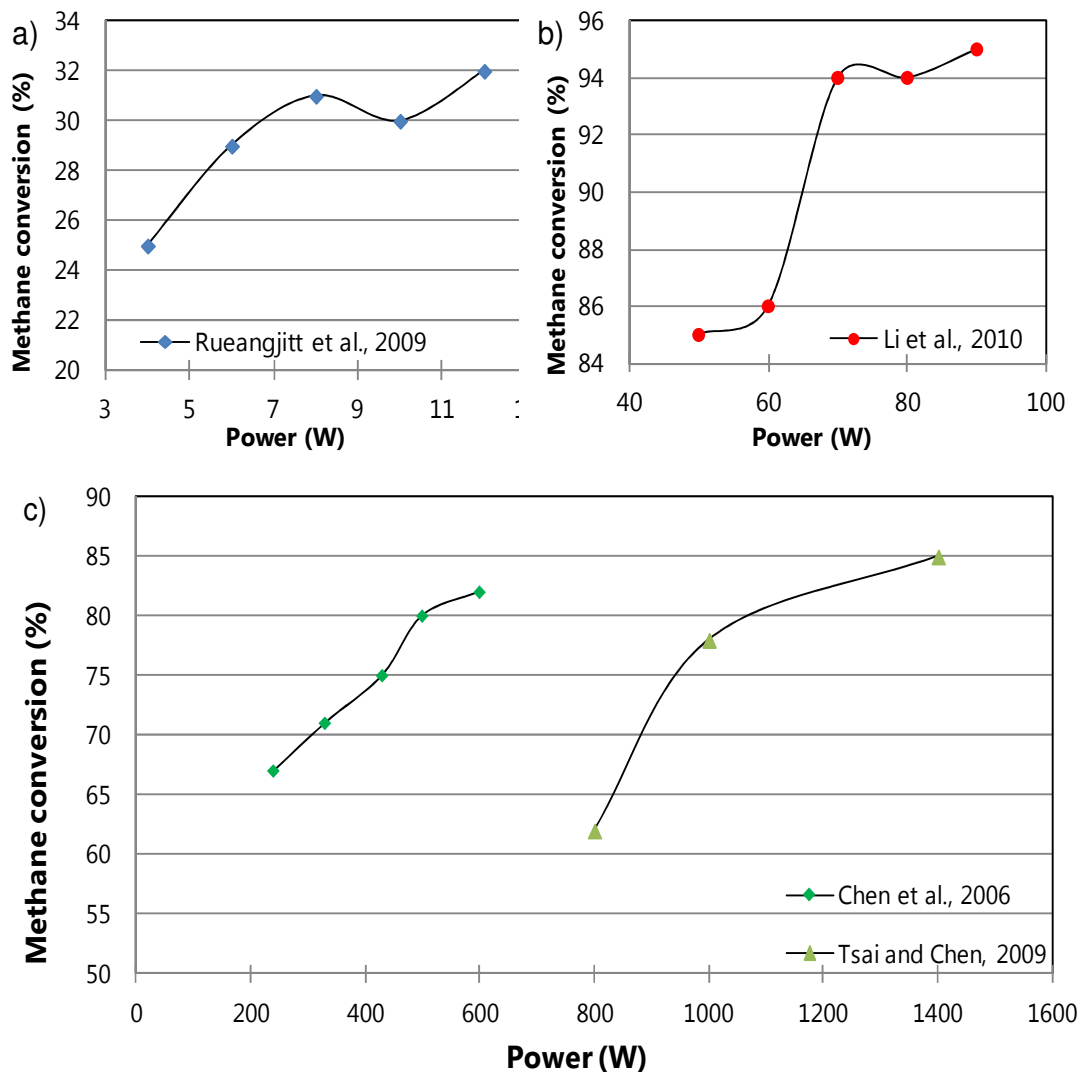


Figure 4.14: The effect of power input on methane conversion reported in literature in the power range of: a) 2 – 12 W; b) 50 – 90 W; c) 200 – 1400 W.

Tsai and Chen (2009) have experimentally shown for pyrolysis of methane in microwave discharge an increase in power input has also resulted in lower hydrogen selectivities (see Figure 4.15) and an increase in SEC and SER values, from 1022 to 1350 kJ/mol and from 646 to 868 kJ/mol respectively. In partial oxidation of methane employing a glow discharge, initially a slight decrease in hydrogen selectivity by 2 % was reported as the power input increased from 240 to 430 W, followed by an increase in hydrogen selectivity (by 3 %) as the power input was further increased to 600 W, see Figure 4.15.

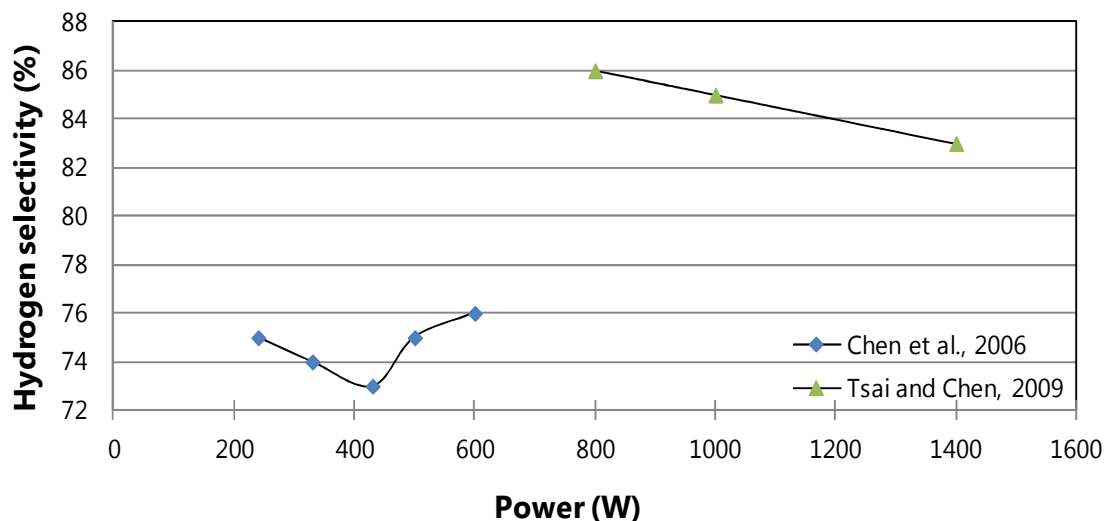


Figure 4.15: Effect of discharge power on hydrogen selectivity reported in the literature.

It is not surprising that higher power inputs favour methane conversion, since at higher power inputs more energy is available for chemical reactions to take place. The decrease in hydrogen selectivity could be explained by the possibility that higher power levels favour the production of higher hydrocarbons such as acetylene. The reason for increase in the SEC and SER values is very clear when looking at formulae (4.3) and (4.4) in section 4.2. Hence, once again as in total flux regulation, optimal conditions for the system regarding the applied power, is a balance between methane conversion rate, hydrogen selectivity and cost.

4.3.6.3. Gas composition

Gas composition, in its essence, is the ratio of methane (can be expressed as percent methane concentration) to other reactants or dilution gases such as nitrogen. For example, the ratio of carbon dioxide to methane in partial oxidation can be expressed as CO_2/CH_4 ratio 0.5 or 1:2, which means there are two parts of methane and one part of carbon dioxide in the gas composition. When the ratio is expressed as one number, lower numbers represent higher methane concentrations. Therefore, increasing this ratio results in lower methane concentration in the gas composition.

Investigations have been carried out for the effects of O_2/CH_4 or air/ CH_4 ratio (Tsai et al., 2005; Sreethawong et al., 2007; Luche et al., 2009; Kim and Chun, 2008) and CO_2/CH_4 ratio (Huang et al., 2000; Long et al., 2008; Ghorbanzadeh et al., 2009; Li

et al., 2010; Ni et al., 2011) in partial oxidation reactions, N_2/CH_4 ratio in pyrolysis reactions (Tsai and Chen, 2009) and H_2O/CH_4 ratio in steam reforming (Wang et al., 2010).

Higher ratios of O_2/CH_4 (lower methane concentrations) have been experimentally shown to achieve higher methane conversion rates when employing microwave discharge (Tsai et al., 2005) and gliding arc discharge (Sreethawong et al., 2007), see Figure 4.16 a). However, hydrogen selectivity was lower at higher O_2/CH_4 ratios, see Figure 4.16 b). Hence, in PO of methane in non-thermal plasmas by oxygen, lower concentrations of methane favour methane conversion. In contrast, hydrogen selectivity is favoured by higher methane concentrations (Luche et al., 2009). Interestingly, thermodynamic analysis of methane PO suggests that the optimal O_2/CH_4 ratio is 0.5 (Zhu et al., 2001), which yields higher hydrogen selectivity with lower methane conversion rates.

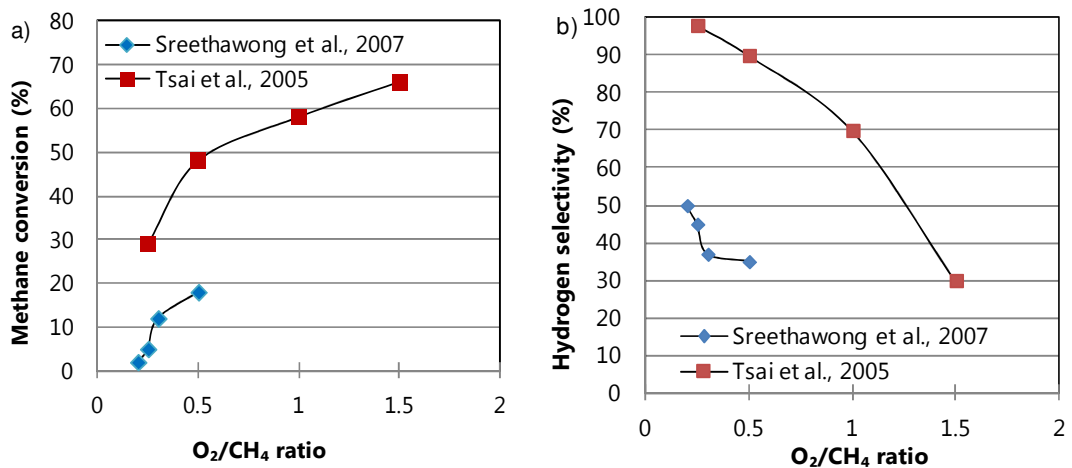


Figure 4.16: Effects of O_2/CH_4 ratio reported in literature on a) methane conversion; b) hydrogen selectivity.

Kim and Chun (2008) investigated the effects of methane concentration in PO in air by employing thermal plasmatron. Interestingly, the authors have discovered that an increase of methane concentration in air from 24 to 38.5 % (ratio decrease from 3.2 to 1.6) resulted in a slight increase in methane conversion from 95 to 99.2 % and a high increase in hydrogen selectivity from 30 to 78.8 %, see Figure 4.17. However, Kim and Chun (2008) have also reported that further increase in methane

concentration up to 47 % (ratio decrease to 1.1) resulted in a decrease of methane conversion. These results might suggest that O_2/CH_4 ratio has different effects on methane conversion in thermal and non-thermal plasmas. It could also be the fact that in the investigation of non-thermal plasma PO with oxygen or air, the ratios were in the range of 0.2 to 1.5, whereas in thermal plasma the effects are observed at higher ratios.

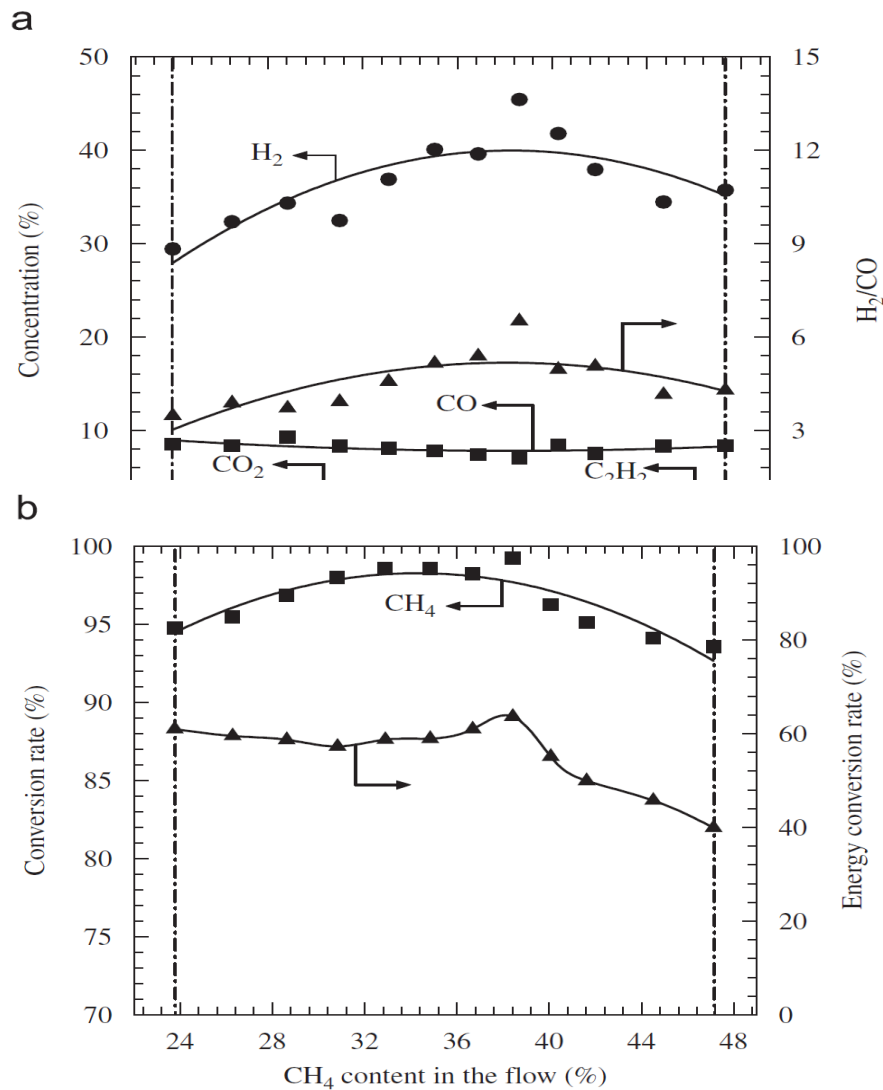


Figure 4.17: Effect of variations in CH_4 flow ratio: a) concentration of hydrogen and H_2/CO ratio; b) conversion rate and energy conversion rate (Kim and Chun, 2008; Fig. 2).

The CO_2/CH_4 ratio has a similar pattern to O_2/CH_4 ratio effects regarding methane conversion. However, slightly different results regarding hydrogen selectivity have been reported. Increasing CO_2/CH_4 ratio led to higher methane conversion in glow

discharges (Chen et al., 2006; Ghorbanzadeh et al., 2009), AC arc (Huang et al., 2000) and cold plasma jets (Long et al., 2008; Li et al., 2010) for partial oxidation reactions and in a thermal water plasma ATR system (Ni et al., 2011), see Figure 4.18. Higher CO_2/CH_4 ratio has been reported to result in lower hydrogen selectivity rate in glow discharges (Chen et al., 2006; Ghorbanzadeh et al., 2009) and cold plasma jets (Long et al., 2008; Li et al., 2010) for partial oxidation reactions, and in a thermal water plasma ATR system (Ni et al., 2011), see Figure 4.19. However, Huang et al. (2000) have noted that in AC arc PO of methane, increasing CO_2/CH_4 ratio from 0.11 to 9 has led to an increase in methane conversion as well as hydrogen selectivity, from 34 to 70 % and 47.9 to 66 % respectively, see Figure 4.20. Intardo et al. (2006) have also reported an increase in hydrogen selectivity with CO_2/CH_4 ratio, see Figure 4.21. Interestingly, the authors have also reported a decrease in methane conversion, see Figure 4.21.

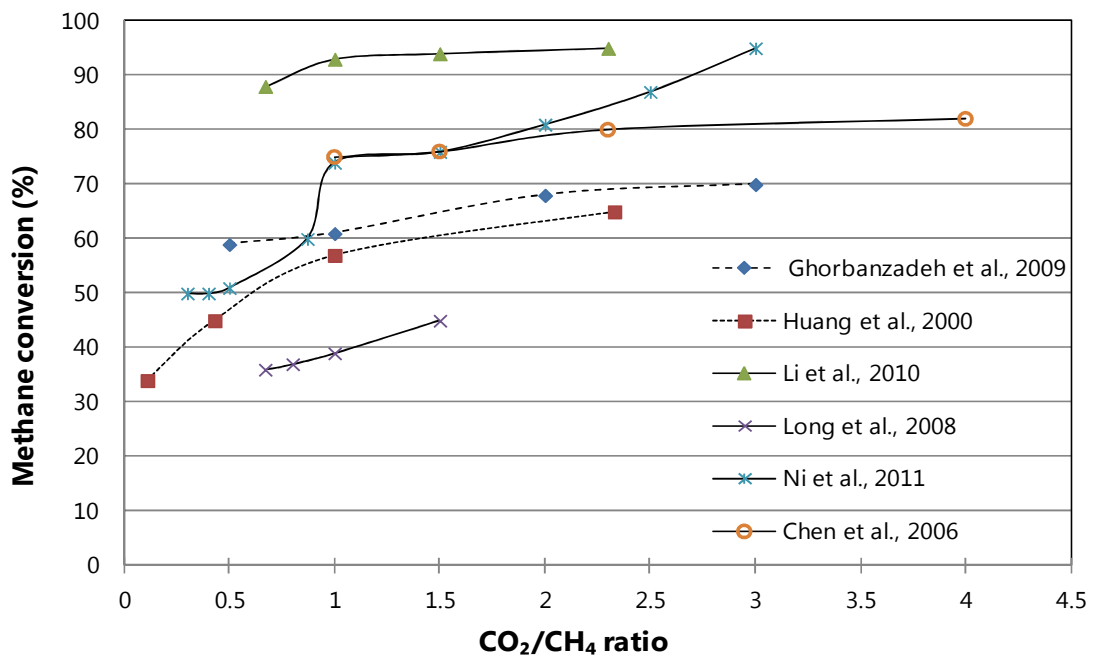


Figure 4.18: The effect of CO_2/CH_4 ratio on methane conversion reported in the literature for partial oxidation and ATR reactions.

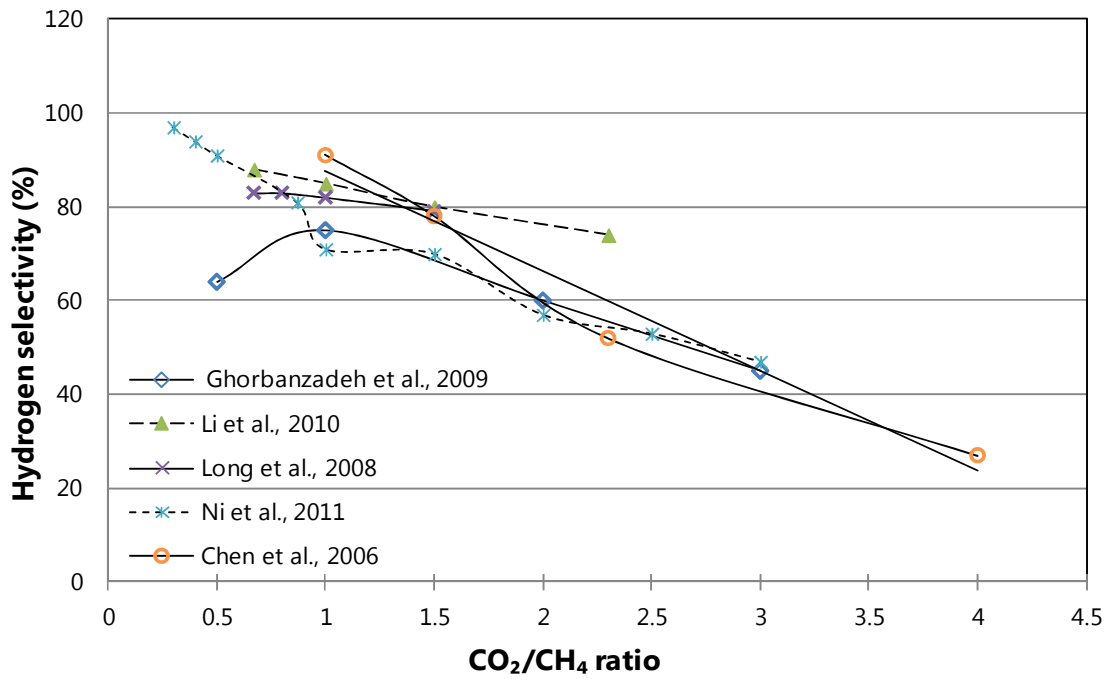


Figure 4.19: The effect of CO_2/CH_4 ratio on hydrogen selectivity reported in the literature.

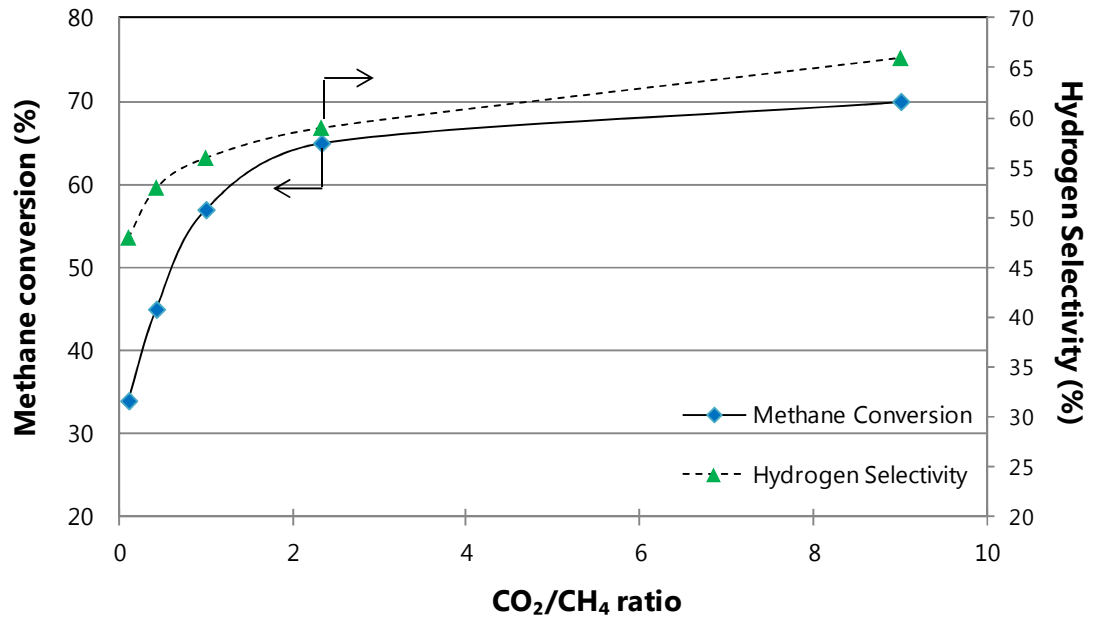


Figure 4.20: The effect of CO_2/CH_4 ratio on methane conversion and hydrogen selectivity reported by Huang et al., 2000.

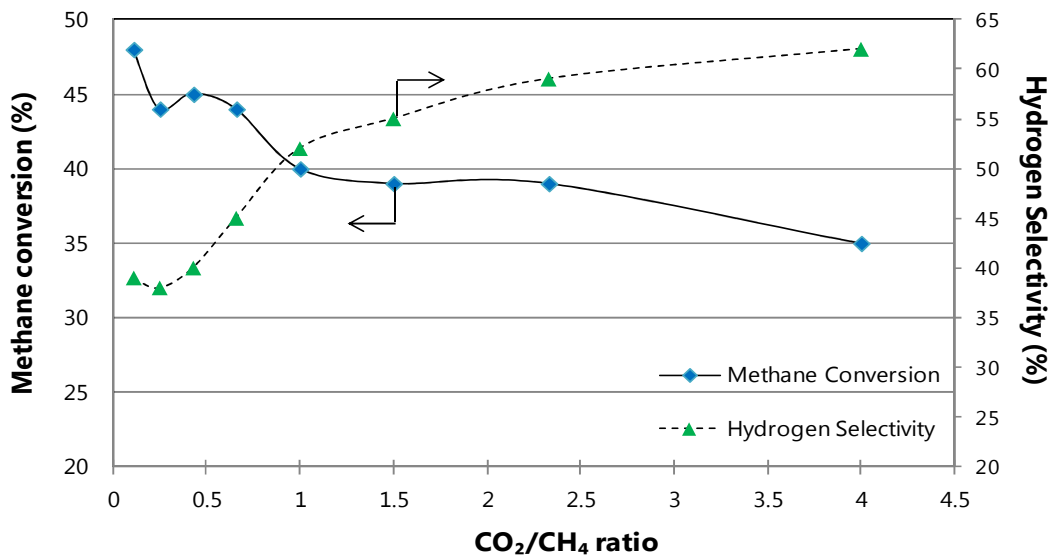


Figure 4.21: the effect of CO₂/CH₄ ratio on methane conversion and hydrogen selectivity in a gliding arc reactor reported by Intardo et al., 2006.

Tsai and Chen (2009) have investigated the effects of the N₂/CH₄ ratio in the pyrolysis reactions employing microwave reactor and have reported that an increase in the ratio from 4 to 19 led to an increase in methane conversion from 57.8 to 81.7 %. Intardo et al. (2006) have reported that increasing the Ar/CH₄ ratio in methane pyrolysis reactions also results in higher methane conversion rates as well as higher hydrogen selectivities, see Figure 4.22.

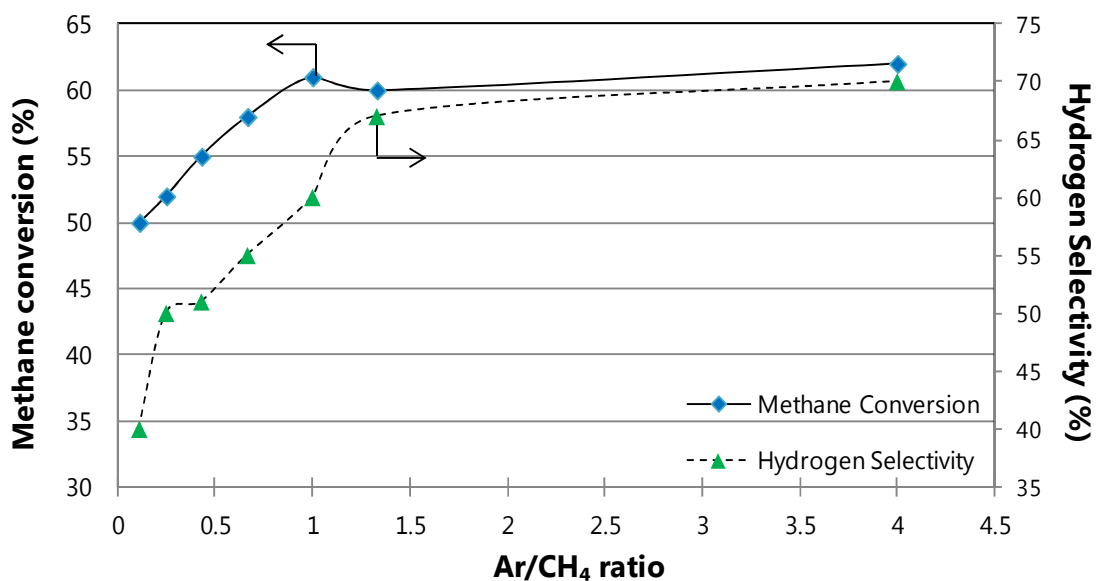


Figure 4.22: The effect of Ar/CH₄ ratio on methane conversion and hydrogen selectivity for direct methane decomposition employing gliding arc, reported by Intardo et al., 2006.

Very interesting results were reported by Wang et al. (2010) for steam reforming of methane by a microwave discharge: as the $\text{H}_2\text{O}/\text{CH}_4$ ratio was increased from 0.5 to 1, methane conversion increased from 88.4 to 91.6 %. However, as the ratio was further increased from 1 to 3, methane conversion decreased from 91.6 to 80 %, see Figure 4.23. Hydrogen selectivity increased in both the cases. Sugasawa et al. (2010) concluded from the experimental results of non-thermal plasma methane steam reforming that, increase in steam in the reaction does not increase hydrocarbon conversion, suggesting the competitive partition of high energies of excited electrons to water and methane in the initial stage.

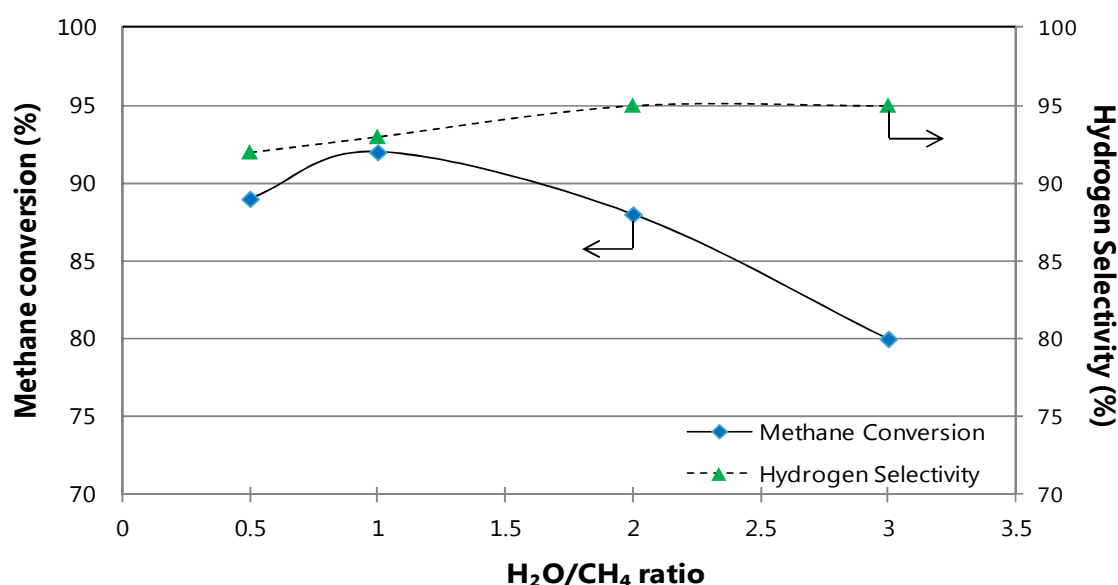


Figure 4.23: The effects of $\text{H}_2\text{O}/\text{CH}_4$ ratio on methane conversion and hydrogen selectivity for SMR employing a microwave discharge, reported by Wang et al., 2010.

Intardo et al. (2006) have investigated the effects of additive gasses, including helium, argon, nitrogen and CO_2 , on methane conversion and product selectivity in a gliding arc discharge. See Figure 4.24 for the following descriptions. The addition of argon to the system increased methane conversion from 48 to 62 % and hydrogen selectivity from 40 to 67 % when compared to pure methane conversion. Similar results were observed with helium, where methane conversion increased to 60 % and hydrogen selectivity to 62 %. Intardo et al. (2006) have concluded that the addition of helium and argon to pure methane in the system has almost the same characteristics. The authors wrote that argon and helium have a meta-stable energy

level which could help the dissociation of the carbon-hydrogen bonds of the methane molecule and could also increase the number of energetically unstable species and the possibility to react with methane. The addition of helium and argon has also decreased the power consumption of methane reforming from 170 W to 120 W, due to lower ionization energy necessary for argon and helium (Intardo et al., 2006). Intardo et al. (2006) have reported that experiments with nitrogen and methane in the feed had similar effects, namely an increase in methane conversion from 48 to 65 % and hydrogen selectivity from 40 to 62 %, as well as power reduction from 170 to 140 W. The authors have also noted that increasing the concentrations of argon, helium or nitrogen in the system produces higher selectivity to hydrogen and reduces the selectivity to acetylene. Introducing CO₂ to the feed had led to negative effects on methane conversion, reducing it from 48 to 35 %. However, hydrogen selectivity has increased from 40 to 60 %. At the same time power consumption has also increased from 170 to 270 W, and the authors concluded that the effect was due to CO₂ having a stronger bond than CH₄ resulting in the requirement of higher energy supply to break the bonds (Intardo et al., 2006), see Figure 4.24. The breakdown voltage for argon to generate plasma is 2.7 kV/cm, which is much lower when compared with nitrogen (35 kV/cm) and helium (10 kV/cm) (Fridman et al., 2008). In fact argon needs the second lowest breakdown voltage, with neon having the lowest at 1.4 kV/cm (Fridman et al., 2008). Electron energy and electron density are two of the key parameters determining the rate of all plasma discharge reactions (Petipas et al., 2007). Hence, the accelerated plasma chemical reactions with the addition of argon as reported by Intardo et al. (2006) are due to the release of extra electrons from argon ionization reactions (Mishra et al., 2007; described in Section 4.3.1, Formulae (4.11)), which initiate the pure plasma effect of decomposition by collision of electrons and methane gas molecules (Lee et al., 2010; described in Section 4.3.1, Formulae (4.5)).

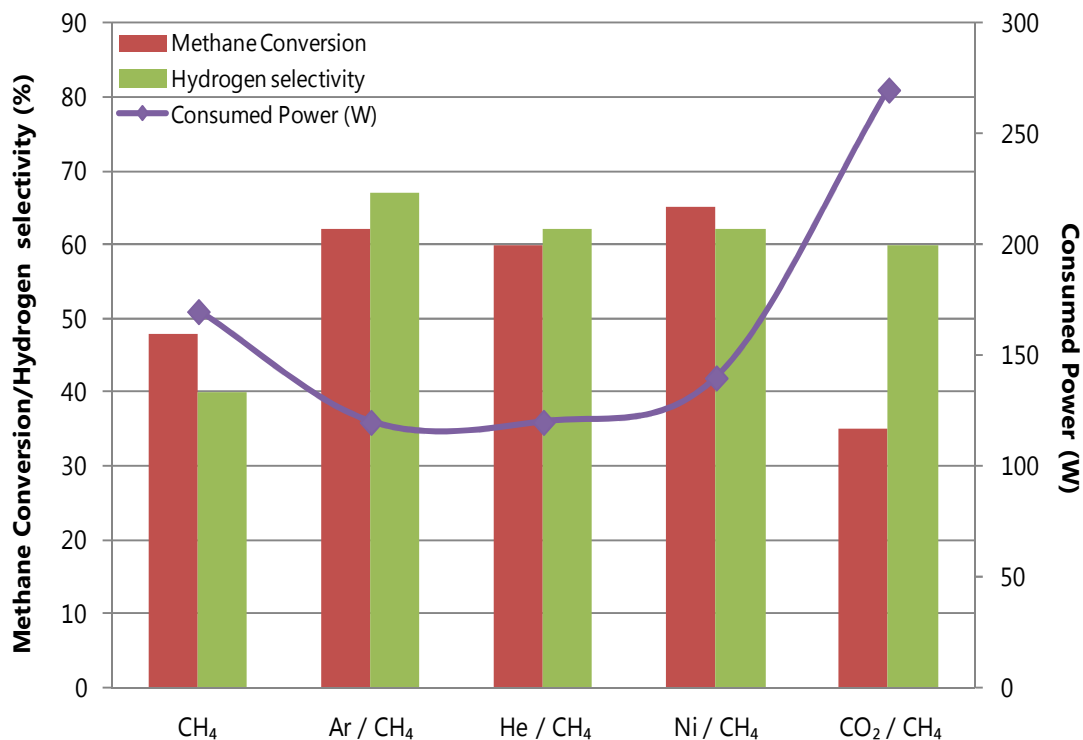


Figure 4.24: The effects of the addition gasses on methane conversion and hydrogen selectivity as reported by Intardo et al., 2006. The gas compositions are as follows: 100 % CH₄, 85 % Ar / 15 % CH₄, 80 % He or Ni or CO₂ to 20 % CH₄.

4.3.6.4. Other parameters investigated

Pulse frequency in corona glow discharges and AC frequency in multistage gliding arc discharges have been reported to have an effect on methane conversion. An increase in pulse frequency in a pulsed corona discharge from 0 to 350 Hz has been shown to increase methane conversion from 0 to 60 % by Kado et al. (2003). Sekine et al. (2003a) have reported an increase of methane conversion from approx 20 to 55 % as pulse frequency in a corona discharge was increased from 50 to 300 Hz, see Figure 4.25. Yao et al. (2001a) have also concluded that higher pulse frequencies in a corona discharge favour methane conversion rate. Increasing the pulse frequency from 1 to 8 kpps resulted in methane conversion increase by 4.2 times (Yao et al., 2001b). Similar effects have been noted in a pulsed glow discharge by Ghorbanzadeh et al. (2009), where pulse frequency increase from 1 to 5 kHz has resulted in a methane conversion increase from 25 to 61 % and hydrogen selectivity increase from 65 to 85 %, see Figure 4.26.

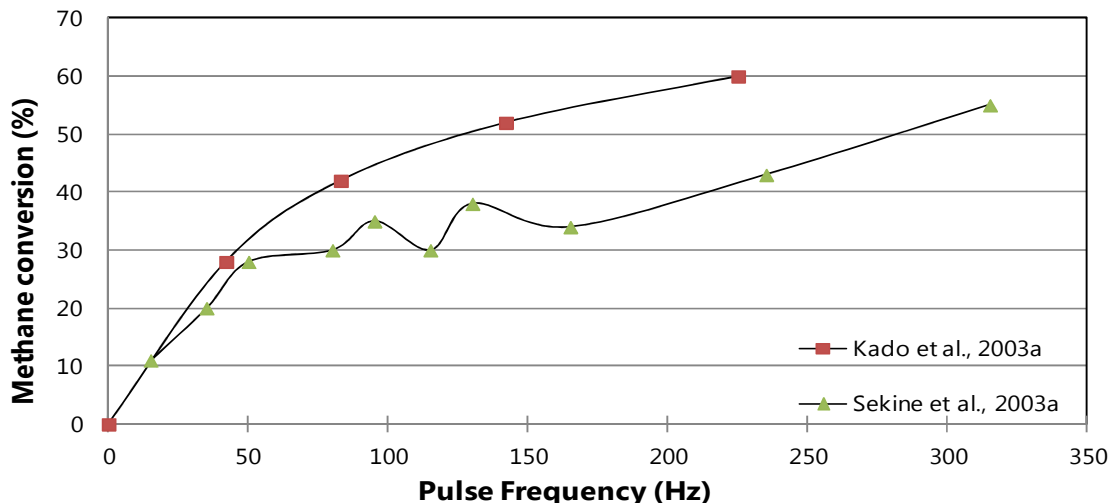


Figure 4.25: The effect of pulse frequency in pulsed corona discharges on methane conversion.

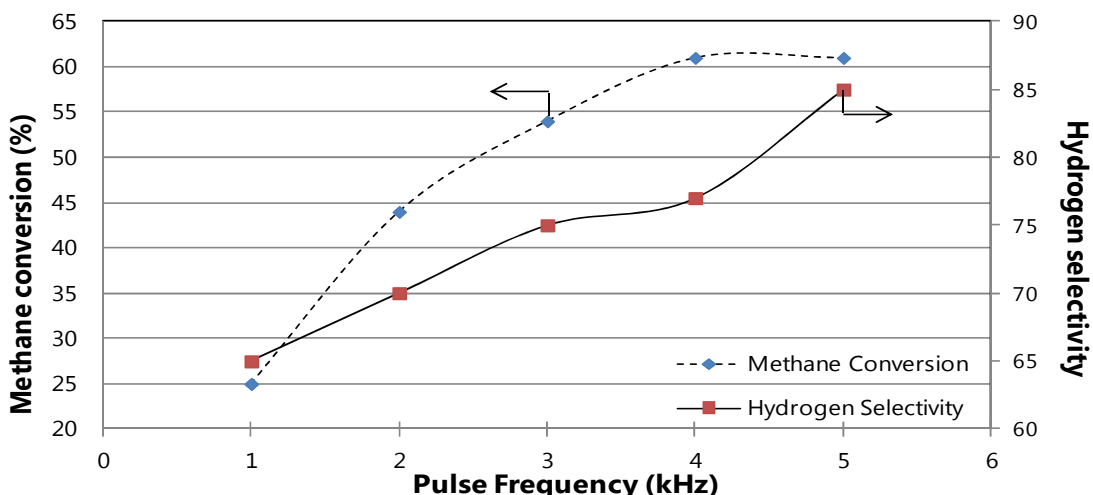


Figure 4.26: The effect of pulse frequency in a glow discharge on methane conversion and hydrogen selectivity, data taken from Ghorbanzadeh et al., 2009.

In AC discharges, each electrode acts as an anode and cathode, where the current periodically reverses in direction due to the reversed polarity in the electric field. The electric current needed to initiate and maintain the discharge plasma is reduced with increasing the input frequency, due to a slower decay rate of space charges. Hence, higher frequencies generate smaller currents or less electrons, resulting in smaller amounts of number of reactive species to activate the plasma-chemical reactions (Sreethawong et al., 2007a). Therefore, in the experimental results presented by Sreethawong et al. (2007), increasing the AC frequency in a gliding arc discharge

from 300 to 700 Hz resulted in a drastic decrease of methane conversion from 65 to 30 % with no effect on product distribution, see Figure 4.27. Interestingly, Intardo et al. (2006) reported that methane conversion and hydrogen selectivity both increase with the AC frequency for pure methane decomposition employing an AC arc, see Figure 4.28. The AC arc employed by Sreethawong et al. (2007) was used for methane partial oxidation experiments with the AC frequencies in the range of 300 – 700 Hz, whereas results reported by Intardo et al. (2006) were for methane pyrolysis and much higher AC frequencies in the range 15 to 21 kHz. Therefore, methane reformation method and plasma configuration could be the two reasons for the different AC frequency effects observed on methane conversion and hydrogen selectivity.

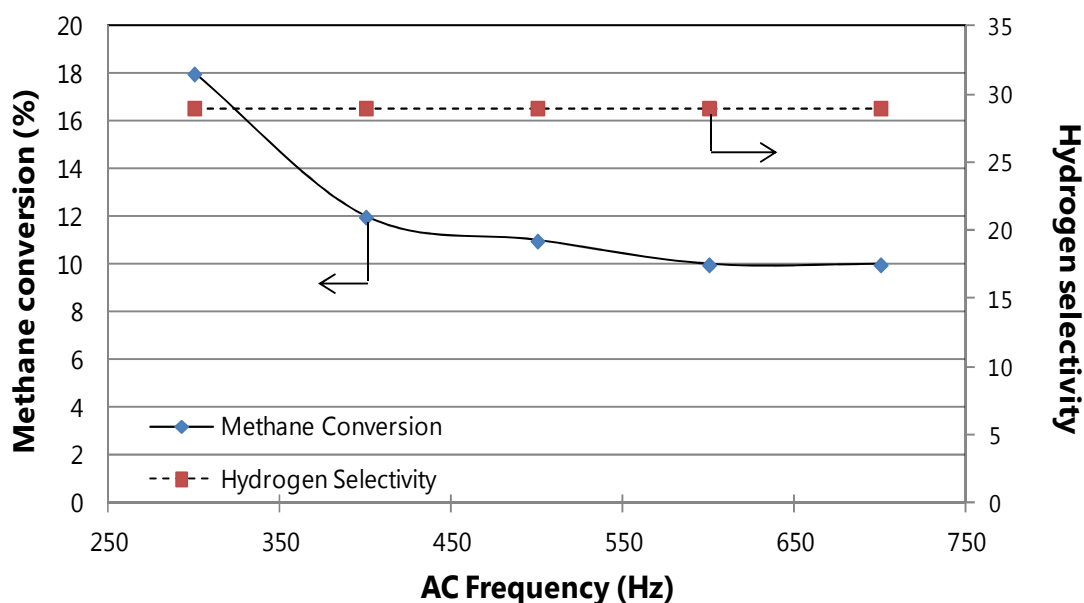


Figure 4.27: The effects of AC frequency in a gliding arc discharge on methane conversion and hydrogen selectivity, data taken from Sreethawong et al., 2007.

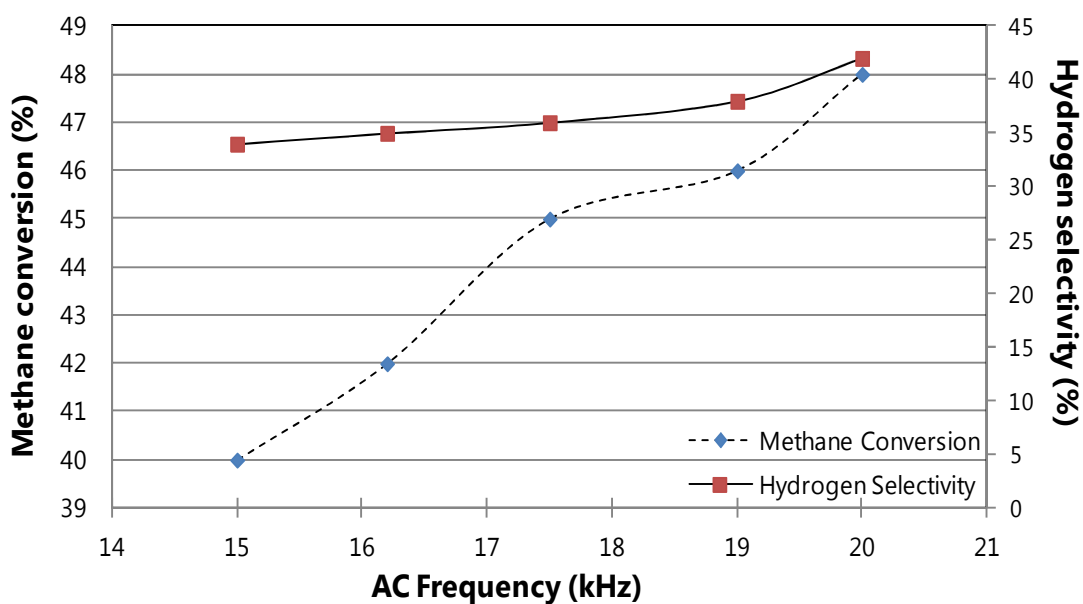


Figure 4.28: The effects of AC frequency in an arc discharge on methane conversion and hydrogen selectivity, data taken from Intardo et al., 2006.

The effects of inter-electrode distance in pulsed corona have been reported by Kado et al. (2003) and Sekine et al. (2003a), AC arc discharge by Sreethawong et al. (2007) and cold plasma jet by Li et al. (2010), see Figures 4.29 and 4.30. In a pulsed corona discharge methane conversion increased from 35 to 90 %, as the inter-electrode distance increased from 0.5 to 10 mm (Kado et al., 2003). An increase in gap distance results in an increase in the inception voltage, Kado et al. (2003a) noted that this has a stronger effect on methane conversion than the increase in residence time and concluded that the energy distribution of electrons was improved in the longer gap. Interestingly, the authors have also reported that methane conversion is slightly higher when employing positive corona compared to negative corona. Sekine et al. (2003a) have also reported an increase of methane conversion from 21 to 29 % as the inter-electrode distance of the corona discharge was increased from 0.7 to 2.1 mm. Sreethawong et al. (2007) have noted similar effects on methane conversion in an AC gliding arc, where an increase in inter electrode distance from 2 to 8 mm has led to an increase in methane conversion from 8 to 20 %. However, the authors noted that this also resulted in a decrease of hydrogen selectivity from 34 to 27 %. Li et al. (2010) have also experimentally shown that increasing the inter-electrode results in an increase in methane conversion as well as hydrogen selectivity in cold plasma jet, see Figures 4.29 and 4.30. Sreethawong et al. (2007) and Li et al.

(2010) both employed PO methane reformation method. However, different plasma configurations were used, i.e. AC gliding arc and cold plasma jet, which could explain the different effects of inter-electrode distance on hydrogen selectivities. Hence, the observations can be made that higher in inter-electrode distances favour methane conversion (see Figure 4.29), whereas hydrogen selectivity follows a more complex path and also depends on plasma configurations (see Figure 4.30).

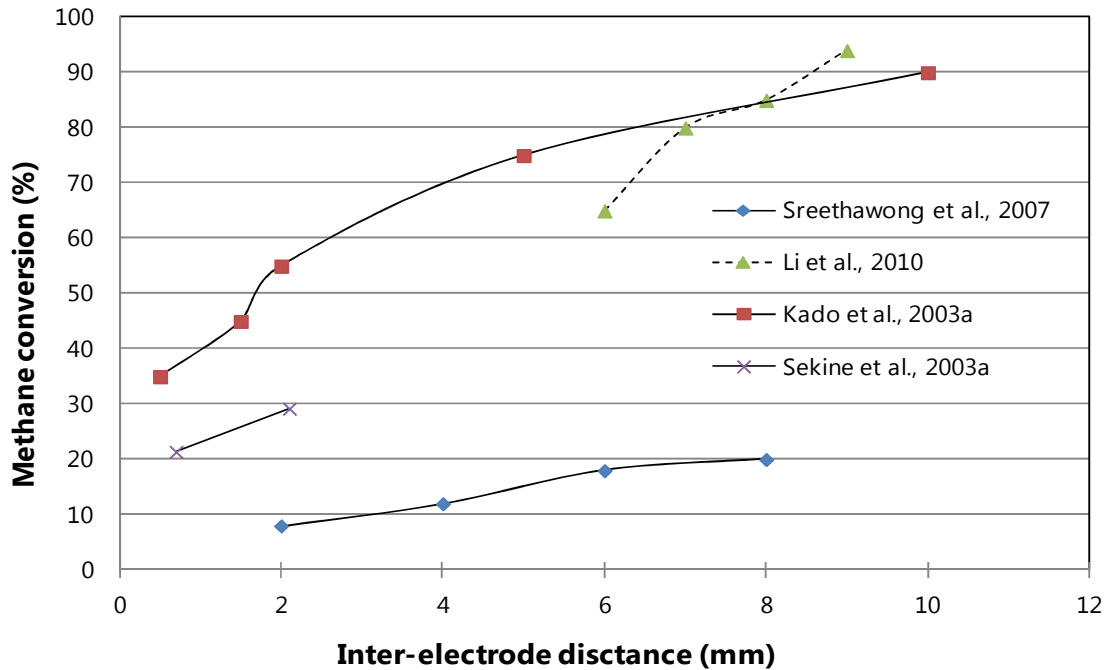


Figure 4.29: The effect of inter-electrode distance on methane conversion reported in the literature.

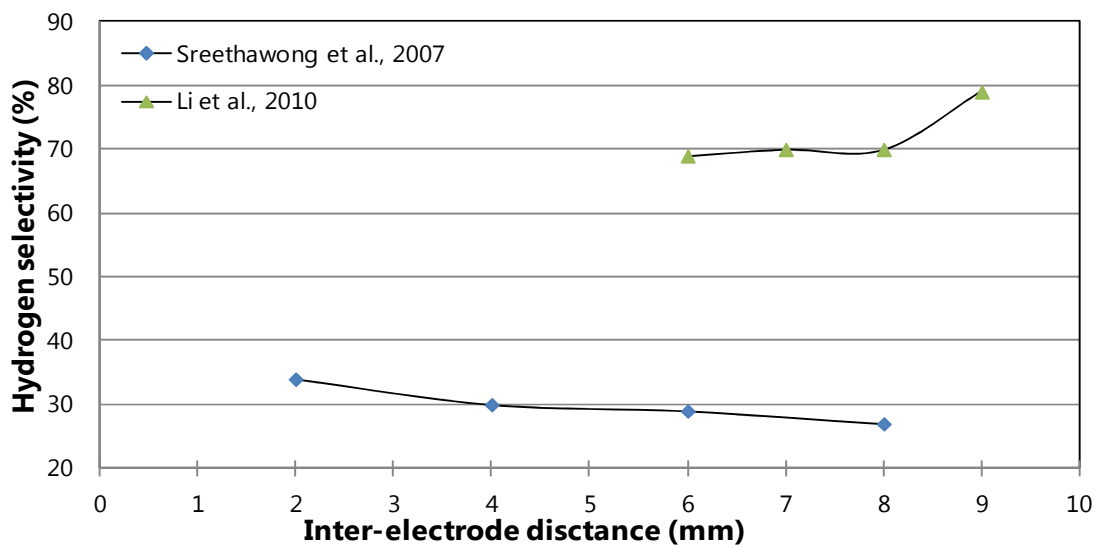


Figure 4.30: The effects of inter-electrode distance on hydrogen selectivity reported in the literature.

Tsai et al. (2005) reported experimental results on the effect of pressure in a microwave discharge. The authors discovered that methane conversion is higher at lower pressures, whereas hydrogen selectivity is higher at near atmospheric pressure, see Figure 4.31.

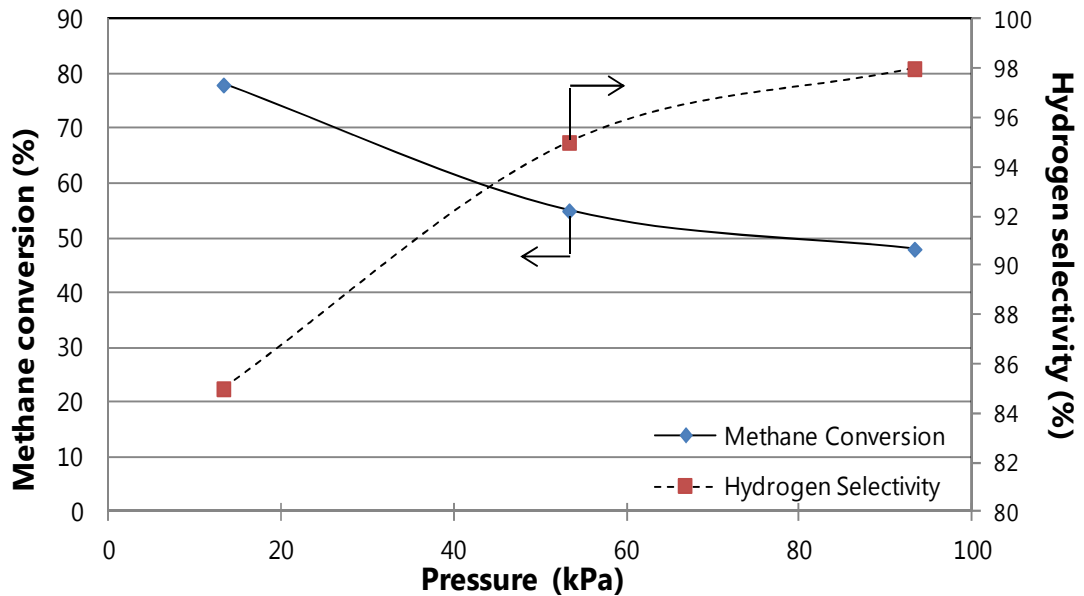


Figure 4.31: The effect of pressure on methane conversion and hydrogen selectivity, Tsai et al., (2005).

Hwang et al. (2007) have performed experiments with a gliding arc discharge adopted to separate the thermal and non-thermal zones to investigate the effects of plasma zones on methane conversion and hydrogen selectivity. The authors have concluded that the highest methane conversion achieved is in the thermal zone with low hydrogen selectivity. On the contrary non-thermal plasma favour hydrogen selectivity with low methane conversion rates. The effects of the reactor temperature in high frequency pulsed plasma was studied by Yao et al. (2001a), where a temperature increase from 0 to 50 °C has led to methane conversion increase from 35 to 48 %. However, a further temperature increase to 300 °C diminished methane conversion to 0 %, see Figure 4.32.

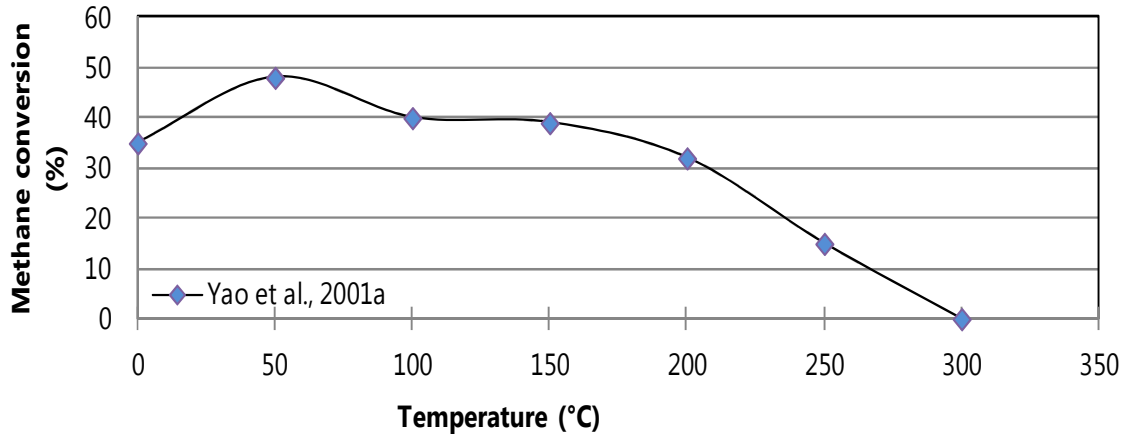


Figure 4.32: The effect of temperature on methane conversion, Yao et al., 2001a.

4.3.6.5. Summary

Tables 4.3 – 4.6 show the summary of the effects of flow, power input, gas composition and other parameters on methane conversion and hydrogen selectivity to generate hydrogen by employing plasma.

A wide range of flow rates for different plasma configuration systems have been investigated, see Table 4.3. It can be clearly seen that in all cases described lower total flows favour methane conversion. However, according to Long et al. (2008) and Luche et al. (2009), high total flow rates allow lower production costs. The total flow effect on hydrogen selectivity is very system dependant. Hence, the optimal flow rate chosen by the authors is in the mid-range of the tested flow rates to balance methane conversion, hydrogen selectivity rate and the cost of production, see Table 4.3.

High power inputs favour methane conversion with no significant effect on hydrogen selectivity, see Table 4.4. However, specific energy consumption and the cost of hydrogen production are favoured at lower power inputs (Sreethawong et al., 2007; Tsai and Chen, 2009). Therefore, the optimum conditions selected by authors differ vastly. Ruengjitt et al. (2009) and Tsai and Chen (2009) have chosen lower range of power inputs to lower specific energy consumption, at a cost of lower methane conversion. Whereas, Li et al. (2010), Chen et al. (2006) and Bromberg et al. (1999a) selected higher powers from the tested range for improved methane conversion, at a cost of higher specific power consumption, see Table 4.4.

Table 4.3: Summary of the effects of total reactant flow and the optimal conditions if selected by authors.

Plasma Form	Reaction Type	Flow Change (ml/min)	CH ₄ conversion rate change (%)	Hydrogen selectivity change (%)	Optimal selected by authors			Reference
					Flow (ml/min)	Methane conversion (%)	Hydrogen selectivity (%)	
AC arc	PO	20 → 71	62 → 54	Not reported	44	57	56	Huang et al., 2000
Multistage gliding arc	PO	50 → 300	22 → 6	30 → 22	150	18	28	Sreethawong et al., 2007
Glow discharge	PO	140 → 500	92 → 70	62 → 78	350	80	75	Chen et al., 2006
Cold plasma jet	PO	360 → 4000	97 → 15	76 → 99	1000	94	79	Li et al., 2010
Thermal water plasma jet	ATR	2000 → 6000	95 → 50	55 → 71	4000	75	71	Ni et al., 2011
Microwave	Pyrolysis	12000 → 18000	62 → 45	Not reported	12000	62	86	Tsai and Chen, 2009
Cold plasma jet	PO	16000 → 25000	46 → 38	78 → 76	16000	46	78	Long et al., 2008
Thermal plasma	PO	27000 → 40000	90 → 71	68 → 65	30,000	90	68	Tao et al., 2008

→ indicates the change from to

Table 4.4: Summary of the effects of power input and the optimal conditions if selected by authors

Plasma Form	Reaction Type	Power Change (W)	CH ₄ conversion rate change (%)	Hydrogen selectivity change (%)	Optimal selected by authors			Reference
					Power (W)	Methane conversion (%)	Hydrogen selectivity (%)	
Gliding arc	Pyrolysis	4 → 12	25 → 32	75 → 75	6	29	75	Rueangjitt et al., 2009
Cold plasma jet	PO	50 → 90	85 → 94	80 → 79	90	94	79	Li et al., 2010
Glow discharge	PO	240 → 600	67 → 82	75 → 76	500	80	75	Chen et al., 2006
Microwave	Pyrolysis	800 → 1400	62 → 85	86 → 83	800	62	86	Tsai and Chen, 2009
Thermal plasma	ATR	2500 → 3500	45 → 70	Not reported	3500	70	35	Bromberg et al., 1999a

→ indicates the change from to

Lower methane concentrations (higher X/CH₄ ratio) favour methane conversion, see Table 4.5 for the following descriptions. For partial oxidation reactions (additive gasses CO₂ or O₂) hydrogen selectivity is favoured by higher methane concentrations, with the exception for the arc plasma systems reported by Huang et al. (2000) and Intardo et al. (2006) where hydrogen selectivity is higher at lower methane concentrations. In general optimal CO₂/CH₄ and O₂/CH₄ ratios chosen by authors are in the mid-range (around 1) to balance the conversion and hydrogen selectivity rates. Higher argon concentrations for pyrolysis reactions favour both methane conversion and hydrogen selectivity rates, hence the highest ratio tested is chosen. For SMR reaction, higher steam concentrations have a positive effect on hydrogen selectivity, mid-range ratio is chosen for optimal methane conversion.

Please refer to Table 4.6 for the following descriptions. Higher pulse frequencies in corona and glow discharges favour higher methane conversion and hydrogen selectivity reported for the glow discharge. For arc discharge pyrolysis reactions higher AC frequencies favour both methane conversion and hydrogen selectivity, the opposite effect has been reported for partial oxidation reactions. Longer inter electrode distances in AC arc, cold plasma jet and pulsed corona discharges favours methane conversion. Hydrogen selectivity has been reported to be favoured by longer inter-electrode distances in cold plasma jet, the opposite effect was observed for gliding arc discharge. In microwave discharges, lower pressures favour methane conversion, near atmospheric pressure discharges favour hydrogen selectivity.

To conclude, it has been shown that parameter choices are a balanced compromise between methane conversion rate, hydrogen selectivity and specific energy consumption. In general, selecting the main parameters, including the total flow, power input and methane ratios, to increase methane conversion would result in lower hydrogen selectivity and vice versa.

Table 4.5: Summary of the effects of gas composition and the optimal conditions if selected by authors.

Plasma Form	Reactants	Ratio change	CH ₄ conversion rate change (%)	Hydrogen selectivity change (%)	Optimal selected by authors			Reference
					Ratio	Methane conversion (%)	Hydrogen selectivity (%)	
AC arc	CO ₂ /CH ₄	0.11 → 9	34 → 70	48 → 66	1	57	56	Huang et al., 2000
Gliding Arc	CO ₂ /CH ₄	0.11 → 4	48 → 35	39 → 62	1	40	50	Intardo et al., 2006
Multistage gliding arc	O ₂ /CH ₄	0.2 → 0.5	2 → 18	50 → 35	0.3	12	37	Sreethawong et al., 2007
Microwave	O ₂ /CH ₄	0.25 → 1.5	29 → 66	98 → 30	0.5	48	98	Tsai et al., 2005
AC arc	CO ₂ /CH ₄	0.11 → 9	34 → 70	48 → 66	1	57	56	Huang et al., 2000
Glow discharge	CO ₂ /CH ₄	0.5 → 1 → 3	59 → 61 → 70	64 → 75 → 45	1	61	77	Ghorbanzadeh et al., 2009
Cold plasma jet	CO ₂ /CH ₄	0.67 → 2.3	88 → 95	88 → 74	1.5	94	79	Li et al., 2010
Cold plasma jet	CO ₂ /CH ₄	0.67 → 1.5	36 → 46	83 → 78	1.5	46	78	Long et al., 2008
Glow discharge	CO ₂ /CH ₄	1 → 4	75 → 82	91 → 27	1.5	80	75	Chen et al., 2006
Thermal water plasma jet	CO ₂ /CH ₄	0.3 → 3	50 → 95	97 → 47	1	75	71	Ni et al., 2011
Gliding arc	Ar/CH ₄	0.11 → 4	50 → 62	40 → 70	4	62	70	Intardo et al., 2006
Microwave	H ₂ O/CH ₄	0.5 → 1 → 3	89 → 92 → 80	92 → 93 → 95	1	92	93	Wang et al., 2010

→ indicates the change from to

Table 4.6: Summary of the effects of other parameters and the optimal conditions if selected by authors.

Plasma Form	Parameter	Change	CH ₄ conversion rate change (%)	Hydrogen selectivity change (%)	Optimal selected by authors			Reference
					Optimal parameter	Methane conversion (%)	Hydrogen selectivity (%)	
Pulsed corona	Pulse Frequency	0 → 225 Hz	0 → 60	Not reported	225	60	Not reported	Kado et al., 2003
Pulsed corona		15 → 315 Hz	11 → 55	Not reported	100 Hz	35	Not reported	Sekine et al., 2003a
Pulsed glow discharge		1 → 5 kHz	25 → 61	65 → 85	4 kHz	61	77	Ghorbanzadeh et al., 2009
AC arc pyrolysis	AC Frequency	15 → 20 kHz	40 → 48	34 → 42	20 kHz	48	42	Intardo et al., 2006
AC gliding arc		300 → 700 Hz	18 → 10	29	300 Hz	18	29	Sreethawong et al., 2007
Pulsed corona	Inter-electrode distance	0.5 → 10 mm	30 → 90	Not reported	Not specified	Not specified	Not specified	Kado et al., 2003
Corona discharge		0.7 → 2.1 mm	21 → 29	Not reported	2.1 mm	29	Not reported	Sekine et al., 2003a
AC gliding arc		2 → 8 mm	8 → 20	34 → 27	6 mm	18	29	Sreethawong et al., 2007
Cold plasma jet		6 → 9 mm	65 → 94	69 → 79	9 mm	94	79	Li et al., 2010
Microwave	Pressure	13.3 → 93.3 kPa	78 → 48	85 → 98	93.3	48	98	Tsai et al., 2005

4.4. Hydrogen generation from propane

As addressed in Chapter 2, propane is attracting more research for on-board hydrogen generation, because it is liquefiable and easy to store and transport (Zeng et al., 2010; Wang et al., 2011). It is also an inexpensive fuel of high energy density, offering a new alternative for more economical hydrogen production (Ledjeff-Hey et al., 2004). In this section reported experimental systems and results for plasma assisted propane reformation to generate hydrogen will be reviewed.

Horng et al. (2009) used a spark discharge to ionize a propane and air mixture, where Pt-Rh/Al₂O₃ catalyst was fixed at the rear to facilitate the partial oxidation reforming to generate a hydrogen rich gas. Reforming reactions took place at high temperatures between 400 – 950 °C. However, according to the authors sufficient heat was generated from the partial oxidation reactions to self-sustain the experiment. Horng et al. (2009) have experimentally shown that propane conversion is favoured at highest oxygen to carbon (O₂/C) ratio of 1, total flow rate of 4 l/min and temperature of 950 °C. However, higher O₂/C ratios increase the generation of carbon monoxide and carbon dioxide, as seen in Figure 4.33, where higher H₂/(CO+CO₂) ratios represent higher production of hydrogen with lower content of CO and CO₂. Hence, at the above conditions (the ratio below 1), the generation of CO_x compounds is higher than hydrogen. Hydrogen yield follows a more interesting route with temperature, see Figure 4.34, with highest at 850 °C of 65 %. (Horng et al., 2009).

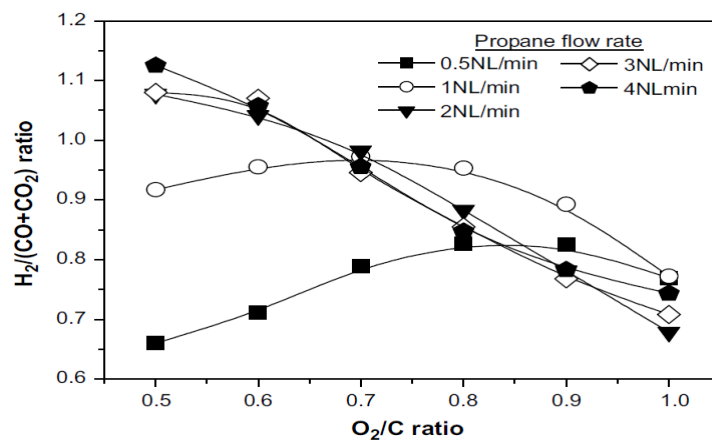


Figure 4.33: The effects of O₂/C ratio on hydrogen to CO_x generation ratio at different propane flow rates (Horng et al., 2009, Fig. 7).

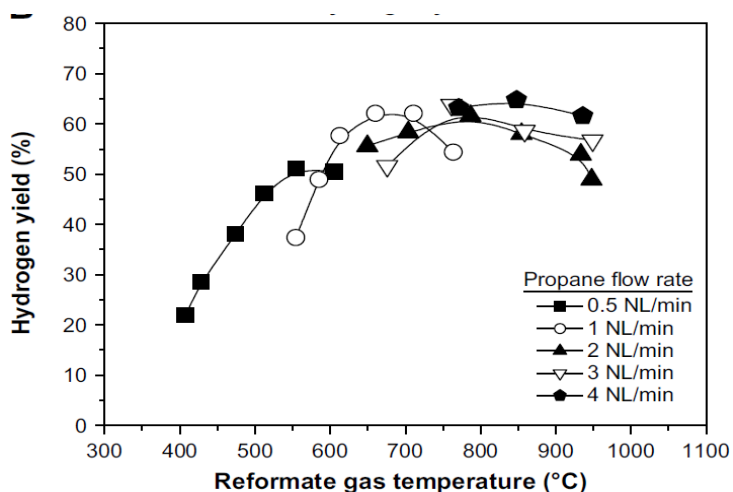


Figure 4.34: The effects of temperature on hydrogen selectivity in plasma assisted catalytic propane reforming at different propane flow rates (Hornig et al., 2009, Fig. 8B).

Yu et al. (2011) developed a DBD reforming reactor with Ni/ γ -Al₂O₃ catalyst within the discharge zone. The DBD reactor consisted of a quartz tube (i.d. 8.5 mm) reforming reactor and dielectric barrier, stainless steel rod electrode (3.5mm o.d.) and an AC power supply. Propane was mixed with carbon dioxide at CO₂/C₃H₈ ratio of 5 and the total flow rate of 60 ml/min. When employing plasma without the catalyst, an increase in discharge power from 12.2 – 21.9 W, resulted in an increased propane conversion from 25 to 43.4 % and hydrogen selectivity from 13.2 to 13.9 %. Other compounds generated and their selectivities include CO 25.6 %, CH₄ 4.4 %, C₂H₄ 6.5 %, C₂H₆ 5.5 %, C₄H₁₀ 13.2 %, C₃H₁₂ 9.7 %, C₅H₁₄ 13.3 % and other 21.8 %, at hydrogen to CO ratio of 0.54 (nearly double the amount of CO generated in comparison to hydrogen content) (Yu et al., 2011). Figure 4.35 shows the results for propane conversion for plasma without the catalyst (plasma mode), catalyst without the plasma (catalyst mode) and combination of catalyst and plasma (combination mode) with increasing the temperature of the reaction, CO₂/C₃H₈ ratio of 5, total flow rate 60 ml/min and discharge power of 18.3 W. In plasma mode, propane conversion decreases with temperature due to decreased discharge intensity (Yu et al., 2011). The opposite effect is seen for catalyst mode. Positive combined plasma and catalyst effect seen at temperatures in the range of 300 – 450 °C, further increase in temperature to 500 °C led to mainly catalytic propane conversion with no apparent plasma contribution (Yu et al., 2011). Figure 4.36 shows the effects of hydrogen selectivity under the above described conditions. Hydrogen selectivity

follows a more complex path when compared to propane conversion with catalytic and combined modes: it increases with temperature from 15 to 40 % (300 – 400 °C), then it decreases as temperature is further increased, see Figure 4.36 (Yu et al., 2011). Similar effect has been reported for hydrogen yield by Horng et al. (2009) in a spark discharge plasma and catalyst reforming of propane described above. The effect of temperature on hydrogen selectivity with plasma system without the catalyst is minimal. This could suggest that temperature effects on hydrogen selectivity within the combined system are mainly due to the catalytic activity. The selectivity of methane increases drastically at temperatures above 400 °C, explaining the decrease of hydrogen selectivity even though propane conversion is higher above 400 °C (Yu et al., 2011). Overall, nearly 100 % propane conversion was achieved using the combination mode at CO₂/C₃H₈ ratio of 5, total flow rate 60 ml/min, discharge power of 18.3 W and temperature of 500 °C, with hydrogen selectivity of 30 %, methane selectivity of 25 % and CO selectivity of 45 % by Yu et al. (2011). The highest hydrogen selectivity of 40 % was achieved under the above conditions, except a lower temperature of 400 °C, where propane conversion of 22 %, and methane and CO selectivities of 3 and 39 % respectively, were observed.

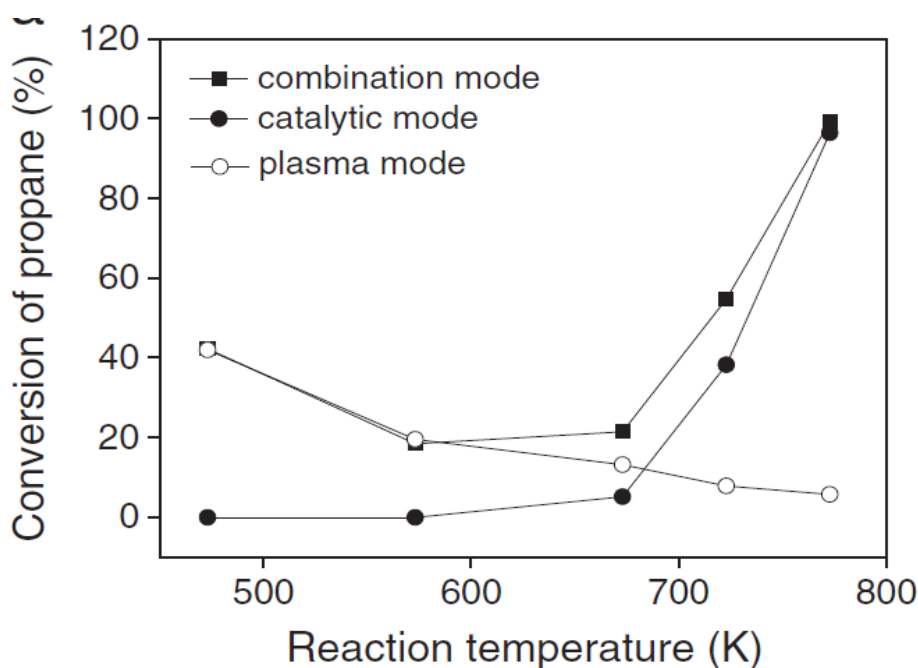


Figure 4.35: The effect of reaction temperature on propane conversion (Yu et al., 2011, Fig. 1a)

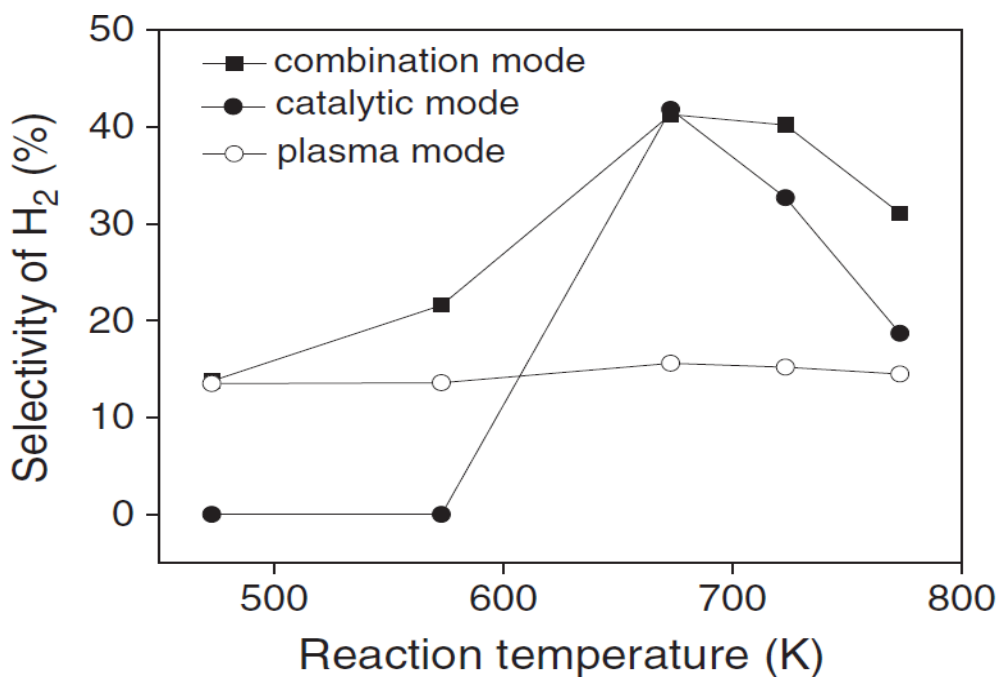


Figure 4.36: Influence of the reaction temperature on hydrogen selectivity (Yu et al., 2011, Fig. 2a).

Tamosiunas et al. (2012) reported a thermal plasma linear DC water vapour plasma torch developed for steam reforming of propane. The reactor chamber was 280 mm long with a 40 mm diameter, experiments were performed at power inputs of 55 – 69 kW DC (approx 390 V, vary 140 to 180 A), at residence times between 6.4 – 8.5 ms, temperature of the plasma gas varied between 1730 – 2730 °C and the H_2O/C_3H_8 ratio varied between 5.6 – 13.1 (higher ratio equals to more water vapour). Argon was also used as shielding gas to protect electrodes from erosion at concentrations of 10 – 13 % of the total mass flow (Tamosiunas et al., 2012). 100 % propane conversion was achieved within all temperature and ratio ranges tested. Overall, this system has achieved 100 % propane conversion, 84 % hydrogen selectivity and 50 % CO selectivity at 1730 °C and H_2O/C_3H_8 ratio 5.6 (Tamosiunas et al., 2012).

Bromberg et al. (2005, 2006) reported work on a plasmatron for partial oxidation of propane, with their best results showing 14.5 % hydrogen concentration, when propane is premixed with air using a swirl port, the O/C ratio kept at 1.3, temperature 720 °C and power input > 100 W. Czernichowski et al. (2003) reported the use of Glid Arc reformer for partial oxidation of propane to generate 3 m³/h syngas. The reformer consisted of 3 knife-shaped electrodes, operating at atmospheric pressure

and with 1 litre capacity, the temperature of the reforming reactions were sustained by the gliding arc at $> 700\text{ }^{\circ}\text{C}$. The power supply used was 10 kV neon-light transformers, with a total average net power of 0.8 kW. However, only 120 W were used for this set of experiments.

4.5. Plasma assisted cracking of liquid hydrocarbons

The possible use of plasma for more energy efficient and environmentally friendly method to crack large hydrocarbon molecules has been recognised in 1995 by Peter C. Kong who presented successful plasma cracking of squalane (shark oil consisting of 30 carbon atoms). In 1997 Peter C. Kong patented a submerged reactive plasma system for hydrocarbon cracking such as crude oil. In this configuration an electrical arc was submerged directly within the composition of hydrocarbons where working gas is delivered to the arc and forms the plasma. High concentrations of highly reactive hydrocarbon free radicals collide and react vigorously with large hydrocarbon molecules, hence breaking them into smaller molecules. Optimal system conditions were recorded at 0.9 – 1.5 kV power input at high currents of 400 – 500 mA AC or DC, and at room temperature (Kong, 1997). Gliding arc discharge has also been proposed for hydrocarbon cracking, where experiments of hexadecane cracking have been performed at power levels of 0.7 – 2 kW and pressure 1 – 3 bar (Czernichowski, 2000).

Xing et al. (2007, 2008) performed experiments with n-hexane in a dielectric barrier discharge catalyst integrated system at a power supply of 10.64 kV and have concluded that C-C bond cracking is the dominant reaction in the gas phase plasma zone. However, interestingly addition reactions dominate at higher voltages of 12 kV. Similarly, experiments with n-octane have also demonstrated that cracking is the major reaction at lower powers. The authors have suggested the possible use of plasma catalysis for hydrocarbon cracking (Xing et al., 2007 and 2008).

Kong et al. (2005) patented a dielectric barrier plasma system for methane activation and hence generation of high concentrations of reactive light hydrocarbons and hydrogen radicals. These light hydrocarbon radicals then would be used to crack the heavy hydrocarbon molecules fed in the system in a form of liquid into multiple lighter fragments. Experiments demonstrated over 30 % conversion of hexadecane

into lighter hydrocarbons at 6 – 7 kV and no production of heavier molecules than the original (therefore, no polymerization). The advantage of methane in the feed system, as noted by the authors, is that methane radicals react with larger molecules and add more side branches. More branched hydrocarbon chains are beneficial in increasing the octane number for fuel liquid product. However, the dielectric barrier discharge reactor is quite a complex system with problems occurring during up-scaling. To this day there is limited information and experimental results presented in the literature for the use of plasma in heavy hydrocarbon cracking in liquid form.

Khani et al. (2011) reported experimental results of hexadecane (C_{16}) cracking using and AC DBD discharge. Voltage inputs were at 8, 10 and 12 kV, equivalent to calculated power inputs of 573, 685 and 823 W respectively. The feed fuel is injected to the plasma area and is left stationary, whereas the reactant gas (air or methane) flows above the surface of the feed fuel at the operation time (Khani et al., 2011). The products were in the range of C_6 to C_{16+} , meaning cracking and radical recombination to generate heavier than hexadecane products occurred. Methane was selected as an optimal working gas. At 7 kV applied voltage, hexadecane conversion in air plasma was at 2.63 %, of which 40.72 % were contributed to cracking reactions. Hexadecane conversion in methane plasma was at 3.85 % of which 64.15 % of the reactions are cracking (Khani et al., 2011). An increase in voltage input from 8 to 12 kV (power from 573 to 823 W) resulted in conversion increase from 3.28 to 6.54 % at a flow rate of 10 ml/min and residence time 30 min, see figure 4.37 a). The cracking process was highest at 12 kV, with 87.33 % of the generated compounds being lighter than hexadecane. Increasing gas flow rate at 12 kV from 10 – 50 ml/min, led to hexadecane conversion increase from 6.54 – 9.41 %, see Figure 4.37 a). Optimum conditions selected by the authors were 12 kV (823 W) power input, methane as a reactant gas at flow rate of 50 ml/min and feed residence time of 30 min, with hexadecane conversion of 9.41 %, of which 84.34 % is cracked to lighter hydrocarbons (Khani et al., 2011).

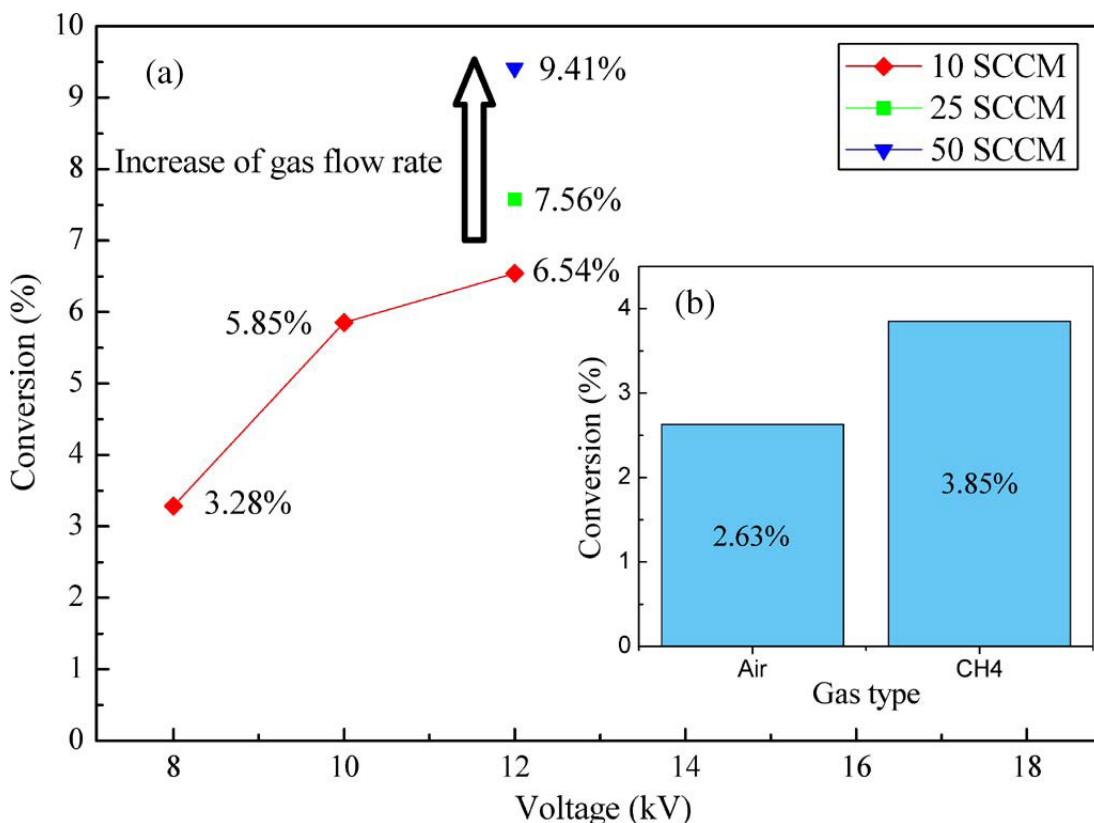


Figure 4.37: Effect of a) voltage along with flow rate and (b) gas type on the conversion percentage of hexadecane (Khani et al., 2011, Fig. 5). Shows that higher voltages and gas flow rates improve hexadecane cracking.

Prieto et al. (1999) reported a plate-to-plate plasma reactor for heavy oil conversion. The reactor consisted of two parallel stainless steel mesh electrodes approx 4 cm diameter, see Figure 4.38. AC voltage max 9 kV at 60 Hz was applied to the top electrode to generate spark discharges, with argon as a carrier gas. Experiments with gas flow rate variation 50 – 400 ml/min, inter-electrode distance variation from 0.3 – 1 cm, and input power 3 – 12 W showed high interaction between the variables of the gap distance and flow, as well as input power and gap distance. The major products obtained were in the range of C₁ to C₄, with ethylene being the main compound generated (Prieto et al., 1999).

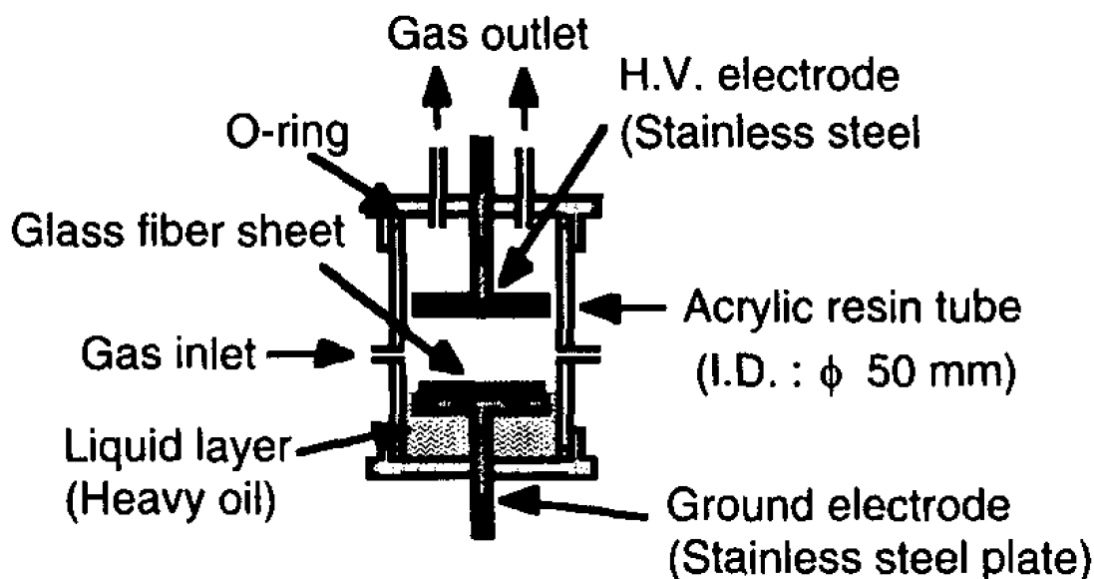


Figure 4.38: Schematic representation of plate-to-plate reactor for liquid hydrocarbon cracking reported by Prieto et al. (1999) (Fig.1).

It is possible to speculate that at lower voltages of approximately < 10 kV, the main reactions induced in plasma processing of hydrocarbons is cracking of the C-C bonds (Kong, 1997; Czernichowski, 2000; Xing et al., 2007 and 2008; Kong et al, 2005). However, higher voltage inputs of ≥ 12 kV favours polymerization.

4.6. Plasma – catalytic systems for hydrocarbon reformation

The combined plasma-catalytic approach is when plasma is used together with a catalyst, to combine the high selectivity of the catalyst and the fast start-up of the plasma. At atmospheric pressure, the catalytic processes may be induced by different plasma activation mechanisms (Hammer et al., 2004):

- i. Gas heating: much faster than conventional heat exchanger due to electronic and ionic collisions.
- ii. When electron energies reach approx 5 eV, efficient ionization and dissociation of molecules occurs.
- iii. Radical formation: allows plasma induced catalytic reactions.

iv. Plasma may be a source of ultraviolet radiation, enabling photo-catalytic reactions.

Plasma-catalytic systems can be either two stage or single stage, depending on the catalyst position in the reactor. In sections 4.6.1 and 4.6.2, plasma-catalytic systems will be reviewed in terms of catalyst effects on methane conversion and product selectivity. In the following section (4.7) plasma-catalytic and plasma-alone systems for hydrogen generation from methane will be compared in terms of SEC and SER values, as well as viability of processes industrialization.

4.6.1. Two stage plasma-catalyst system

In a two stage system, the catalyst can be either positioned before (plasma post-processing) or after (plasma pre-processing) the plasma zone. In plasma pre-processing, the main role of plasma is to change the gas composition, i.e. enrich the gas with reactive species, which is then fed into the catalyst reactor. Plasma generated products play a key role to induce interactions in the two-stage plasma pre-processing system. Plasma post-processing means that plasma is used to treat exhaust gasses from the catalytic unit, intended to complete the reformation process or to destroy un-wanted products generated during catalytic reactions (Fridman, 2008; Chen et al., 2008).

Two stage plasma systems have been investigated for hydrogen rich gas generation in non-thermal plasmas such as: reformation of isooctane using pulse plasma discharge (Sobacchi, 2002), reformation of propane by gliding arc discharge (Chun and Song, 2008), and methane reformation using cold plasma jet (Long et al., 2008) and microwave plasma (Jasinski et. al., 2008). Plasma pre-processing and post-processing has been investigated in a pulsed corona reactor for hydrogen production from isooctane by Sobacchi et al. (2002). The authors concluded that plasma pre-processing has a higher increase in hydrogen production than post-processing of isooctane. Both methane conversion and hydrogen production have been shown to increase with use of nickel catalysts in a two stage plasma pre-processing reactor (Jasinski et al., 2008; Long et al., 2008; Yang et al., 2009). For example in the experiment with cold jet plasma reported by Long et al. (2008), the addition of nickel treatment after plasma reaction increased methane conversion by 14 % and hydrogen yield by 18 % compared to plasma treatment alone. The highest hydrogen yield

increase has been achieved by Chun and Song (2008) using gliding arc discharge and nickel catalyst. Chao et al. (2008) reported a very high hydrogen selectivity of 99.6 % and methane conversion rate of 90 % when employing gliding arc pre-processing with nickel catalyst. However, elevated temperatures between 400 – 1200 °C were used. Cheng et al. (2006) have reported that glow discharge plasma preparation of a nickel catalyst prior to methane reformation with CO₂ improved the catalyst activity at low temperatures and enhanced the overall stability of the catalyst. Cold plasma jet pre-processing and the use of a nickel catalyst has shown a high hydrogen selectivity of 90 % and a reasonable methane conversion of 60 % (Long et al., 2008), see Table 4.7.

Table 4.7: Summary of the results on the two stage pre-processing plasma-catalyst systems.

Plasma type and discharge power	Catalyst	Main reactant	Effects on reactant conversion		Effects on product composition					Reference
			Increase (%)	Max achieved (%)	Major Product	Max Yield (%)	Yield increase	Max selectivity (%)	Selectivity increase (%)	
Microwave 3 kW	Nickel	CH ₄	Not reported	Not reported	Hydrogen	Not reported	15	Not reported	Not reported	Jasinski et al. 2008
Gliding Arc 32.4 W	Nickel	CH ₄	Not reported	90	Hydrogen	Not reported	Not reported	99.6	Not reported	Chao et al., 2008
Cold Plasma Jet 0.77 kW	Nickel	CH ₄	14	60	Hydrogen	54	18	90	8	Long et al. 2008
Gliding Arc 1.37 kW	Nickel	Propane	Not reported	62.6	Hydrogen	Not reported	44.4	Not reported	Not reported	Chun and Song, 2008

4.6.2. Single stage plasma-catalyst system

In a configuration of single stage plasma-catalytic system the catalyst is placed within the plasma zone, where the plasma and the catalyst influence each other's properties and functions. Chen et al. (2008) wrote in their review of plasma-catalytic systems, that the presence of catalytic pellets would significantly enhance the electric field. Field enhancement would depend on the contact angle, curvature and dielectric constant of the packing pellets. Plasma influences on catalysts, as reported by Chen et al. (2008), include the change of the reactants status and catalyst properties itself. Plasma generates chemically active species, hence reduces the activation energy barrier for dissociative adsorption of the catalyst, increasing energy efficiency of catalytic reactions. Plasma improves metal dispersion of the catalyst, and together with the increase in internal energy and work function, might improve the rate of thermal catalysis and therefore the working temperature of the catalyst can be significantly reduced. The improvement of metal dispersion also allows suppression of coke formation, lessening the deactivation of catalyst and hence extending catalyst durability. The authors concluded that thermal plasmas cannot be used in a single stage plasma-catalyst system, due to their high gas temperature effects on the catalyst; whereas non-thermal plasmas can be used for single and two stage plasma-catalyst systems. However, experimental work has been successfully carried out with two-stage thermal plasma-catalyst systems (Kim and Chun, 2008; Tao et al., 2008).

Single stage non-thermal plasma-catalyst systems have been investigated for the reformation of hydrocarbons such as methane for hydrogen generation using zinc and chromium catalysts in dielectric barrier discharge (Intardo, 2008). Nickel catalysts have been used in gliding arc reactors (Rueangjitt et al., 2009; Yang et al., 2000), dielectric barrier discharge reactors (Heintze and Pietruszka, 2004; Song et al., 2004; Sentek, 2010; Gallon et al., 2011; Wang et al., 2011), corona discharge (Li et al., 2006; Bozorgzadeh et al., 2009) and microwave plasma reactors (Wang et al., 2010). Silver and palladium catalysts have been applied in a dielectric barrier discharge reactor (Sentek, 2010). Sodium zeolite catalyst has been used for methane conversion to acetylene (Liu et al., 1998) and palladium and silver for ethylene production (Gordon et al., 2003) in corona discharges. Copper and oxide zinc catalysts have been applied for methane conversion to ethane (Gorska et al., 2011),

and lanthanum oxide catalyst for methane conversion to ethane and ethylene (Pham et al., 2011) in DBDs. Experimental work for hydrogen generation from other hydrocarbon sources such as isooctane over nickel catalysts in dielectric barrier discharge (Biniwale et al., 2004) and biogas over nickel catalysts in gliding arc discharge (Chun et al., 2009) have also been investigated. Plasma-catalytic systems enhance methane conversion, and hydrogen and higher hydrocarbon yields. However, different catalysts present different effects: some increase the conversion rate of methane, whereas some increase the selectivity to specific products (Istadi and Amin, 2006).

As already mentioned in Chapter 2, Section 2.5.1., for thermo-catalytic methane decomposition most research is focused on nickel catalyst due to its high activity at lower temperatures and low cost (Suelves et al., 2005; Li et al., 2011). For the same reasons, much experimental work on plasma-catalytic work reported in the literature focuses on nickel catalysts, see Table 4.8. It has been reported that nickel catalysts in a plasma-catalytic system increases hydrogen yields and methane conversion in a dielectric barrier discharge and microwave plasma reactor (Heintze and Pietruszka, 2004; Wang et al., 2010). Wang et al. (2011) have reported a very impressive hydrogen selectivity of 99 % (increase of 24 %) and methane conversion of 90 % (increase of 70 %) when incorporating a nickel catalyst in DBD plasma system. Very high improvement in hydrogen production (selectivity increase of 32 %) and methane conversion (increase of 18 %) has also been achieved by Yang et al. (2009) using gliding arc with integrated nickel catalyst, refer to Table 4.8. The hydrogen selectivity of 93 % achieved by the authors is slightly above the highest value of 92.7 % achieved in plasma alone system using microwave discharge by Wang et al. (2010). However, Yang and the team (2009) have reported the highest methane conversion rate of 69 %, which is much lower than the 91.6 % achieved by Wang and the team (2010) using plasma-alone system. Gallon et al. (2011) have achieved a very impressive hydrogen selectivity equalling to 99 % with a nickel catalyst incorporated into the DBD reactor. However, a very low methane conversion of only 37 % was reported. The authors have also noted a very interesting observation: power input increased from 70 to 117 W as the operation time of the unit increased from 50 to 100 min at a constant voltage input of 21 kV at 33 kHz. This was mainly due to the increased conductivity of the nickel catalyst and hence higher currents of

the discharge (Gallon et al., 2011). Interestingly, Bozorgzadeh et al. (2009) have reported a decrease in hydrogen selectivity from 62 to 54.2 % when a nickel catalyst was placed in the corona discharge reactor, methane conversion rate reported increased from 27.64 to 35.64 % as expected. Similar effects were reported by Li et al. (2006), where nickel catalyst in the corona discharge decreased both, hydrogen selectivity and methane conversion by approximately 1 %. Rueangjitt et al (2009) have reported that a nickel catalyst in a gliding arc discharge has a promotional effect on methane conversion, but no significant effect on product selectivity. The authors have pointed out that this could be explained by the microreactor residence time being too short to promote subsequent reactions, such as coupling, dehydrogenation and cracking. This could indicate that residence time plays an important role in plasma-catalytic systems for product selection. Overall, in most cases the use of a nickel catalyst promotes better methane conversion as well as hydrogen selectivity, see Table 4.8.

Gordon et al. (2003) reported that the use of a silver-palladium-Y-zeolite catalyst in a GA reactor for methane conversion increases ethylene selectivity, with no effect on the methane conversion rate. The authors concluded that the palladium-Y-zeolite catalyst selectively hydrogenates acetylene to ethylene and ethane, whereas the addition of silver-Y to the catalyst increases ethylene selectivity reducing the over-hydrogenation to ethane (Gordon et al., 2003). Similarly, a palladium catalyst on alumina support has been shown to increase ethane selectivity in dielectric barrier discharge (Sentek, 2010) and gliding arc reactors (Mlotek et. al., 2009). Ethane selectivity has also been shown to increase on the addition of copper and oxide zinc catalyst in DBD (Gorska et al., 2011).

Bimetallic palladium-nickel catalysts have been shown to increase methane conversion and acetylene selectivity (Cho et al., 2010). Horng et al. (2009) have shown that the palladium and rhodium bimetallic catalyst works well with spark discharge plasma for gaseous hydrocarbon decomposition, where 85 % propane conversion and 65 % hydrogen selectivity has been achieved at a propane flow rate of 4 l/min. However at a very high reformat gas temperature of 850 °C. At the lowest temperature tested of 400 °C, propane conversion and hydrogen selectivity were both much lower at 49 and 22 % respectively (Horng et al., 2009).

Table 4.8: Summary of the results on the single stage plasma-catalyst systems.

Plasma type and discharge power	Catalyst	Reactant	Effects on reactant conversion		Effects on product composition			Reference
			Increase (%)	Max achieved (%)	Product affected (increased)	Max selectivity (%)	Selectivity increase (%)	
DBD	Nickel	CH ₄	70	90	Hydrogen	99	24	Wang et al., 2011
Gliding arc 1.3kW	Nickel	CH ₄	18	69	Hydrogen	93	32	Yang et al., 2009
Microsized Gliding arc	Nickel	CH ₄	15	50	None	Approx 80%	None	Rueangjitt e al., 2009
Single-anode thermal plasma	Nickel	CH ₄	2.48	92.32	Hydrogen	75.43	6.83	Tao et al., 2008
DBD	Nickel	CH ₄	Not reported	37	Hydrogen	99	Not reported	Gallon, et al., 2011
DBD 80 W	Oxide zinc and chromium	CH ₄	18	50	Hydrogen	55	20	Intardo, 2008
Corona Discharge 8.4 W	Sodium Zeolite	CH ₄	26	38	Acetylene	32.3	Not reported	Liu et al., 1998
DBD 18 – 19 W	Palladium	CH ₄	-7.1	50.9	Ethane	9.45	2.05	Sentek et al., 2010
Corona Discharge 4.55 W	Silver-palladium-Y-zeolite	CH ₄	0	33	Ethylene	52	46	Gordon et al. , 2003

4.6.3. Plasma-catalytic systems – conclusions

To conclude, plasma-catalytic reforming of hydrocarbons for hydrogen production and/or higher hydrocarbon formation has been shown to be more selective than plasma use on its own in DBD, corona, gliding arc, microwave discharges and cold plasma jet. Experimental results revealed higher conversion rates and a possibility of better product selectivity and control. According to Chen et al. (2008) single stage plasma-catalytic systems due to direct plasma-catalyst interactions present some advantages over two stage systems such as better energy efficiency, reduced working temperature of the catalyst, and extended catalyst durability. Product selectivity of methane reformation in a single stage plasma-catalytic system strongly depends on the selection of the catalyst, where a nickel catalyst seems to favour hydrogen production, and in contrast palladium-Y and silver-Y zeolites favour polymerization reactions and hence selectivity of C₂ hydrocarbon formation, see Table 4.8.

4.7. Summary

In section 4.3.5, Table 4.2, different plasma-alone systems for hydrogen generation from methane have been compared. Partial oxidation of methane was shown to be the most effective method, with cold plasma jet being at the top of the race for the cost of production and the capacity of conversion. Li et al. (2010) has presented the most efficient plasma jet without any catalyst with SEC and SER as low as 312 and 197.9 kJ/mol respectively, methane conversion and hydrogen selectivity of 94.99 % and 79 % respectively, and total flow of 1 L/min. Another cold plasma jet system presented by Long et al. (2008) is also promising for industrial application with SEC and SER as low as 682 kJ/mol and 437 kJ/mol respectively, methane conversion and hydrogen selectivity of 45.68 % and 78.11 % respectively, and total flow of 8.3 L/min. The addition of nickel catalyst to this system has been shown to have a great improvement, by increasing methane conversion rate and hydrogen selectivity to 60.6 % and 96.87 % respectively, and consequently reducing SEC and SER to 514 kJ/mol and 265 kJ/mol respectively (Long et al., 2008).

Jasinski et al. (2008) have achieved the lowest SEC and SER values in the reviewed plasma systems, of 174 kJ/mol and 90 kJ/mol respectively, by employing microwave

discharge with nickel catalyst for methane pyrolysis. The authors reported high hydrogen selectivity of 96.8 % and a very high feed flux of 1750 L/min. However, methane conversion in this system is very low of only 13.2 %. Tsai and Chen (2009) have achieved approximately 40 % methane conversion and 86 % hydrogen selectivity, with SEC and SER values of 1022 kJ/mol and 646 kJ/mol respectively, by employing microwave discharge alone for methane pyrolysis. Comparing the two systems, it is very clear that the use of nickel catalyst has a profound effect on energy efficiency by lowering SEC and SER values by approximately 7 times, as well as hydrogen selectivity increase of 10.8 %. However, it seems to show a negative effect on methane conversion, lowering by 26.8 %. Interestingly, the addition of a nickel catalyst to thermal plasma partial oxidation of methane shows a positive effect on methane conversion and hydrogen selectivity. However, no major improvement in SEC and SER values (Tao et al., 2008; Tao et al., 2009)

Table 4.9 presents the summary of the lowest SEC and SER achieved by plasma-alone and plasma-catalytic systems for hydrogen production from methane. It is very clear that catalyst addition has a profound positive effect, especially in microwave discharges and cold plasma jet. To conclude, cold plasma jet with or without the nickel catalyst shows the highest potential to become industrially viable. The advantages of this system include very low cost, high capacity, good methane conversion rate and very impressive hydrogen selectivity.

Table 4.9: Summary of the results of plasma-catalytic and plasma alone systems for hydrogen generation from methane.

Plasma form	Reaction type	Feed flux (ml/min)	CH ₄ to other reactants ratio	Discharge power (W)	CH ₄ conversion rate (%)	Hydrogen selectivity (%)	SEC kJ/mol CH ₄ converted	SER kJ/mol H ₂ produced	Reference
Microwave plasma and nickel catalyst	Pyrolysis	1.75 X 10 ⁵	CH ₄	3 X 10 ³	13.2	96.8	174	90	Jasinski et al., 2008
Plasma jet	PO	2200	4/6 CH ₄ /CO ₂	69.85	60.97	89.30	174	98	Li et al., 2009a
Plasma jet	PO	1000	4/6 CH ₄ /CO ₂	88.4	94.99	79	312	198	Li et al., 2010
Cold plasma jet And nickel catalyst	PO	8.3 X 10 ³	4/6 CH ₄ /CO ₂	770	60.6	96.87	514	265	Long et al., 2008
NTP – glow like	PO	10.5	25% CH ₄ in air	155	-----	-----	-----	324	Luche et at., 2009
Cold plasma jet	PO	8.3 X 10 ³	4/6 CH ₄ /CO ₂	770	45.68	78.11	682	437	Long et al., 2008
Glow discharge	PO	120	1/1 CH ₄ /CO ₂	23	61	77	845	548	Ghorbanzadeh et al., 2009
AC corona discharge	PO	-----	-----	14	10-20	-----	960	-----	Supat et al., 2003
Microwave discharge	Pyrolysis	1.2 X 10 ⁴	20% CH ₄	800	Approx 40	86	1022	646	Tsai and Chen, 2009
Thermal water plasma torch	ATR	2 X 10 ³	1/1 CH ₄ /CO ₂	1.05 X 10 ³	62.2	81.2	1135	700	Ni et al., 2011

Chapter 5: Experimental Rig

5.1. Introduction: rationale of this study

It can be seen from Chapter 2 that there is a high necessity for the development of environmentally friendly chemical process technologies in the energy sector. In the oil industry, heavy hydrocarbons, such as hexadecane cracking in two octanes, and possible reactions to increase branching could be very attractive for applications to increase octane number in gasoline. At the same time, the stress to implement clean, sustainable and economically viable alternative energy systems is growing. A hydrogen infrastructure has been recognised to be a key for the latter, with CO₂ free hydrogen generation being the main challenge in the industry due to catalyst deactivation problems in conventional thermo-catalytic processes. Hence, technology development for CO₂ free hydrogen generation to utilize an abundant supply of methane, as well as the exploration of other inexpensive fuels such as propane, to generate hydrogen is beneficial in terms of the economy and the environment. Non-thermal plasmas, especially, are considered to be very promising for the above applications. As reviewed in Chapter 4, a vast amount of experimental work has been dedicated to plasma assisted hydrocarbon conversion processes. In summary, plasma-assisted cracking of liquid hydrocarbons could offer a more selective hydrocarbon cracking method compared to catalytic and thermal cracking, due to the low bulk temperature. Whereas the use of plasmas for gaseous hydrocarbon decomposition would provide a more environmentally friendly hydrogen production technology, eliminating problems associated with catalysts.

From Chapters 3 and 4 it can be clearly seen that there are a number of different types and configurations of non-thermal plasma discharges. Corona discharges, in particular, have been recognised to be very efficient in transferring source power into promoting chemical reactions (Uhm, 1998). In non-thermal plasmas the rate of all discharge reactions depends on electron energy, electron density, gas temperature, gas pressure and the properties of gases. Intardo et al. (2006) has shown that the use of argon as an additive gas for methane decomposition reactions can achieve the lowest energy consumption compared to other gasses. As described in Chapter 4, Section 4.3.6.3., the accelerated plasma chemical reactions with the addition of argon

as reported by Intardo et al. (2006) are due to the release of extra electrons from argon ionization reactions, which initiate the pure plasma decomposition by collision of electrons and methane gas molecules. Both, the extra electrons from argon and the consequent pure plasma effect accelerate radical generation rates. The efficiency of a corona reactor is correlated with the radical production rate during the discharge period (Eichwald et al., 2008). Hence, argon is considered as an excellent plasma forming gas (Zou et al., 2007), whilst also acting as a catalyst.

Based on the rationale above, our present work is focused on: i) achieving the cracking of hexadecane to generate smaller liquid hydrocarbon molecules, and ii) decomposition of propane and methane to generate CO_x free hydrogen, using the corona discharge non-thermal plasma method with argon as a an additive gas. This chapter presents the scope and objectives of this research, a detailed description for the experimental facility, experimental methodology, methodology for hydrocarbon characterization and uncertainty analysis. The chapter is organised as follows: section 5.2 details the scope and the objectives of the PhD research; section 5.3 gives a description for the experimental facility; section 5.4 presents the experimental methodology; section 5.5 describes the methodology for hydrocarbon characterization; uncertainty analysis is given in section 5.6 and section 5.7 summarizes the chapter.

5.2. Scope and objectives

The purpose of this research is to design, construct and test a non-thermal corona discharge plasma reactor for liquid and gaseous hydrocarbon reformation. To this day, the literature available on the experimental results for plasma use to crack liquid hydrocarbons is limited. The use of corona discharge for this purpose has not been previously reported. With this and the findings in the literature in mind, the ultimate goal of this work is to achieve hexadecane cracking under a corona discharge and the key objectives are:

1. **Crack hexadecane in a liquid form:** it is desired to keep the feedstock in the liquid state due to the added cost of hydrocarbon vaporization at high temperatures.

2. **Functioning electrode (the pin) not submerged:** Kong (1997) achieved liquid hydrocarbon cracking with the functioning electrodes submerged within the feedstock, where electrode corrosion problems occurred.
3. **Use argon as working gas:** it is not consumed in the process and can be recycled. Kong et al (2005) and Khani et al. (2011) achieved cracking using hydrogen and/or methane gas, both being fuels increasing the cost of the process.
4. If cracking is achieved: perform a parametric study to determine the effects of discharge power, residence time and inter-electrode distance to improve hexadecane conversion. Low conversion rates of 30 % (Kong et al., 2005) and 9.41 % (Kahn et al., 2011) have been reported in the literature.

Methane and propane: the ultimate objective is to assess the capability of the corona discharge to become an efficient CO_x free hydrogen generation technology. This will be achieved by comparing and evaluating the reformer efficiency, hydrogen production and conversion capability with the results reported in the literature. A parametric study is necessary to gain deeper knowledge and understanding of the plasma chemical conversion of gaseous hydrocarbons. The behaviour of plasma in decomposition reactions for hydrogen generation under different conditions is of high interest to the academic research, with many questions still to be answered. Tsai and Chen (2009) reported the highest energy efficiency for plasma methane decomposition of 24 % (without the use of a catalyst), where energy efficiency is highly dependent on hydrogen selectivity. Hence, the key objectives for methane decomposition experiments in this work, is to investigate the following parameters focusing on hydrogen production and selectivity:

1. **Flow or residence time:** higher flow resulted in lower methane conversion for decomposition reactions in the microwave discharge (Tsai and Chen, 2009); the effect on hydrogen selectivity was not reported. In PO systems controversial results reported, as some show an improvement, some a decrease in hydrogen selectivity. The aim is to investigate the effects of residence time on both methane conversion and hydrogen production in plasma assisted methane decomposition, and identify the optimal residence time for highest hydrogen selectivity.

2. **Discharge power:** in decomposition reactions higher discharge powers lead to increased methane conversion rates, no real effect on hydrogen selectivity reported in gliding arc (Rueangjitt et al., 2009) and microwave discharges (Tsai and Chen, 2009). For PO reactions, higher discharge power leads to increased hydrogen selectivity. However, in most cases reported higher discharge powers also result in lower overall energy efficiency of the system. A range of discharge powers will be tested and assessed, especially in terms of hydrogen selectivity and energy efficiency. The key aim is to determine optimal discharge power for the reformer with competitive energy conversion efficiency above 20 %.

3. **Inter-electrode distance:** tested inter-electrode distance range reported in the literature is 0.5 – 10 mm. Higher distances achieved overall improvement in methane conversion in all cases reported. Only Kado et al. (2003) reported effects of inter-electrode distance for decomposition reactions, using a pulsed corona discharge. The behaviour of hydrogen production with the change in inter-electrode distance has not been reported for corona discharges. The aim in this work is to test higher inter-electrode distances above 10 mm, showing the extent of the inter-electrode distance effects for decomposition reactions providing novel results for hydrogen production.

4. **Polarity:** Kado et al. (2003) reported that in pulsed corona decomposition of methane positive polarity is slightly better for methane conversion when compared to negative. The effect of polarity on hydrogen production has not been reported. In this work both polarities will be investigated for hydrogen production from methane.

5. **The effects of carbon build-up on plasma functionality:** as described in Chapter 1, the biggest challenge in thermo-catalytic methane decomposition is the deactivation of the catalyst due to solid carbon build-up. In this work, the ability of the plasma to function with the carbon build up on the electrodes will be assessed. This will be achieved by allowing the ground plate electrode to be covered with a layer of carbon. The effect of carbon build-up in plasma assisted decomposition has not been reported in literature.

The key objectives for work with propane include the parametric testing as described for methane above, points 1 to 5. Plasma alone decomposition of propane has not been reported in the literature yet. Therefore, the parametric study is based on the

knowledge and results for methane decomposition, providing a novel data set for propane. Drawing from the literature available, described in Chapter 4, the key objectives for the plasma assisted propane decomposition experiments are:

1. **No catalyst use:** propane conversion has been successfully achieved in plasma-catalytic PO systems. For example Horng et al. (2009) used Pt-Rh/Al₂O₃ as a catalyst in spark discharges, Yu et al., (2011) employed a DBD system with Ni/Y-Al₂O₃ catalyst. The problems with catalyst deactivation in decomposition reactions have been addressed previously, and this work aims to achieve plasma assisted propane decomposition without the use of catalysts.
2. **Room temperature:** propane conversion has been successfully achieved in plasma-catalytic PO systems at high temperatures. For example, optimal operating temperatures selected by authors include 850 °C (Horng et al., 2009), 400 °C (Yu et al., 2011), 720 °C (Bromberg et al., 2005). In this work, the aim is to achieve propane decomposition at room temperature, without any external heating supply.
3. **No oxygen species present:** high propane conversions have been reported when employing plasma-catalytic PO and SMR systems. However, in all cases CO_x compound selectivities were higher or at the same level as hydrogen selectivities (Horng et al., 2009; Yu et al., 2011; Tamosiunas et al., 2012). In this work the aim is to decompose propane to hydrogen and carbon without any oxygen species present, this has not been reported in any literature yet.
4. **Achieve hydrogen selectivity above 14 %:** Yu et al. (2011) achieved hydrogen selectivity of 13.9 % when employing DBD plasma alone system for PO reactions. In this work the aim is to achieve improved hydrogen selectivity and hence improved energy efficiency.

5.3. Plasma reactor

5.3.1. Overview

The experimental facility can be divided into two major parts: the experimental system and the product analysis system. The experimental set-up consists of a plasma reactor, high voltage power supply, vacuum pump and temperature and pressure data logging system. The plasma reactor has a stainless steel pin-to-plate electrode configuration contained in a glass cylinder with stainless steel disks at each end, and a copper disk with integrated cartridge heater and temperature control system. The plate electrode contains a well, where a measured amount of liquid hydrocarbon is subjected to corona discharge using argon as a working gas. The pin serves as an active electrode and is supplied with either positive or negative high voltage. Samples are subjected to the plasma in a batch process. The chamber contains a gaseous product outlet controlled by a manual valve and the liquid product is collected using a gas tight syringe directly from the well. Temperature and pressure are monitored and recorded during the experimental procedure using a data logger connected to a computer. The cartridge heater integrated in the copper disk can be used to adjust the temperature of the reaction well to the desired level and is controlled by the set up feedback system.

The glass cylinder is 150 mm in length, 100 mm outer diameter and 5 mm in thickness, made of borosilicate glass and can sustain a maximum short time working temperature of 500 °C and a maximum pressure of 73.7 bar (Labglass Ltd). The top disk is made of 316 stainless steel, 142 mm in diameter and 23 mm thickness. The bottom section contains two disks: a 30 mm thick C103 copper disk and a 23 mm thick stainless steel disk, both 142 mm in diameter. The top and the bottom disks are connected and stabilized by three metal support rods, see Figure 5.1.

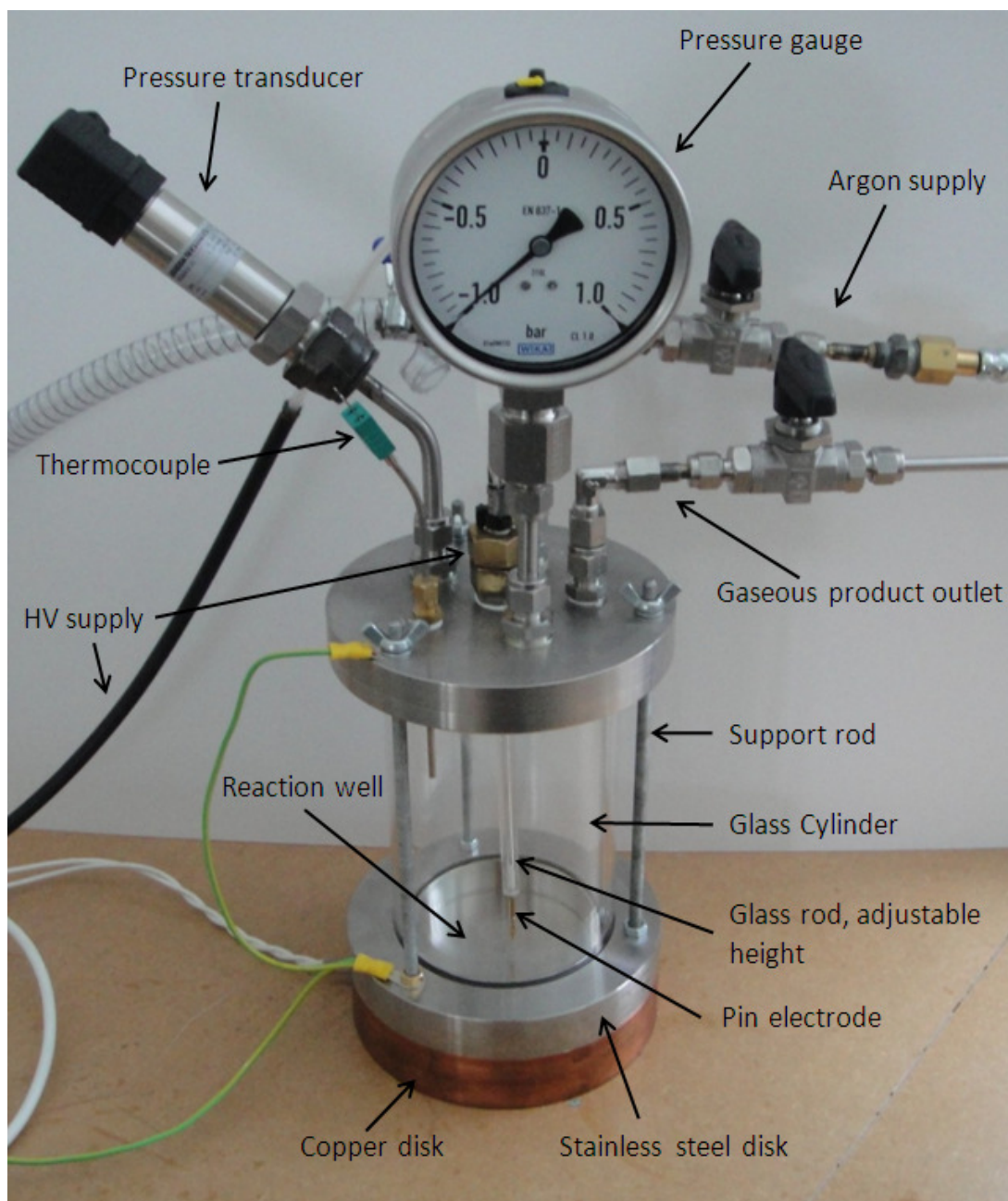


Figure 5.1: Picture of the plasma chamber design, showing all relevant components.

5.3.2. Top plate

A groove of 89 mm inner diameter, 100 mm outer diameter and 6 mm depth is made in the centre of the disk to fit the glass cylinder, see Figure 5.2. Nitrile rubber o-rings, located in the glass fitting groove (5 mm section and 90 mm bore), are used to seal the unit whilst under pressure from the support rods and were selected because they have good resistance to various chemicals.

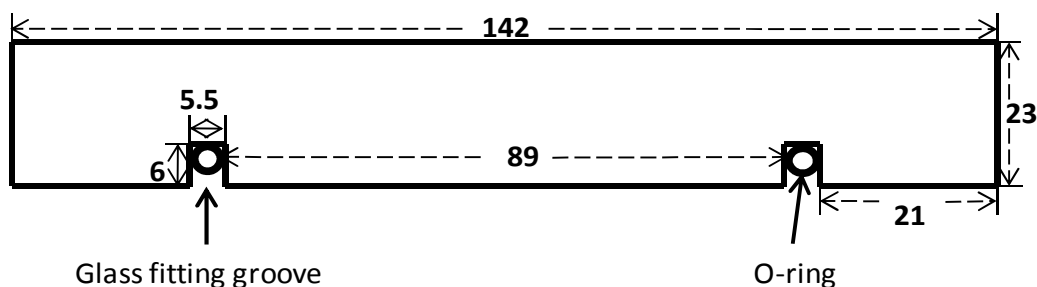


Figure 5.2: Shows the side view of the stainless steel top disk: glass fitting groove.
The units in the diagram are in millimetres.

Please refer to Figure 5.3a for the following description. In the region of 89 mm within the internal diameter of the disk, compression fittings are fitted to install a pressure transducer and a type K thermocouple that feeds to the data logger. The pressure gauge is fitted to monitor pressure during the experiments. The pressure transducer used is manufactured by Sensortech, and is able to sense pressure in the range of +/- 1bar, at maximum operating temperature of 100 °C. The pressure gauge, which is manufactured by WIKA, operates in a pressure range of +/- 1 bar and is suitable for use in corrosive environments and gaseous media. Within the same region of 89 mm internal diameter, two 8 mm outer diameter stainless steel tubes are fitted using compression fittings: one is for the product gas release, the other is connected to a T-compression fitting allowing separate connections to the vacuum pump and the argon gas supply. Ball valves are installed to manually control product gas release, vacuum of the system as well as working gas input. A two stage rotary pump manufactured by Edwards is used to create a vacuum in the system. The working gas is pure grade argon (inert gas), and a 0 – 4 bar argon regulator is used, both supplied by BOC gasses.

For the experiments with gaseous hydrocarbons, the pressure gauge is replaced by the gaseous product outlet septa and the gaseous outlet valve is fitted with propane feed, please see Figure 5.3b.

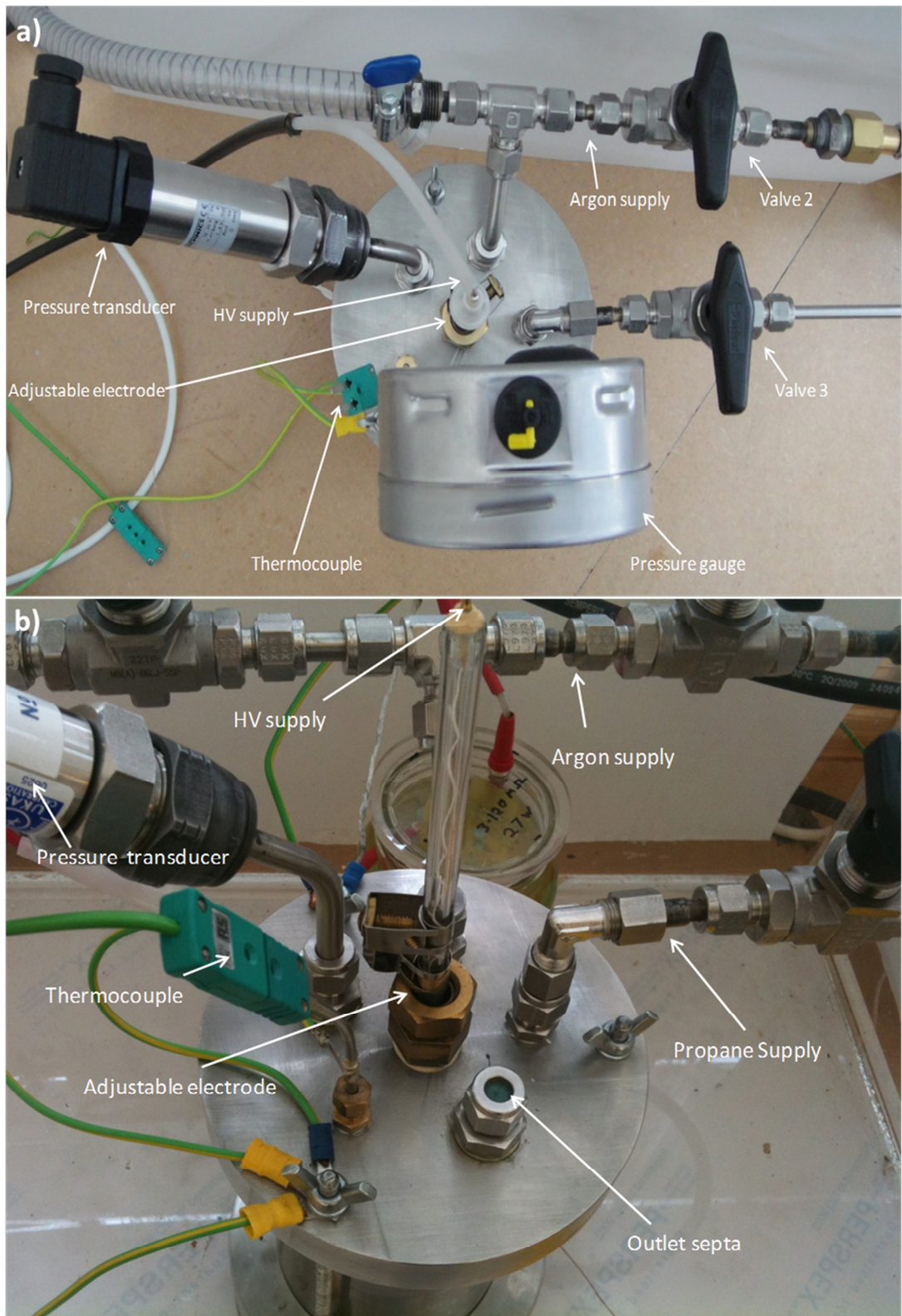
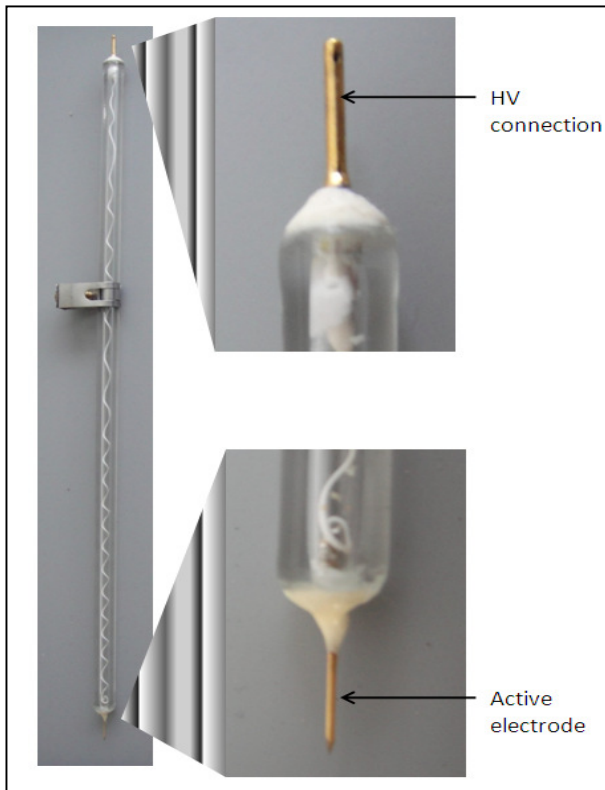


Figure 5.3: Picture of a) Top plate showing the positions of high voltage supply and the active electrode, argon and vacuum supply, gas outlet, thermocouple and pressure transducer; b) Top plate showing the addition of outlet septa and propane supply.

The active electrode is installed at the centre of the top disk. A glass rod serves as an insulator as well as for electrode stability purposes. It can be moved up or down to change the inter-electrode distance, see Figure 5.4. The outer end of the rod is connected to an extra high tension (EHT) lead to provide power for the active electrode at the inner end of the rod. High voltages are only necessary for the plasma



ignition. After ignition, the plasma can sustain itself at much lower voltages. Therefore, high voltage is applied to the active electrode from a HV generator through a 3.14 M Ω in-house built resistor, see Figure 5.5. It shows the connection of three 1 M Ω resistors connected in parallel, joined to two other sets in series. The resistor allows the plasma ignition and sustainability by lowering the voltage input after the ignition.

Figure 5.4: Picture of the design of the pin electrode.

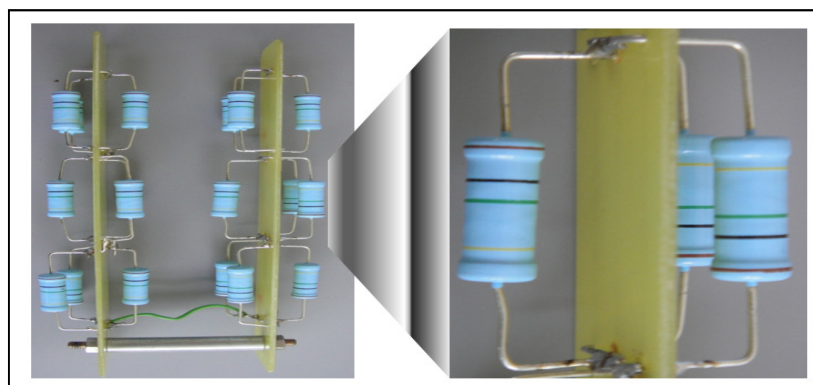


Figure 5.5: Picture of the in-house built resistor, consisting of three 1 M Ω resistors connected in parallel. The total amount of resistors is 27 and the total resistance is 3.12 M Ω , 27 W.

5.3.3. Bottom plates

A groove of 89 mm inner diameter, 100 mm outer diameter and 6 mm depth is made in the centre of the stainless steel disk to fit the glass cylinder with an o-ring. A well with dimensions of 18 mm depth and 85 mm diameter is cut out for the reaction media 2 mm from the inner side of the groove, see Figure 5.6 and Figure 5.7. The 2 mm rise between the glass fitting groove and the reaction media is for glass fitting stability and the prevention of glass damage if media splashing occurs. Nitrile rubber o-rings (5 mm section and 90 mm bore) are used, as they have good sealing properties and are resistant to various chemicals.

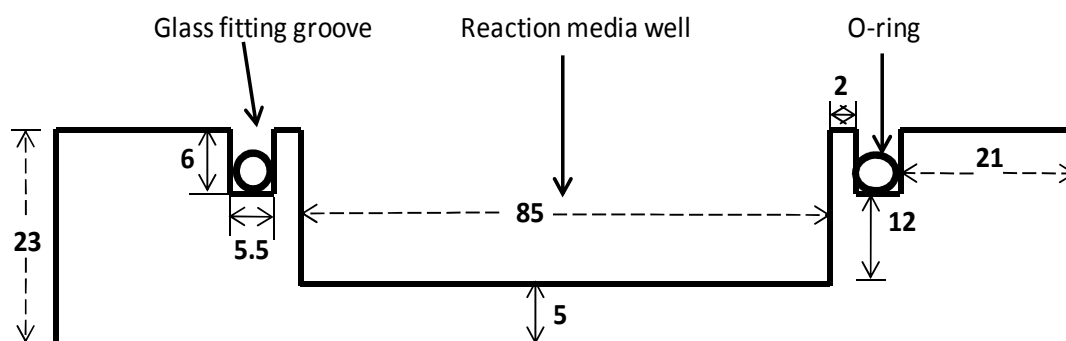


Figure 5.6: Side view of the stainless steel bottom disk: reaction media well, glass fitting groove and inlet/outlet grooves. The units in the diagram are in millimetres.

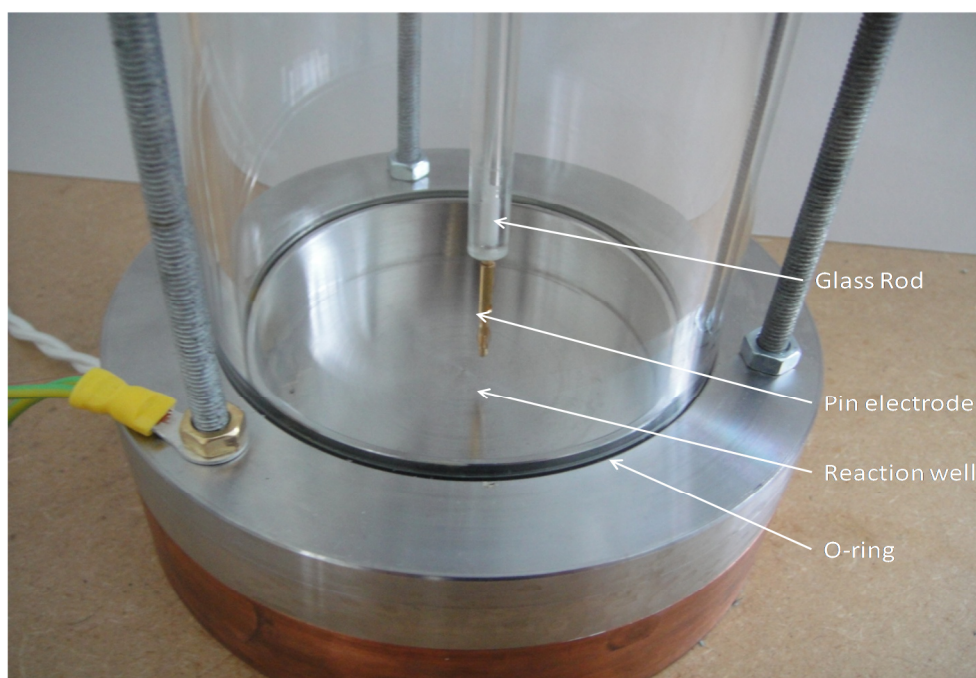


Figure 5.7: Picture of the close up view of the reaction well and the pin electrode.

A copper disk containing a cartridge heater, see Figure 5.8, is used to provide heat for the reaction media. The heat will be spread evenly, due to the high thermal conductivity of copper, before it reaches the stainless steel disk and hence the reaction media. A cartridge heater is installed inside the copper disk: a groove with dimensions of 13 mm diameter and 82.6 mm length horizontally is cut out; it is in the region of 30 mm from the outer boundary of the disk, 7 mm from the bottom and 10 mm from the stainless steel plate connected, see Figure 5.8. Conducting tape is used to install the heater in the groove so that the heat spreads efficiently into the copper disk. The cartridge heater used is manufactured by Redring, has a diameter of 12.7 mm and is 82.55 mm in length. The power output is 500 W. The cartridge heater is connected to the PID temperature control system. The copper and stainless steel plates are connected using conducting tape to efficiently conduct the heat from the copper disk to the reaction media well. Three M5 Allan screws hold the plates together safely.

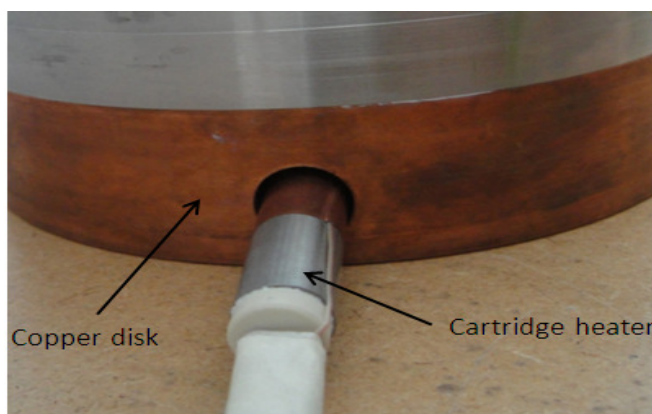


Figure 5.8: Picture of the cartridge heater installation into the copper disk.

5.3.4. Temperature and pressure measure and control

An in house Proportional Integral Derivative (PID) controller box was constructed, with a purpose to control the main power to the cartridge heater and hence the temperature, by feedback from the type K thermocouple. The control box contains the housing case, the PID, the Solid State Relay (SSR) and on/off safety mains switch, see Figure 5.9.

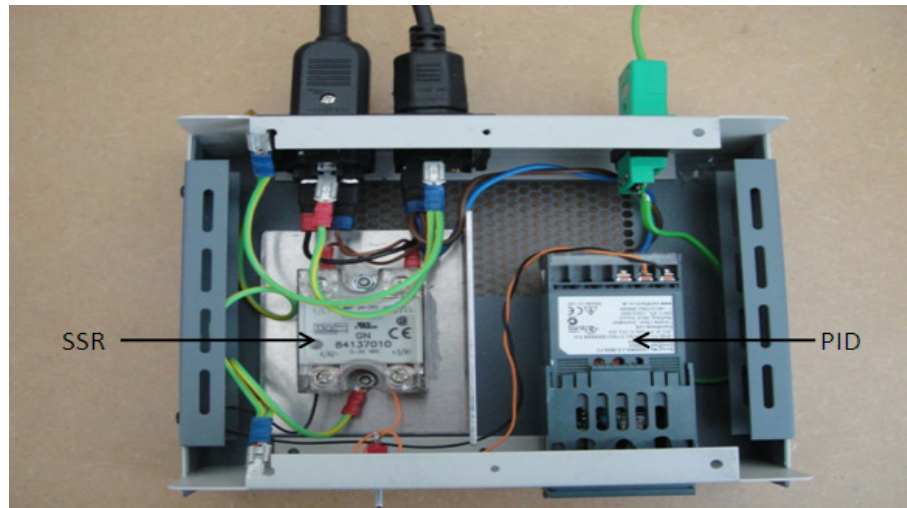


Figure 5.9: Picture of the cartridge heater control box showing the setup of the SSR and PID.

The SSR is manufactured by Crouzet, with DC control voltage type, max control current 14 mA, min control current 7 mA, thyristor output type. The PID temperature controller is manufactured by Eurotherm Controls and provides 0.25 % accuracy. The type K thermocouple is attached to the cartridge heater and feeds the temperature sensed to the PID, see Figure 5.10. The required temperature is set at the PID control display. Once the PID controller receives the feedback from the thermocouple, it will feed the information to the SSR if the temperature needs to be raised. The SSR would then pass the feedback to switch the mains to the cartridge heater, which would heat the copper disk. The temperature is constantly sensed by the thermocouple and feedback to the PID. Hence, the feedback system is continuous. However, no loop feed to SSR occurs when the temperature sensed is at the pre-set level.

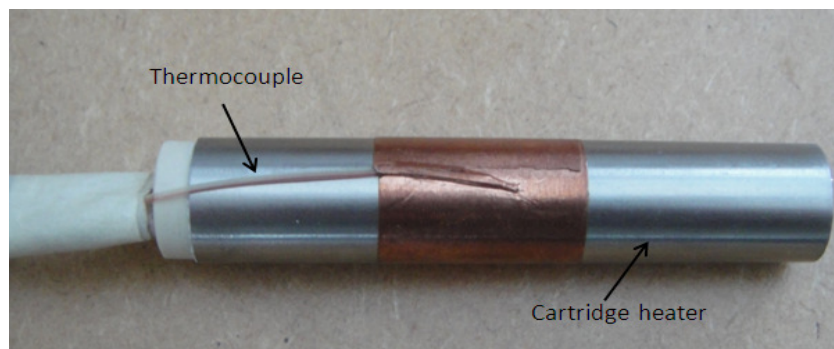


Figure 5.10: Picture of the cartridge heater and the thermocouple attached to it.

The pressure gauge installed at the top plate is for a fast reference of the chamber pressure. This is mainly to prevent large gaseous reactants build up in the system, causing a high pressure increase and possible damage to the unit. A pressure transducer and a type K thermocouple are installed at the top of the stainless steel disk; both are connected to the data logger for accurate data logging during the experimental runs. The thermocouple is placed between at the top plate of the chamber to monitor the temperature within the chamber. A USB TC-08 Thermocouple Data Logger is used, it is supplied by Pico Technologies, with input voltage ± 70 mV, resolution 20 bits, conversion time 100 ms, see Figure 5.11. The voltage accuracy is the sum of $\pm 0.2\%$ of the reading (in μV) and $\pm 10\ \mu\text{V}$. The data logger does not require power supply and is simply connected to the computer via a USB port. Pico Data loggers are supplied with PicoLog software, which allows data collection, analysis and display. With this software, the data is viewable during and after the data collection in both, spreadsheet and graphical formats. Data can also be exported for use in other applications. The data logger will be used throughout each experiment to monitor accurate temperature and pressure changes and the effects on the product composition.



Figure 5.11: Picture of the USB TC-08 Thermocouple Data Logger; a) USB connection to the computer, b) type K thermocouple measuring room temperature, c) type K thermocouple measuring reactor temperature, d) terminal board for reactor pressure measurement.

5.4. Experimental methodology

5.4.1. Liquid samples

Hexadecane in a liquid state is subjected to corona discharge in a pin-to-plate electrode configuration. The plasma forming gas is either air, argon or air/argon mixture. A measured amount of liquid is placed in the reaction well using a syringe. Then the chamber is flushed with argon by exhausting to vacuum and then filling with argon (2 cycles) to ensure that there is no air in the system. The chamber is filled either with 1 atmosphere of argon or air or with 0.5 atmosphere argon, followed by 0.5 atmosphere air. High voltage direct current power is supplied to the pin electrode initiating electrical break down of the argon gas and hence generating active plasma species of electrons and ions. Power supply is switched off once the set time of the experiment has been reached. The system is allowed to stabilize and cool. Liquid samples are removed using a gas tight syringe and stored in labelled glass bottles in a safety cupboard until tested. To avoid the contamination the syringes and the reaction well are rinsed with acetone, and then with dichloromethane (DCM), and allowed to air dry after each run.

5.4.2. Gaseous samples

Propane or methane is subjected to a corona discharge with argon as a working gas, total volume of 1 atmosphere and ratio 1:1. As described in Chapter 4, Section 4.3.6.3., it has been experimentally shown that argon addition enhances the rate of methane conversion to its radicals in plasma assisted methane decomposition (Mishra et al., 2004) as well as lowers the input energy required to maintain the plasma (Intardo et al., 2006). As shown by Intardo et al. (2006), lower methane concentrations favor methane conversion, with the highest methane conversions and selectivities towards hydrogen at 80 % argon and 20 % methane input. However, at such a low methane concentration the conversion rate and hydrogen production rate per unit of time would be very low. Increasing methane concentration to 50 % (and argon addition of 50 %) has a very minor effect on the conversion rate and hydrogen selectivity of approximately 5 % decrease. A further increase, however, shows a major decrease in both. Therefore, for this work a ratio of 1:1 methane or propane to argon has been selected. Partial pressures are used for measuring propane or methane and argon entering the system (Abbas and Daud, 2009a) using a pressure transducer.

The chamber is first flushed with argon by exhausting to vacuum and then filling with argon (2 cycles) to ensure that there is no air in the system. Then the chamber is filled with 0.5 atmospheres argon, followed by 0.5 atmospheres of propane or methane. The system is allowed to settle until the temperature is stabilized. Pressure and temperature are monitored and recorded by the data logger for 40 seconds to show stability before starting the experiment. High voltage direct current power is supplied to the pin electrode initiating electrical break down of the argon gas and hence generating active plasma species such as electrons and ions. Cracking of hydrocarbon molecules is achieved by plasma ionization of the hydrocarbon molecules by an impact of an energetic electron or photo-ionic decomposition. The power supply is switched off once the set time of the experiment has been reached. The system is allowed to stabilize and cool. Two gaseous samples are collected after each experiment via the septa installed at the top disk using a gas tight syringe (Hamilton, 1000 Series Gastight, Fixed Needle, 5ml).

5.4.3. Residence time and flow

In this work the corona discharge is operated in a batch process. The residence time for both liquid and gaseous sample processing is defined as the amount of time (seconds) the reactants are subjected under an active plasma discharge, i.e. the time elapsed between the discharge power switched on and off. In the literature, the flow of the reactants (ml/min) is mostly used as a parameter instead of the residence time. Therefore, for comparison the equivalent flow for liquid and gaseous samples in this work is calculated. For liquid samples the flow is calculated by dividing the amount of hexadecane in ml by the residence time in min. For gaseous samples, the total volume of the unit (979 ml) is divided by the residence time (min) to acquire the equivalent of total gas flow (ml/min).

The calculations for the flow in this work are only theoretical, due to different plasma behavior and gaseous reactants mixing under true flow conditions when compared to the stationary. The calculated equivalent flow parameter will only be used for the comparisons of methane experimental results with those reported in the literature. Otherwise, the residence time will be reported as defined above.

5.5. Sample characterization

5.5.1. Overview

Product analysis is carried out using gas-chromatography mass-spectrometer (GC-MS) instrumentation (Hewlet Packard series 5890 GC and a Trio-1 MS) as well as Mass Lab programme for liquid and gaseous hydrocarbon product characterization. The GC-MS set up only allows the analysis of gases or liquids at one time, therefore some modifications such as the change of column, inlet and the method set up will be required when switching the instrument between the two. Gaseous samples can be analysed directly by the instrument. However, liquid samples are either extracted or diluted in a solvent to prevent column contamination. A Mass Lab programme installed on the computer facilitates control of the GC-MS parameter settings and the acquisition of the data. The same programme is used for sample characterization. NIST and NBS libraries are connected to the programme allowing accurate determination of the compounds present, based on the ions present within the peak of the chromatogram.

Gaseous products are also tested by the GC (CP9001 GC) set up for accurate hydrogen only measurement.

5.5.2. GC-MS instrument

Gaseous and liquid samples are run on the GC-MS instrumentation for further characterization, see Figure 5.12. The gas-chromatography instrument used is manufactured by Hewlet Packard series 5890 and the mass spectrometer is Trio-1. The main purpose of the GC is to separate a mixture of chemicals into individual components depending on their size and chemical properties. This is done in the GC column in an enclosed oven, which is programmed to increase temperature gradually. As the temperature increases, compounds that have lower boiling point will elute from the column faster than those with higher boiling points. Helium gas was selected as a carrier gas for this study. The separated compounds enter the mass spectrometer detector at different retention times, these signals are recorded by a computer during the run into a chromatogram. The MassLab software installed on the computer is used to control GC-MS run parameters and record the run chromatogram, which can be saved, accessed and analysed after the run.

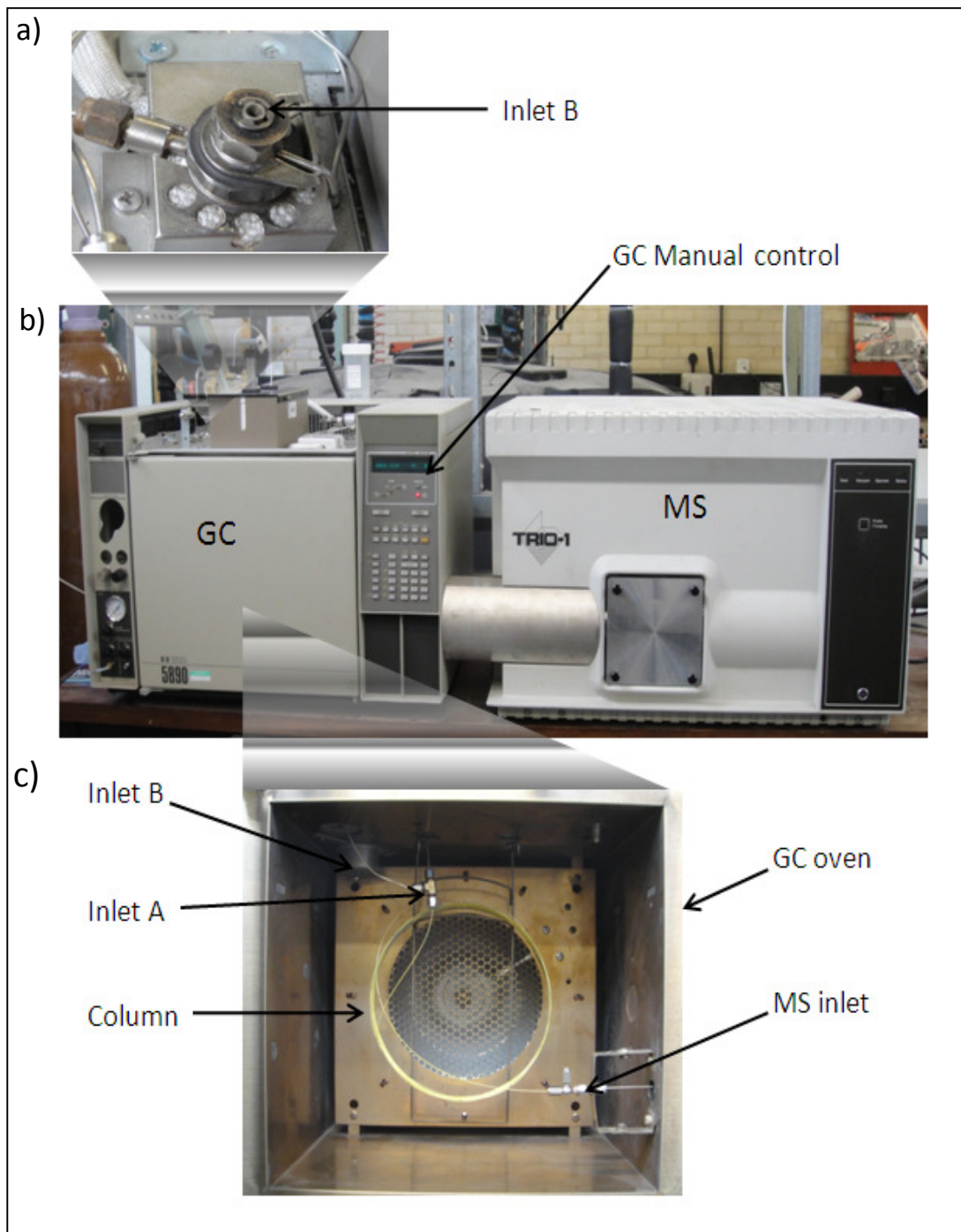


Figure 5.12: Picture of the Gas-Chromatography- Mass Spectrometer showing, a) Inlet B for liquid sample injection; b) the overall set up of the GC and the MS; c) GC oven showing the column, inlet A and inlet B for gaseous and liquid column installation respectively, and the MS inlet where the column is connected to the MS.

5.5.2.1. GC-MS configuration for liquid analysis

As mentioned in the introduction, the GC-MS can only analyse either liquids or gases at one time. This is mainly due to the requirement of different column specifications, as well as the use of high temperature inlet to vaporize liquid samples before entering the column. Hence, the main modification is the installation of an appropriate column to measure liquid hydrocarbons. The column chosen for our purpose is the DB5-MS (60 m, operating inlet pressure 14 – 15 bar), which allows us to analyse compounds consisting of up to 38 carbon atoms. To improve the resolution of retention time, the oven temperature was programmed as follows:

Initial temperature: 50 °C for 2 minutes

50 – 300 °C at the rate of 6 °C/min

Final temperature: 300 °C for 25 minutes

1 µl of sample is injected under the splitless injection conditions. After finishing the analysis of the sample, the GC was purged repeatedly running without injection of any sample to ensure that no residue liquid was trapped in the column.

5.5.2.2. Liquid hydrocarbon characterization

After sample analysis by the GC-MS instrument, a result is obtained in the form of a chromatogram. Figure 5.13 a) shows the chromatogram obtained by analysing C7 to C40 saturated alkanes standard, purchased from Supelco (1000 µg/mL each component in hexane), see Table 5.1. Each peak represents a compound, starting at C7 up to C19 (above C19 cannot be seen due to the chosen configuration of the method). Figure 5.13 b) shows a zoomed in peak of C14 compound, where the peak is integrated to measure the size (the programme measures the size of the peak by comparing it to the total size of other peaks). The spectrum in Figure 5.13 b) shows the ions that were recorded by the MS representing the peak, each group of compounds have distinctive ions, for example:

- Alkenes: 55, 69, 83;
- Alkanes: 57, 71, 85;
- Aromatic compounds: 105, 119.

Within these groups, the different compounds would have further distinctive ions, for example naphthalene: 128, 142, 156, 170, 184, 198. MassLab software has a compound to ion library installed, which using the specific ions automatically identifies the unknown compound. This method of compound identification applies to both liquid and gaseous sample analysis. The C7 – C40 known standard is analysed by the GC-MS before the analysis of the test samples, as mentioned above this provides the information of the carbon range of each carbon compound with different carbon number. This will allow a quick determination of the carbon range of the unknown sample composition.

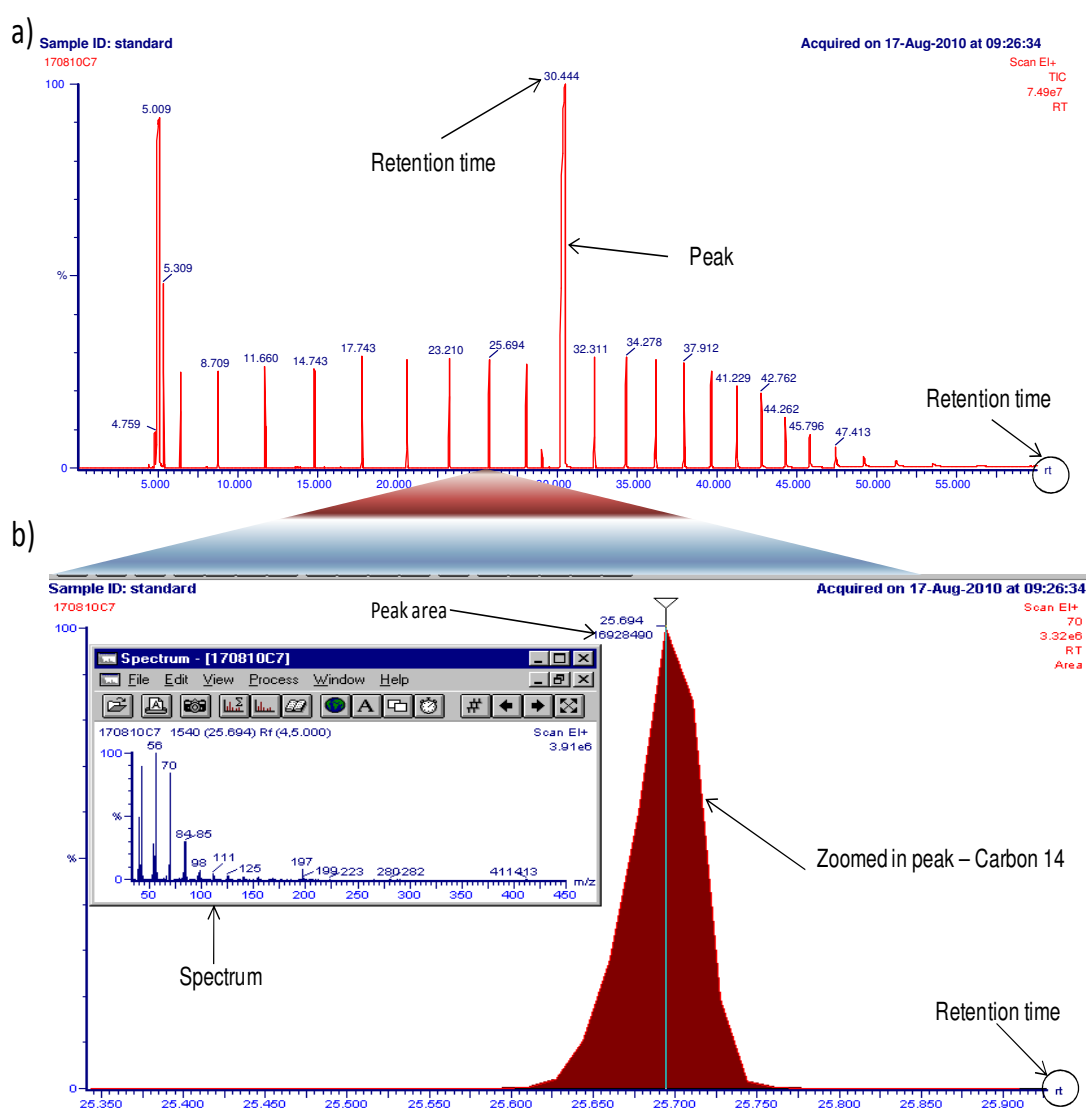


Figure 5.13: Chromatogram obtained from C7-C40 standard analysis by the GC-MS instrument; a) the chromatogram shows the peaks and the retention times of compounds with different number of carbon atoms; b) zoomed in view of the carbon 14 peak showing the area and the spectrum of the peak.

Table 5.1: Liquid C7 – C40 standard specification; shows the components and their nominal and certified concentrations.

Component	Nominal Concentration (µg/ml)	Certified concentration (+/- 0.5 %)
Heptatriacontane	1000	924
N-Decane	1000	986
N-Docosane	1000	1021
N-Dodecane	1000	990
N-Dotriacontane	1000	931
N-Eicosane	1000	1014
N-Heneicosane	1000	1016
N-Hentriacontane	1000	969
N-Heptacosane	1000	1023
N-Heptadecane	1000	1004
N-Heptane	1000	984
N-Hexacosane	1000	1018
N-Hexadecane	1000	1001
N-Hexatriacontane	1000	931
N-Nonacosane	1000	979
N-Nonadecane	1000	1014
N-Nonane	1000	990
N-Octacosane	1000	1008
N-Octadecane	1000	1028
N-Octane	1000	988
N-Pentacosane	1000	1001
N-Pentadecane	1000	999
N-Pentatriacontane	1000	938
N-Tetracontane	1000	978
N-Tetracosane	1000	1004
N-Tetradecane	1000	999
N-Tetratriacontane	1000	934
N-Triacontane	1000	973
N-Tricosane	1000	993
N-Tridecane	1000	992
N-Tritriacontane	1000	944
N-Undecane	1000	992
Nonatriacontane	1000	905
Octatriacontane	1000	967
Hexane	Solvent	Solvent

5.5.2.3. GC-MS configuration for gas analysis

The column used for testing is a capillary tube (Chromopack Poraplot Q type porous polymer) with 0.32 mm ID, 10 µm film thickness, and 30 metres length. This type of column is well suited for C1 – C6 hydrocarbons, ketones, solvents and alcohols. For gases of high concentrations (up to 50 %) a 100 µl injector loop is used. The split is set to 100 ml/min to ensure no over-saturation occurs whilst achieving high peak resolution. The GC oven temperature is programmed as follows:

Initial temperature: 50 °C for 2 minutes

50 – 220 °C at the rate of 10 °C/min

Final temperature: 220 °C for 10 minutes

The MS is tuned using the MassLab Tune page according to the concentrations of the compounds measured to achieve the best resolution. Tune conditions for measuring high concentration of gasses up to 50 % are set as follows:

Repeller:	1	LM Resolution:	12.5
Emission:	100	HM Resolution:	12.9
Lens 1:	21	Electron Energy:	70
Lens 2:	12	Ion energy:	2.0
Lens 3:	205	Electron Ramp:	1
Lens 4:	21	Detector:	350

The full scan acquisition method to determine the scan parameters is set on the MassLab software as follows:

Start mass:	15	Inter-scan Delay:	0.5 s
Finish mass:	300	Start retention:	0 min
Scan Time:	1.00 s	Finish Retention:	30 min

Gastight Hamilton Syringe (1000 Series Gastight, TLL - PTFE luer lock, 5ml) is used to take 3ml of gaseous sample from the plasma unit. The syringe is capped until the sample is injected into the GC-MS. After finishing the analysis of the gas sample,

the GC is purged by repeatedly running without the injection of sample to ensure that no residue gas was trapped in the column.

5.5.2.4. Gaseous hydrocarbon characterization

i. Propane and methane quantification and conversion calculations

The principle of gaseous sample analysis using MassLab is the same as described for liquids in section 5.5.2.2. The GC-MS was calibrated for propane and methane measurements in the range of 30 – 50%, described in section 5.6.2 (5 and 6). The calibration curve equation is then used to calculate the percentage by volume of propane in the sample. For the gas phase compounds, the percent by volume of a given gas is on a mole per mole basis, referring to the amount of moles of the compound per 100 moles total (Hites, 2007). Dividing the percentage value of the compound by a 100 would give a fraction of moles of the compound in question, normally referred to as the fractional form of mole-part per total moles:

$$F = \frac{i_{\%}}{100} \quad (5.1)$$

where

F fractional part of mole parts per total moles

$i_{\%}$ percentage of a compound i

At an average room temperature of 296 K, one mole of ideal gas occupies 24.3 litres at standard pressure of 101.3 kPa, calculated using the ideal gas law (Kotz et al., 2009):

$$pv = n_i RT \quad (5.2)$$

where

p pressure (kPa)

n_i moles of a compound i

v volume the gas occupies (L)

T temperature (K)

R universal gas constant (8.3145 J/mol K)

Hence, the moles of the compound in question equals to:

$$n_i = \frac{F}{24.3} \quad (5.3)$$

where

n_i moles of the compound i measured by the GC

A gaseous sample is collected and tested to measure propane concentration by the GC-MS before and after the experiments to determine the conversion of propane. Equation (5.3) is used to calculate the moles of propane in and out of the system. Propane conversion is then calculated using the equation (4.1):

$$X_i (\%) = \frac{n_{in} - n_{out}}{n_{in}} \times 100$$

ii. *Quantification of C₁-C₂ hydrocarbons*

A certified standard gas (BOC gases) was used as a reference gas for retention time and quantification of all other compounds, Table 5.2 shows the compounds and their concentrations, and Figure 5.14 shows the chromatogram and the retention times. Compounds are identified as described in 5.5.2.2 and quantified using the reference value of the gas with certified concentration:

$$i_{\%} = \frac{A_{Test}}{A_{ref}} \times i_{ref} \quad (5.4)$$

where

$i_{\%}$ compound concentration in percentage

A_{Test} peak area of the compound in the test sample

A_{ref} peak area of the compound in the reference gas

i_{ref} certified concentration of the reference compound (%)

Table 5.2: Standard gas specification; shows the components and their nominal and certified concentrations.

Component	Nominal Concentration (%)	Certified concentration
Benzene	0.0500	0.0502 +/- 0.0011
Butadiene 1,3-	0.0500	0.0502 +/- 0.0011
Butane n-	0.0500	0.0500 +/- 0.0011
Butene 1-	0.0500	0.0500 +/- 0.0010
Cyclopropane	0.0500	0.0484 +/- 0.0010
Ethane	0.0500	0.0503 +/- 0.0011
Ethylene	0.0500	0.0522 +/- 0.0011
Hexane n-	0.0500	0.0504 +/- 0.0011
Hexene 1-	0.0500	0.0460 +/- 0.0014
Methane	0.0500	0.0506 +/- 0.0011
Pentane n-	0.0500	0.0498 +/- 0.0010
Pentene 1-	0.0500	0.0503 +/- 0.0011
Propane	0.0500	0.0503 +/- 0.0011
Propylene	0.0500	0.0495 +/- 0.0010
Nitrogen	Balance	

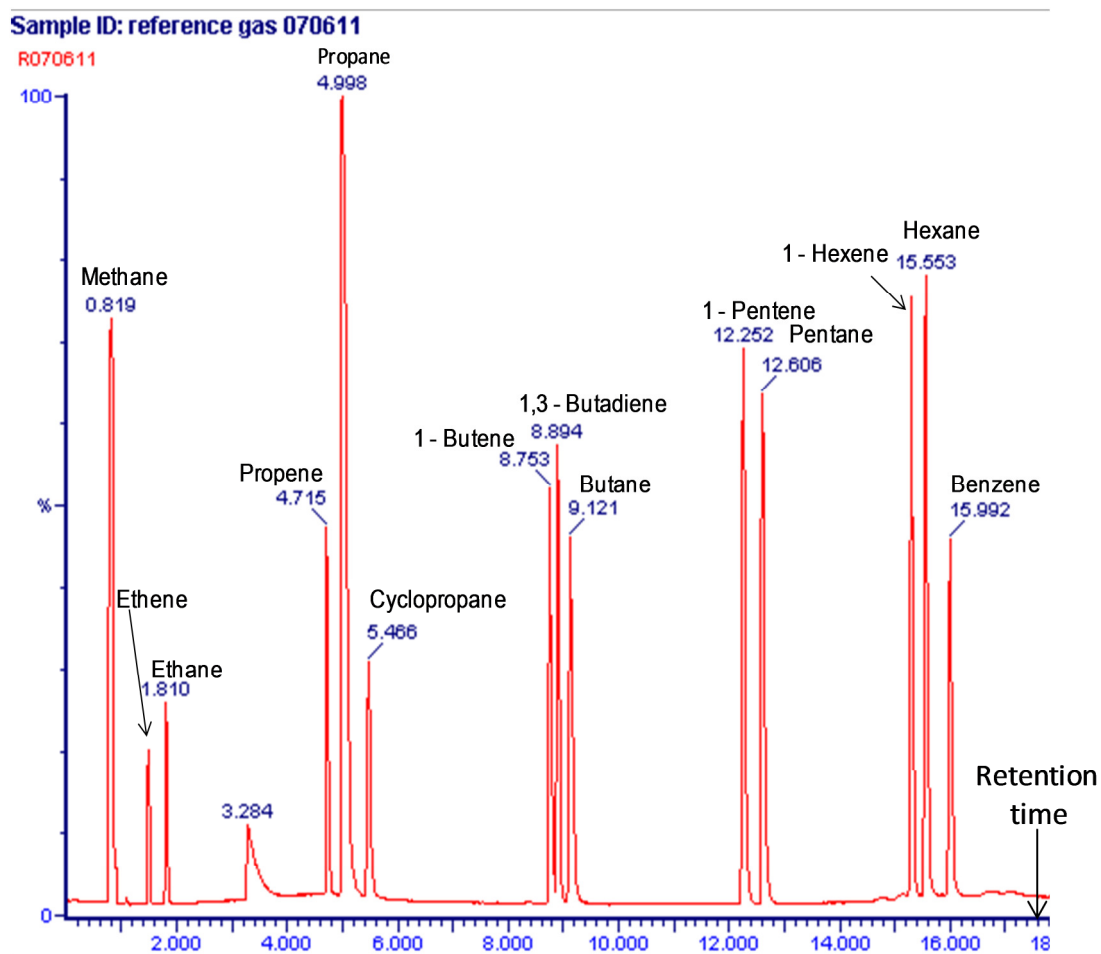


Figure 5.14: Mass Spectrum of the standard gas, showing the retention time for each compound.

Once the compound percentage by volume is calculated, equations (5.1) and (5.3) can be used to calculate the moles of the compound generated. As described in section 5.5.2.2, compounds can be identified using the ion-compound library installed on MassLab software. However, for compounds that are not present in standard gas mixture, the values extracted are in arbitrary units, i.e. the measured areas of the peaks on the chromatograms. Arbitrary units do not give enough information to quantify the compounds. However, they can be used for comparison of compound behaviour and appearance between the samples and the sets.

5.5.3. Chromopack CP9001 GC

After each experiment, 2.5 ml of the gaseous sample is collected in a separate gastight syringe with PTFE luer Lock (Hamilton, 81520), which allows accurate sample injection into the GC instrumentation for hydrogen measurement. The syringe is capped to prevent contamination. The gas-chromatography instrument used is Chromopack CP9001 GC and has been set up specifically for hydrogen analysis. Nitrogen gas was selected as a carrier gas for this study at the flow rate of 13 ml/min. Thermal Conductivity Detector (TCD) is used for hydrogen measurement, where the detection mechanism is based on the measurement of the difference in thermal conductivity of the pure carrier gas and the carrier gas/sample component mixture. The TCD has a reference cell, through which pure carrier gas flows, and a measuring cell through which the carrier gas/sample component mixture flows. The PicoLog data logger records the mV signals received from the detector which are used to create the chromatogram. OriginPro programme is used to integrate the peak areas from obtained signals.

5.5.3.1. GC configuration for hydrogen measurement

The column chosen for hydrogen measurement is the Molecular Sieve 5A, 60 – 80 mesh. The GC temperatures are constant and are set as follows:

Oven temperature:	100 °C
Det temperature:	250 °C
Column limit:	250 °C

The main TCD setting is the range of the detector (X.Y), which includes the attenuation (X) defining the range of sensitivity to certain concentrations of hydrogen, and the polarity (Y). Polarity can be either normal (Y = 0) or reversed (denoted Y = 2). The attenuation can be in the range of 1 – 16, with 1 for the lowest concentrations of hydrogen and 16 for the highest to prevent oversaturation. The instrument was set for hydrogen measurements in the range of 0 – 30 %, with parameters as follows:

Range: 3.2
 Attenuation: 16

5.5.3.2. Hydrogen quantification

PicoLog data logger records the mV signals from the detector in the form of a table. These signals are then transferred to the OriginPro programme creating a chromatogram and calculating the area of the peak, see Figure 5.15.

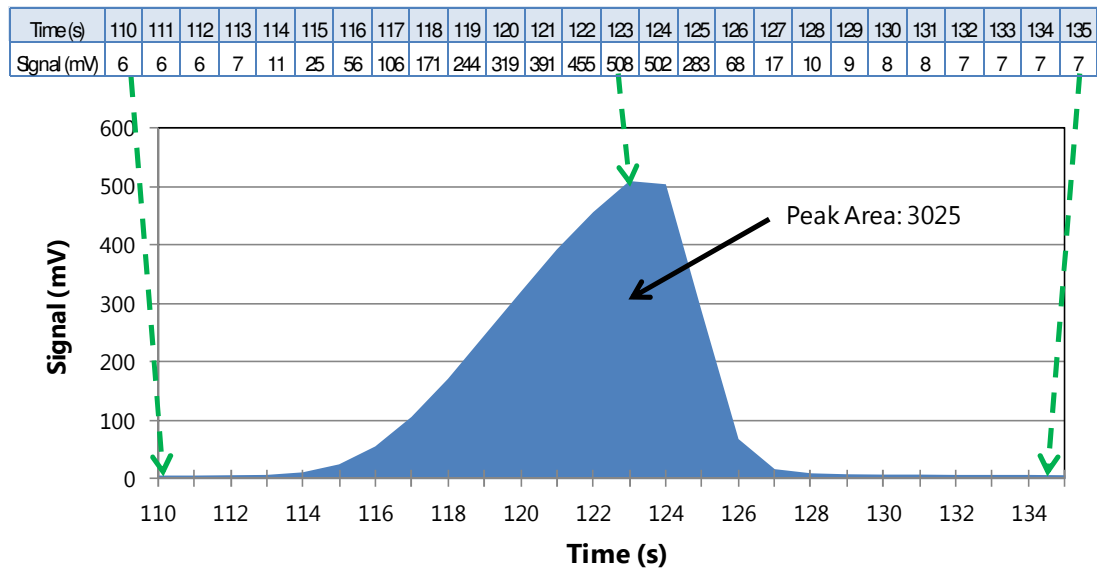


Figure 5.15: Shows a table generated by the data logger used to create a chromatogram and calculate the peak area; in this example the 10 % test sample is shown.

The instrument is calibrated in the range of 5 – 30 % described in section 5.6.2 (4). To calculate hydrogen percentage by volume, the peak area is calculated and inserted

into the formulae obtained from the calibration. Then equations (5.1) and (5.3) can be used to calculate moles of hydrogen generated and, hence, the selectivity towards hydrogen for propane (Horng et al., 2009):

$$S_{H_2}(\%) = \frac{2}{8} \times \frac{n_{H_2}}{\dot{n}_{C_3H_8}} \times 100 \quad (5.5)$$

where

S_{H_2} hydrogen selectivity

n_{H_2} moles of product hydrogen

$\dot{n}_{C_3H_8}$ moles of propane converted

Formulae (4.2), described in Chapter 4 section 2 is used for calculating hydrogen selectivity from methane:

$$S_{H_2}(\%) = \frac{n_{H_2}}{2 \times \dot{n}_{CH_4}} \times 100$$

5.5.4. Energy conversion efficiency calculations

Decomposition and reforming reactions of methane and propane are processes of energy conversion. Therefore, Tao et al. (2011) defined the energy conversion efficiency (ECE) for methane partial oxidation to syngas as:

$$ECE = \frac{n_{H_2} \times LHV_{H_2} + n_{CO} \times LHV_{CO}}{P + \dot{n}_{CH_4} \times LHV_{CH_4}} \quad (5.6)$$

where

n_{H_2} moles of product hydrogen

\dot{n}_{CH_4} moles of methane converted

LHV_i lower heating value of a compound i (kJ/mol), higher heating value can also be used

P input power in plasma (kW)

In this work a 3.14 M Ω in house built resistor was used to stabilize the plasma. Therefore, the discharge voltage is lower than the input voltage due to the voltage drop at the resistor. Hence, for calculations system input power is defined as P and

discharge power is defined as P_D , with the efficiencies defined as energy conversion efficiency of the system (ECE) and energy conversion efficiency of the plasma discharge (ECED).

Formulae (5.6) can be adapted for the ECE of methane decomposition without oxygen species using higher heating values as follows:

$$ECE_{CH_4} = \frac{n_{H_2} \times HHV_{H_2}}{P + \dot{n}_{CH_4} \times HHV_{CH_4}} \quad (5.7)$$

where

ECE_{CH_4} energy conversion efficiency of methane

P power in (W)

HHV_{H_2} 141.80 MJ/kg

HHV_{CH_4} 55.50 MJ/kg

The energy conversion efficiency for propane can then be defined as:

$$ECE_{C_3H_8} = \frac{n_{H_2} \times HHV_{H_2}}{P + \dot{n}_{C_3H_8} \times HHV_{C_3H_8}} \quad (5.8)$$

where

$ECE_{C_3H_8}$ energy conversion efficiency of propane

P power in (W)

$\dot{n}_{C_3H_8}$ moles of propane converted

$HHV_{C_3H_8}$ 50.35 MJ/kg

ECED values for methane ($ECED_{CH_4}$) and propane ($ECED_{C_3H_8}$) are calculated as above (formulae 5.7 and 5.8 respectively) using the value of P_D instead of P .

5.6. Calibration and uncertainty analysis

5.6.1. General theory

The total experimental error is the sum of the bias error and the precision error. Bias error is the fixed, constant, systematic component of the total error. It can be grouped into calibration error (bias in a measuring standard), data acquisition error and data reduction error. The combined bias error is calculated as a root-sum-square (RSS) combination of the above elemental bias errors. Bias error can be reduced by a calibration, but only to the limit of the bias error associated with the standard used in the calibration procedure. Precision error, on the other hand, is random and can be referred to as repeatability error. Precision error follows the Gaussian distribution, and can be reduced by increasing the number of measurements. Coleman and Steele (1999) proposed 95 % confidence level to calculate the random uncertainty of a measured variable X as follows:

$$u_{random} = t_{95\%} S_X \quad (5.9)$$

$$S_X = \sqrt{\frac{1}{N-1} \sum_{i=1}^N (X_i - \bar{X})^2} \quad (5.10)$$

$$\bar{X} = \frac{1}{N} \sum_{i=1}^N X_i \quad (5.11)$$

where $t_{95\%}$ is the value from the t distribution that achieves 95 % confidence level, S_X is the standard deviation of the sample population and \bar{X} is the mean value.

According to the ISO guide (1993) cited in Coleman and Steele (1999), the overall uncertainty (U) of a measured variable is given as:

$$U = t_{95\%} u_c \quad (5.12)$$

where u_c is the combined uncertainty (bias and precision):

$$u_c = \sqrt{S_{BX}^2 + S_X^2} \quad (5.13)$$

where S_{BX} is the standard deviation of the systematic uncertainty (B_X) given as:

$$S_{BX} = B_X / 2 \tag{5.14}$$

Considering a general case, an experimental result, r , is a function of the measured variables X (Coleman and Steele, 1999):

$$r = r(X_1, X_2, \dots, X_j) \tag{5.15}$$

Then the uncertainty of r can be calculated from the following equations:

$$U_r^2 = \left(\frac{\partial r}{\partial X_1}\right)^2 U_{X_1}^2 + \left(\frac{\partial r}{\partial X_2}\right)^2 U_{X_2}^2 + \dots + \left(\frac{\partial r}{\partial X_j}\right)^2 U_{X_j}^2 \tag{5.16}$$

Can also be written in a dimensionless form given to give the relative uncertainty:

$$\frac{U_r^2}{r^2} = \left(\frac{X_1}{r} \frac{\partial r}{\partial X_1}\right)^2 \left(\frac{U_{X_1}}{X_1}\right)^2 + \left(\frac{X_2}{r} \frac{\partial r}{\partial X_2}\right)^2 \left(\frac{U_{X_2}}{X_2}\right)^2 + \dots + \left(\frac{X_j}{r} \frac{\partial r}{\partial X_j}\right)^2 \left(\frac{U_{X_j}}{X_j}\right)^2 \tag{5.17}$$

5.6.2. Calibration process and error analysis

(1) Pressure transducer

The pressure transducers convert pressure into analogue electronic signal accepted by the data logger in mV. The voltage output for the pressure transducer ranges from 1 – 5 V. Hence, terminal board is fitted to convert 0 – 5 V pressure transducer output to 0 – 50 mV input into the data logger. The data logger exports digital signals to a computer, in which the pressures are monitored and recorded by PicoLog software.

The pressure transducer has been calibrated by LabCal Ltd (accredited UKAS calibration, certificate number K25231P), in the range of -1 to 1 bar (g). The accuracy of the applied pressure for the instrument used is $\pm 0.01 \%$ plus the resolution of the instrument of ± 0.0002 bar. The maximum resolution error is 0.1% , see Table 5.3. Hence, the total calibration standard accuracy is 0.11% . The output signals were compared with the applied pressure and best fit equation was produced for the transducer, see Table 5.3 and Figure 5.16. The combined uncertainty of the

pressures is calculated using the root-sum-square (RSS) combination of the elemental systematic errors, see Table 5.4.

Table 5.3: The calibration data for the pressure transducer; including the calculated resolution error of the calibration standard.

Applied pressure		Indicated pressure bar (g)	Measured voltage	Error (bar/ %)	Resolution error (bar/%)
bar (g)	kPa				
-0.9889	-98.89	-0.9890	1	0.01	-0.02
-0.5896	-58.96	-0.5897	2	0.02	-0.03
-0.1917	-19.17	-0.1918	3	0.05	-0.10
0.2065	20.65	0.2065	4	0	0.10
0.6052	60.52	0.6054	5	0.03	0.03

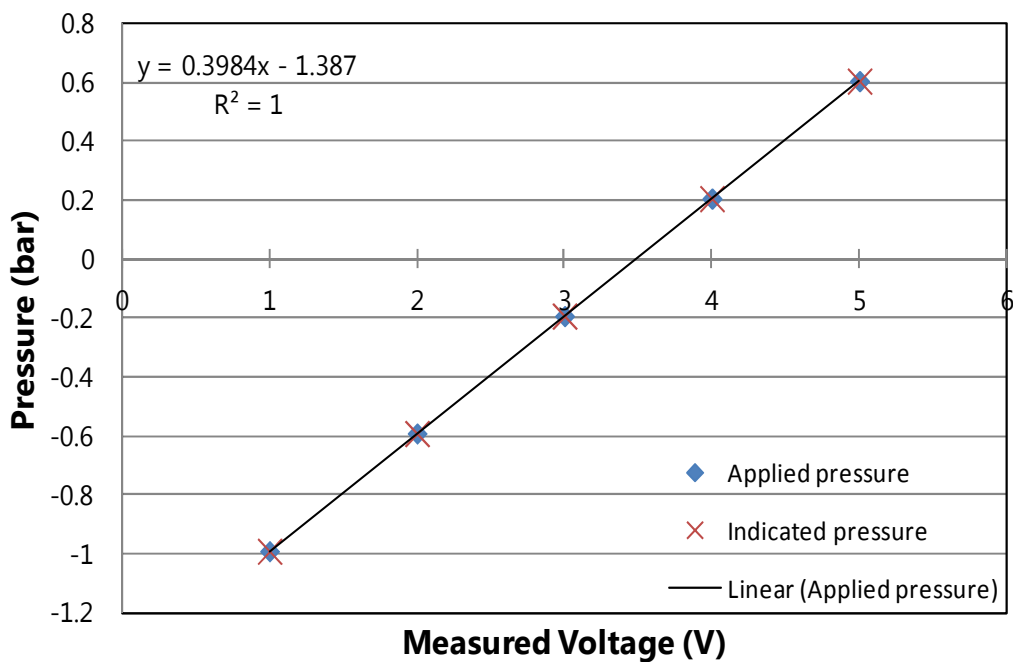


Figure 5.16: Pressure vs voltage calibration for the pressure transducer; shows the best fit equation.

Table 5.4: Combined uncertainty of the pressure measurement.

Elements	Calibration standard	Calibration equation	Data logger	Combined uncertainty
Systematic error	0.11 %	0.05 %	0.21 %	0.24 %

(2) Thermocouple

Thermocouples convert temperature difference into a voltage difference, which is then converted into the temperature by the data logger. A type K thermocouple was used in this work, which was calibrated using a precision thermometer (F250 Mr11, ± 0.01 K). The thermocouple and the precision thermometer were both placed in an insulated bath of cold water. Temperature change was achieved by adding hot water to the bath and mixing thoroughly. At each change point, a temperature reading from the precision thermometer and the data logger (connected to the thermocouple) were recorded, see Table 5.5 and Figure 5.17. The combined uncertainty of the temperatures is RSS combination of the calibration standard (0.01 K) and the maximum error of the best fit equation (0.42 K), totalling to 0.42 K.

Table 5.5: The calibration data for the thermocouple.

Precision thermometer reading (°C)	Data logger reading (°C)	Error (K)
16.82	17.24	0.42
18.93	19.32	0.39
20.85	21.23	0.38
22.75	23.13	0.38
24.52	24.84	0.32
26.2	26.47	0.27
27.9	28.12	0.22
29.36	29.57	0.21
30.8	30.97	0.17
32.26	32.41	0.15
33.59	33.71	0.12
34.86	34.94	0.08
36.04	36.09	0.05
37.24	37.28	0.04
39.44	39.44	0
40.56	40.56	0
41.62	41.6	-0.02
42.45	42.42	-0.03
44.61	44.56	-0.05
46.39	46.32	-0.07
48.41	48.33	-0.08
50.26	50.15	-0.11

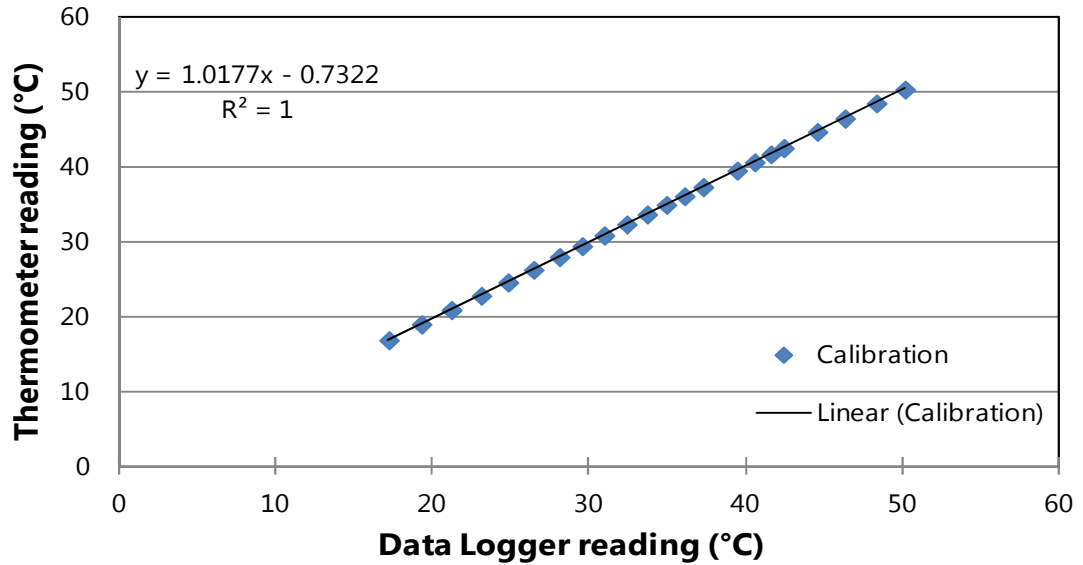


Figure 5.17: Thermocouple calibration data; shows the best fit equation.

(3) Power input

High voltage was applied to the active electrode from a HV generator (Matsusada, AU-30R5-L) through a 3.14 M Ω in house built resistor. The applied voltage and current were recorded from the display of the generator, the accuracy of which is 1 % of the maximum output (Matsusada), equalling to 0.3 kV and 0.05 mA (maximum output 30 kV, 5 mA). The maximum error (%) is at the lowest voltage (14 kV) and current (1 mA) used, equalling to 2.14 % and 5 % respectively, see Table 5.6.

Table 5.6: Voltage and current error (%) at different inputs.

Voltage (kV)	Voltage Error (%)	Current (mA)	Current Error (%)
10	3	0.5	10
11	2.72	1	5
12	2.5	1.5	3.33
13	2.30	2	2.5
14	2.14	2.5	2
15	2	3	1.66
16	1.87	3.5	1.42
17	1.76	4	1.25
18	1.66	4.5	1.11
19	1.57	5	1
20	1.5		
21	1.42		
22	1.36		
23	1.30		
24	1.25		
25	1.2		

The total power input is calculated using the formulae:

$$P = IV \quad (5.18)$$

where

P power input in watts

I current in amps

V voltage in volts

Therefore, the general uncertainty analysis expression becomes:

$$U_P^2 = \left(\frac{\partial P}{\partial I}\right)^2 U_I^2 + \left(\frac{\partial P}{\partial V}\right)^2 U_V^2 \quad (5.19)$$

The partial derivatives in this case are:

$$\frac{P}{I} = V$$

$$\frac{P}{V} = I$$

Substituting back into the general uncertainty analysis expression:

$$U_P^2 = (V)^2 U_I^2 + (I)^2 U_V^2 \quad (5.20)$$

Simplification of the algebraic expression can be achieved by dividing the equation by the square root of the experimental result:

$$\left(\frac{U_P}{P}\right)^2 = \left(\frac{U_I}{I}\right)^2 + \left(\frac{U_V}{V}\right)^2 \quad (5.21)$$

where

$$\frac{U_I}{I} = 1-5$$

$$\frac{U_V}{V} = 1.2 - 2.14$$

Therefore the uncertainty range of the power input is:

$$\frac{U_P}{P} = \left[(1)^2 + (1.2)^2 \right]^{1/2} \quad (5.22)$$

$$\frac{U_P}{P} = \left[(5)^2 + (2.14)^2 \right]^{1/2}$$

= 1.56 – 5.44% for 125 – 14 W respectively

A 3.14 MΩ in house built resistor, measured with 0.5 % accuracy, was used to stabilize the plasma. Therefore, the discharge power (W) is calculated using the formulae:

$$P_D = I(V - IO) \quad (5.23)$$

where

P_D discharge power (W)

O resistance (ohms)

The general uncertainty analysis expression becomes:

$$U_{P_D}^2 = 2 \left(\frac{\partial P_D}{\partial I} \right)^2 U_I^2 + \left(\frac{\partial P_D}{\partial V} \right)^2 U_V^2 + \left(\frac{\partial P_D}{\partial O} \right)^2 U_R^2 \quad (5.24)$$

The partial derivatives in this case are:

$$\frac{P_D}{I} = V - IO$$

$$\frac{P_D}{V} = \frac{I(V - IO)}{V}$$

$$\frac{P_D}{O} = \frac{I(V - IO)}{O}$$

Substituting back into the general uncertainty analysis expression:

$$U_{P_D}^2 = 2(V - IO)^2 U_I^2 + \left(\frac{I(V - IO)}{V} \right)^2 U_V^2 + \left(\frac{I(V - IO)}{O} \right)^2 U_O^2 \quad (5.25)$$

Simplification of the algebraic expression can be achieved by dividing the equation by the square root of the experimental result:

$$\left(\frac{U_{P_D}}{P_D} \right)^2 = 2 \left(\frac{U_I}{I} \right)^2 + \left(\frac{U_V}{V} \right)^2 + \left(\frac{U_O}{O} \right)^2 \quad (5.26)$$

where

$$\frac{U_I}{I} = 1 - 5$$

$$\frac{U_V}{V} = 1.2 - 2.14$$

$$\frac{U_O}{O} = 0.5$$

Therefore the uncertainty range of discharge power is:

$$\frac{U_{P_D}}{P_D} = \left[2(1)^2 + (0.5)^2 + (1.2)^2 \right]^{1/2} \quad (5.27)$$

$$\frac{U_{P_D}}{P_D} = \left[2(5)^2 + (0.5)^2 + (2.14)^2 \right]^{1/2}$$

= 1.92 – 7.40% for 46.5 – 10.86 W respectively

(4) Hydrogen quantification

Standard gasses (supplied by BOC) at 10, 20 and 30 % hydrogen concentration in nitrogen, at Beta certification with the accuracy of ± 2 %, were used to calibrate the GC Chromopack. Two readings were recorded for each of the concentrations to determine the repeatability (or calibration equation) error, see Table 5.7 and Figure 5.18.

Table 5.7: The calibration data for the GC Chromopack.

Hydrogen Concentration (%)	10	20	30
Reading 1	3025.84	5768.14	8896.95
Reading 2	3010.69	5748.33	8883.97
Average	3025.84	5758.23	8890.46
Repeatability error (%)	0.50	0.34	0.15

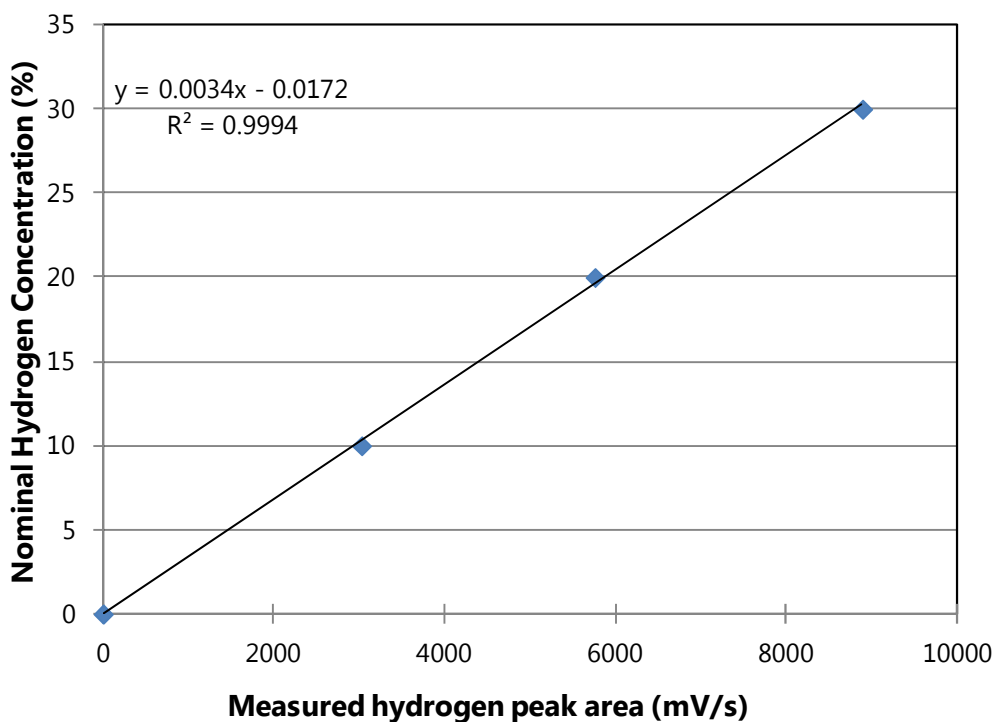


Figure 5.18: The best fit equation for the hydrogen measurement calibration data for the range of 0 – 30 %.

The combined uncertainty for hydrogen measurement is RSS combination of the calibration standard ($\pm 2\%$) and the maximum error of the best fit equation ($\pm 0.5\%$), resulting in the combined uncertainty of $\pm 2.06\%$ of the reading value.

(5) Propane quantification

Standard gasses (supplied by BOC) at 30, 40 and 50 % propane concentration in nitrogen, at Beta certification with the accuracy of $\pm 2\%$, were used to calibrate the GC-MS. Two readings were recorded for each of the concentrations to determine the repeatability (or calibration equation) error, see Table 5.8 and Figure 5.19.

Table 5.8: Propane calibration data for the GC-MS.

Propane Concentration (%)	30	40	50
Reading 1	251878752	332658560	407523744
Reading 2	251114144	331385472	405183744
Average	251878752	332658560	406353744
Repeatability error (%)	0.30	0.38	0.58

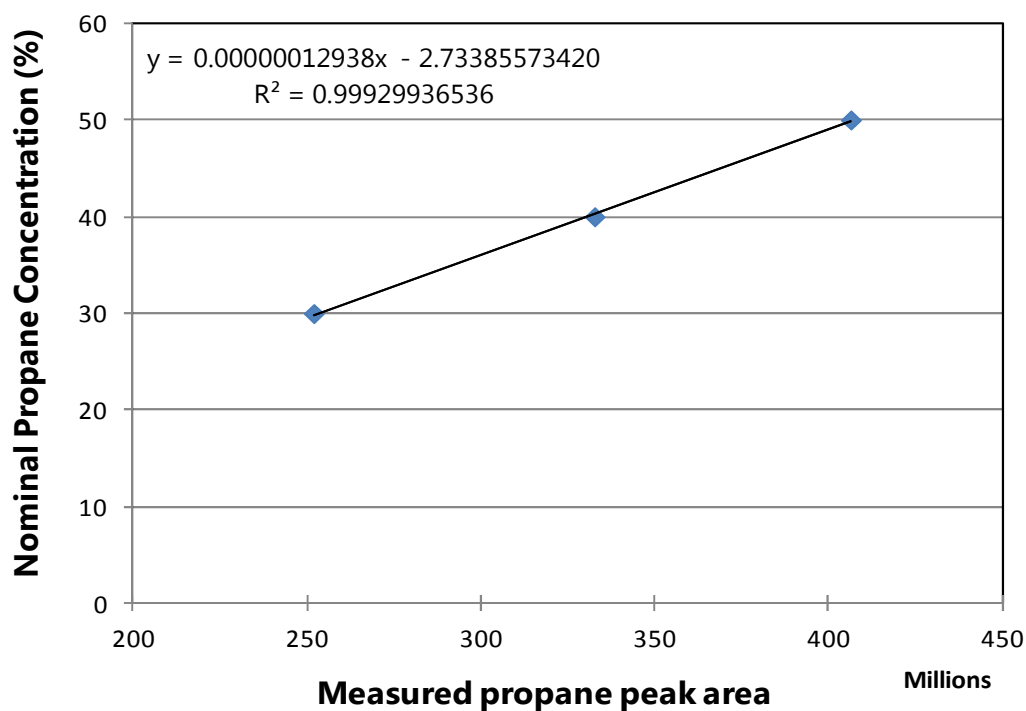


Figure 5.19: The best fit equation for the propane measurement calibration data.

The combined uncertainty for propane measurement is RSS combination of the calibration standard ($\pm 2\%$) and the maximum error of the best fit equation ($\pm 0.58\%$), resulting in the combined uncertainty of $\pm 2.08\%$ of the reading value.

(6) Methane quantification

Standard gasses (supplied by BOC) at 30, 40 and 50 % methane concentration in nitrogen, at Beta certification with the accuracy of $\pm 2\%$, were used to calibrate the GC-MS. Two readings were recorded for each of the concentrations to determine the repeatability (or calibration equation) error, see Table 5.9 and Figure 5.20.

Table 5.9: Methane calibration data for the GC-MS.

Methane Concentration (%)	30	40	50
Reading 1	14547923	17029230	19409254
Reading 2	13828400	16486217	18602834
Average	14188161.5	16757723.5	19006044
Repeatability error (%)	5.0	3.2	4.2

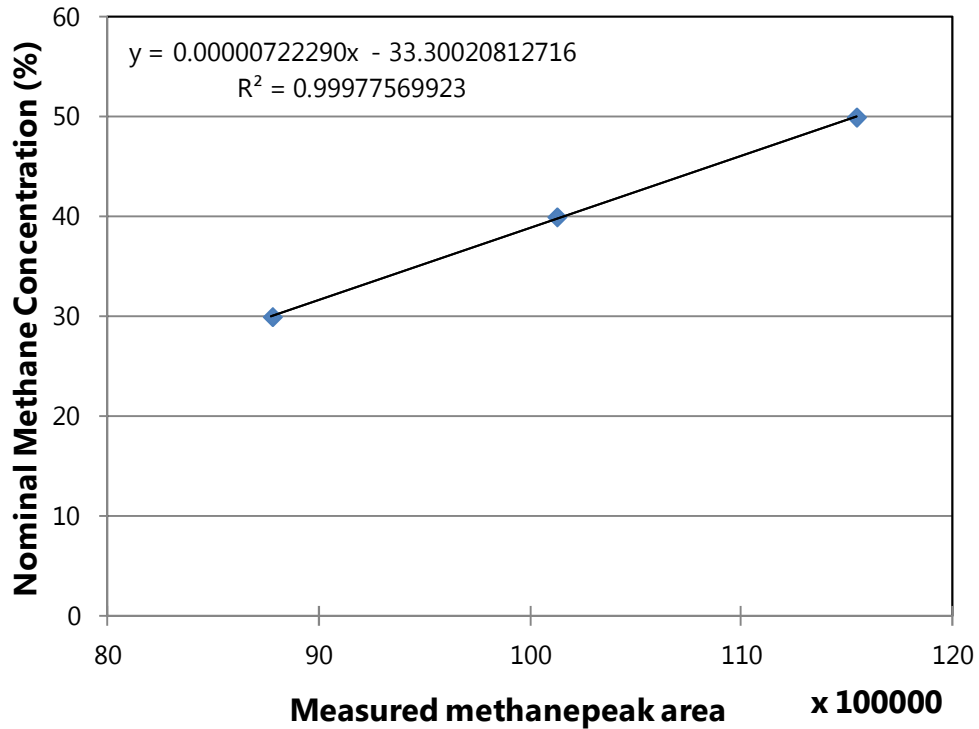


Figure 5.20: The best fit equation for the methane measurement calibration data.

The combined uncertainty for methane measurement is RSS combination of the calibration standard ($\pm 2\%$) and the maximum error of the best fit equation ($\pm 5\%$), resulting in the combined uncertainty of $\pm 5.39\%$

(7) Propane conversion, hydrogen selectivity and energy conversion efficiency

Propane conversion is calculated using the formulae:

$$\dot{n}_{C_3H_8} = n_{C_3H_8_{in}} - n_{C_3H_8_{out}} \quad (5.28)$$

where

$\dot{n}_{C_3H_8}$ propane conversion (moles)

$n_{C_3H_8_{in}}$ propane input into the system (moles)

$n_{C_3H_8_{out}}$ propane left after the reaction (moles)

The uncertainty in propane quantification is 2.08 %. Therefore, the absolute uncertainty in propane conversion can be calculated according to Eq. (5.16) as:

$$\frac{U_{\dot{n}_{C_3H_8}}}{\dot{n}_{C_3H_8}} = \sqrt{\left(\frac{U_{n_{C_3H_8_{in}}}}{n_{C_3H_8_{in}}}\right)^2 + \left(\frac{U_{n_{C_3H_8_{out}}}}{n_{C_3H_8_{out}}}\right)^2} = 2.94 \% \quad (5.29)$$

Hydrogen selectivity has been defined in section 5.4.3.2, formulae (5.5):

$$S_{H_2}(\%) = \frac{2}{8} \times \frac{n_{H_2}}{\dot{n}_{C_3H_8}} \times 100$$

The uncertainty in hydrogen quantification is 2.06 %. Therefore, the general uncertainty analysis expression becomes:

$$\frac{U_{S_{H_2}}}{S_{H_2}} = \sqrt{\left(\frac{U_{n_{H_2}}}{n_{H_2}}\right)^2 + \left(\frac{U_{\dot{n}_{C_3H_8}}}{\dot{n}_{C_3H_8}}\right)^2} = 3.59 \% \quad (5.30)$$

Energy conversion efficiency has been defined in section 5.5.4, formulae (5.8):

$$ECE_{C_3H_8} = \frac{n_{H_2} \times HHV_{H_2}}{P + \dot{n}_{C_3H_8} \times HHV_{C_3H_8}}$$

The uncertainties of propane conversion and hydrogen quantification are 2.94 % and 2.06 % respectively. Assuming there is no uncertainty in higher heating values, the absolute uncertainty in energy efficiency conversion of the system (ECE_I) can be calculated according to Eq. (5.16) as:

$$\frac{U_{ECE_{C_3H_8}}}{ECE_{C_3H_8}} = \sqrt{\left(\frac{U_{n_{H_2}}}{n_{H_2}}\right)^2 + \left(\frac{U_{\dot{n}_{C_3H_8}}}{\dot{n}_{C_3H_8}}\right)^2 + \left(\frac{U_P}{P}\right)^2} \quad (5.31)$$

= in the range of 3.91– 6.52 %

where $\frac{U_P}{P}$ is in the range of 1.56 – 5.44 % for 125 – 14 W power input respectively

And the absolute uncertainty in energy efficiency conversion of the discharge (ECED) can be calculated according to Eq. (5.16) as:

$$\frac{U_{ECED_{C_3H_8}}}{ECED_{C_3H_8}} = \sqrt{\left(\frac{U_{n_{H_2}}}{n_{H_2}}\right)^2 + \left(\frac{U_{\dot{n}_{C_3H_8}}}{\dot{n}_{C_3H_8}}\right)^2 + \left(\frac{U_{P_D}}{P_D}\right)^2} \quad (5.32)$$

= in the range of 4.07 – 8.22 %

where $\frac{U_{P_D}}{P_D}$ is in the range of 1.92 – 7.40 % for 46.5 – 10.86 W discharge power respectively

(8) Methane conversion, hydrogen selectivity and energy conversion efficiency

Methane conversion is calculated using the formulae:

$$\dot{n}_{CH_4} = n_{CH_4in} - n_{CH_4out} \quad (5.33)$$

where

- \dot{n}_{CH_4} methane conversion (moles)
- n_{CH_4in} methane input into the system (moles)
- n_{CH_4out} methane left after the reaction (moles)

The uncertainty in methane quantification is 5.39 %. Therefore, the absolute uncertainty in methane conversion can be calculated according to Eq. (5.16) as:

$$\frac{U_{\dot{n}_{CH_4}}}{\dot{n}_{CH_4}} = \sqrt{\left(\frac{U_{n_{CH_4in}}}{n_{CH_4in}}\right)^2 + \left(\frac{U_{n_{CH_4out}}}{n_{CH_4out}}\right)^2} = 7.61 \% \quad (5.34)$$

Hydrogen selectivity has been defined in Chapter 4, section 4.2, formulae (4.2):

$$S_{H_2}(\%) = \frac{1}{5} \times \frac{n_{H_2}}{\dot{n}_{CH_4}} \times 100$$

The uncertainty in hydrogen quantification is 2.06 %. Therefore, the general uncertainty analysis expression becomes:

$$\frac{U_{S_{H_2}}}{S_{H_2}} = \sqrt{\left(\frac{U_{n_{H_2}}}{n_{H_2}}\right)^2 + \left(\frac{U_{\dot{n}_{CH_4}}}{\dot{n}_{CH_4}}\right)^2} = 9.3 \% \quad (5.35)$$

Energy conversion efficiency has been defined in section 5.5.4, formulae (5.7):

$$ECE_{CH_4} = \frac{n_{H_2} \times HHV_{H_2}}{P + \dot{n}_{CH_4} \times HHV_{CH_4}}$$

The uncertainties of methane conversion and hydrogen quantification are 7.61 % and 2.06 % respectively. Assuming there is no uncertainty in higher heating values, the absolute uncertainty in energy efficiency conversion of the system (ECE_I) for methane can be calculated according to Eq. (5.16) as:

$$\frac{U_{ECE_{CH_4}}}{ECE_{CH_4}} = \sqrt{\left(\frac{U_{n_{H_2}}}{n_{H_2}}\right)^2 + \left(\frac{U_{\dot{n}_{CH_4}}}{\dot{n}_{CH_4}}\right)^2 + \left(\frac{U_P}{P}\right)^2} = \text{in the range of } 5.97 - 7.9 \% \quad (5.36)$$

where $\frac{U_P}{P}$ is in the range of 1.56 – 5.44 % for 125 – 14 W power input respectively

And the absolute uncertainty in energy efficiency conversion of methane of the discharge ($ECED$) can be calculated according to Eq. (5.16) as:

$$\frac{U_{ECED_{CH_4}}}{ECED_{CH_4}} = \sqrt{\left(\frac{U_{n_{H_2}}}{n_{H_2}}\right)^2 + \left(\frac{U_{\dot{n}_{CH_4}}}{\dot{n}_{CH_4}}\right)^2 + \left(\frac{U_{P_D}}{P_D}\right)^2} = \text{in the range of } 6.1 - 9.4 \% \quad (5.37)$$

where $\frac{U_{P_D}}{P_D}$ is in the range of 1.92 – 7.40 % 46.5 – 10.86 W discharge power respectively

(9) Uncertainty analysis summary

The uncertainty in each measured quantity and the calculated power input is summarized in Table 5.10.

Table 5.10: The uncertainty value in each measured parameter and calculated power input.

Parameter	Measuring instrument	Uncertainty
Inter-electrode distance	Vernier calliper	± 0.1 mm
DC voltage	Matsusada HV supply AU-30R5-L(220V)	± 0.3 kV (manufacturer)
DC current		± 0.05 mA (manufacturer)
Resistor	3.12 M Ω (in-house built)	± 0.5 % (Calibration)
Power Input	Calculation	Range from 1.56 – 5.44 %
Discharge power	Calculation	Range from 1.92 – 7.40 %
Pressure	Pressure transducer BTE6N01G1-FL	± 0.24 % (Calibration)
Temperature	K-Type Thermocouple	± 0.42 K (Calibration)
Hydrogen Measurement	Chromopack CP9001 GC	± 2.06 % (calibration)
Propane Measurement	HP5890 GC - Trio1 MS	± 2.08 % (calibration)
Propane conversion	Calculation	± 2.94 %
Hydrogen selectivity from propane	Calculation	± 3.59 %
$ECE_{C_3H_8}$	Calculation	Range from 3.91 – 6.52 %
$ECED_{C_3H_8}$	Calculation	Range from 4.07 – 8.22 %
Methane Measurement	HP5890 GC - Trio1 MS	± 5.39 % (calibration)
Methane conversion	Calculation	± 7.61 %
Hydrogen selectivity from methane	Calculation	± 9.3 %
ECE_{CH_4}	Calculation	Range from 5.97 – 7.9 %
$ECED_{CH_4}$	Calculation	Range from 6.1 – 9.4 %

5.7. Summary

The experimental rig is composed of three main facilities: plasma reactor, Trio GC-MS for characterization and quantification of hydrocarbons and the Chromopack CP9001 GC for hydrogen quantification. The plasma reactor is designed so that both liquid and gaseous hydrocarbons can be subjected to the corona discharge. The parameters such as temperature and pressure can be accurately monitored and recorded by the data logger for each experiment. The analysis system provides accurate measurement of gaseous and liquid hydrocarbon samples. The current experiments involve four parametric measurements, namely inter-electrode distance, pressure, temperature and power input. The analysis consists of hydrogen, propane and methane quantification, including measurement of other hydrocarbons in arbitrary units. All measuring instruments were carefully calibrated and the corresponding uncertainties are given and the propagated uncertainty analysis was conducted according to the standards in the deduced parameters.

Chapter 6: Experimental results for hexadecane cracking under corona discharge

6.1. Introduction

This chapter presents the rationale of the underlying theory and details of the experimental conditions for the experiments of hexadecane cracking under corona discharge. Experiments were performed to evaluate the ability of the positive corona for hexadecane cracking in air plasma, argon plasma and air/argon mixture plasma. The parameters investigated for each set-up include power input, inter-electrode distance, the amount of liquid sample and residence time. Experiments were also performed to evaluate the ability of the negative corona for hexadecane cracking in air plasma, argon plasma and air/argon mixture plasma. The parameters investigated for each set-up include power input and inter-electrode distance. The theory of plasma processing of liquid hexadecane with argon plasma is given in section 6.2. The experimental conditions are summarized in section 6.3. No successful cracking of hexadecane was achieved under the experimental conditions investigated. Section 6.4 presents discussion and summary of the chapter, followed by conclusions in section 6.5.

6.2. Underlying theory

Non-thermal plasmas are able to produce very high concentrations of energetic and chemically active species keeping the bulk temperature at room temperature. Ionization and chemical reactions are directly determined by electron temperature (Fridman, 2008). These properties are especially attractive for initiating chemical reactions in organic compounds. In theory, cracking of hydrocarbons can be achieved by plasma ionization of the hydrocarbon molecule by an impact of energetic electron (Slovetskii, 2006), with argon as a second gas, refer to Figure 6.1. Argon is considered as an excellent plasma forming gas (Zou et al., 2007).

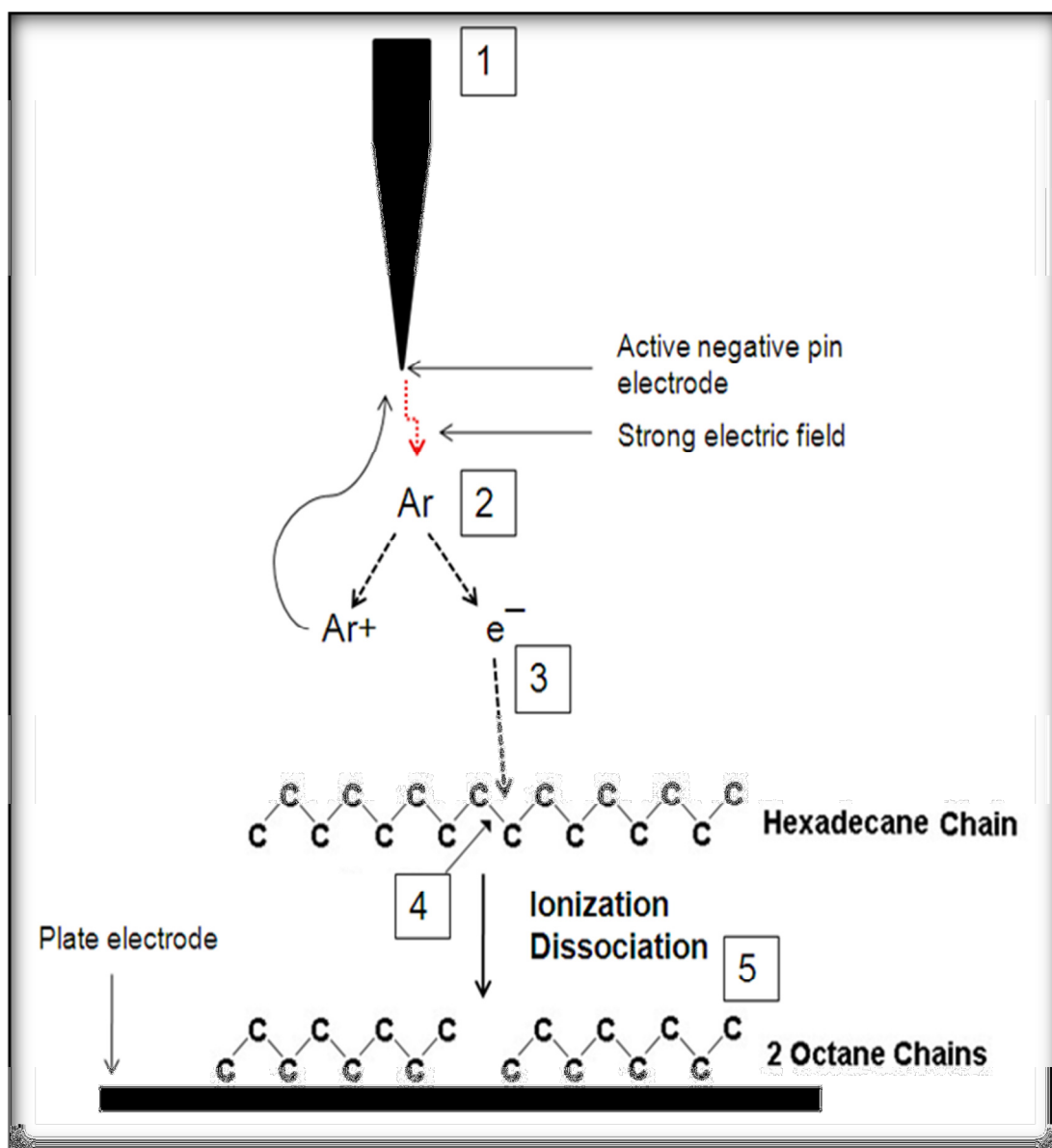


Figure 6.1: Expected plasma cracking of hexadecane in Argon at atmospheric pressure in a negative pin-to-plane electrode configuration. The mechanism is described below and the numbers in the figure represent the steps: 1) High voltage is supplied to the pin electrode; 2) Electrical breakdown of argon molecule and the generation of positive ion and an electron; 3) Electron accelerates to the positive plate electrode; 4) Ionization of hexadecane molecule at the C-C bond by an impact of an energetic electron; 5) Hexadecane molecule dissociation at the C-C bond.

There are numerous pathways that the hydrocarbon molecule can follow once introduced to the plasma and using hexadecane as a model compound some of these pathways are listed below:

(1) Types of electron molecular reactions

Interaction of a high energy electron may cause the hydrocarbon to break into two neutral radical molecules:



Interaction of a high energy electron may cause the hydrocarbon to break into a cationic and anionic carbon species:



Association of a high energy electron may generate a neutral radical and anionic carbon species:



Interaction of a high energy electron may liberate an electron from a neutral molecule, generating a carbocation:

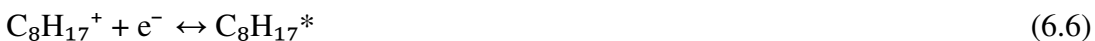


Association of a high energy electron may generate a carbanion:



(2) Reactions of cations

Recombination of an electron with a carbocation would yield a neutral radical species:

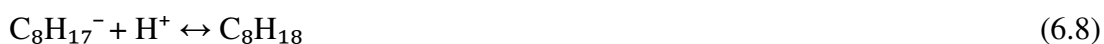


Loss of a proton would generate an alkene:



(3) Reactions of anions

Recombination of a carbanion with a proton would generate an alkane:



Recombination of a carbanion with a cationic hydrocarbon fragment would generate an alkane*:



*It is very important to note that if the bonds are broken at different positions these reactions could generate numerous possibilities.

(4) Reactions of radicals

Loss of hydrogen radical would generate an alkene:



Recombination of a hydrocarbon radical with hydrogen radical would generate an alkane:



Recombination of two hydrocarbon radicals would generate an alkane:



The reactions above represent the outcome if hexadecane is cracked in its middle C-C bond. However different bonds might be broken. While the principle of possible reactions would stay the same different products could be generated, for example:

Interaction of a high energy electron may cause the hydrocarbon to break into two neutral radical molecules of different sizes, such as pentane and undecane:



Or hexane and decane:



Recombination of two hydrocarbon radicals would generate an alkane – numerous possibilities depending on the original radical molecule sizes, for example pentane and hexane would form undecane:



Or hexane and undecane may form a heptadecane molecule:



6.3. Experimental conditions

Three sets of experiments were performed to investigate the ability of positive air plasma, argon plasma and argon and air mixture plasma cracking of hexadecane in liquid form. Each set contains a parametric study of power input variation at 10 mm, 15 mm and 20 mm inter-electrode distance, sample amount and residence time. The data sets are presented in tables B.1 – B.15 in Appendix B, describing the experimental conditions for each variable.

The same experimental procedure was used to test the negative air plasma, argon plasma and argon and air mixture plasma with the data sets presented in tables B.16 – B.23 in Appendix B.

6.4. Discussion

Positive and negative corona discharge polarities were assessed for hexadecane cracking in liquid form, and the main parameters were tested, including the gas composition, power input, inter-electrode distance, residence time and sample amount. No successful cracking of hexadecane was achieved under the experimental conditions investigated.

A major assumption made in the hexadecane cracking theory via electron collision described in 6.2 is the possibility that the gaseous plasma would interact with the hydrocarbon in a liquid state. As described in Chapter 4 (section 4.5) liquid hydrocarbons have been successfully cracked under different types of plasma. The hydrocarbon feedstock used during successful cracking was in the vapour form for the systems reported, whereas the approach in this work was to treat the feedstock in

liquid form. Kong (1997) has achieved hydrocarbon cracking in a submerged reactive system. Electrical arc was submerged in the feedstock, operating at 0.9 – 1.5 kV and 400 – 500 mA (AC or DC), with a gas flow within the arc (Kong, 1997). In this system the functioning electrodes were submerged within the feedstock, where electrode corrosion problems occurred. Due to the added cost of hydrocarbon vaporization at high temperatures it is desired to keep the feedstock in the liquid state and hence the purpose of this work. However, the above could indicate the possibility that no positive result was achieved in our system because of the absence of the chosen plasma gas interaction with the liquid hexadecane.

Kong et al (1995) has reported plasma cracking of squalane ($C_{30}H_{62}$). Interestingly, out of the four gases tested, namely argon, methane, hydrogen and a mixture of methane and hydrogen, the team reported that argon was not reactive with the heavy hydrocarbon mixture (Kong et al., 1995). As described in Chapter 4 (section 4.5) Kong et al (2005) patented a DBD system for heavy hydrocarbon cracking, at high currents of approximately 30 mA. However, in this system methane was used as a plasma gas. It would be more beneficial to use argon (recyclable) or air to crack hydrocarbons as the use of either hydrogen or methane would increase the cost of the process. However, the negative result in this work and the success of Kong (2005) could indicate that other reactive gasses such as methane are necessary for cracking of heavy hydrocarbons in a liquid state.

Another important parameter to consider from the above results is the current used to achieve liquid hydrocarbon cracking. The current of the discharge in this work was below 5 mA (the maximum available), which is much lower than those reported in the literature of 400 mA (Kong et al., 1997) and 30 mA (Kong et al., 2009). Such high currents could only be obtained by AC system, requiring new instrumentation and systems configuration.

6.5. Conclusions

Different variables and conditions (described in Appendix B) were tested to attempt hexadecane cracking during eight months of work. It is clear that plasma gas interaction with the liquid hexadecane did not occur, hence, no cracking achieved. However, the use of argon and low currents for plasma decomposition of methane

has been reported to be effective, as described in Chapter 4. Hence, the key conclusions to be drawn from this work are:

1. For plasma gas to liquid hexadecane interaction higher currents (above 5 mA) are necessary.
2. Argon is not a suitable gas for hexadecane cracking in a liquid state under the conditions tested.
3. The corona discharge reactor designed for this study and the methodology chosen are more suitable for gaseous hydrocarbon reformation.

Chapter 7: Experimental results for methane decomposition under corona discharge

7.1. Introduction

This chapter presents the results for the experiments of methane decomposition under corona discharge. Experiments were performed for positive corona discharge to evaluate the effects of discharge power and residence time on methane conversion, hydrogen selectivity, the energy conversion efficiency and other compounds generated at 15 mm inter-electrode distance. The effect of inter-electrode distance on hydrogen generation was also investigated. Methodology for the experiments and the quantification of the compounds have been described in Chapter 5, sections 5.4 and 5.5 respectively. This chapter provides the details of the experimental conditions, results data and analysis for positive and negative corona discharges in sections 7.2 and 7.3 respectively.

7.2. Methane decomposition under a positive corona discharge

The first experimental set was for inter-electrode distance of 15 mm and includes the testing of different discharge powers at different residence times, described in section 7.2.1. The effects of inter-electrode distance at 15, 20, 25, 30 and 35 mm are described in section 7.2.2.

For all of the experiments carbon build-up at the plane electrode occurred. Electrodes were polished with fine sand paper after each experiment. However, the plasma became very unstable with multiple spark discharges. It is possible that sand paper polishing introduces new sharp edges for the sparks to be attracted. When only the dry carbon was cleaned off, a very thin layer of carbon was still present. Plasma then occurred to be much more stable in a single more powerful stream, see Figure 7.1. Therefore, the ground electrode was dry cleaned only for all of the experiments reported. Carbon build-up also occurred in the form of a carbon string, see Figure 7.2. This in effect shortened the inter-electrode distance of the plasma resulting in much brighter and more powerful spark discharge. Eventually, with time, the carbon string reaches the pin electrode and the plasma process comes to a halt. The spark discharge can be re-ignited immediately by switching the power supply

off and back on. Once the carbon string starts to build up the spark appears visibly shorter. Therefore, at that point the power supply is switched off and on immediately (takes about 1 s), imitating a long pulse. This is sufficient for the carbon string to detach before the normal plasma process continues. This technique was performed for all experiments reported to ensure that inter-electrode distance was kept constant. It is important to note, that the carbon string build up is not likely to affect the continuous flow process. Since carbon fibre string is so weak, gas flow could be sufficient to remove it, also the use pulses would assist in carbon removal.

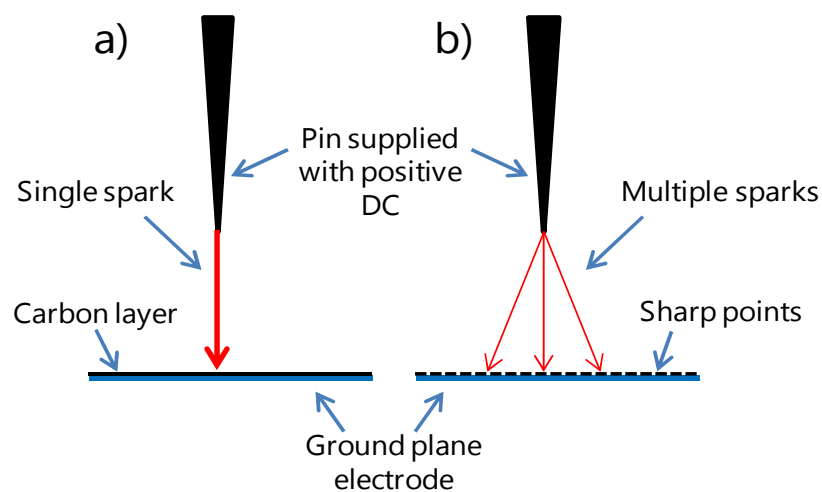


Figure 7.1: Shows the discharge characteristic of a positive pin-to-plane corona for a) unpolished, and b) polished plane electrode.

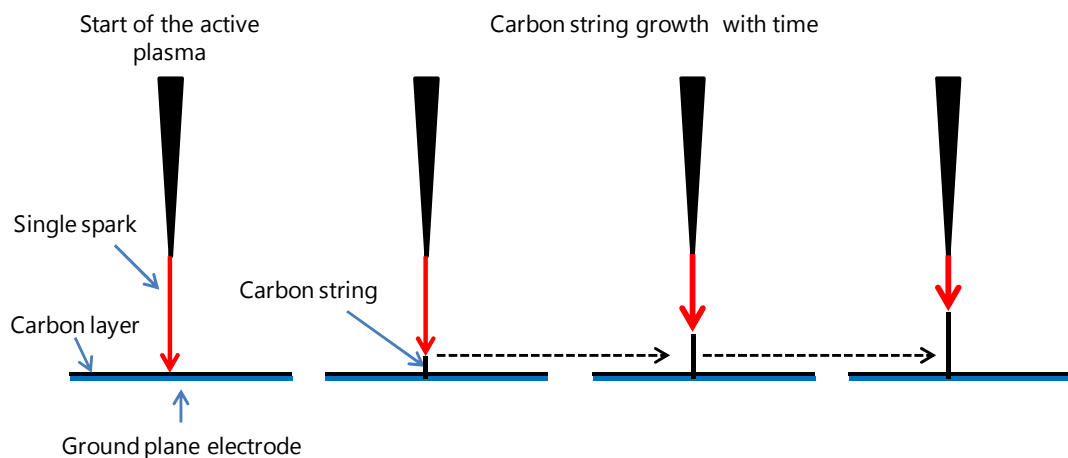


Figure 7.2: Shows the carbon string growth and the shortening of the active plasma area between the active positive pin and the ground electrode with time.

7.2.1. 15 mm inter electrode distance: Effects of discharge power and residence time

Five sets of experiments were performed to evaluate the effect of discharge power and residence time on hydrogen production from methane at an inter-electrode distance of 15 mm. Each set consists of 4 samples, with a set voltage input of 16, 17, 18 and 19 kV and each sample is allowed a maximum residence time of 60 s, 120 s, 180 s and 240 s between the sets. Table 7.1 shows the experimental conditions and the results for each of the sample.

In the following section of results analysis, the effects of power input and residence time reported in the literature for various methane reformation methods using plasmas, described in Chapter 4 (section 4.3.6) will be used for comparisons and validations.

Table 7.1: Experimental conditions and the results showing the data of methane conversion, hydrogen selectivity, hydrogen production and plasma energy efficiency for the experiments, testing the effects of discharge power and residence time at 15 mm inter-electrode distance.

Sample	Time (s)	Equivalent Flow (ml/min)	Input kV	Discharge kV	Average Current (mA)	Discharge Power (W)	Discharge Energy (kJ)	Methane conversion (%)	Hydrogen Selectivity (%)	Hydrogen production		Discharge Efficiency (%)
										(mol)	(%)	
M1	60	979	16	3.60	3.95	14	0.84	13	10.00	0.0005	1.26	4.55
M2	60	979	17	3.81	4.20	16	0.96	17	22.00	0.0015	3.69	10.52
M3	60	979	18	4.34	4.35	19	1.14	19	27.90	0.0021	5.24	13.33
M4	60	979	19	4.24	4.7	20	1.20	20	34.00	0.0026	6.52	16.21
M5	120	490	16	3.44	4	13	1.56	14	18.00	0.0010	2.43	6.74
M6	120	490	17	3.81	4.20	16	1.92	22	33.00	0.0029	7.27	14.24
M7	120	490	18	4.18	4.40	18	2.16	26	43.00	0.0042	10.42	18.11
M8	120	490	19	4.24	4.9	20	2.40	26	47.00	0.0047	11.64	19.41
M9	180	326	16	3.60	3.95	14	2.52	19	27.00	0.0021	5.27	9.95
M10	180	326	17	3.81	4.2	16	2.88	28	38.00	0.0042	10.42	15.43
M11	180	326	18	4.18	4.40	18	3.24	30	42.00	0.0055	13.63	17.00
M12	180	326	19	4.09	4.75	19	3.42	31	55.99	0.0068	16.81	21.68
M13	240	245	16	3.60	3.90	14	3.36	25	31.12	0.0034	8.36	11.60
M14	240	245	17	3.81	4.20	16	3.84	32	38.73	0.0048	12.00	14.61
M15	240	245	18	4.03	4.45	18	4.32	35	39.97	0.0071	17.55	16.50
M16	240	245	19	3.93	4.80	19	4.56	41	48.09	0.0083	20.64	19.33

7.2.1.1. Methane conversion

Methane conversion is affected by both the discharge power and the residence time. As shown in Figure 7.3 higher discharge powers and higher residence times both lead to higher methane conversion. For example, increasing the discharge power from 14 to 19 W at a given residence time of 4 min leads to an increase in methane conversion from 25 to 41 %. Conversely, increasing the residence time from 1 to 4 min for a given discharge power of 19 W resulted in an increase from 19 to 41 %. In terms of the calculated equivalent total flow, increasing the flow from 245 to 979 ml/min resulted in a decrease in methane conversion from 41 to 21 %. Results of Tsai and Chen (2009), who employed microwave plasma discharge for direct methane decomposition, are consistent with our batch results. They reported that an increase in a total flow from 12, 000 to 18, 000 ml/min resulted in a decrease in methane conversion from 62 to 45%.

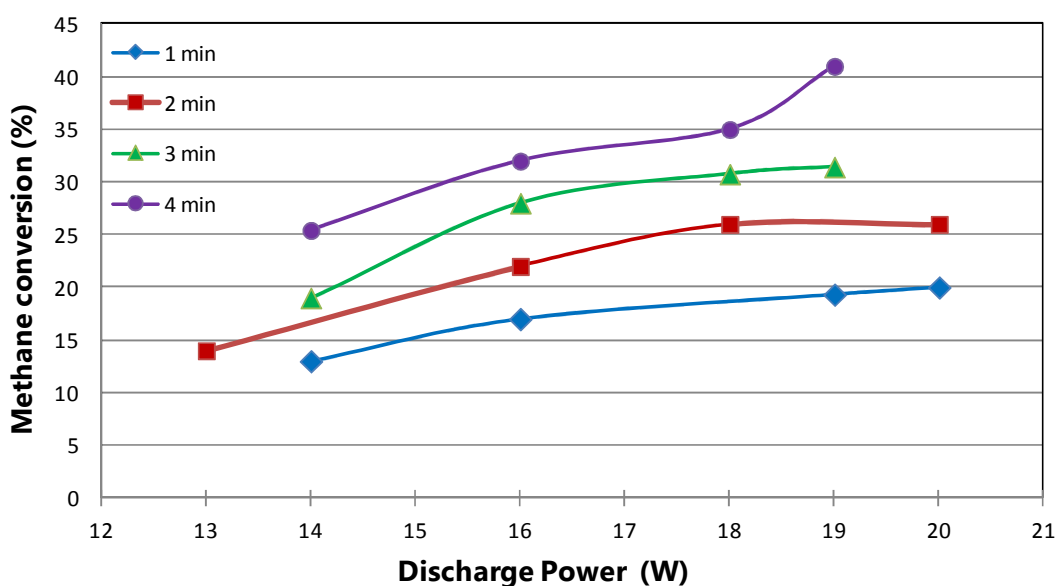


Figure 7.3: Shows the effects of discharge power and residence time on methane conversion.

The more general research literature on plasma assisted hydrogen generation from methane further supports our findings. As reviewed in Chapter 4, partial oxidation of methane has been the most widely applied method to generate hydrogen and carbon monoxide (syngas). In the literature lower flow rates (Huang et al., 2000; Sreethawong et al., 2007; Chen et al., 2006; Tao et al., 2008; Long et al., 2008; Li et

al., 2009b; Luche et al., 2009) and higher discharge powers (Huang et al., 2000; Tsai et al., 2005; Li et al., 2004; Chen et al., 2006; Sreethawong et al., 2007; Li et al., 2009b;) have both been reported to favour conversion of methane. Figure 7.4 shows the effect of the flow rate on methane conversion reported in the literature for the partial oxidation employing different types of plasma and this work. The effects of the discharge power cannot be graphically presented, due to different ranges of the discharge power reported in the literature when compared to this work. Overall, these findings suggest that the flow rate and the discharge power are the two key parameters for methane conversion in plasma processing of methane, irrespective of the specific processing approach.

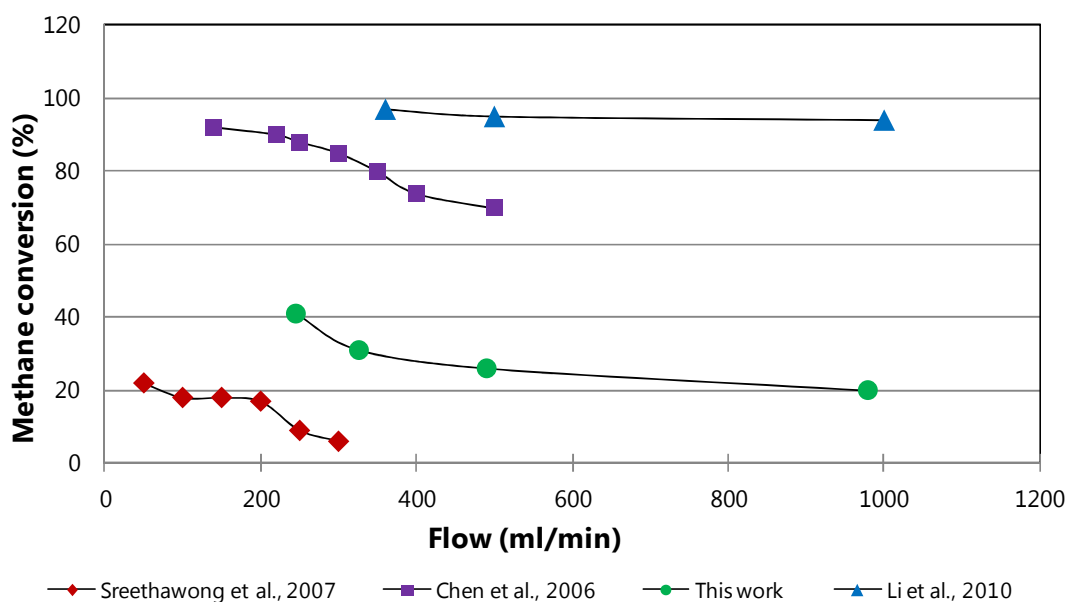


Figure 7.4: The effect of the flow rate on methane conversion reported in the literature and this work.

Figure 7.5 gives the variation of methane conversion with the discharge energy input into the system, i.e. the product of discharge power and residence time. There is a very clear trend of increase in methane conversion with discharge energy. In chemical terms the energy deposited on the methane molecules increases with increasing power input and residence time: for example, from Figure 7.5 an increase in discharge power from 1 to 4.56 kJ leads to methane conversion increasing from 13 to 41 %. However, the results for the lowest current of 3.9 mA (points circled in red Figure 7.5) show methane conversion rates much lower than the rest of the data. This

could indicate that a minimum current is needed for a good conversion percentage. The maximum methane conversion achieved in this experimental series is 41 % at discharge power of 19 W, residence time of 4 min and the highest total discharge energy of 4.56 kJ.

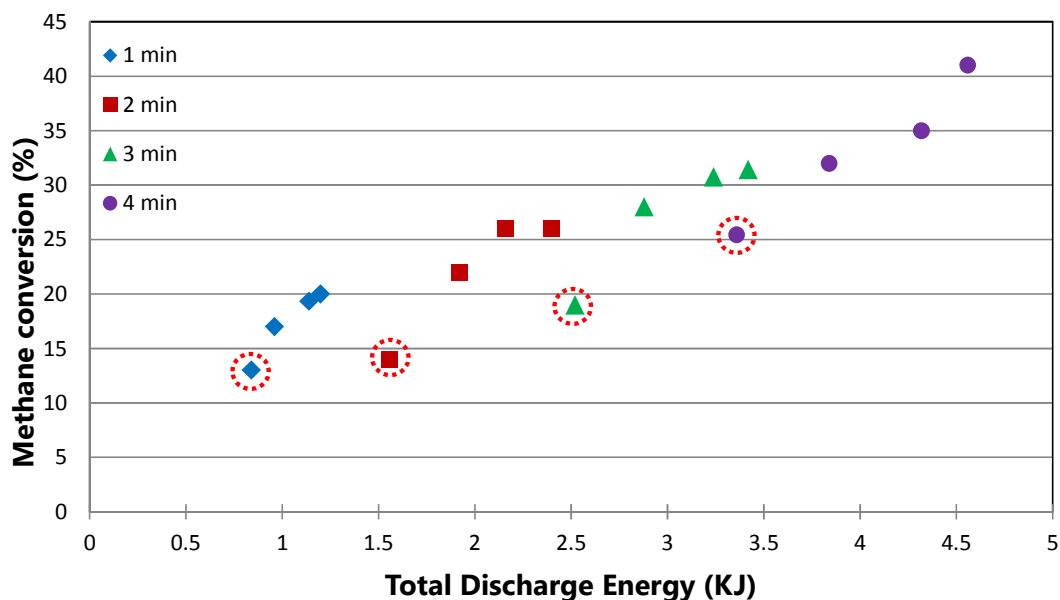


Figure 7.5: Shows the effects of total discharge energy on methane conversion.

7.2.1.2. Hydrogen production and selectivity

Figure 7.6 shows that hydrogen production increases both with increasing discharge power and residence time. For example, increasing the discharge power from 14 to 19 W at a given residence time of 4 min leads to hydrogen production increase from 0.005 to 0.008 moles. Conversely, increasing residence time from 1 to 4 min at a given discharge power of 19 W gave an increase in hydrogen production from 0.0021 to 0.008 mol. The corona discharge reactor used in this work has been designed as a small scale batch process to assess the future capability of a flow system. Hence, only low total flow and hydrogen production rates in moles achieved.

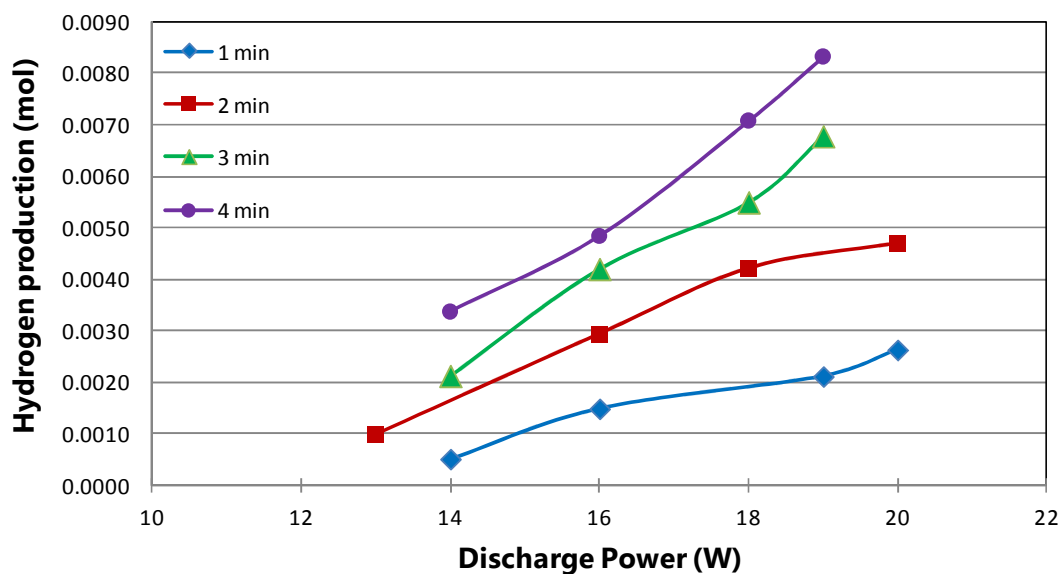


Figure 7.6: Hydrogen production against discharge power and residence time.

Figure 7.7 shows that hydrogen selectivity increases with both discharge power and residence time. For an increase in discharge power from 14 to 19 W at a residence time of 3 min hydrogen selectivity doubles to 56 %. It increases with discharge power at all residence times. When the residence time increases from 1 to 2 min at a discharge power of 20 W the hydrogen selectivity rises from 34 to 47 %. However, above 2 min there is a diminishing return, for instance at 16 W discharge power, only a 5% improvement when residence time increases from 2 to 3 min and a negligible effect from 3 to 4 min. There is similar behaviour at other discharge powers. In fact at 18 W discharge power and residence times of 3 and 4 min there seems to be a negative effect of residence time. This needs to be assessed fully and is discussed later in section 7.2.1.4. In terms of the calculated equivalent total flow rate, our results are consistent with those reported by Sreethawong et al., (2007), see Figure 7.8. However, an increase in hydrogen selectivity with the total flow rate have also been reported in the literature, see Figure 7.8. This suggests that, unlike methane conversion, hydrogen selectivity follows a more complex path where the effects of total flow rate differ between processing approaches. The maximum hydrogen selectivity achieved in this experimental series is 56 % at a discharge power of 19 W, a residence time of 3 minutes with a methane conversion of 31 %.

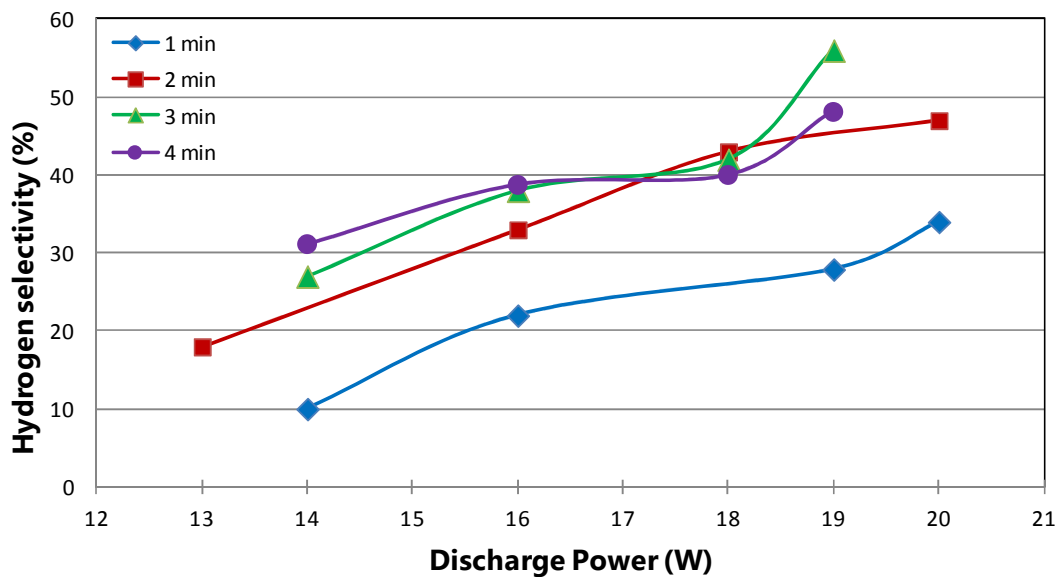


Figure 7.7: The effects of discharge power and residence time on hydrogen selectivity.

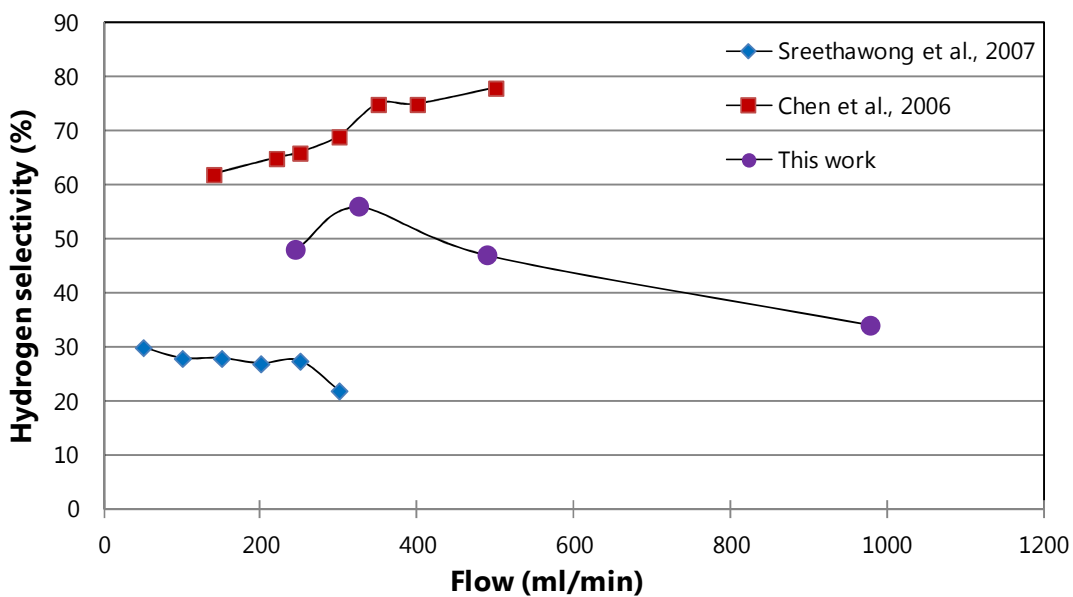


Figure 7.8: The effect of flow rate on hydrogen selectivity, results reported in the literature compared to this work.

7.2.1.3. Energy conversion efficiency

The energy efficiency is depicted in Figure 7.9 as a function of discharge power and residence time. This performance criterion, as with the previous parameters, increases with discharge power and residence time, although there is a quite consistent diminishing effect with residence time above 2 min. Energy conversion efficiency (Figure 7.9) and hydrogen selectivity (Figure 7.7) follow nearly identical trends, and this is confirmed when plotting them together in Figure 7.10, where the energy conversion efficiency increases nearly proportionally with hydrogen selectivity. It is to be expected that energy conversion efficiency is mainly to be governed by hydrogen selectivity, due to high calorific value of hydrogen, i.e. 141.80 MJ/kg (higher heating value).

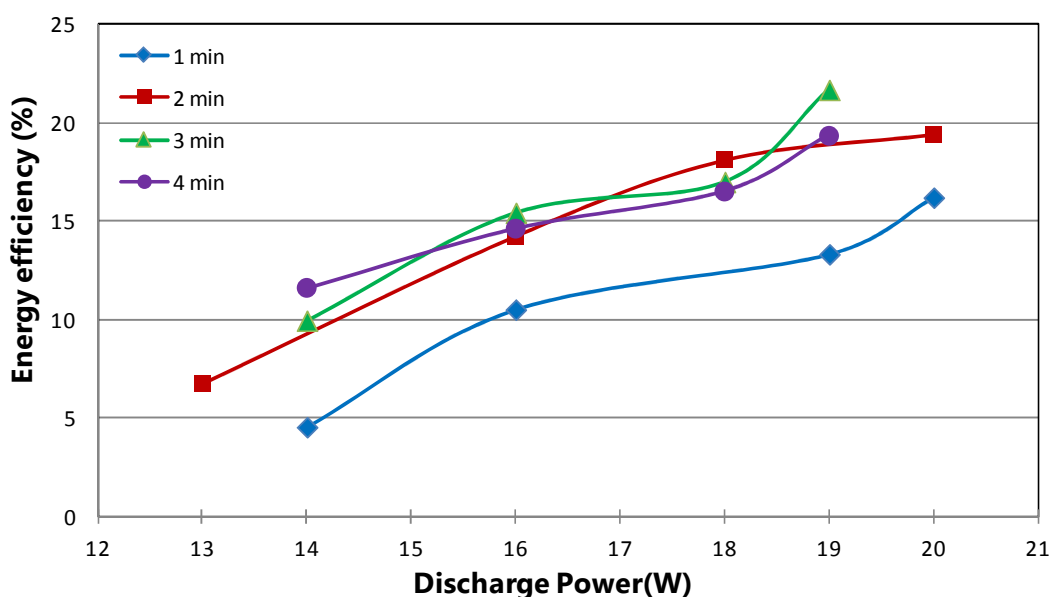


Figure 7.9: The effects of discharge power and residence time on energy conversion efficiency of the plasma.

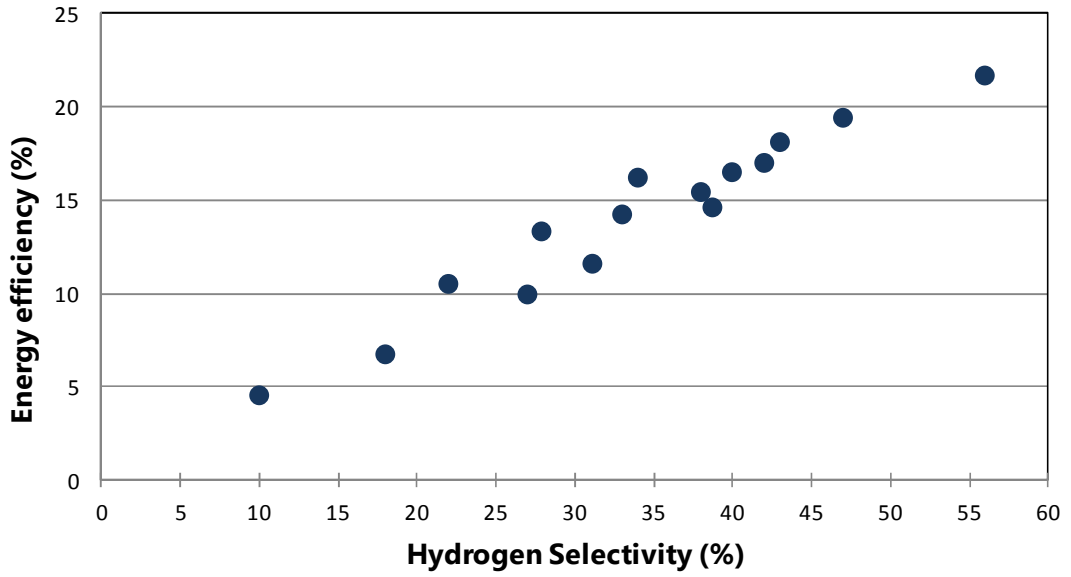


Figure 7.10: Energy efficiency versus hydrogen selectivity.

Figure 7.11 shows that the energy consumption for this plasma process is mainly in the form of methane. It is beneficial to have low electricity consumption especially if the system is combined with the fuel cell for decentralized applications.

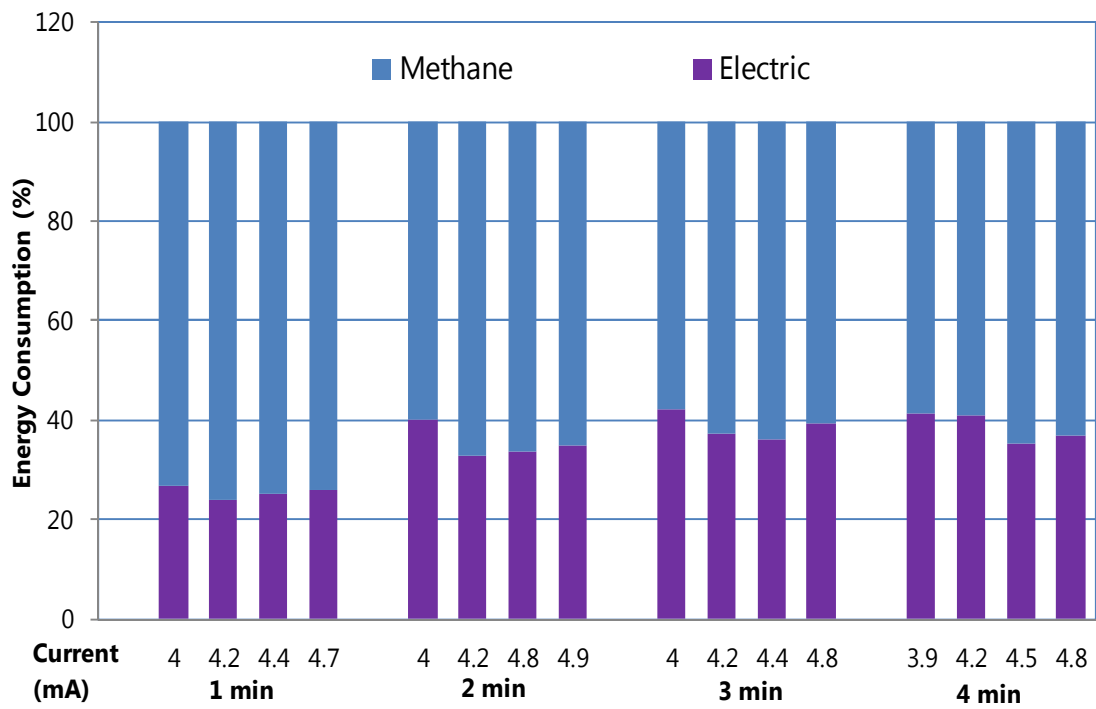


Figure 7.11: The percentages of methane and electric energy consumption.

Table 7.2 compares the key parameters and outputs for this work with other systems reported in the literature for plasma decomposition of methane to generate hydrogen. The highest system efficiency of 52 % was achieved by Jasinski et al. (2008) using a combination of microwave plasma and nickel catalyst. Interestingly, of the five systems, they had the highest hydrogen selectivity (96.8 %) and the lowest methane conversion rate (13.2 %). This confirms the dependence of energy efficiency on hydrogen selectivity as described above. The problem of nickel catalyst deactivation caused by solid carbon when used for methane thermo-catalytic decomposition has already been discussed in Chapter 2. Therefore, for the system of Jasinski et al. (2008) to be industrially viable, experimental evidence is necessary to show that the catalyst is resistant to carbon deactivation over time.

Table 7.2 also shows that the application of corona discharge to the decomposition of methane to hydrogen (this work) is competitive with the stand alone microwave discharge reported by Tsai and Chen (2009). However, the system proposed by Tsai and Chen (2009) uses nitrogen as plasma forming gas and the authors reported generation of toxic hydrogen cyanide as a by-product. This could be a major disadvantage for commercialization from a health and safety point of view. Further, this work has achieved a much higher energy efficiency than the use of a combined gliding arc/ nickel catalyst system (Rueangjitt et al., 2007) or the pulsed spark discharge of (Li et al., 2004).

Table 7.2: Important parameters and results for plasma decomposition of methane to generate hydrogen reported in literature.

Plasma type	Feed flux (ml/min)	CH₄ content in the feed (%)	Discharge power (W)	CH₄ conversion rate (%)	Hydrogen selectivity (%)	Energy conversion efficiency (%)	Reference
Microwave plasma and nickel catalyst	1.75 X 10 ⁵	100	3 X 10 ³	13.2	96.8	52	Jasinski et al., 2008
Microwave discharge	1.2 X 10 ⁴	20	800	Approx 40	86	24	Tsai and Chen, 2009
Corona discharge (positive)	Batch process	50	19	31	56	22	This work
Microsized Gliding arc and nickel catalyst	100	5	6	50	80	10	Rueangjitt et al., 2007
Pulsed spark discharge (corona)	10	100	12	69	51	9	Li et al., 2004

7.2.1.4. Other compounds generated

As described in the section 5.5.2.4 (ii) for compounds that are not present in the standard gas mixture, the values extracted are in arbitrary units, i.e. the measured areas of the peaks on the chromatograms. Arbitrary units do not give enough information to quantify the compounds. However, they can be used for comparison of compound behaviour and appearance between the samples and the sets.

Hydrocarbons generated during the plasma decomposition of methane include ethene, ethane and acetylene. Figures 7.12 and 7.13 show that both discharge power and residence time, have positive effects on ethene and acetylene generation respectively. Figure 7.12 also shows that ethene generation is highest at 18 W for residence times of 3 and 4 minutes, displaying somewhat anomalous behaviour above 18W. Acetylene generation is highest at discharge powers above 18 W and residence time of 3 and 4 minutes. In Figure 7.7 it was clearly shown that hydrogen selectivity decreases at 18 W discharge power and residence times above 2 min. This effect could potentially be explained by the enhanced ethene production rate at 18 W above 2 min (Figure 7.12) combined with the steep increase in acetylene production at discharge powers above 18 W and residence times greater than 2 min (Figure 7.13). Figure 7.14 shows that generation of a third additional compound - ethane is favoured at lower discharge powers and residence times. The compounds are combined in Figure 7.15 using a residence time of 4 min as an example and this shows that at higher discharge powers acetylene is the dominant by-product of the process.

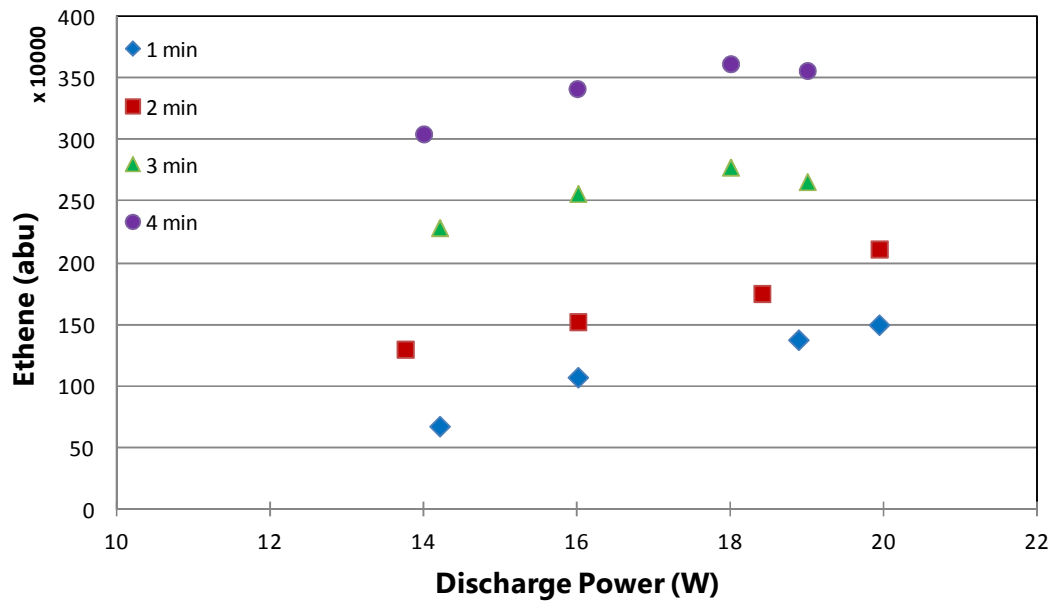


Figure 7.12: Generation of ethene against the discharge power and residence time.

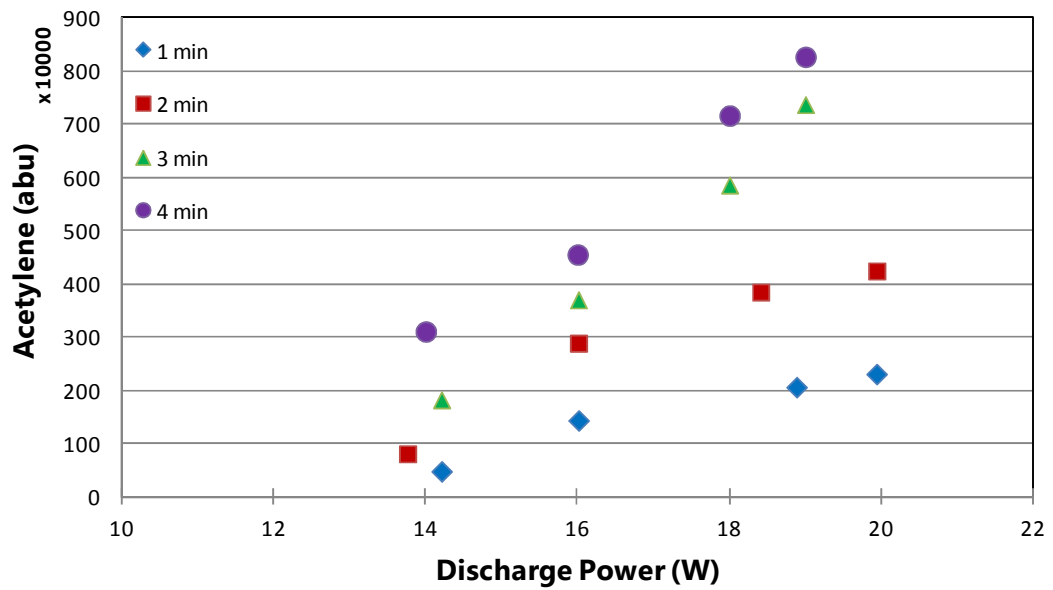


Figure 7.13: Generation of acetylene against the discharge power and residence time.

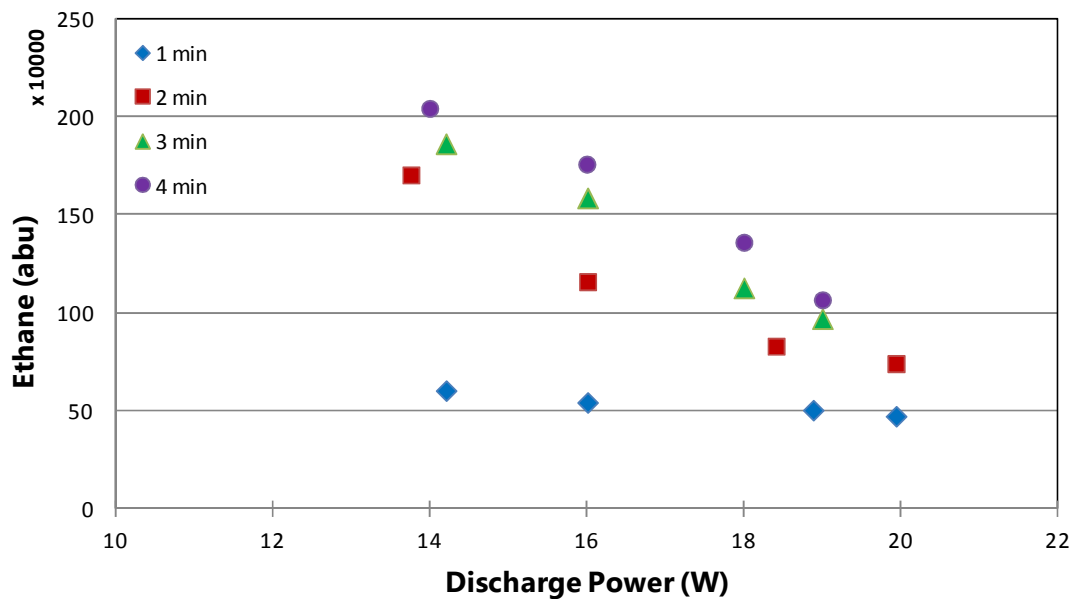


Figure 7.14: Generation of ethane against the discharge power and residence time.

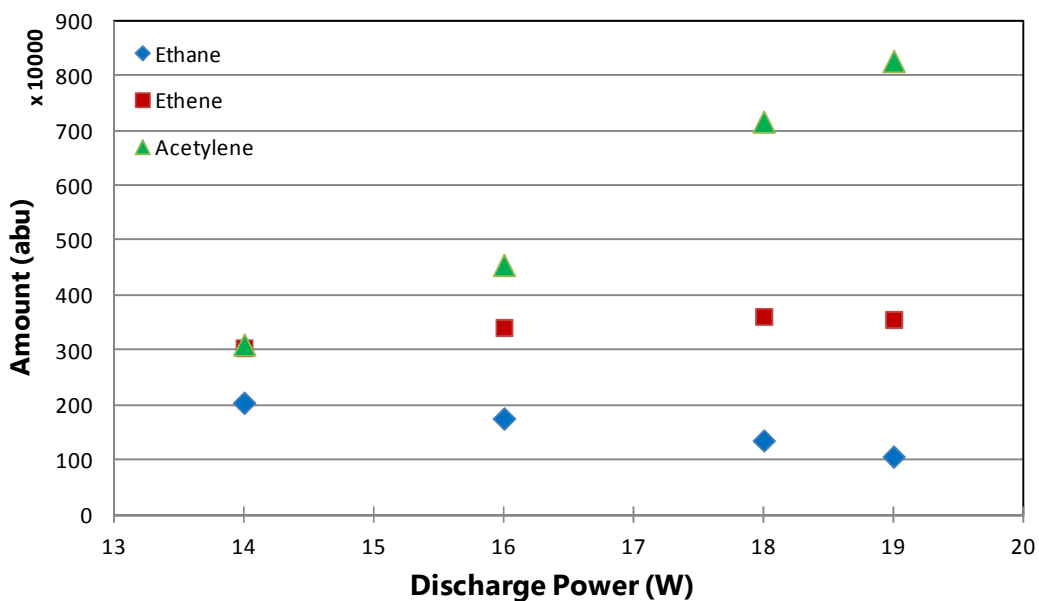


Figure 7.15: Other compound generation during methane conversion to hydrogen at residence time 4 minutes.

7.2.1.5. Summary

A series of experiments have been performed for positive corona discharge at 15 mm inter-electrode distance to study the effects of discharge power and residence time on methane conversion, hydrogen selectivity and energy efficiency. Higher discharge powers and longer residence times favour the conversion of methane and the production of hydrogen. Energy conversion efficiency is mainly governed by hydrogen selectivity, due to its high calorific value. Hydrogen selectivity is highly affected by other compound generation, especially the generation of acetylene and ethene at higher powers and residence times. The generation of ethene is highly favoured at 18 W and residence times 3 and 4 minutes. This could explain the dip in hydrogen selectivity at the same conditions. In general, acetylene has been shown to be a major by-product in the plasma decomposition of methane to generate hydrogen.

For corona discharge at 15 mm inter-electrode distance, highest hydrogen selectivity achieved was 56 % whilst achieving 31 % methane conversion with an energy conversion efficiency of 21.7 % at 19 W discharge power and 180 s residence time.

7.2.2. The effects of inter-electrode distance on hydrogen production

Experiments were performed at inter-electrode distances of 15, 20, 25, 30 and 35 mm to evaluate the effects of inter-electrode distance on hydrogen generation, see Table 7.3. Figure 7.16, provides data for the entire series, and shows that hydrogen generation at all inter-electrode distances increases with the power input and residence time. In general, increasing the inter-electrode distance leads to a systematic increase in hydrogen generation. For example, taking the data in Figure 7.16 for 4 min residence time, hydrogen production for 15, 20, 30 and 35 mm is respectively 20.64, 27.18, 32.54 and 34.13 % by volume. Experimental results of Kado et al. (2003) showed that in a pulsed corona discharge methane conversion increased from 30 to 90 %, as the inter electrode distance increased from 0.5 to 10 mm. When the gap distance is increased a higher breakdown voltage is needed, and Kado et al. (2003) observed that this has a stronger effect on methane conversion than the increase in residence time. They concluded that the energy distribution of electrons is improved in a longer gap. Sekine et al. (2003a) and Sreethawong et al.

(2007) have also reported higher methane conversion ability with an increase in inter-electrode distance. Li et al. (2010) have experimentally shown that increasing the inter-electrode distance results in an increase in methane conversion as well as hydrogen selectivity in cold plasma jet. Our results confirmed these observations, which related to 0.5 to 10 mm inter-electrode distances, extending its validity to higher distances up to 35 mm. It can also be seen from Figure 7.16, that the discharge powers differ widely for different inter-electrode distances. This is expected since, as noted above, longer distances require higher breakdown voltages to generate active plasma (Raizer, 1991). The breakdown voltage is constant at a given inter-electrode distance and it is the increase in current that result in higher discharge powers. Increasing the inter-electrode distance required an increase in the applied voltage by 1 kV to achieve similar current characteristics. For instance, for 15 mm with an applied voltage of 16 kV, the discharge voltage and current are 3.92 kV and 3.9 mA respectively, whereas for 20 mm at an applied voltage of 17 kV the discharge voltage and current are 5.04 kV and 3.7 mA.

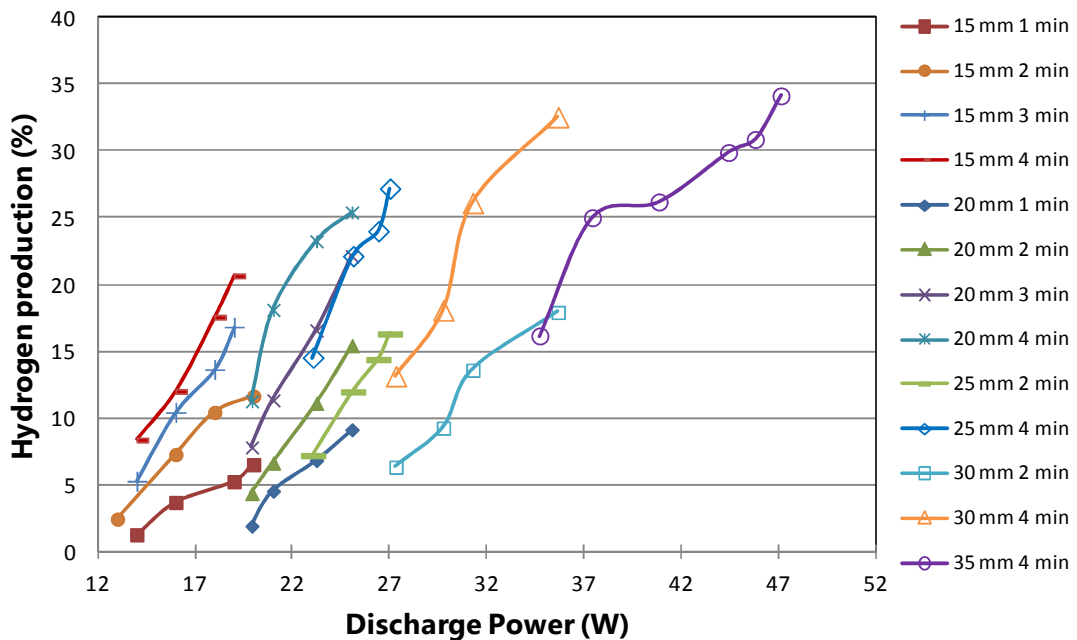


Figure 7.16: The effects of discharge power and residence time on hydrogen generation at inter electrode distances of 15, 20, 25, 30 and 35 mm.

Table 7.3: Data table for the effects of inter-electrode distance on hydrogen production at different residence times and discharge powers.

Sample	Time (s)	Input kV	Discharge kV	Average current (mA)	Discharge power (W)	Hydrogen production (%)
Inter-electrode distance 20 mm						
M17	60	17	4.91	3.70	18.91	1.90
M18	60	18	5.13	4.10	21.02	4.52
M19	60	19	5.03	4.35	22.37	6.83
M20	60	20.5	5.11	4.90	25.06	9.12
M21	120	17	4.91	3.70	18.91	4.35
M22	120	18	5.13	4.10	21.02	6.64
M23	120	19	5.03	4.35	22.37	11.10
M24	120	20.5	5.11	4.90	25.06	15.43
M25	180	17	4.91	3.70	18.91	7.80
M26	180	18	5.13	4.10	21.02	11.33
M27	180	19	5.03	4.35	22.37	16.57
M28	180	20.5	5.11	4.90	25.06	22.13
M29	240	17	4.91	3.70	18.91	11.27
M30	240	18	5.13	4.10	21.02	18.10
M31	240	19	5.03	4.35	22.37	23.24
M32	240	20.5	5.11	4.90	25.06	25.40
Inter-electrode distance 25 mm						
M33	120	18	6.07	3.80	23.06	7.19
M34	120	19	6.13	4.10	25.12	11.96
M35	120	20	5.87	4.50	26.42	14.38
M36	120	21	5.46	4.95	27.01	16.31
M37	240	18	6.07	3.80	23.06	14.52
M38	240	19	6.13	4.10	25.12	22.13
M39	240	20	5.87	4.50	26.42	24.01
M40	240	21	5.46	4.95	27.01	27.18
Inter-electrode distance 30 mm						
M41	120	19	7.38	3.70	27.31	6.32
M42	120	20	7.44	4.00	29.76	9.25
M43	120	21	7.03	4.45	31.27	13.58
M44	120	22.5	7.43	4.80	35.65	17.91
M45	240	19	7.38	3.70	27.31	13.13
M46	240	20	7.44	4.00	29.76	18.06
M47	240	21	7.03	4.45	31.27	26.11
M48	240	22.5	7.43	4.80	35.65	32.54
Inter-electrode distance 35 mm						
M49	240	21	9.38	3.70	34.71	16.16
M50	240	22	9.13	4.10	37.42	25.01
M51	240	23	9.50	4.30	40.84	26.19
M52	240	24	9.87	4.50	44.42	29.89
M53	240	24.5	9.74	4.70	45.79	30.87
M54	240	25	9.61	4.90	47.11	34.13

As shown by Figure 7.17, for all inter-electrode distances tested an increase in current leads to an increase in hydrogen production. For example an increase in current from 3.7 to 4.9 mA at 9.54 kV (35 mm gap) resulted in hydrogen generation increasing from 16 to 34 %. Other observations made from Figure 7.17 are as follows: when results are compared for increasing inter-electrode distances but at the same current the increase in discharge power is essentially due to the required increase in breakdown voltage, with average voltages for 15, 20, 25, 30 and 30 mm sets being 3.92, 5.04, 5.88, 7.32 and 9.54 kV respectively. Further, in general an increase in discharge voltage leads to an increase in hydrogen generation, for example a rise in voltage from 5.04 to 9.54 kV at 4.9 mA results in an increase in hydrogen generation from 25 to 34 %. However, a somewhat more complex progression can be seen at 7.32 kV, as below 4.3 mA the hydrogen generation rate is slightly lower than at 5.88 kV. This phenomenon requires further study.

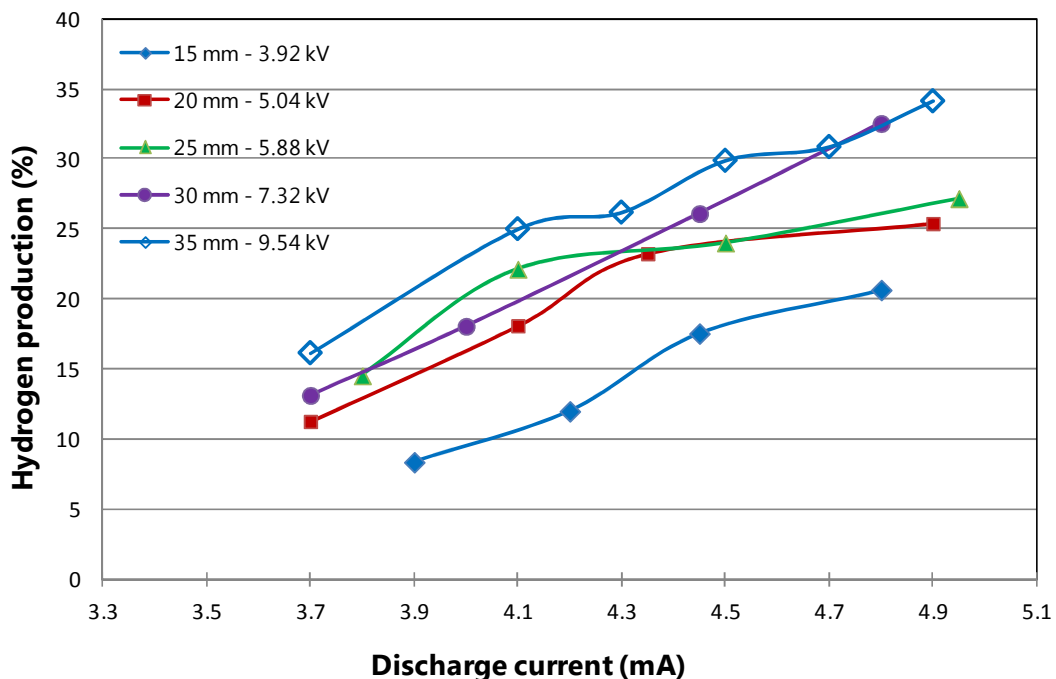


Figure 7.17: Shows the hydrogen production trend against the discharge current at different discharge voltages at 4 min residence time.

7.2.3. Experimental repeatability

To test the repeatability of the plasma chemical activity a set of experiments was repeated at an inter-electrode distance of 20 mm and residence time 2 min, discharge power was varied in the same manner as for the original samples. Hydrogen is the smallest and the most important compound measured in this system. Therefore, the repeatability of the plasma unit is based on hydrogen production by volume. Figure 7.18 shows that hydrogen production is repeatable within the $\pm 2.06\%$ error bars (the uncertainty for the hydrogen measurement by the GC).

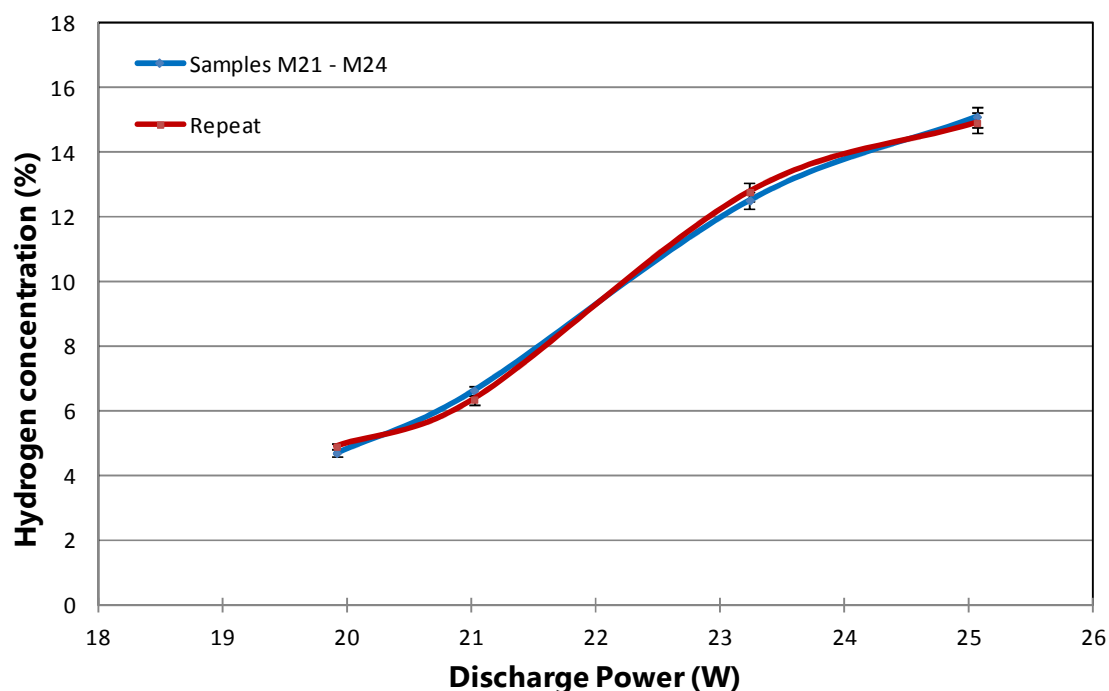


Figure 7.18: Hydrogen production repeatability at inter-electrode distance of 20 mm, residence time 2 min; the error bars for hydrogen measurement are at $\pm 2.06\%$.

7.3. Methane decomposition under a negative corona discharge

All previous work used a positive corona polarity, so in the final series of experiments the effect was investigated on the ability to generate hydrogen of a change in polarity. Both polarities were tested at inter-electrode distances of 15, 20, 25 and 30 mm. The common residence time was 4 min, except at 25 mm which used 2 and 3 min times for positive polarity. Results are given in Table 7.4 and show that

much higher hydrogen production is achieved with positive corona discharges. Indeed, at distances of 15 and 20 mm negative corona discharge achieved a negligible hydrogen production of 1.28 and 1.3 %, compared with the corresponding positive corona discharge values of 17 and 23 % respectively. The maximum negative polarity output of hydrogen was 18 % at a distance of 30 mm, but this was still only about half the value of 33 % achieved by a positive corona discharge. For an inter-electrode distance of 35 mm a stable plasma discharge could not be achieved with a negative polarity. The discharge showed very little visibility and that was only around the pin. Also no increase in pressure was observed.

Table 7.4: Comparing the hydrogen generation ability of positive and negative corona discharge at different inter-electrode distances.

Sample	Inter-electrode distance (mm)	Polarity	Time (s)	Discharge kV	Average mA	Discharge Power (W)	Hydrogen production (%)
M55	30	-	240	8.00	4.60	37.00	18.00
M48	30	+	240	7.43	4.80	35.65	32.54
M58	25	-	180	5.77	4.85	27.99	4.20
M35	25	+	120	5.90	4.50	26.42	14.38
M39	25	+	240	5.90	4.50	26.42	24.01
M57	20	-	240	4.70	4.55	21.44	1.30
M28	20	+	240	5.34	4.35	23.23	23.24
M56	15	-	240	2.77	4.85	13.00	1.28
M15	15	+	240	4.03	4.45	18.00	17.00

Kado et al. (2003) also reported that using a positive pulsed corona for partial oxidation of methane, the methane conversion (and hence hydrogen production) was slightly improved than when the polarity was negative at the same pulse frequency.

According to the modelling results of positive and negative DC corona discharges carried out by Chen and Davidson (2003a), negative corona discharges generate more than 50 times more electrons when compared to the positive. However, positive discharges generate a higher number of energetic electrons in the relatively high electric field near the active electrode. The lower energy of the electrons in negative corona discharges will result in a lower rate of chemical reactions which require higher electron energy. This is confirmed by Wan et al. (2011), who performed experiments for the decomposition of formaldehyde and reported that the power requirement of negative DC corona discharge is much higher than positive to achieve the same conversion rate. In general, positive corona discharge showed a better ability and higher efficiency for formaldehyde decomposition when compared to the negative (Wan et al., 2011). Therefore, a low production of hydrogen with negative corona discharge in this work is due to the electron energy in a negative corona discharge being too low for effective methane decomposition reactions to take place. This also shows the importance of electron involvement in methane decomposition reactions and is in sync with the theory of the pure plasma effect of decomposition by collision of electrons and methane gas molecules (Lee et al., 2010, Formulae (4.5)), described in Section 4.3.1).

7.4. Summary

Three series of batch-process experiments have been performed to investigate the application of non-thermal plasmas to generate CO_x-free hydrogen from methane. The main series used an inter-electrode distance of 15 mm and a positive corona discharge. The effects of discharge power and residence time were studied on methane conversion, hydrogen selectivity and energy efficiency. Higher discharge powers and longer residence time favour the conversion of methane and the production of hydrogen. Energy conversion efficiency is mainly governed by hydrogen selectivity, due to its high calorific value. Hydrogen selectivity is affected by the generation of other compounds, especially acetylene and ethene at discharge powers above 18 W and residence times above 2 min. Maximum generation of ethene occurred at 18 W and residence times above 2 min which explain the dip in hydrogen selectivity at the same conditions. In general in the present work, acetylene has been the major by-product. In the second series of experiments the effect of

varying inter-electrode distance was investigated, resulting in increasing hydrogen generation along with increased inter-electrode distance. In the final experimental series the effects of corona polarity was tested and it was found that positive polarity produced more hydrogen so is therefore preferable in terms of hydrogen production.

In the main series of experiments, with 15 mm inter electrode distance, the highest hydrogen selectivity of 56 % was achieved with methane conversion of 31 % and energy conversion efficiency of 21.7 % at 19 W discharge power and 3 min residence time. These figures compete directly with comparable results in the literature, for non-thermal plasmas generated by microwave discharge, by gliding arc with nickel catalyst and by pulsed spark discharges. In conclusion, from an energy efficiency point of view, corona discharge has shown to be a promising approach for hydrogen generation by plasma assisted methane decomposition.

Chapter 8: Experimental results for propane decomposition under corona discharge

8.1 Introduction

This chapter presents the results for the experiments of propane decomposition under corona discharge. Experiments were performed for positive corona discharge at 15 mm inter-electrode distance to evaluate the effects of discharge power and residence time on propane conversion, hydrogen selectivity, the energy conversion efficiency and other compounds generated. The effect of inter-electrode distance on hydrogen generation was also tested. Methodology for the experiments and the quantification of the compounds have been described in Chapter 5, sections 5.4 and 5.5 respectively. This chapter provides the details of the experimental conditions, results data and analysis for positive corona discharge. In section 8.2 the effects of discharge power and residence time at 15 mm inter-electrode distance are given. The effects of inter electrode distance on hydrogen production are given in section 8.3 and section 8.4 provides a summary of the chapter.

8.2 15 mm inter electrode distance: Effects of discharge power and residence time

Five sets of experiments were performed to evaluate the effect of discharge power and residence time on hydrogen production from propane at an inter-electrode distance of 15 mm. Each set consists of 4 samples, with a set voltage inputs of 16, 18, 20 and 21.7 kV and each sample is allowed a maximum residence time of 60 s, 120 s, 180 s and 240 s or until the plasma cut-off point is reached, see section 8.2.1. Table 8.1 shows the experimental conditions and the results for each of the samples. For set 1 (samples 1 – 4) and set 2 (samples 5 – 8) the residence time was exactly at 60 s and 120 s respectively whilst the voltage inputs varied according to the above values. For set 3 the allowed residence time was 180 s. However, the plasma activity for samples 9 (16 kV) and 10 (18 kV) only lasted for 160 and 167 s respectively. The plasma cut-off phenomena occurred for all of the input voltage ratings as the maximum allowed residence time was increased, see Table 8.1. This phenomenon will be looked at in more detail in the next section. From Table 8.1 it can also be

seen that due to the nature of the corona discharge and the current fluctuations the discharge power is never exactly the same even at the same voltage input. Therefore, due to this plasma phenomenon, only the results from the first two sets of samples can be compared separately for residence time and discharge power. To compare the whole set and gain a deeper understanding into plasma chemistry the total discharge energy (discharge power in J/s X residence time in s) will be presented for result analysis in sections 8.2.2 – 8.2.5.

Table 8.1: Experimental conditions and the results showing the data of propane conversion, hydrogen selectivity, hydrogen production and energy efficiency for the experiments, testing the effects of discharge power and residence time at 15 mm inter-electrode distance.

Sample	Time (s)	Input kV	Average Current (mA)	Discharge Power (W)	Total Discharge Energy (kJ)	Propane conversion (%)	Hydrogen Selectivity (%)	Hydrogen production (mol)	Discharge Efficiency (%)	Cut off pressure (kPa)
1	60	16	2.00	19.44	1.17	12.24	18.81	0.002	7.83	none
2	60	18	3.74	23.40	1.40	15.85	22.65	0.003	9.58	none
3	60	20	4.34	27.66	1.66	17.49	23.43	0.003	9.81	none
4	60	21.7	4.99	30.10	1.81	19.19	25.49	0.004	10.58	none
5	120	16	3.08	19.49	2.34	21.75	23.63	0.004	9.52	none
6	120	18	3.60	24.11	2.89	23.81	30.49	0.005	11.86	none
7	120	20	4.24	28.35	3.40	24.39	31.39	0.005	11.87	none
8	120	21.7	4.85	31.38	3.77	26.41	31.40	0.006	11.95	none
9	160	16	2.00	19.44	3.11	20.89	23.01	0.003	8.53	12.96
10	167	18	3.17	25.51	4.26	25.74	31.96	0.006	11.52	21.62
11	180	20	3.86	30.42	5.47	36.15	28.39	0.008	10.77	none
12	180	21.7	4.77	32.06	5.77	40.88	27.97	0.009	10.71	none
13	164	17	2.30	22.49	3.69	23.68	26.84	0.005	9.95	17.24
14	178	18	2.86	25.80	4.59	25.23	31.46	0.006	11.16	22.08
15	210	20	4.42	29.33	5.68	37.52	29.85	0.008	10.97	31.28
16	216	21.7	4.80	31.81	6.87	39.66	33.32	0.010	11.89	35.82
17	153	16	1.02	13.05	2.00	23.79	15.61	0.003	6.63	10.91
18	189	18	2.33	24.89	3.23	29.81	28.37	0.004	10.47	20.33
19	228	20	3.73	30.91	7.05	39.10	31.18	0.009	11.00	34.92
20	303	21.7	4.39	34.75	10.53	48.02	33.48	0.011	10.93	49.05

8.2.1 Plasma cut-off phenomenon

As described in Chapter 3 (section 3.4), the breakdown voltage depends only on the product of the gas pressure and inter-electrode distance (pd) for a given gas and the cathode material (Nehra et al., 2008; Raizer, 1991) and the experimental breakdown Paschen curves show that the minimal breakdown voltage for a discharge gap exists (Raizer, 1991). Therefore, increasing either the inter-electrode distance or the pressure in the system for a given gas mixture would require a higher breakdown voltage for the plasma processes to occur. The inter-electrode distance was kept at 15 mm for all five sets and the voltage input was set for each individual experiment. However, the pressure of the system gradually increased with time as propane is reformed into smaller molecules. Figure 8.1 shows the characteristics of pressure increase until plasma cut-off point for voltage inputs of 16 and 21.7 kV.

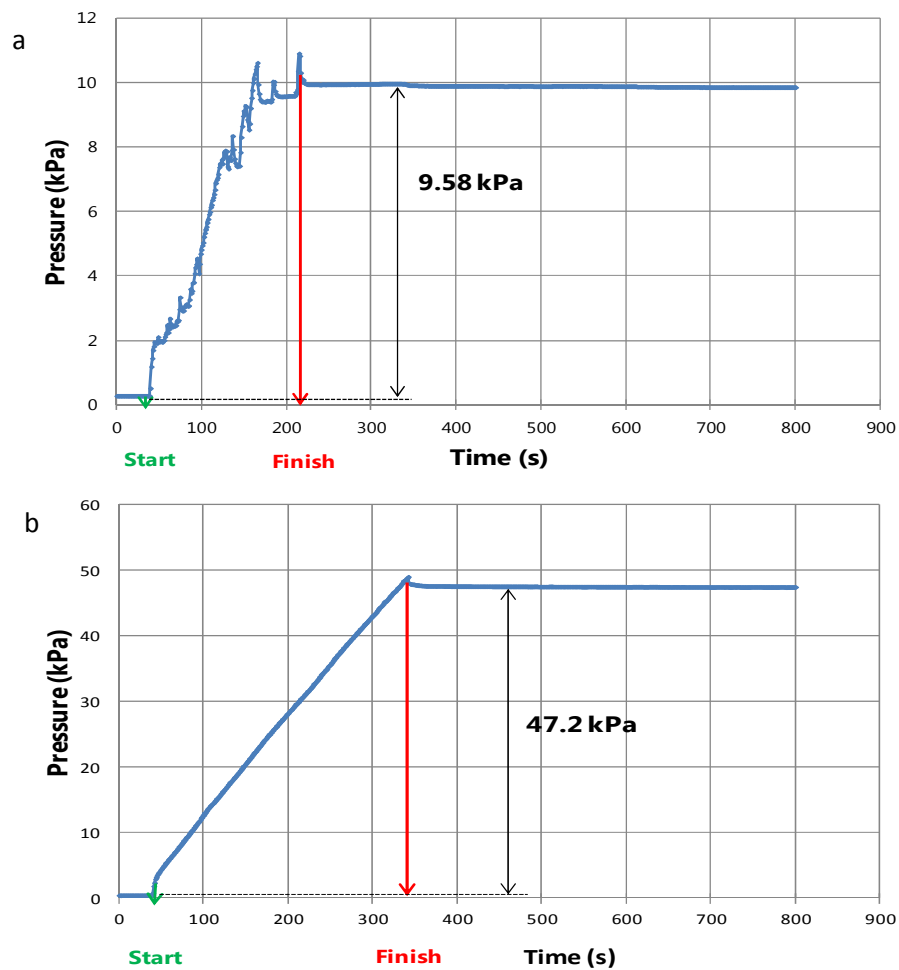


Figure 8.1: Characteristics of pressure change with time during propane decomposition experiments at voltage input of a) 16 kV; b) 21.7 kV.

Figure 8.2 shows the relationship between the input voltage to the plasma system and the plasma cut-off pressure. It can be clearly seen that at higher voltage inputs the pressure for the plasma cut-off is also higher, and each voltage input value has its own range of pressure tolerance, which is directly proportional to voltage breakdown value. All this suggests that the plasma cut-off point is caused when the breakdown voltage, due to pressure increase, becomes higher than that supplied to the plasma system.

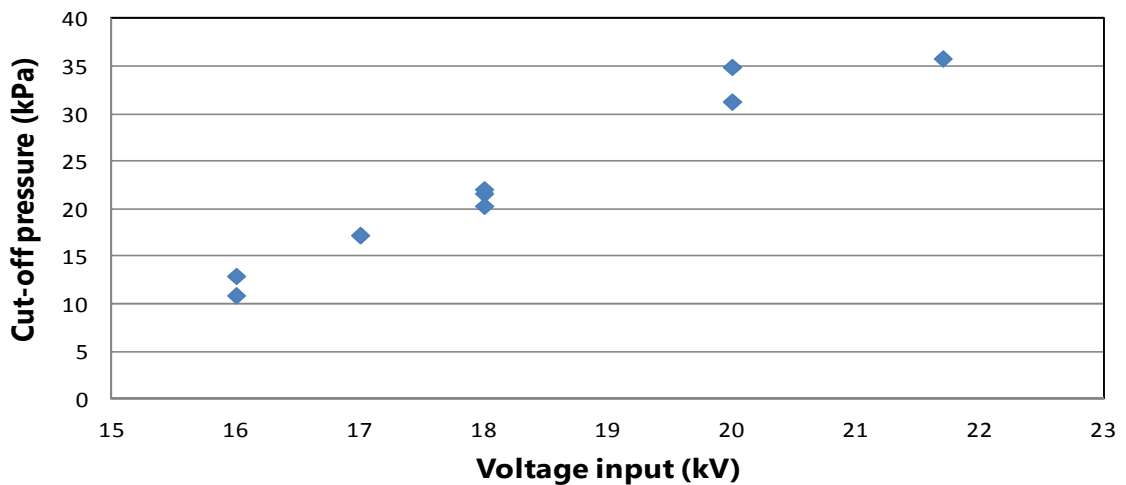


Figure 8.2: Shows the pressure of the plasma cut-off point compared to the voltage input into the system.

8.2.2 Propane Conversion

Propane conversion is affected by both the discharge power and the residence time, as shown in Figure 8.3. Higher discharge power and higher residence time both lead to higher propane conversion. For example, an increase in discharge power from 19 to 31 W at 2 min residence time resulted in an increase in propane conversion from 22 to 26 %, where an increase in the residence time from 1 to 2 min at approximately 30 W discharge power showed an increase in propane conversion from 19 to 26 %. These results are in agreement with the results reported by Yu et al. (2011) for dielectric barrier discharge employed for partial oxidation of methane where an increase in discharge power from 12.2 – 21.9 W resulted in increased propane conversion from 25 to 43.4 %. The energy deposited on propane molecules increases

with increasing discharge power and residence time, this is shown in Figure 8.4 where propane conversion is compared to the total discharge energy into the system. For example, increasing the total discharge energy from 2 to 10 kJ resulted in propane conversion increase from 22 to 48 %. The maximum propane conversion achieved in this set is 48.02 % at a discharge power of 35 W, residence time of 303 s and the highest total discharge energy was 10.5 kJ.

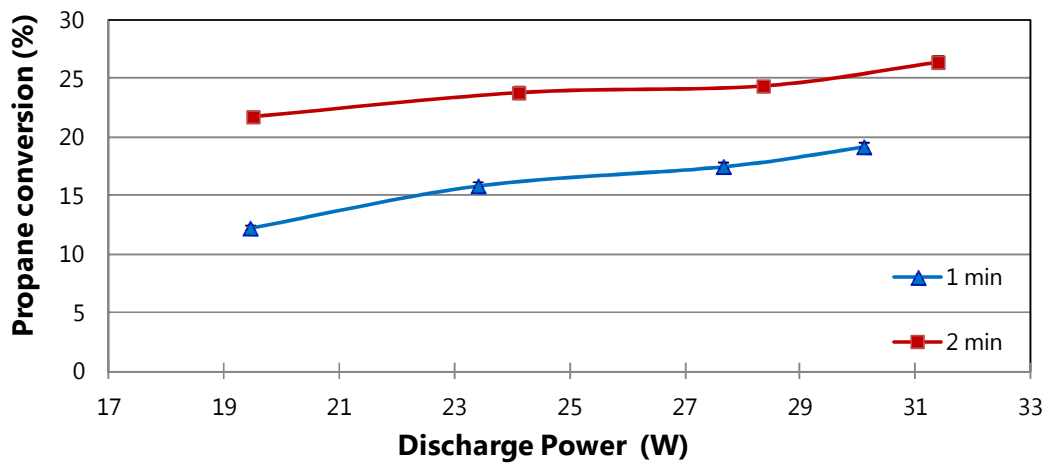


Figure 8.3: Shows the effects of discharge power and residence time on propane conversion, with combined error of ± 2.06 % of the reading value.

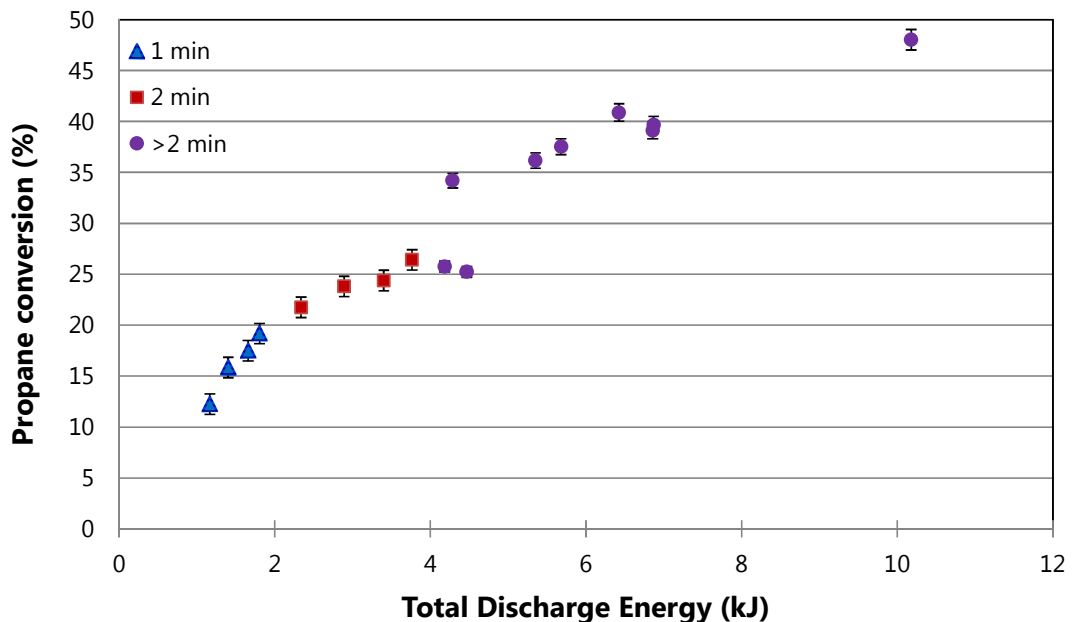


Figure 8.4: Shows the effects of total discharge energy on propane conversion, with combined error of ± 2.06 % of the reading value.

8.2.3 Hydrogen production and selectivity

Hydrogen production increases with increasing discharge power and residence time, see Figure 8.5 a). Figure 8.5 b) shows the production of hydrogen increases nearly linearly with the total discharge energy.

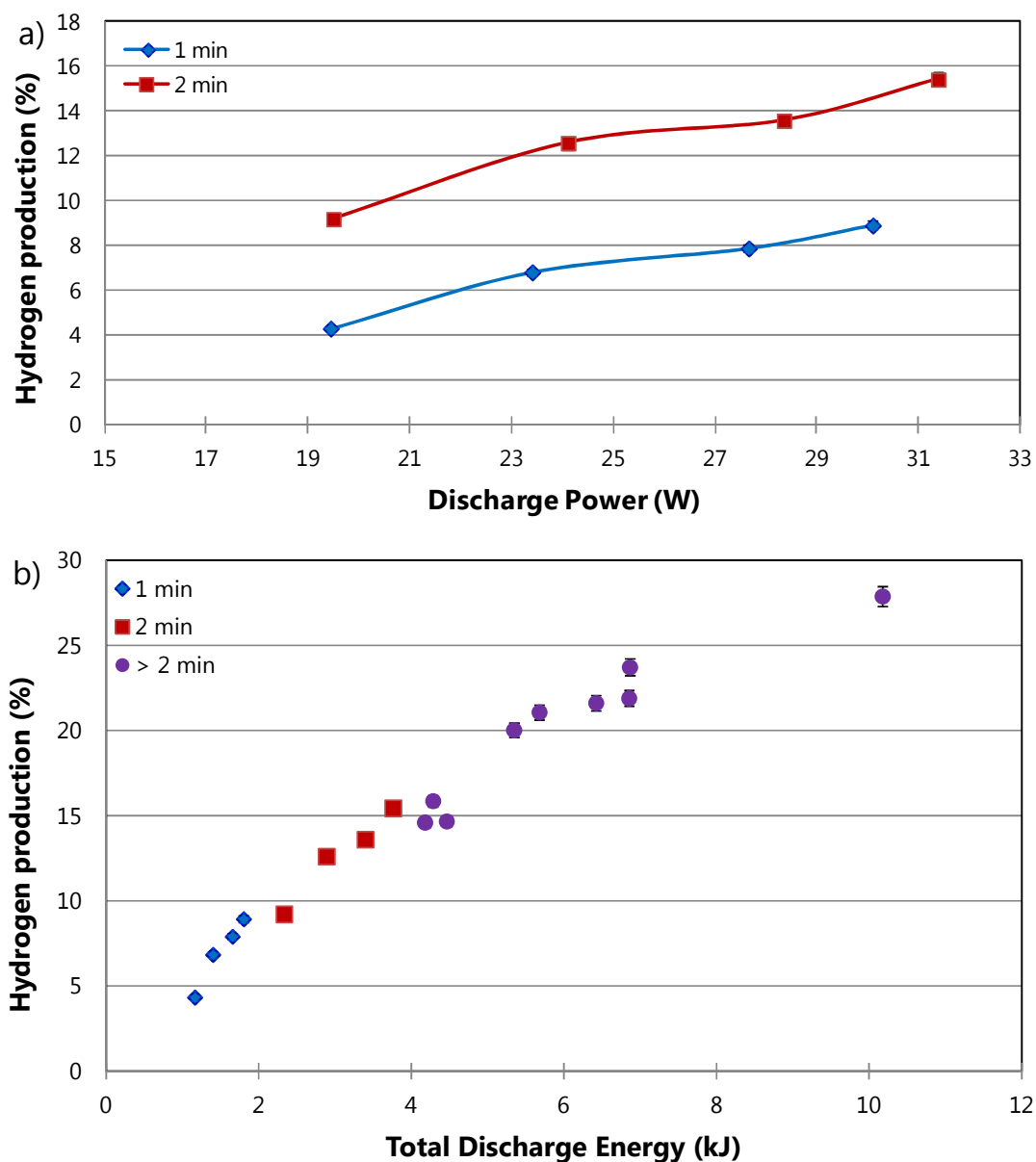


Figure 8.5: a) Hydrogen production compared to discharge power and residence time; b) Hydrogen production compared to the total discharge energy; with combined error of ± 2.08 % of the reading value.

Figure 8.6 a) shows that hydrogen selectivity increases with both, the discharge power and the residence time. However, there is a diminishing effect on hydrogen selectivity with discharge power at residence times above 2 minutes, Figure 8.6 a). Figure 8.6 b) shows that hydrogen selectivity also increases with the total discharge energy. However, it can also be seen that there is a diminishing effect with total discharge energy, i.e. the increase from 7 to 10 kJ is very small (0.16 %), even though as seen in Figure 8.5, hydrogen generation increases nearly linearly with discharge power. The diminishing effect in hydrogen selectivity can be explained by the generation of other compounds in the system and will be described in section 8.2.5.

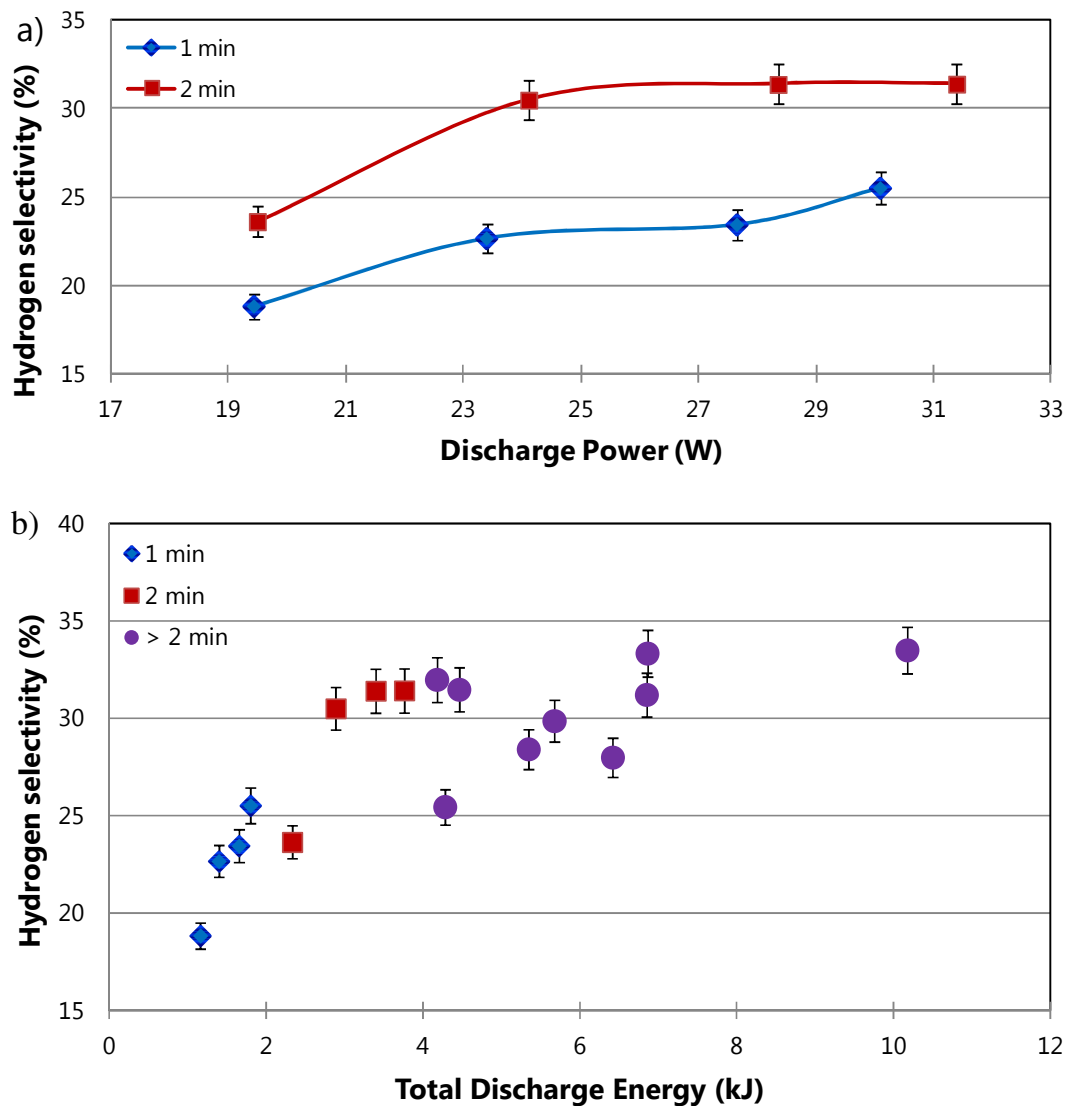


Figure 8.6: Shows the effect of a) discharge power and residence time and b) total discharge energy on hydrogen selectivity, with combined error of $\pm 3.59\%$ of the reading value.

8.2.4 Energy conversion efficiency

Energy conversion efficiency for the system determines how efficiently propane energy and electric energy is converted to the desired fuel – hydrogen. From Figure 8.7 it can be seen that energy efficiency increase with discharge power. Increasing the residence time from 1 to 2 minutes has a positive effect on the efficiency at approximately 23 W; a diminishing affect is seen as the discharge power is further increased at 2 minutes residence time. Figure 8.8 shows that a diminishing effect occurs at total discharge energy above 4 kJ. From Figure 8.9, it can be seen that the energy conversion efficiency increases nearly proportionally with hydrogen selectivity. Due to the very low energy input in the form of electricity and high calorific value of hydrogen, the energy conversion efficiency is mainly governed by hydrogen selectivity. The highest energy conversion efficiency achieved for this set is 12 % at 216 seconds residence time and 32 W discharge power with a propane conversion rate of 40 % and hydrogen selectivity at 33 %.

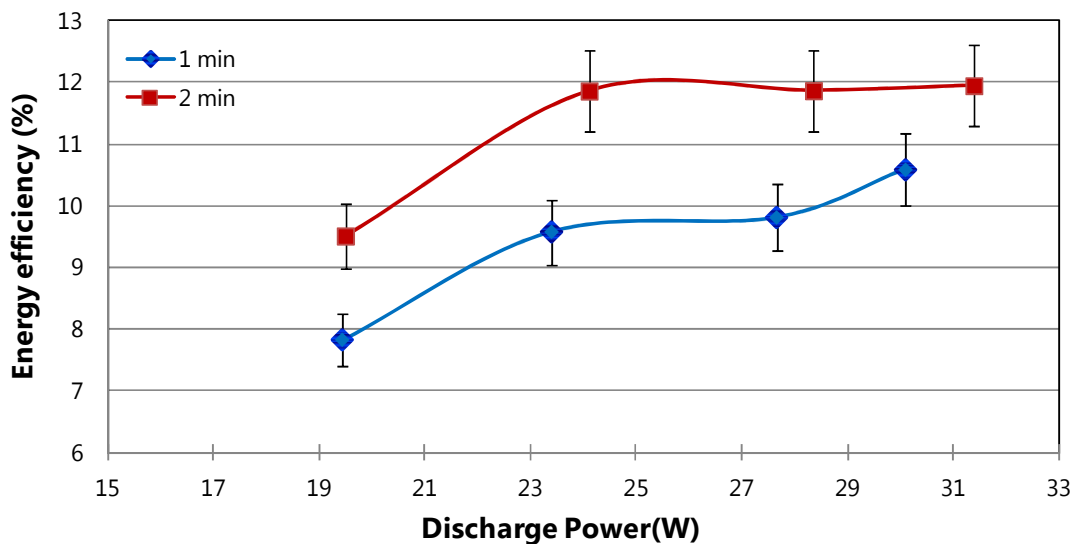


Figure 8.7: Shows the relationship of energy efficiency between the discharge power and residence time, with the combined total error of $\pm 5.5\%$ of the reading value.

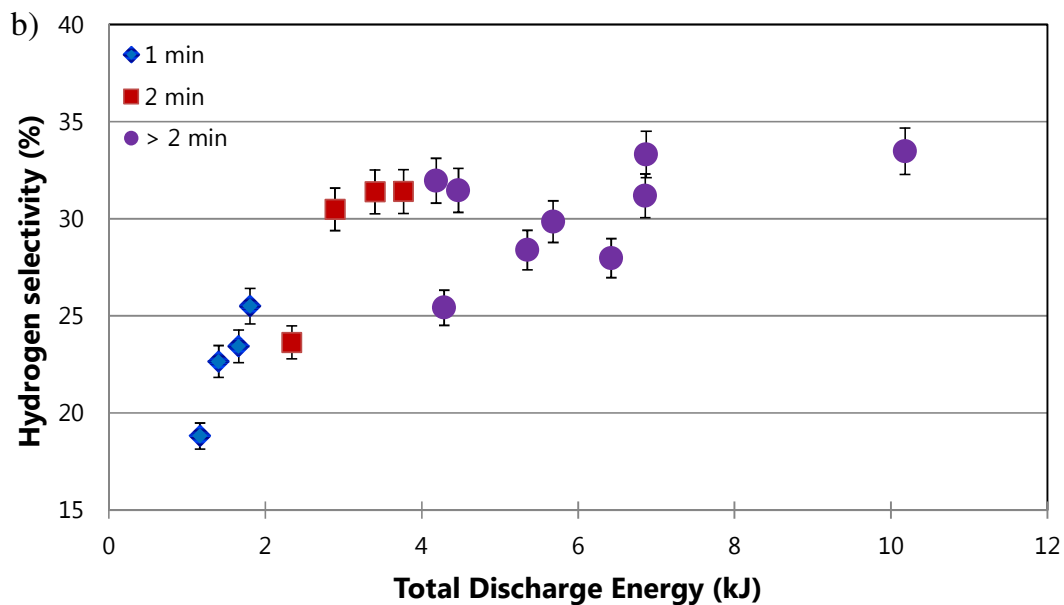


Figure 8.8: Shows the relationship between energy efficiency and total discharge energy, with the combined total error of $\pm 5.5\%$ of the reading value.

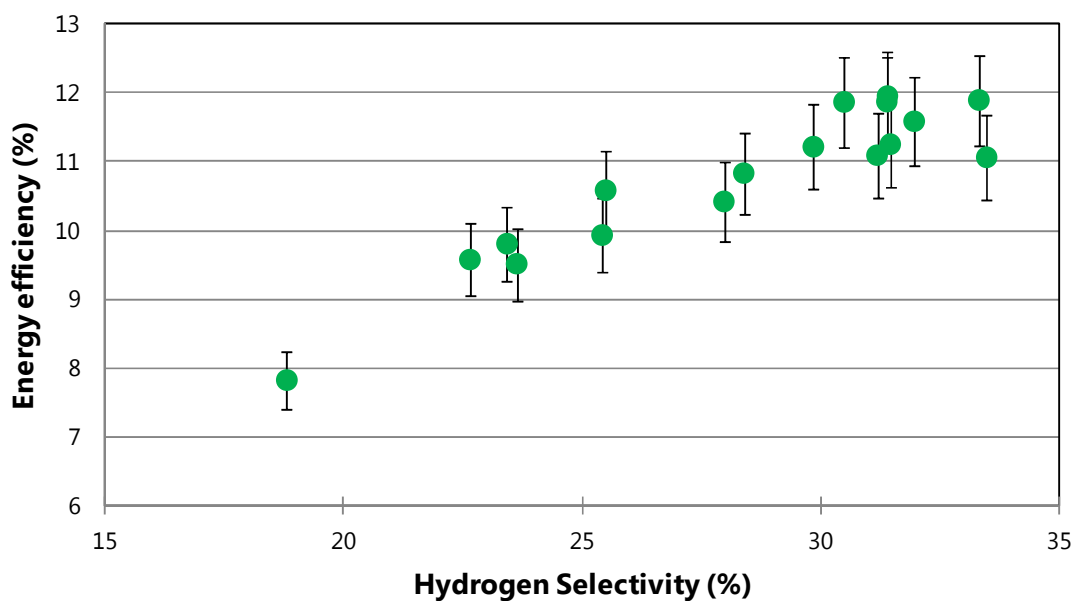


Figure 8.9: Shows the relationship between energy efficiency and hydrogen selectivity, with the combined total error of $\pm 5.5\%$ of the reading value.

8.2.5 Other compounds generated

As described in Chapter 5, section 5.5.2.4 (ii) for compounds that are not present in standard gas mixture, the values extracted are in arbitrary units, i.e. the measured areas of the peaks on the chromatograms. Arbitrary units do not give enough information to quantify the compounds. However, they can be used for comparison of compound behaviour and appearance between the samples and the sets.

Other compounds generated after the experiments are shown in Figure 8.10 against the discharge power. The pattern of compound generation can be very clearly seen from Figure 8.10, with ethene being the dominating compound, followed by methane and cyclopropane. Much smaller amounts of butane are present with only traces of pentanes and hexanes. Yu et al. (2011) reported a similar composition of compounds formed in DBD partial oxidation of propane, including methane, ethene, ethane, butane and others. The pattern of the compound formation will be analysed further in this section.

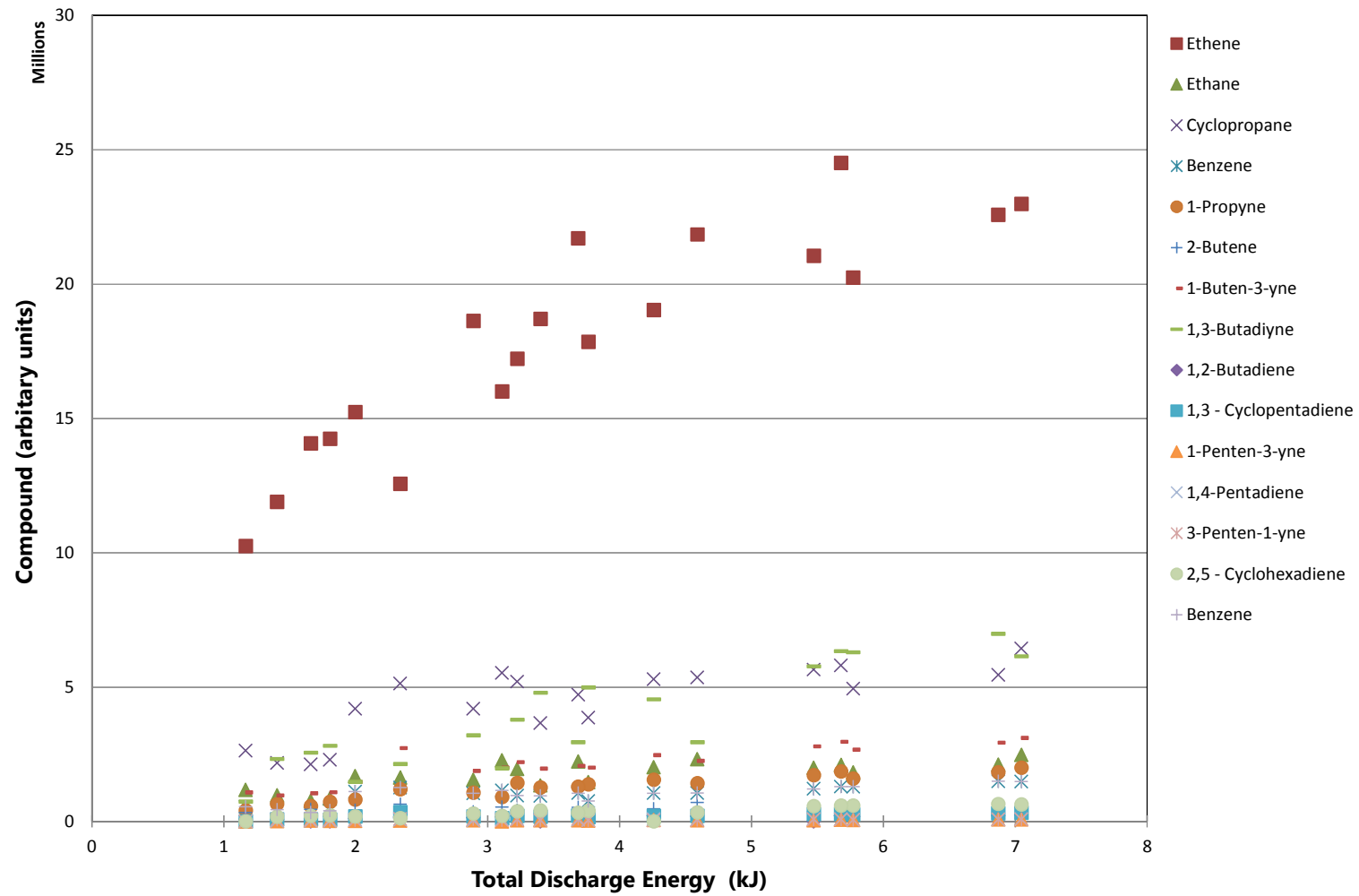


Figure 8.10: Other compound generation compared to the total discharge energy.

From Figure 8.11 a) it can be seen that ethene generation increases with discharge power and residence time. However, at residence time of 120 s ethene generation increases with discharge power up to 24 W, then a gradual decrease is seen as the discharge power is increased further. Even so, Figure 8.11 b) demonstrates a very clear pattern of ethene generation increasing with total discharge energy, and the above suggests this is mainly due to the residence time effect. A similar pattern is seen for the formation of 2,5 – cyclohexadiene, with compound generation increasing together with the discharge power and residence time, where residence time shows a higher effect. Figure 8.12 a) shows slight dip at residence time 2 min as the discharge power is increased to the maximum 31 W. A very clear pattern of 2,5 – cyclohexadiene generation increasing with total discharge energy is seen, and the above suggests this is mainly due to the residence time effect, see Figure 8.12 b).

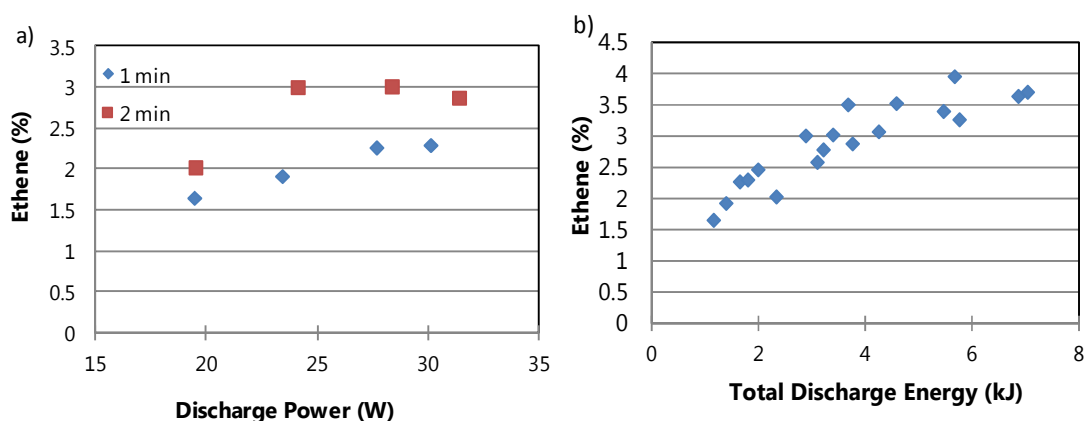


Figure 8.11: Shows the pattern of ethane generation against a) discharge power and residence time; b) total discharge energy.

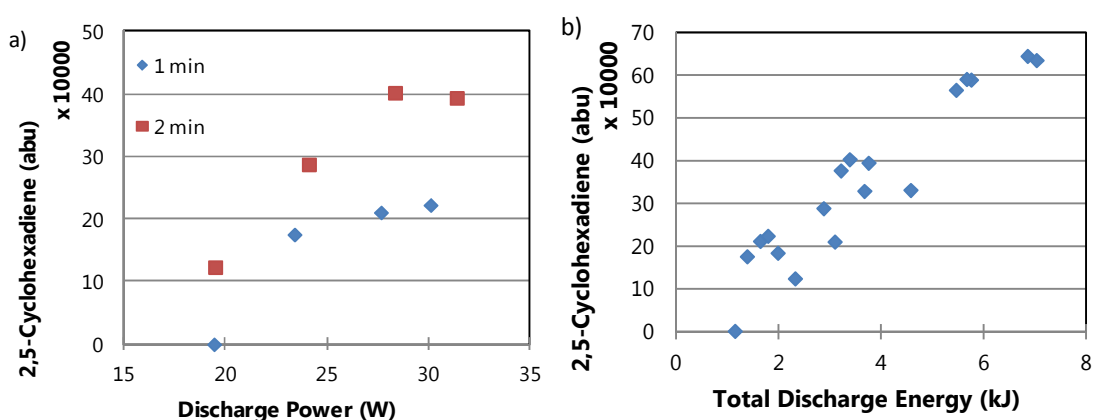


Figure 8.12: Shows the pattern of 2,5 - cyclohexadiene generation against a) discharge power and residence time; b) total discharge energy.

The generation of ethane decreases with the discharge power increase from 19 to 28 W, and then shows a slight increase at 30 W. However, the effects of residence time follows a distinctive trend as increasing the time from 1 to 2 min leads to an increase of ethane generation at all discharge powers, see Figure 8.13 a). Even at the counteracting effects of discharge power and residence time compound generation shows an increase with total discharge energy suggesting a very strong positive effect of residence time, see Figure 8.13 b). Interestingly, a nearly identical pattern is seen for cyclopropane generation, see Figure 8.14.

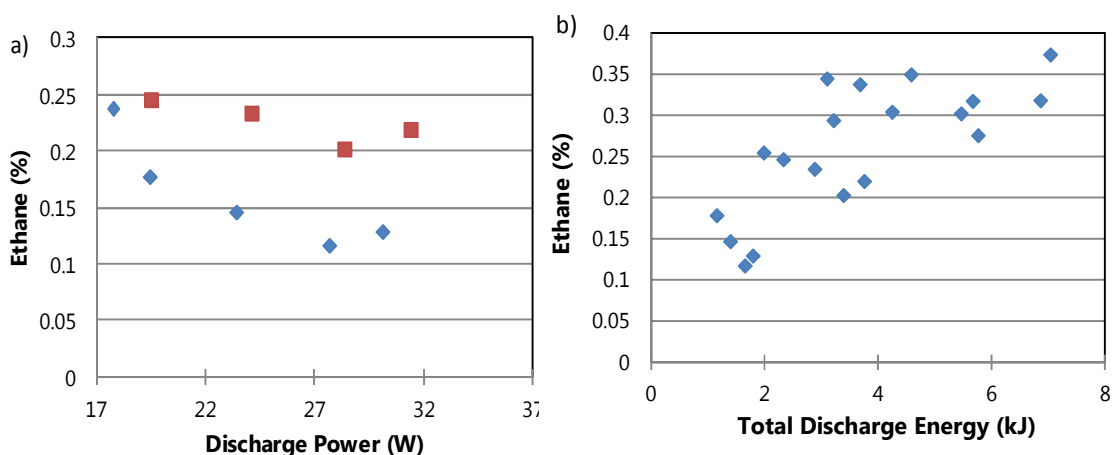


Figure 8.13: Shows the pattern of ethane generation against a) discharge power and residence time; b) total discharge energy.

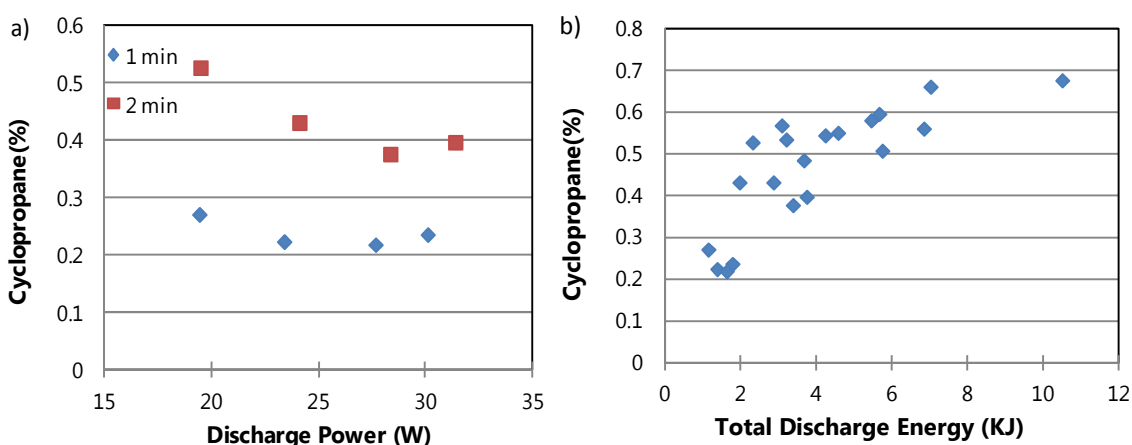


Figure 8.14: Shows the pattern of Cyclopropane generation against a) discharge power and residence time; b) total discharge energy.

Generation of 1-propyne and 1-buten-3-yne follows a very similar path, see Figures 8.15 and 8.16. In general discharge power has a positive effect on compound generation, with a decrease at certain power level only. Compound generation increases with the residence time at all discharge powers. Both compounds follow the trend of generation increase with overall discharge power increase. From Figures 8.15 a) and 8.16 a) it can be seen that the compound generation is mainly governed by the residence time.

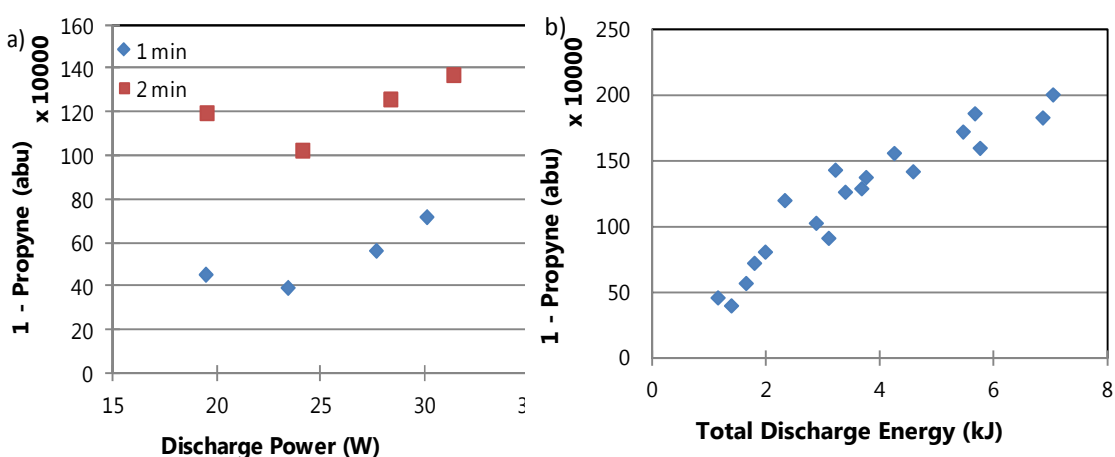


Figure 8.15: Shows the pattern of 1-propyne generation against a) discharge power and residence time; b) total discharge energy.

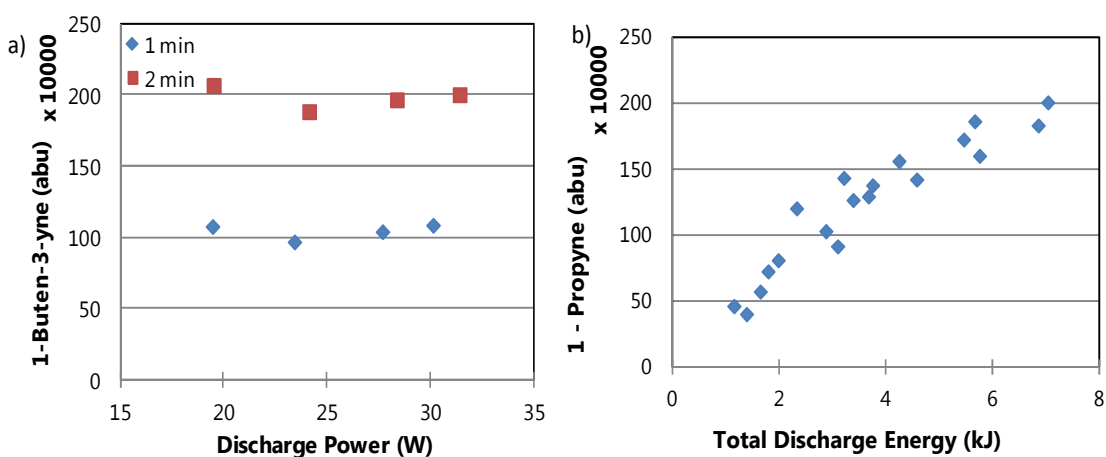


Figure 8.16: Shows the pattern of 1-buten-3-yne generation against a) discharge power and residence time; b) total discharge energy.

The generation of 1-penten-3-yne increases with discharge power up to 28 W, then a sharp decrease is seen at 31 W. Product generation increases with increasing residence time from 1 to 2 min at all discharge powers, see Figure 8.17 a). In general, 1-penten-3-yne generation increases with the total discharge energy, see Figure 8.17 b). Generation of 1,3-pentadiene follows a nearly identical trend, see Figure 8.18.

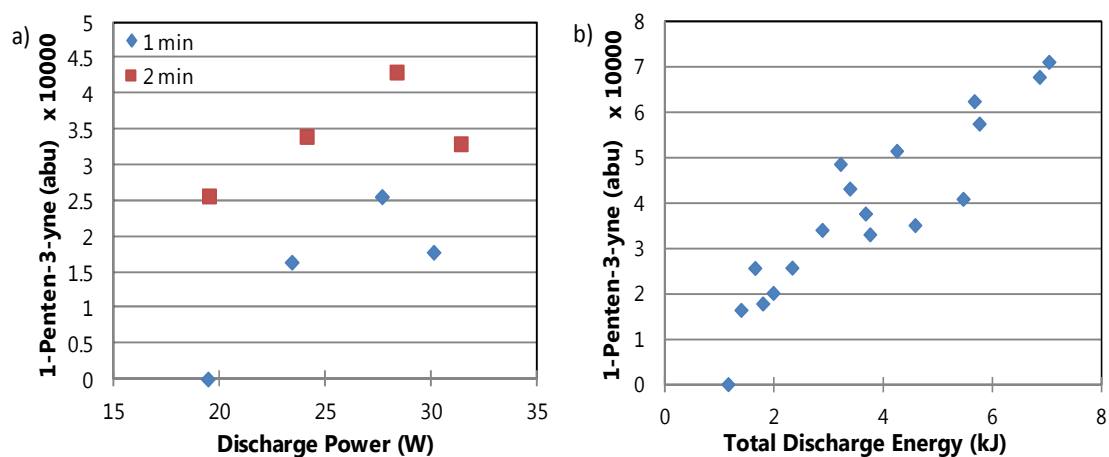


Figure 8.17: Shows the pattern of 1-penten-3-yne generation against a) discharge power and residence time; b) total discharge energy.

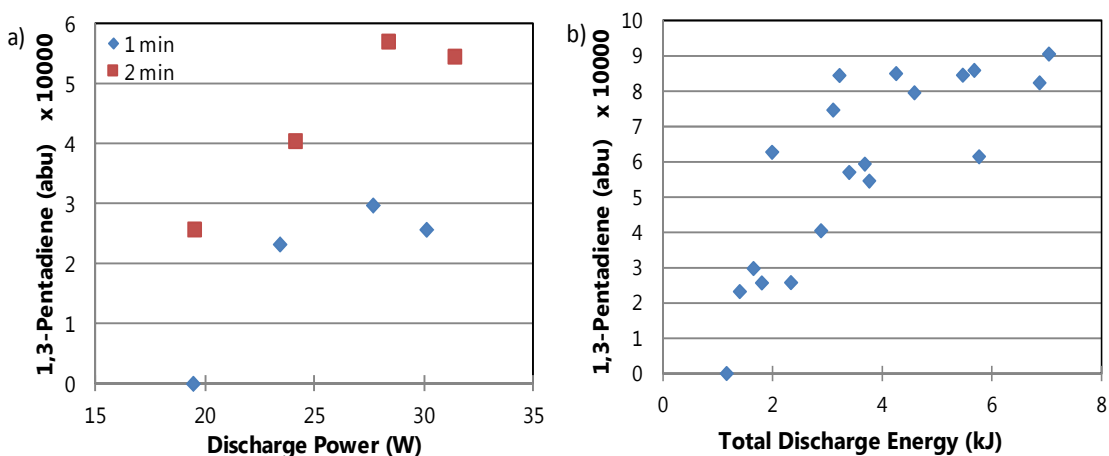


Figure 8.18: Shows the pattern of 1,3-pentadiene generation against a) discharge power and residence time; b) total discharge energy.

Benzene generation is favoured at lower discharge powers and higher residence times, see Figure 8.19 a). Figure 8.19 b) shows that in general benzene generation increases with total discharge energy suggesting a very strong positive effect of increasing residence time on benzene generation counteracting the negative effect of higher discharge powers. A very similar trend is seen for 1,3 – Cyclopentadiene generation, see Figure 8.20.

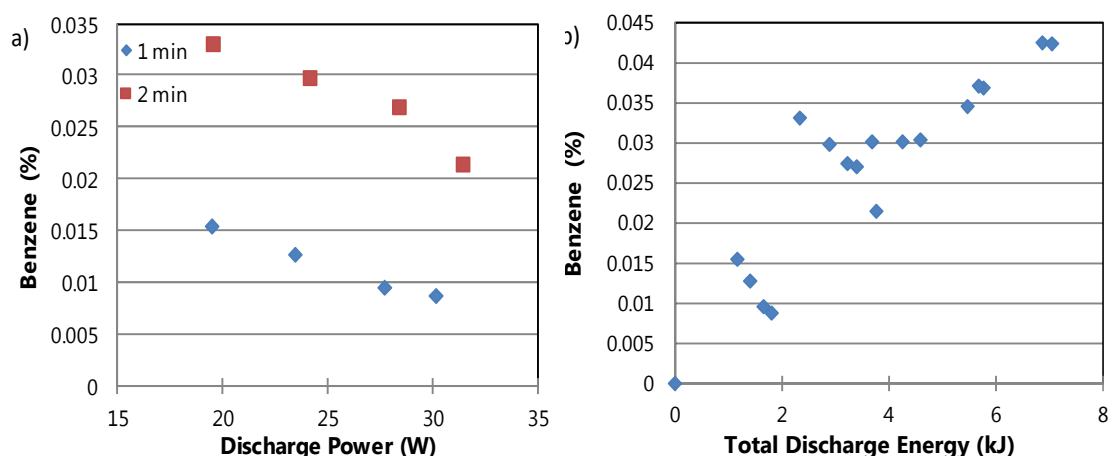


Figure 8.19: Shows the pattern of benzene generation against a) discharge power and residence time; b) total discharge energy.

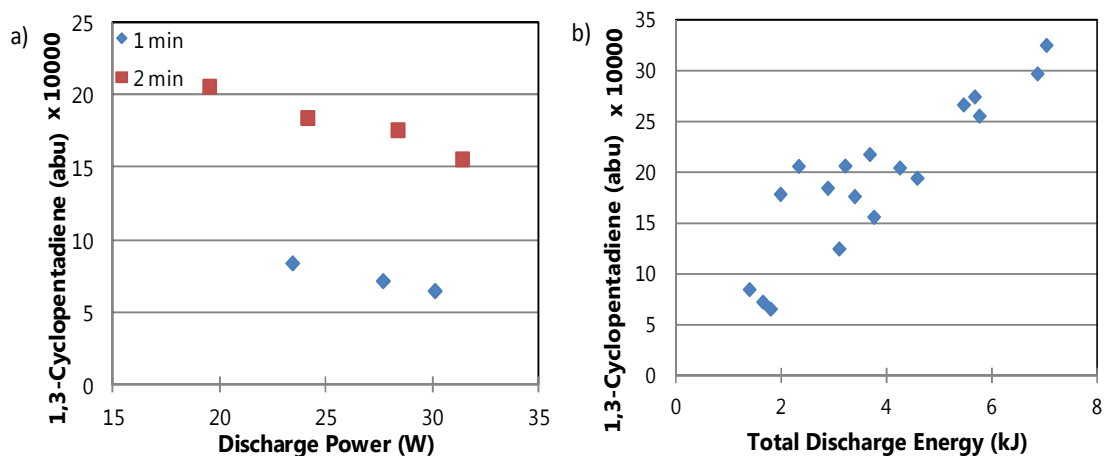


Figure 8.20: Shows the pattern of 1,3 - cyclopentadiene generation against a) discharge power and residence time; b) total discharge energy.

In general, the generation of 2-butene is favoured at lower discharge powers and higher residence times, see Figure 8.21 a). Therefore, due to the counteracting effects of discharge power and residence time, no distinctive trend with total discharge energy is seen, see Figure 8.21 b).

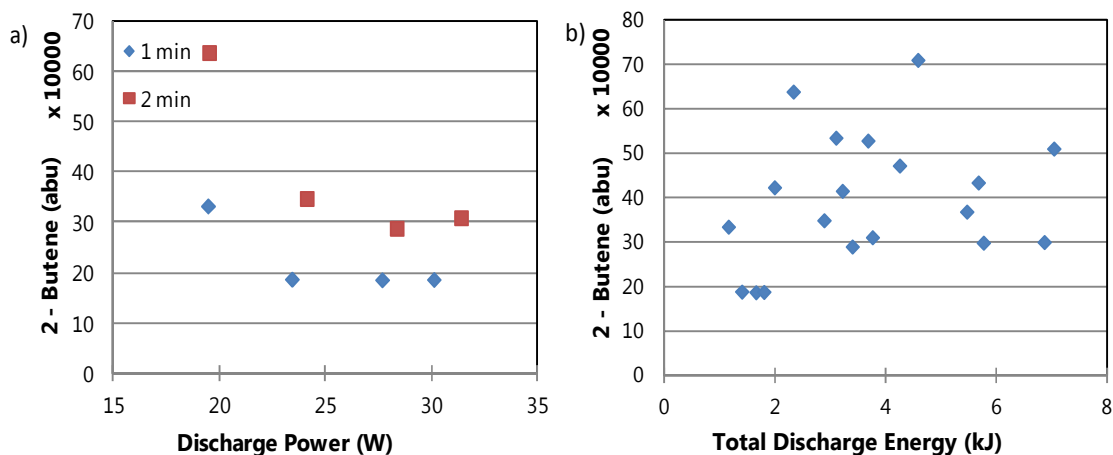


Figure 8.21: Shows the pattern of 2-butene generation against a) discharge power and residence time; b) total discharge energy.

The generation of 1,3-butadiyne, however, follows a very distinctive trend of increasing with both, the discharge power and the residence time, see Figure 8.22 a). Therefore, the overall effect results in compound generation increasing with total discharge energy, see Figure 8.22 b).

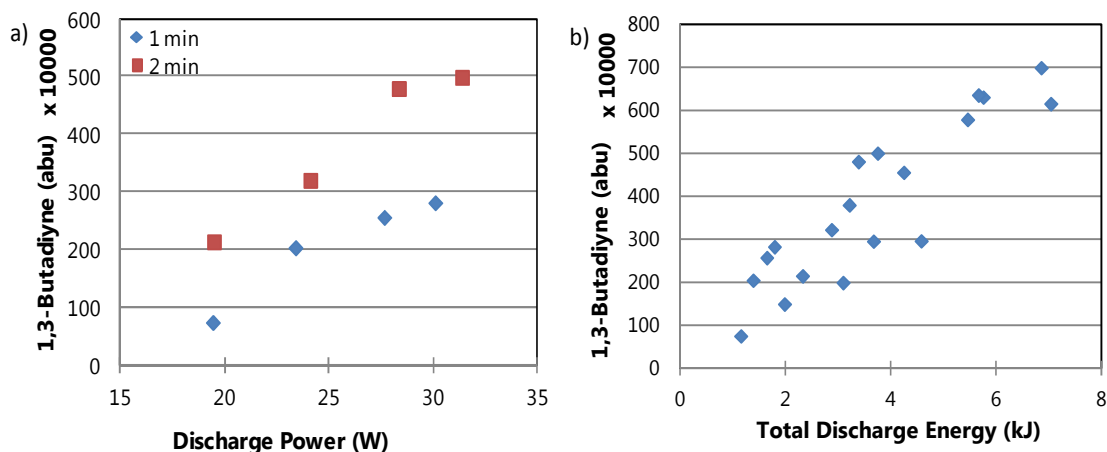


Figure 8.22: Shows the pattern of 1,3-butadiyne generation against a) discharge power and residence time; b) total discharge energy.

8.3 The effects of inter-electrode distance on hydrogen production

To evaluate the effects of inter-electrode distance on hydrogen generation experiments were performed at inter-electrode distances of 10, 15, 20, 25 and 30 mm, see Table 8.2 (the results for 15 mm inter-electrode distance have been presented in Table 8.1). Figure 8.23 shows that hydrogen generation at an inter-electrode distance of 20 mm follows the same trend of increasing with discharge power and residence time, as indicated in the first series at a distance of 15 mm. In general, an increase in inter-electrode distance led to an increase in discharge power and hydrogen production. The effect of discharge power is clearly seen when comparing the results at 1 min for the 15 and 20 mm inter electrode distances. Discharge power overlaps at 24, 29 and 31 W show identical hydrogen production percentages of 7, 8 and 9 % respectively, see Figure 8.23. Figure 8.24 shows the effect of total discharge energy on hydrogen generation at different residence times and inter-electrode distances. It is clearly seen that the total discharge energy, i.e. the combined effects of discharge power and residence time, are the key parameters affecting hydrogen production. Figure 8.25 shows that hydrogen generation increases nearly linearly with the total discharge energy with R^2 at 0.9459, regardless of the inter-electrode distance. For example, an increase in total discharge energy from 1 to 9.5 kJ has led to a hydrogen production increase from 4.7 to 28 %.

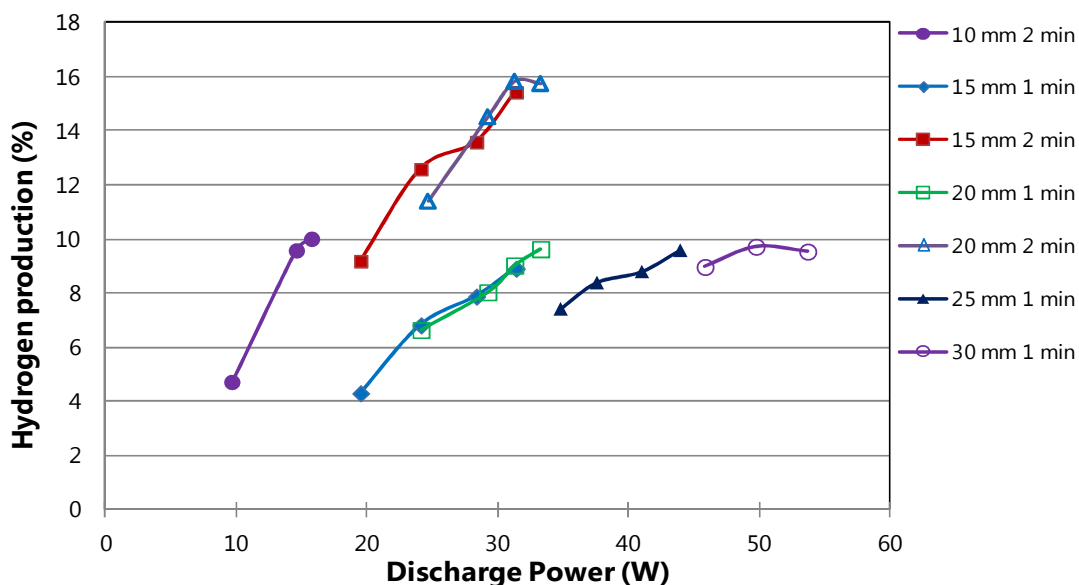


Figure 8.23: Shows hydrogen generation against discharge power at different residence times and inter-electrode distances.

Table 8.2: Experimental conditions and the results showing the data of hydrogen production for the experiments, testing the effects of inter-electrode distance.

Sample	Time (s)	Input kV	Discharge kV	Average current (mA)	Discharge power (W)	Total discharge energy (kJ)	Hydrogen production (%)
Inter-electrode distance 10 mm							
33	120	14	2.70	3.60	9.71	1.16	4.70
34	120	16	3.75	3.90	14.64	1.76	9.56
35	120	18	3.40	4.65	15.80	1.90	9.99
Inter-electrode distance 20 mm							
21	60	18	6.7	3.60	24.11	1.45	6.65
22	60	20	7.1	4.10	29.22	1.75	8.04
23	60	21	7.0	4.45	31.27	1.88	9.03
24	60	22	6.9	4.80	33.25	2.00	9.64
25	120	18	6.7	3.60	24.11	2.96	11.39
26	120	20	7.1	4.10	29.22	3.51	14.51
27	120	21	7.0	4.45	31.27	3.75	15.82
28	120	22	6.9	4.80	33.25	3.99	15.74
29	110	18	6.7	3.60	24.11	2.68	11.27
30	183	20	7.1	4.10	29.22	5.42	19.07
31	200	21	7.0	4.45	31.27	6.43	20.87
32	230	22	6.9	4.80	33.25	7.91	25.22
Inter-electrode distance 25 mm							
36	105	21	9.64	3.62	34.9	3.66	12.36
37	110	22	10.34	3.71	38.08	4.19	13.59
38	125	23	10.17	4.09	41.27	5.16	16.33
39	120	24	9.56	4.60	43.78	5.25	17.74
40	60	21	9.54	3.65			
41	60	22	9.28	4.05	34.81	2.08	7.42
42	60	23	9.65	4.25	37.59	2.25	8.39
43	60	24	9.56	4.6	41.03	2.47	8.80
Inter-electrode distance 30 mm							
44	60	24	12.02	3.82	45.83	2.75	8.98
45	60	25	12.44	4.00	49.73	2.98	9.72
46	60	26	12.62	4.26	53.68	3.22	9.54

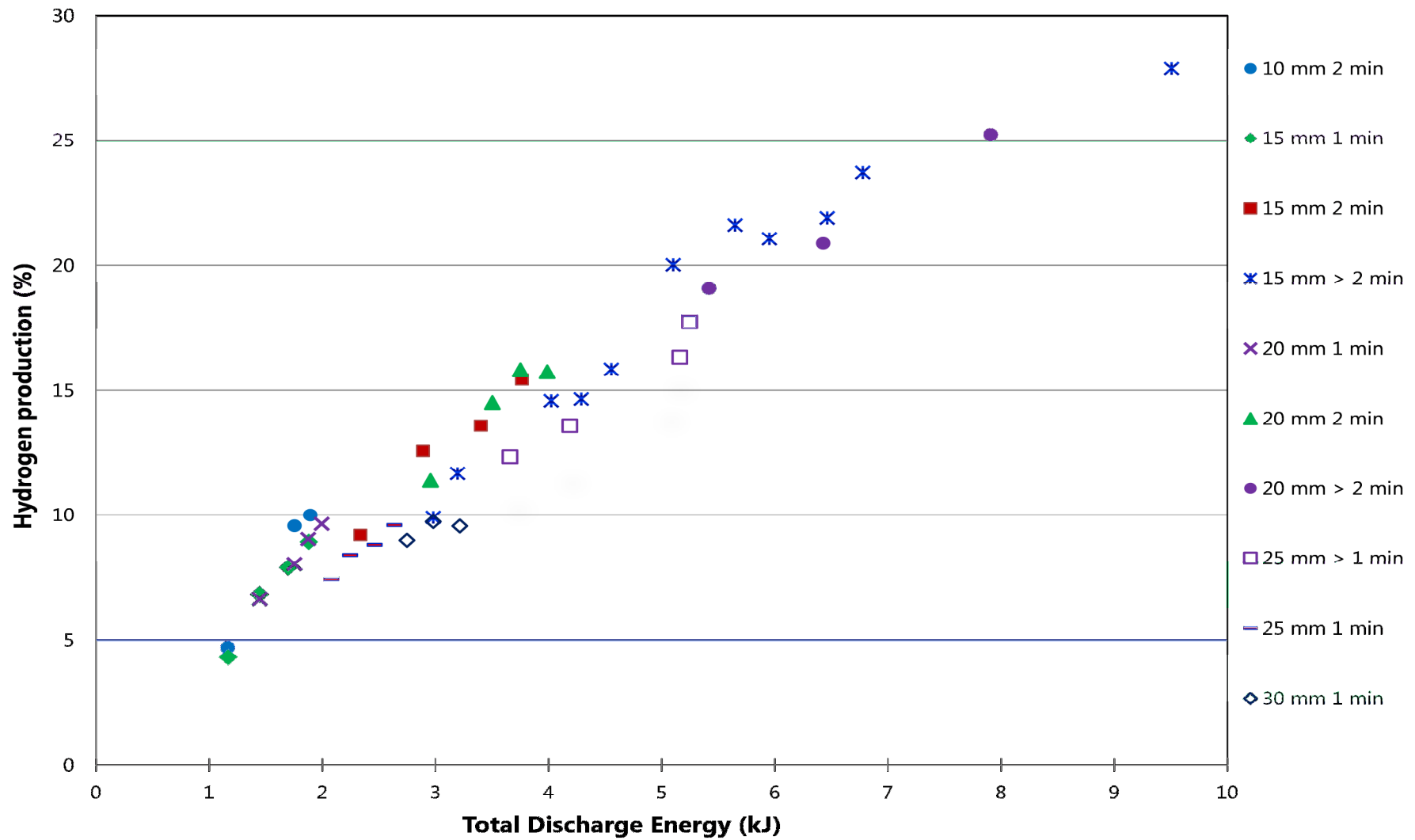


Figure 8.24: Shows hydrogen generation against total discharge energy at different residence times and inter-electrode distances.

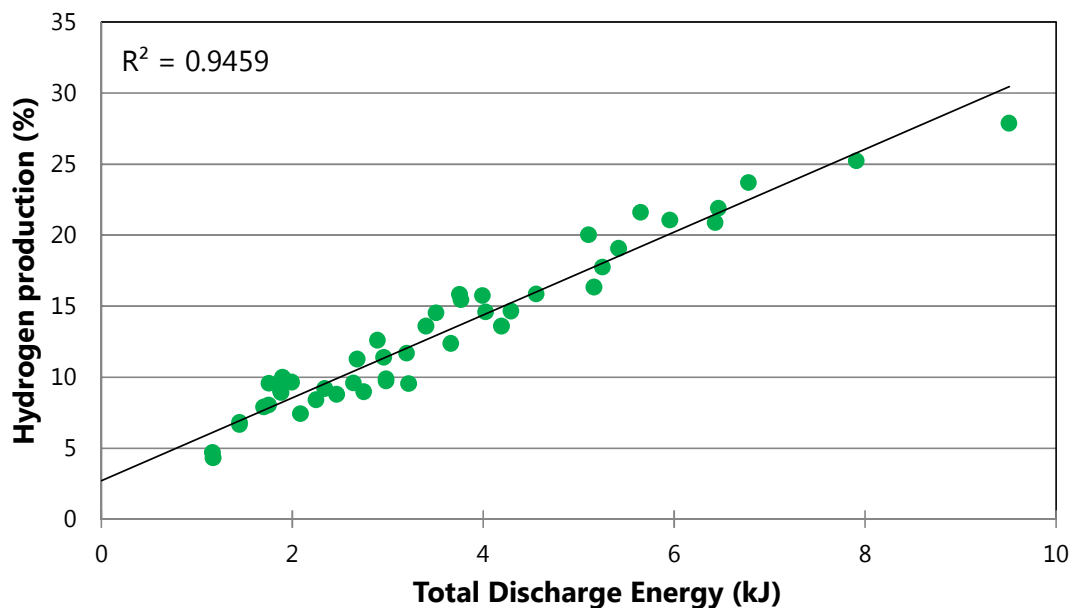


Figure 8.25: Shows nearly linear hydrogen increase with the total discharge energy at all inter-electrode distances.

8.3.1 Experimental Repeatability

To test the repeatability of the plasma chemical activity a set of experiments was repeated at an inter-electrode distance of 15 mm and a residence time 2 min, discharge power was varied in the same manner as for the original samples. Hydrogen is the smallest and the most important compound measured in this system. Therefore, the repeatability of the plasma unit is based on hydrogen production by volume. Figure 8.26 shows that hydrogen production is repeatable within the +/- 2.06 % error bars (the uncertainty for the hydrogen measurement by the GC).

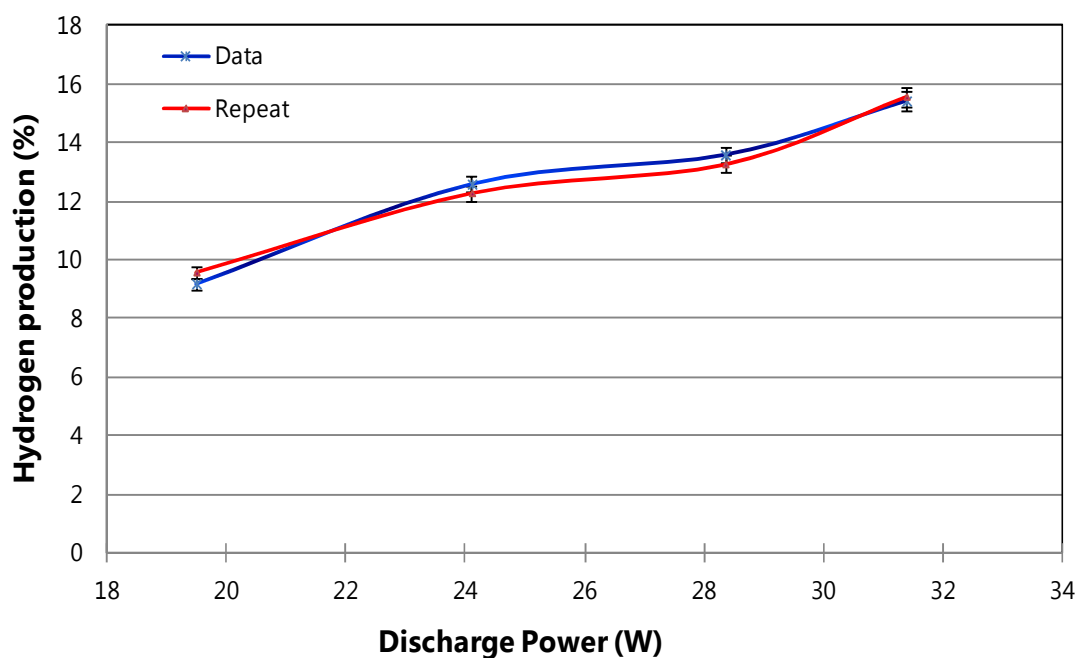


Figure 8.26: Hydrogen production repeatability at inter-electrode distance of 15 mm, residence time 2 min; the error bars for hydrogen measurement are at +/- 2.06 %

8.4 Summary

Three series of batch-process experiments have been performed to investigate the application of non-thermal plasmas to generate CO_x-free hydrogen from propane decomposition. The main series of experiments used an inter-electrode distance of 15 mm and a positive corona discharge. The effects of discharge power and residence time were studied on propane conversion, hydrogen selectivity and energy efficiency. Higher discharge powers and longer residence time favour the conversion of propane and the production of hydrogen. Energy conversion efficiency is mainly governed by hydrogen selectivity, due to its high calorific value. Hydrogen selectivity is affected by the generation of other compounds, most of which also increase with residence time and total discharge energy. In the second series of experiments the effects of varying inter-electrode distance was investigated, showing that hydrogen generation increases with increasing distance. A key conclusion from these tests is: hydrogen production is mainly governed by the total discharge energy, regardless of the inter-electrode distance.

In the main series of experiments, with 15 mm inter electrode distance, the highest percentage of hydrogen selectivity achieved was 33 % with propane conversion at 48 % and energy conversion efficiency of 11 % at 35 W discharge power and 303 s residence time.

Chapter 9: A comparative study of hydrogen generation methods and the potential of integrated PEMFC-CHP energy system

9.1. Introduction

The mitigation options to meet the ambitious carbon reduction targets set by the UK government are discussed in this chapter, including the use of carbon capture and storage technology (CCS), clean renewable energy integration and, a proposed system of integrated fuel cell combined heat and power (FC-CHP) technology. Analysis shows that the use of CCS technology within the current infrastructure can abate half the electricity associated CO₂ emissions. However, this comes at a high cost penalty. The emissions associated with domestic heat cannot be prevented without changes in the energy infrastructure. Hydrogen powered fuel cells can provide clean energy at a range of scales and high efficiencies, especially when employed as CHP systems. Production of CO₂ free hydrogen is essential for fuel cell technology to contribute substantially to a low carbon economy globally. In this work three methods are investigated for small scale distributed hydrogen production, namely steam methane reforming (SMR), water electrolysis (WE) and cold plasma jet (CPJ). The criteria used for comparisons include the associated CO₂ emissions and the cost of energy production. Cold plasma jet decomposition of methane shows a high potential when combined with integrated FC-CHP technology for economically viable and CO₂ free generation of energy, especially in comparison to water electrolysis. Including the value of the solid carbon product makes the plasma system most attractive economically.

The chapter is organised as follows. Section 9.2 describes the challenges in domestic energy supply together with the mitigating options available. Section 9.3 provides the data inputs and the description of methodology used for the analysis. Where in sections 9.4 and 9.5 the results and discussion of the study cases are presented, with the conclusions in section 9.6.

9.2. The domestic energy supply and CO₂ mitigating options

9.2.1. Domestic energy emissions

‘The built environment needs to develop more sustainable, less energy-intensive systems. The UK government has identified the house building industry as a key sector in delivering carbon reduction’ (Monahan and Powell, 2011). Domestic energy consumption for space and water heating, cooking, lighting and appliances is approximately 30 % of total energy use in the UK and contributes to 26 % of total UK carbon dioxide emissions, with average household emissions of 78 kg CO₂/m²/yr. Within a typical UK household, 58 % of the energy is used for space heating, 24 % for hot water and 19 % for cooking, lighting and appliance use (Monahan and Powell, 2011). As already been addressed throughout this work, hydrogen has long been recognised as a key alternative fuel to replace carbon based fossil fuels (Utgikar et al., 2011; Tseng et al., 2005; EC, 2003) in conjunction with the fuel cell technology (Aleknavičiute et al., 2012). The use of fuel cells could well be more acceptable to residential markets for on-site domestic heat and electricity production, than engine-based technologies involving moving parts, noise and vibration (Brown et al., 2007). The use of fuel cells can also reduce environmental emissions: carbon dioxide by 49 %, nitrogen oxide by 91%, carbon monoxide by 68 % and volatile compounds by 93 % when compared with traditional combustion technologies (Onovwiona and Ugursal, 2006). Fuel cells applied to distributed energy systems have the highest efficiencies (40 – 85 %) when compared to conventional means such as reciprocating diesel engine (35 %), turbine generator (29 – 42 %) photovoltaic (6 – 19 %) and wind turbine (25 %) (Mekhilef et al., 2011).

9.2.2. The PEMFC-CHP system

The main advantages of Proton Exchange Membrane Fuel Cells (PEMFCs) include reduced corrosion and electrolyte management problems due to the use of solid electrolyte, low temperature operation (50 – 100 °C) when compared to other fuel cell types; the systems are lightweight and compact with rapid start-up process. The main applications of PEMFCs include back-up power, portable power, small distributed generation, speciality vehicle and transportation (Mekhilef et al., 2011). PEMFCs are an attractive type of fuel cells due to their reliability and robustness (Venturelli et al., 2009). Venturelli et al. (2009) have shown that PEMFCs provide a

rapid response in the following electric load change at a constant efficiency. This benefits PEMFC systems for domestic applications, especially for comparisons with traditional technologies. PEMFCs are ‘currently the ones with the most advanced technological development and some cogenerative units are already commercialized’ (Barelli et al., 2012). In the industry review 2011, Fuel Cell Today wrote that ‘in terms of commercial success, the leader by far in terms of units shipments is the PEMFC’ contributing 97.03 % of shipments and 73.8 % of MW supplied when compared to other fuel cell types in 2010 (Fuel Cell Today, 2011). Japan Gas Association plans to market a high efficiency PEMFC residential cogeneration system with hot water storage tank equipped with back-up burner, a battery for electrical storage and self-diagnostic system; with a number of companies developing residential PEMFC systems (see Onovwiona and Ugursal, 2006). To date, more than 13, 307 CHP systems based on PEMFCs have been installed in general homes in Japan (Aki et al., 2012). A 2 year demonstration project has shown that PEM-CHP systems are technologically viable, without any faults or problems experienced during the experimental period whilst demonstrating a reduction in primary energy consumption and CO₂ emissions by 6 % and 11 %, respectively (Aki et al., 2012). Ling et al. (2010) have also concluded that PEM fuel cell CHP systems are currently technologically and economically feasible.

Compared to other fuel cell types, namely Solid Oxide Fuel Cell (SOFC) which can operate on natural gas directly (Yi et al., 2005), PEMFCs are more demanding because due to low operation temperature they require a supply of high purity hydrogen. The presence of CO and CO₂ can have detrimental effects on PEM fuel cells, as hydrogen dilution with CO₂ can cause a decrease in PEM electrical efficiency by 5 to 10 % (Atilla, 2008). Small scale stationary hydrogen generation is of high importance for advancement of the already most commercialized domestic PEMFC-CHP systems, when compared to other fuel cell types. At present hydrogen is produced almost exclusively through steam methane reforming (SMR), generating a significant amount of atmospheric CO₂ emissions (Abbas, 2010; Muradov and Veziroglu, 2005). Hence, for hydrogen powered fuel cells to contribute substantially to a low global carbon economy, hydrogen will need to be generated in an environmentally friendly manner. Mitigating options include the use of Carbon Capture and Storage technology and clean renewable technologies to reduce

electricity associated emissions, as well as alternative hydrogen generation method namely decomposition.

9.2.3. Carbon capture and storage (CCS)

CCS technology is endorsed by the IPCC and the UK government as ‘a key mitigation option for reducing the emissions from stationary sources such as fossil fuel power stations’ (Gough et al., 2010). CCS includes carbon capture, transportation and storage. The main cost of the CCS is the CO₂ capture ranging from 24 – 52 euro/tonne (equivalent to £ 19 – 43 at the exchange rate of € 1 = £ 0.8287). Transportation effects can vary depending on pipeline dimensions, CO₂ pressure and landscape characteristics, costing from 1 – 6 euro/tonne (£0.8287 – 5) per 100 km pipeline (Pires et al., 2011).

Different methods of CCS are being addressed, research focusing on economic feasibility and storage safety issues. However, technologies under development focus on large scale CO₂ sources such as power stations. Small scale CCS applications have not yet been shown to be viable, major problems occurring in the transport and storage of CO₂. Transportation from the distributed sources to storage sites is very costly and storage technologies are more economical when large amounts are stored at a time. A viable alternative technique proposed for small scale CCS is storage in shallow aquifers. But the technology has not yet been proven safe, and the possibility of leakage and contamination of usable groundwater is a specific uncertainty (Tokoro et al., 2011). With regards to CO₂ transport, the UK CCS Roadmap specifies that new pipelines will have to be built, necessitating a whole transport infrastructure. The main challenges within storage, include the design, quality of baseline, leakage, monitoring and liability (Gough et al., 2010), with safety and potential damage to the environment at the top of the list (Koorneef et al., 2012). The risk assessment and monitoring is still under research for long term geological storage (Fu and Gundersen, 2012). Storage and use of CO₂ in sites for enhanced fuel such as oil and gas recovery could be beneficial, as CO₂ can recover up to 12 % of the remaining fuels. However, for this to be possible the location of industrial sites becomes an important factor (Fu and Gundersen, 2012). The Department of Energy and Climate Change has recognised that reducing the risks

associated with CCS are some of the key challenges for deployment in the UK, even for large scale applications (DOECC, 2012a).

CCS has not yet been fully demonstrated on a commercial scale so the cost performances reported are based on feasibility studies and pilot projections, which still bear some uncertainty (IEA, 2011). It is difficult to predict the cost of CCS as it includes the transport and storage of carbon, of which transport is the major variant. Studies show that the cost of electricity generation with CCS post 2020 would increase by an average of 45 % (ZEP). CCS viability for applications in UK electricity generating industries was performed by Element Energy for the Committee on Climate Change (EECCC, 2010). The analysis shows that CCS has the potential to address up to 38 Mt of CO₂ emissions per annum in 2030 (decreasing to 37 Mt by 2050) for a cost range of £30 to £150 per tonne of CO₂ abated. The findings also reveal that the capital cost of the addition of post-combustion carbon capture equipment to gas powered stations almost doubles the total capital cost of the plant. Additional complications include gaining permission for a CO₂ pipeline route which combined with other factors is likely to lengthen the overall build time, if not a shut-down for the power station (EECCC, 2010).

9.2.4. CO₂ free hydrogen generation

Hydrocarbon pyrolysis is one alternative method for hydrogen generation, involving direct decomposition of gaseous hydrocarbons into hydrogen and carbon black (Fridman, 2008). The environmental advantages and the challenges of pyrolysis have already been addressed in Chapter 2, section 2.5, and plasma assisted hydrocarbon reforming has been addressed in Chapter 4. As a short summary, pyrolysis is environmentally friendly as it does not produce any CO_x compounds (Abbas and Daud, 2010; Ahmed et al., 2009; Dufour et al., 2009, 2010; Muradov and Veziroglu, 2005; Fulcheri and Schwob, 1995) and is more economical than SMR with carbon capture (Bockris, 2002). The current decomposition methodology employing catalysts is challenging due to catalyst degradation and instability (Rakib et al., 2010). However, problems associated with catalyst sensitivity and deterioration, can be eliminated or decreased by careful application of plasma technology, thereby achieving higher conversion efficiencies and increased specific productivity (Holladay et al., 2009; Fridman, 2008; Bromnerg et al., 2000).

Based on the above rationale, our case studies have focused on comparing a cold plasma jet with SMR (the most competitive fuel processor) and water electrolysis (another technology at an R&D stage). The cases are:

- (i) The current stage of hydrogen generation with the carbon charge;
- (ii) Hydrogen generation post 2020 with the integration of CCS;
- (iii) Hydrogen generation post 2035 with the integration of clean renewable energy
- (iv) PEMFC-CHP integration for direct electricity and heat generation. The UK National Grid energy supply for 2010 is also presented, showing the issues arising. The aim of this work is to identify the most economical path to eliminate or reduce CO₂ emissions for hydrogen production when applied to the domestic CHP supply chain.

9.3. Data inputs and methodology

9.3.1. National grid energy supply, emissions and costing

Energy supply and emissions data for the UK national grid for 2010 (DOECC, 2011) are used and given in Table 9.1. Also in Table 9.1 the total domestic energy supply efficiency is specified. This is calculated as follows. The Total domestic electricity supply (118, 681 GWh, at 39 % efficiency) means the total fuel consumed for domestic electricity supply is 304, 310 GWh (total supply divided by the efficiency factor of 0.39). The Total domestic heat supply from natural gas (350, 635 GWh, at 90 % boiler efficiency) means the total fuel consumed for domestic heat provision is 389, 594 GWh (total heat supply divided by the boiler efficiency factor of 0.9). Then, using a generic definition for the total efficiency (E_T) of a system:

$$E_T = \frac{\text{Output energy}}{\text{Total primary input energy}} \quad (9.1)$$

and taking into account the transmission and distribution (TD) losses gives the overall efficiency of the energy supply system as 67.6 %.

Table 9.1: National grid energy supply and carbon dioxide emissions for 2010.

National Grid (2010)	Electricity		Heat
	Natural gas	Coal	Natural gas
Fuel used			
Total fuel consumed	371,736 GWh ¹	297,301 GWh ¹	
Electricity generated	175,003 GWh ¹	107,694 GWh ¹	
Used on works	3,180 GWh ¹	5,428 GWh ¹	
Supplied (gross)	171, 822 GWh ¹	102,266 GWh ¹	
Transmission losses	1.5 % ²	1.5 % ²	
Distribution losses	6.0 % ²	6.0 % ²	
Efficiency	42.5 %	34 %	
Total supply	63 %	37 %	
Average efficiency	39 %		90 % (boiler)
Total Domestic supply	118, 681 GWh ³		350, 635 GWh ⁴
Total domestic energy supply efficiency	67.6 %		
CO ₂ emissions	398 tonne/ GWh ⁵	909 tonne/ GWh ⁵	185 tonne/GWh ⁵
Average CO ₂ emissions	587 tonne/ GWh		
Domestic CO ₂ emissions 2010	69.66 Mt		64.87 Mt
	134.53 Mt		

All data taken from DOECC (2011): ¹ p. 143, table 5.6; ² p. 167, table 6H; ³ p138, table 5.2; ⁴ p. 112, table 4.2; ⁵ p. 126, table 5.A.

The second set of general data inputs are for the carbon, CCS and renewable energy integration cost calculations. These are given in Table 9.2. The data are for household ('end-user') energy prices for November 2011 (Europe's Energy Portal). Consequent hydrogen production calculations assume that the methane feedstock is via natural gas supply from the grid. The constitution of methane in natural gas is 70 – 90 %; taking the average 80 %, the price of methane is £ 0.048 per kWh. The Traded Carbon (TC) value is taken for 2010, and under the European Union Emissions Trading Scheme (EU ETS) is £13 tonne/CO₂ (£ 0.013 kg/CO₂) (DOECC, 2011a). Power station generated electricity in this scenario is part of the traded scheme, and its cost including the TC charge is £ 0.1465 kW/h. The corresponding Non-Traded Carbon (NTC) charge for 2010 under EU ETS is £55 tonne/CO₂ (£ 0.055 kg/CO₂). Household emissions from heating and small scale SMR both fall under this scheme (DOECC, 2011a).

Table 9.2: Data input for cost calculations.

		Cost reported	Cost calculated (£)
Natural gas		€ 0.0465 per kWh	0.0385 per kWh
Electricity		€ 0.1676 per kWh	0.1389 per kWh
	With TC		0.1465 per kWh
	With CCS		0.2014 per kWh
	Renewables		0.190 per kWh
Methane			0.0480 per kWh
Traded carbon value		£13 tonne/CO ₂	0.0130 kg/CO ₂
Non-traded carbon value		£55 tonne/CO ₂	0.0550 kg/CO ₂
Solid carbon Value	Low Quality	£ 200 tonne/C _S	£ 0.2 kg/C _S
	High Quality	£ 1000 tonne/C _S	£ 1 kg/C _S

The reduction in efficiency for coal and gas power plants with CCS is approximately 8 % (IEA). Hence, the net average efficiency for UK grid electricity supply with CCS in 2010 is 31 %. For post 2020 conditions it has been estimated that the cost of electricity generation with CCS will have increased by 45 % (ZEP). Therefore, it can be reasonably assumed that retail electricity will increase by the same rate to £ 0.2014 per kWh, as in Table 9.2. Again it has been estimated that CCS will be able to process up to 38 Mt of CO₂ emissions per annum by 2030 (EECCC, 2010), which is equivalent to 55 % of total electricity related CO₂ emissions for 2010. A US Department of Energy analysis predicts that electricity related CO₂ emissions can be reduced by 60 % by 2035 under the Clean Energy Standard. This involves the integration of clean energy: nuclear, hydro, geothermal, municipal waste, solar, wind and biomass (EIA, 2011). However, this integration will result in a 27 % increase in the electricity price to £ 0.190 per kWh.

Turning to emissions, the total CO₂ released by a) domestic electricity consumption is 69.66 Million tonnes (average CO₂ emissions per GWh supplied X GWh supplied); these are accounted as TC emissions with a total carbon cost of £ 905.58 Million. The corresponding CO₂ emissions from b) domestic heat consumption are 64.87 Million tonnes these are accounted as NTC emissions, the carbon cost being £ 3,568 Million. The retail costs of electricity and natural gas are given in Table 9.2 as £0.1389 and £0.0385 per kWh respectively. The total annual cost is based on the retail cost of the energy supplied, excluding the carbon cost.

Finally, the Cold Plasma Jet has the potential to generate not only hydrogen, but solid carbon as well. This can be harvested and used in a variety of industrial processes. It has a commercial value of £ 200 to £ 1000 /tonne for Low Quality Solid Carbon (LQ C_S) and High Quality Solid Carbon (HQ C_S) respectively (Alibaba).

The fuel conversion efficiency (E_C) for the system is calculated as follows:

$$E_C = \frac{\dot{p}_{H_2} \times HHV_{H_2}}{\dot{c}_i \times HHV_i + P} \times 100 \quad (9.2)$$

where

\dot{p}_{H_2} amount of hydrogen generated (kg/s)

P is the electric power input (kJ/s)

HHV_{H_2} Higher Heating Value Hydrogen (141, 880 KJ/kg) (HARC)

\dot{c}_i amount of fuel consumed, i can be methane or natural gas (kg/s)

HHV_i Higher Heating Value of methane (55, 500 KJ/kg) or natural gas (52, 210 KJ/kg) (HARC)

9.3.2. Compound composition conversions

For gaseous compositions expressed volumetrically, rates of hydrogen production, natural gas consumption or carbon dioxide generation in kg/s are calculated using gas densities as:

$$\dot{m}_i = \dot{v}_i \times \check{D}_i \quad (9.3)$$

where

\dot{m}_i the flow rate of compound i (kg/s)

\dot{v}_i specified volumetric flow of compound i (m³/s)

\check{D}_i density of compound i (kg/m³)

At the standard pressure and temperature (STP) of 101.3 kPa and 273 K, one mole of an ideal gas occupies 22.4 litres, given by the ideal gas law (Kotz et al., 2009):

$$pv = n_i RT \quad (9.4)$$

where

n_i is the moles of a compound i

- v is the volume the gas occupies (L)
 T is the temperature (K)
 R is the universal gas constant (8.3145 J/mol K)

The density of a gas is defined by:

$$\check{D}_i = \frac{MW_i}{22.4} \quad (9.5)$$

where

\check{D}_i is the density of the gas i

MW_i is the molecular weight of the gas i

This gives the densities of hydrogen, methane and carbon dioxide at STP respectively as:

$$\check{D}_{H_2} = \frac{2}{22.4} = 0.089 \text{ kg/m}^3 \quad (9.5a)$$

$$\check{D}_{CH_4} = \frac{16}{22.4} = 0.71 \text{ kg/m}^3 \quad (9.5b)$$

$$\check{D}_{CO_2} = \frac{44}{22.4} = 1.96 \text{ kg/m}^3 \quad (9.5c)$$

9.3.3. Hydrogen generation cost

The alternative methods of reforming methane will require different forms and quantities of energy and will generate different amounts of hydrogen. The consumption of fuel, whether methane or natural gas, to generate 1 kg of hydrogen is given by:

$$C_i = \frac{\dot{c}_i}{\dot{p}_{H_2}} \quad (9.6)$$

where

i is the fuel: methane or natural gas

C_i amount of fuel i to generate 1 kg H_2 (kg)

\dot{c}_i consumption rate of fuel i (kg/s)

\dot{p}_{H_2} production rate of hydrogen (kg/s)

The electric power consumed is:

$$\dot{C}_{elec} = \frac{P}{\dot{p}_{H_2}} \quad (9.7)$$

where

\dot{C}_{elec} amount of electricity consumed to generate 1 kg H₂ (kW)

P electrical power rating of the reformer (kW/s)

\dot{p}_{H_2} production rate of hydrogen (kg/s)

Equation (9.7) gives the mass of fuel consumed in kg per kg of hydrogen. The price of natural gas, methane or electricity is normally expressed in £ per kWh. For costing calculations, the costs of methane and natural gas are obtained by conversion as follows:

$$\ddot{C}_i = \frac{C_i \times HHV_i}{3600} \quad (9.8)$$

where

\ddot{C}_i amount of fuel i to generate 1 kg H₂ (kWh)

C_i amount of fuel i to generate 1 kg H₂ (kg)

HHV_i Higher Heating Value of methane (55, 500 KJ/kg) or natural gas (52, 210 KJ/kg) (HARC)

3600 conversion factor from kW to kWh

For electricity conversion only the factor 3600 is required:

$$\ddot{C}_{elec} = \frac{\dot{C}_{elec}}{3600} \quad (9.9)$$

where

\ddot{C}_{elec} amount of electricity consumed to generate 1 kg H₂ (kWh)

\dot{C}_{elec} amount of electricity consumed to generate 1 kg H₂ (kW)

CO₂ emissions per kg H₂ generated by the SMR unit are calculated in a similar manner to equation (9.9):

$$C_{CO_2} = \frac{\dot{p}_{CO_2}}{\dot{p}_{H_2}} \quad (9.10)$$

where

C_{CO_2} amount of carbon dioxide emitted from the reformer to generate 1 kg of hydrogen (kg)

\dot{p}_{CO_2} production rate of fuel i (kg/s)

\dot{p}_{H_2} production rate of hydrogen (kg/s)

CO₂ emissions from UK power station electricity generation are calculated using data from Table 9.2 (0.587 kg CO₂ per kWh supplied):

$$CO_{2\ elec} = 0.587 \times \dot{C}_{elec} \quad (9.11)$$

where

$CO_{2\ elec}$ carbon dioxide emissions from the power station (kg)

\dot{C}_{elec} amount of electricity consumed to generate 1 kg H₂ (kWh)

The cost of generating hydrogen is the sum of the price of the input fuels, in the form of electricity and or methane/natural gas, as given by equations (9.9) – (9.11). For a SMR unit the Non-Traded Carbon Charge (NTCC) is also added. The cost is calculated as follows:

$$\pounds\ kg\ H_2 = \dot{C}_i \times \pounds_i + \dot{C}_{elec} \times \pounds_{elec} + C_{CO_2} \times NTCC \quad (9.12)$$

where

\dot{C}_i amount of fuel x to generate 1 kg of hydrogen, where i is natural gas or methane (kWh)

\pounds_i the cost of fuel i , where i is natural gas or methane (£/kWh)

\dot{C}_{elec} consumption of electricity to generate 1 kg of hydrogen (kWh)

\pounds_{elec} the cost of electricity (£/kWh)

C_{CO_2} amount of carbon dioxide emitted from the reformer to generate 1 kg of hydrogen (kg)

NTCC Non Traded Carbon Charge (£0.055)

9.3.4. Input data for hydrogen generation systems

The specifications for a commercial SMR unit (Helbio APS 1000) are given in Table 9.3.

Table 9.3: Steam methane reformer input and calculated data.

SMR (Helbio APS 1000 reformer)	Supplier Specifications	Calculated
Hydrogen production rate	1.2 Nm ³ /h	2.97 X 10 ⁻⁵ kg/s
Natural gas consumption rate	0.43 Nm ³ NG/ Nm ³ H ₂	1.02 X 10 ⁻⁴ kg/s
Electrical rating	0.096 kW	
Reformate Stream constituents by volume	74 % H ₂ 24 % CO ₂ 2 % CH ₄	2.12 X 10 ⁻⁴ kg /s
CO ₂ emissions		2.12 X 10 ⁻⁴ kg /s 7.14 kg/kg H ₂
Efficiency		77.7 %

From these the following input data are calculated. The content of hydrogen and CO₂ in the product stream are 74 % and 24 % respectively by volume, the production rate of hydrogen is 3.33 X 10⁻⁴ m³/s (1.2 m³/h as supplied divided by 3600) and the density of CO₂ is 1.96 kg/m³ (equation 8.3). The production rate of CO₂ is calculated from:

$$\dot{p}_{CO_2} = \dot{p}_{H_2} \times Cr_{H_2:CO_2} \times \check{D}_{CO_2} = 2.12 \times 10^{-4} \text{ kg/s} \quad (9.13)$$

where

\dot{p}_{CO_2} production rate of CO₂ (kg/s)

\dot{p}_{H_2} production rate of H₂ (3.33 X 10⁻⁴ m³/s)

$Cr_{H_2:CO_2}$ the ratio of CO₂ to H₂ production to by volume (0.324)

\check{D}_{CO_2} density of CO₂ (1.96 kg/m³)

Using equation (9.10), for generation rates of CO₂ (2.12 X 10⁻⁴ kg/s) and H₂ (2.97 X 10⁻⁵ kg/s) gives 7.14 kg of CO₂ generated per 1 kg of H₂.

Domestic electrolyser technology is at the ‘R&D’ stage. The data used for this work was reported for the DOE by EPRI funded research (Rastler, 2008) as given in Table 9.4.

Table 9.4: Home water electrolyser specifications and calculated data.

Home Electrolyser	Specifications reported (Rastler, 2008)	Calculated
Power rating	6.3 kW	
Hydrogen production rate	1 kg/day at 8h operation	3.47×10^{-5} kg/s
Energy Conversion Efficiency		78.1 %

Cold plasma conversion of methane to hydrogen is also at the R&D stage. The data used for this work is from the non-thermal plasma jet experiments reported by Li et al. (2009). These are given in Table 9.5.

Table 9.5: Data input for the plasma jet.

Plasma Jet Parameters	Reported parameters (Li et al., 2009)	Calculated parameters
Power rating	69.85 W	
Methane conversion	60.97 %	
Hydrogen selectivity	89.3 %	
Methane flow rate	880 ml/min	1.04×10^{-5} kg/s
Methane consumption rate		6.4×10^{-6} kg/s
Hydrogen production rate		1.43×10^{-6} kg/s
Conversion Efficiency		47.7 %

The mass flow rate of methane \dot{m}_{CH_4} was calculated from equation (9.3), its density being 0.71 kg/m^3 (equation (9.5b)). The methane consumption rate \dot{c}_{CH_4} is calculated from the mass flow rate, using the reported methane conversion rate of 60.97 % (Table 9.5):

$$\dot{c}_{CH_4} = \dot{m}_{CH_4} \times Conv_{CH_4} \quad (9.14)$$

where

\dot{c}_{CH_4} methane consumption rate (kg/s)

\dot{m}_{CH_4} methane flow rate (kg/s)

$Conv_{CH_4}$ methane conversion rate (percent fraction)

The hydrogen generation rate is calculated from the reported hydrogen selectivity of 89.3 % and the methane consumption rate:

$$\dot{p}_{H_2} = \dot{c}_{CH_4} \times 2 \times S_{H_2} \quad (9.15)$$

where

\dot{p}_{H_2} hydrogen production rate (mol/s)

\dot{c}_{CH_4} methane conversion rate (mol/s)

S_{H_2} hydrogen selectivity (percent fraction)

9.3.5. FC-CHP system specifications

The final comparison study involving an integrated Fuel Cell-Combined Heat and Power system (FC-CHP), uses as input data the specifications for the commercial PEMFC-CHP system developed by Ballard MK5-E PEMFC stack (Laurencelle et al., 2001). These, together with other (calculated) data are given in Table 9.6.

Table 9.6: Fuel Cell CHP system.

Fuel Cell Specifications (Ballard MK5-E PEMFC stack)	
Temperature	70 °C
Max output electric	4 kW
Max thermal recovered	3 kW
Power to heat ratio	1.33
Electrical efficiency	45 %
Thermal efficiency	35 %
CHP efficiency	80 %

The power to heat ratio (σ) for FC-CHP systems is defined by (Nesheim and Ertsevåg, 2007):

$$\sigma = \frac{w}{Q} \quad (9.16)$$

where

w is the electric energy generated
 Q is the thermal energy delivered in the stream

Electrical (E_{elec}) and thermal (E_Q) efficiencies are defined as the fractions of the input energy that are converted to electric and heat energy respectively (Nesheim and Ertsevåg, 2007):

$$E_{elec} = \frac{w}{HHV_{H_2}} \quad (9.17)$$

$$E_Q = \frac{Q}{HHV_{H_2}} \quad (C.18)$$

The overall efficiency (E) of systems that generate electricity and heat is defined as (Nesheim and Ertsevåg, 2007):

$$E = \frac{w+Q}{f} \quad (9.19)$$

where

f is the primary fuel input

Electricity generation from 1 kg hydrogen input using the data from Table 9.3 is calculated as follows:

$$w = E \times HHV_{H_2} \times \dot{p}_H \quad (9.20)$$

$$w = 0.45 \times 141880 \times 1 = 63846 \text{ kJ or } 17.735 \text{ kWh}$$

The power to heat ratio is 1.33 hence, the heat generated is 13.301 kWh (electricity generated/heat to electricity ratio).

9.4. UK National grid 2010 conditions

Figure 9.1 summarises diagrammatically the UK energy supply from the national grid in 2010 together with the costing and the associated CO₂ emissions, calculations and data inputs are given in section 9.3.1. Figure 9.1 a) shows an annual input of Natural Gas (NG) to meet the annual heat demand for UK households in 2010, assuming a high boiler efficiency of 90 %. The indicated outputs from the boiler

include: i) the amount of CO₂ released into the atmosphere along with the associated cost calculated from the non-traded carbon charge (top arrow); ii) the amount of the domestic heat supplied and the cost to the consumers (right arrow). Figure 9.1 b) shows the annual input of NG and coal that is required by the various power stations in the UK to meet the household electricity demands for 2010. The outputs from the power station include: i) the amount of CO₂ released into the atmosphere and the associated cost calculated using the traded carbon charge (top arrow); ii) the amount of domestic electricity supplied including the distribution losses as well as the cost to consumers (right arrow). From Figure 9.1 it can be seen that the demand for domestic heat in the UK is nearly three times higher than that for electricity. The annual CO₂ emissions from power stations and domestic boilers is similar, but the CO₂ cost is nearly four times higher for the domestic boiler, and this can be attributed to higher charges for non-traded carbon compared to traded carbon, see section 9.3.1, Table 9.2.

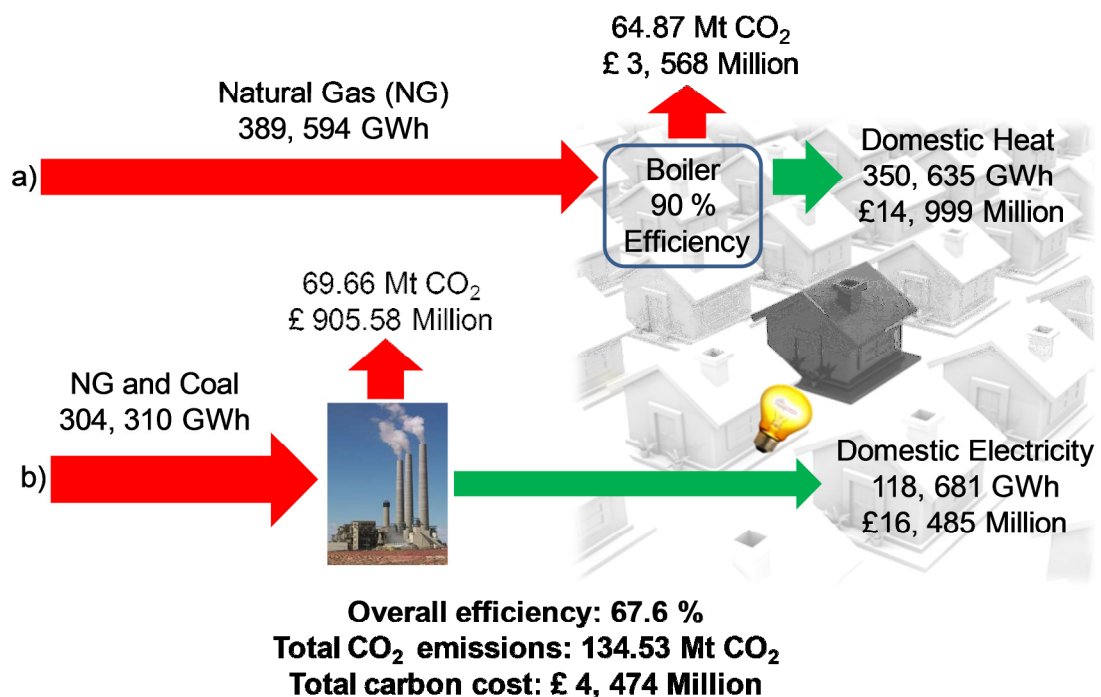


Figure 9.1: Summary of domestic a) heat and b) electric energy supply from the National Grid in 2010 and associated carbon dioxide emissions. Notes: i) the costing is for the retail price for total energy consumed; ii) the heat and electricity cost does not include the stated carbon charge.

Using the same 2010 data and principles shown in Figure 9.1, but now incorporating CCS into the power station results in changes illustrated in Figure 9.2. As discussed in section 9.2.3 CCS is not viable at small scale, in the foreseeable future, and therefore emissions from domestic heat generation cannot be reduced by CCS. This means the inputs and outputs shown in Figure 9.2 a) for domestic heat supply are the same as for Figure 9.1 a). It has been shown that the incorporation of CCS would decrease the efficiency of the power station by approximately 8 % (IEA). Therefore, the NG and coal demand for the power stations shown in Figure 9.1 b) will need to increase to meet the same domestic electricity demand, as illustrated in Figure 9.1 b). The addition of CCS to the power station would result in an increase in the cost of electricity to the consumer of 45 % (ZEP), this can be seen when comparing the total annual cost of electricity to the consumer in Figure 9.1 b) (£ 16, 500) with Figure 9.2 b) (£ 24,000). The overall process efficiency is decreased and the retail cost of electricity steeply increases with the addition of CCS. If large scale CCS becomes commercially viable as planned post 2020 over half of the emissions from the UK electricity supply sector can be eliminated. However, as shown this brings a financial penalty to the power stations and the consumer. CO₂ emissions from domestic heating cannot be abated by CCS, and the major cost of CO₂ emissions remains.

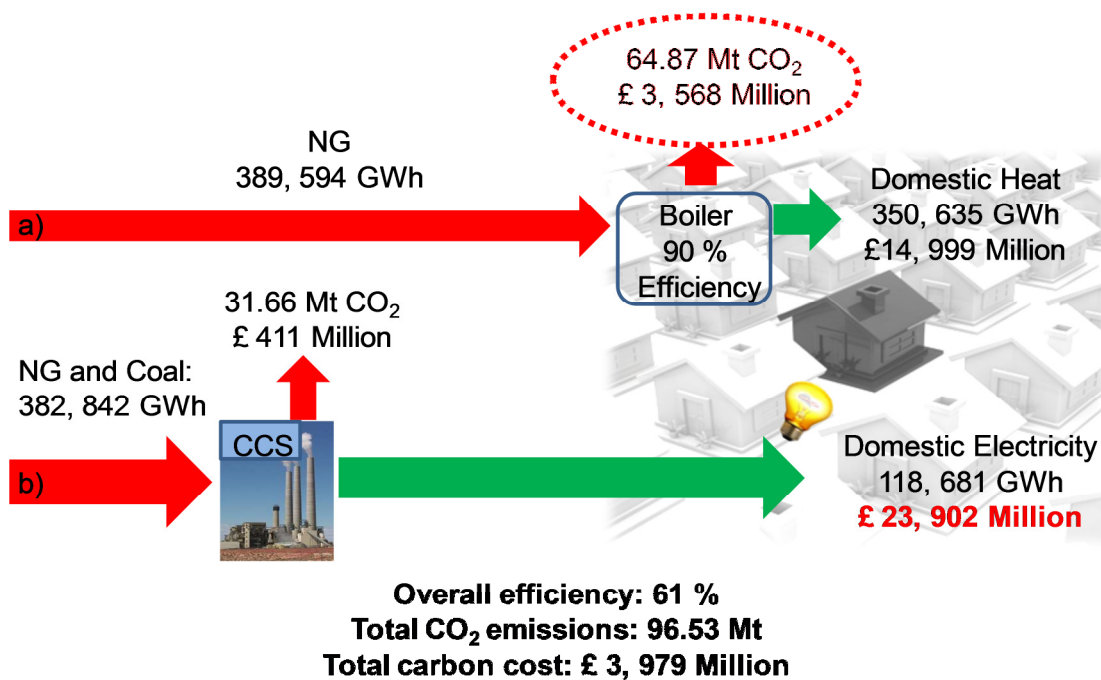


Figure 9.2: Summary of domestic a) heat and b) electric energy supply from the National Grid using 2010 data with future anticipated CCS. Notes: i) the costing is for the retail price for total energy consumed. ii) the heat and electricity cost does not include the stated carbon charge.

9.5. Comparison of hydrogen generation systems

9.5.1. Current conditions with carbon value

The rationale of this study is to compare three hydrogen generation alternatives which are: Steam Methane Reforming (SMR), Water Electrolysis (WE) and Cold Plasma Jet (CPJ). Calculations for cost and CO₂ emissions to generate 1 kg of hydrogen under current conditions (data for 2010), leads to the results shown in Figure 9.3 and Table 9.7. Figure 9.3 shows the amount of NG and coal required by the power station along with the CO₂ emissions from the power station to generate the electricity needed by the reformer to produce 1 kg of hydrogen (including transmission and distribution losses), and the associated end-user cost has also been calculated. The inputs and outputs of the three reformers are not limited to just electricity and hydrogen respectively: i) for SMR the amount of natural gas input and the end-user cost is shown, together with the amount of CO₂ emissions released from the reformer and the cost at non-traded carbon rate; ii) for WE water is required with oxygen output; iii) for CPJ the amount of natural gas input and the end-user cost is shown, together with the amount of solid carbon generated.

The following conclusions can be drawn from these calculations. CPJ is competitive with SMR in terms of CO₂ emissions, the overall hydrogen cost is lowest using SMR (with CPJ coming second ahead of WE, see Figure 9.3 and Table 9.7). It is important to note that CPJ also generates commercially valuable solid carbon (C_S), hence, the cost of hydrogen should be analysed under the following conditions: no C_S credit (£0 per kg C_S), Low Quality Carbon credit (LQ C_S - £0.2 per kg C_S) and High Quality Carbon credit (HQ C_S - £1 per kg C_S), see Table 9.2. When the value of the solid carbon product of CPJ is taken into account, the effective hydrogen cost reduces from £ 5.304 kg/H₂ (no C_S credit) to £ 4.704 and £ 2.304 kg/H₂, for LQ C_S and HQ C_S respectively. The HQ value makes CPJ directly competitive with SMR. *The striking effect of the C_S credit (especially for HQ) holds for all of the cases in this study.* WE shows substantially lower potential than CPJ in terms of hydrogen generation cost and CO₂ emissions.

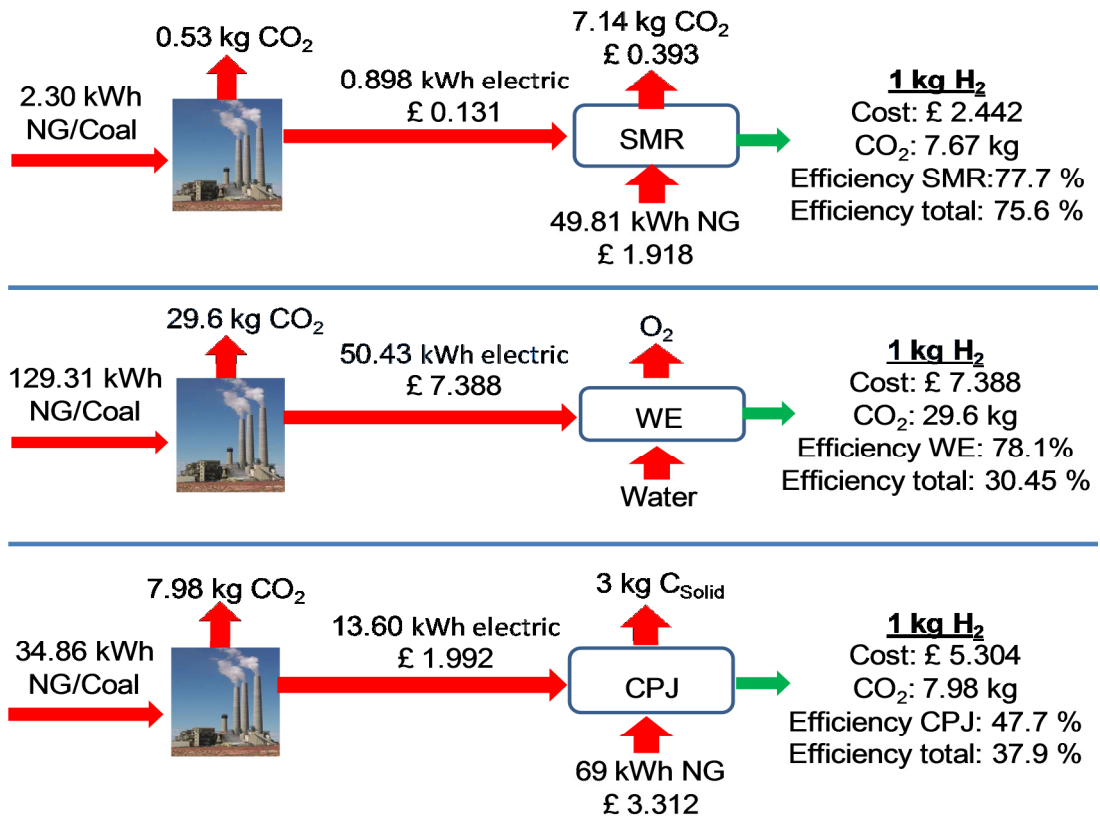


Figure 9.3: Summary diagrams for system analysis for hydrogen generation under current conditions, carbon charges included.

Table 9.7: Summary of system analysis for hydrogen generation under current conditions, where LQ C_s and HQ C_s stand for low and high quality solid carbon price respectively.

	SMR	WE	CPJ		
			No C _s credit	LQ C _s	HQ C _s
Energy Conversion Efficiency	77.7	78.1	47.7	47.7	47.7
Overall System Efficiency	75.6	30.45	37.9	37.9	37.9
Hydrogen cost (£/kg)	2.442	7.388	5.304	4.704	2.304
CO₂ emissions (kg CO₂/kg H₂)	7.67	29.60	7.98	7.98	7.98

9.5.2. Post-2020 scenario with CCS

For a post-2020 scenario, allowing for the inclusion of CCS, results of the comparative system analysis of the three reformers are shown in Figure 9.4 and Table 9.8. Figure 9.4 follows the same approach as for Figure 9.3 showing all inputs, outputs and costs to generate 1 kg of hydrogen. As already addressed in Section 9.4, the addition of CCS could reduce the CO₂ emissions from the power station by 55 % at a cost of decreasing the efficiency of the power station by 8 %, whilst increasing the end-user electricity cost by 45 %. This is taken into account when comparing the three systems.

The addition of CCS has a very low impact on SMR as the electricity consumption is very low and the majority of the emissions associated are from the SMR itself. Since the CO₂ emissions for WE and CPJ are only related to the electricity consumption both cases decrease by 55 %. For this scenario the hydrogen generation cost for WE increases drastically by nearly £3 per kg H₂ as all of the primary energy for WE comes in the form of electricity. The hydrogen cost using CPJ only increases by £0.806 per kg H₂ as CPJ is not primarily electricity dependant, the majority of energy required is in the form of methane. CO₂ emissions for CPJ in this scenario are nearly half those of SMR; for WE the CO₂ emissions are again the highest.

Table 9.8: Summary of the system analysis for hydrogen generation post 2020 with CCS.

	SMR	WE	CPJ		
			No C _s credit	LQ C _s	HQ C _s
Energy Conversion Efficiency	77.7	78.1	47.7	47.7	47.7
Overall System Efficiency	74.8	24.2	34.9	34.9	34.9
Hydrogen cost (£/kg)	2.495	10.320	6.098	5.498	3.098
CO₂ emissions (kg CO₂/kg H₂)	7.38	13.32	3.59	3.59	3.59

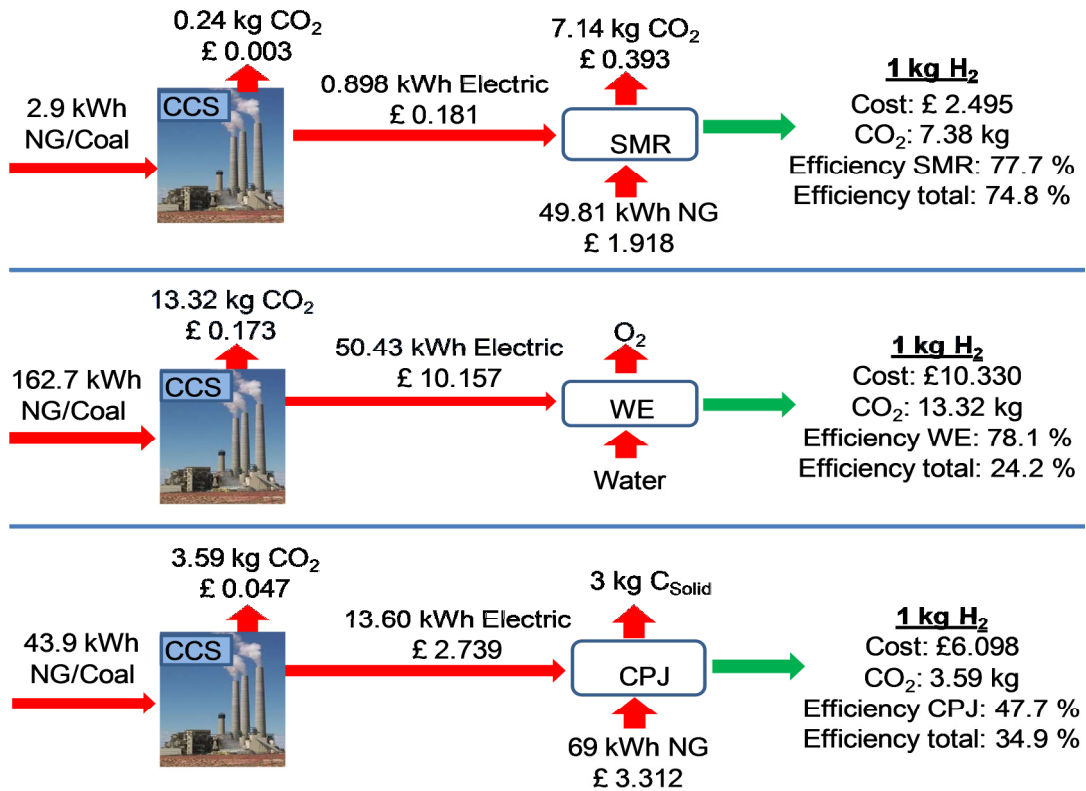


Figure 9.4: Summary of the system analysis for hydrogen generation post 2020 with CCS.

9.5.3. Post- 2035 scenario with renewables integration

Another important scenario for 2035 will be the penetration of renewable and their contributing to the national energy mix. It is anticipated that the integration of renewable could address up to 60 % of the CO₂ emissions from power stations at a penalty of end-user electricity costs increasing by 27 %. Results of the system analysis are shown in Figure 9.5 and Table 9.9. With this scenario little effect is seen for the SMR system *vis a vis* the post-2020 scenario. WE and CPJ both show lower CO₂ emissions and hydrogen cost with renewables integration when compared to the post-2020 scenario with CCS. The cost of hydrogen for WE and CPJ is higher with renewable integration than under the current conditions, as expected due to the increase of the electricity cost. Cold plasma jet has the lowest CO₂ emissions under this scenario with SMR coming second.

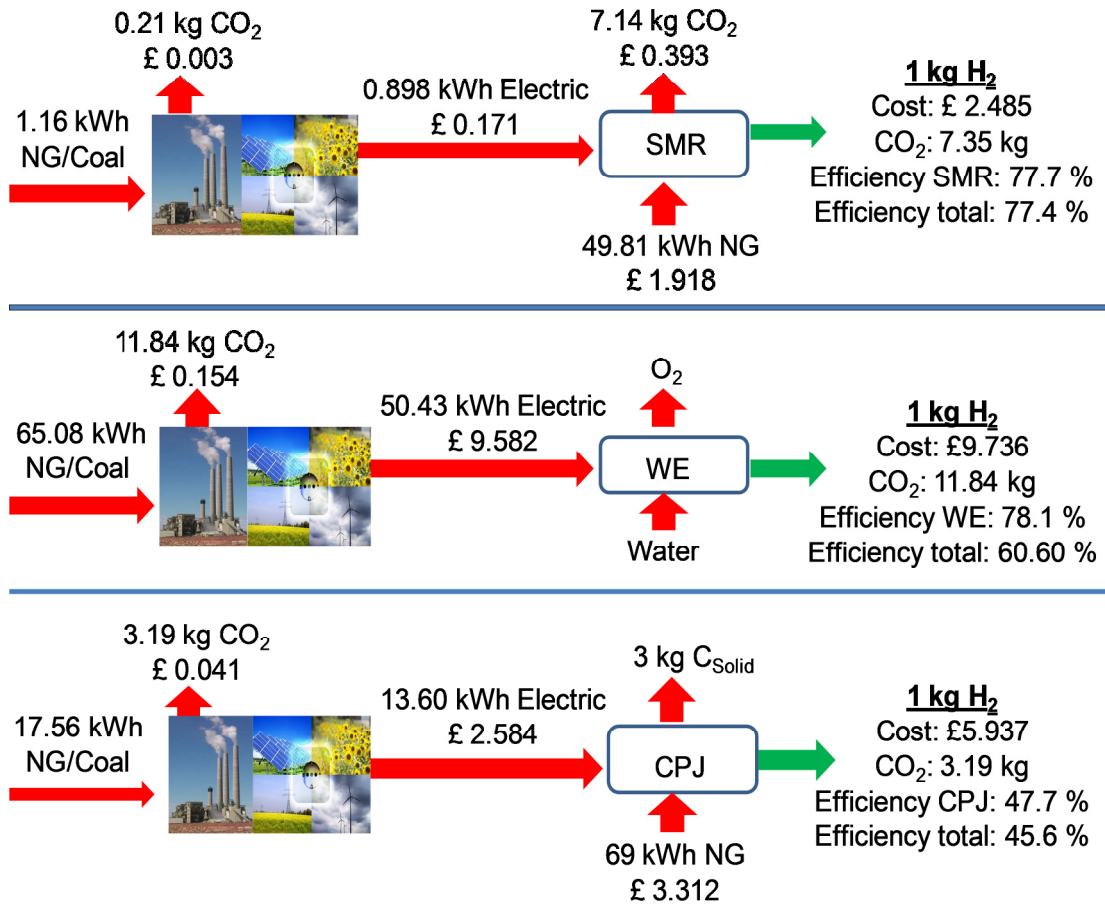


Figure 9.5: Summary of the system analysis for hydrogen generation: post 2035 with clean renewable energy integration.

Table 9.9: Summary of the system analysis for hydrogen generation: post 2035 with clean renewable energy integration.

	SMR	WE	CPJ		
			No C _S credit	LQ C _S	HQ C _S
Energy Conversion Efficiency	77.7	78.1	47.7	47.7	47.7
Overall System Efficiency	77.4	60.5	45.6	45.6	45.6
Hydrogen cost (£/kg)	2.485	9.736	5.937	5.337	2.937
CO₂ emissions (kg CO₂/kg H₂)	7.35	11.84	3.19	3.19	3.19

9.5.4. Combination with an integrated FC-CHP system

The most important requirements for stand-alone power generation are independence of the system from the electricity grid and the use of available fuels and infrastructure such as natural gas (Calo et al., 2010). Since the electricity consumption for both the SMR and CPJ is lower than that generated by a fuel cell, using a combined PEMFC-CHP system, means that SMR and CPJ can be self-sustained and decentralised from the electricity grid. Results of the system analysis are shown in Figure 9.6 and Table 9.10. Figure 9.6 shows all the inputs and outputs for each reformer, to generate 1 kg of hydrogen, which is then used as a fuel in a FC-CHP system to generate domestic electricity and heat. For SMR and CPJ systems the external energy input is only in the form of natural gas and methane respectively, and the hydrogen produced fuels the FC-CHP system to generate electricity and heat with some of the electricity feeding back to sustain the reformer. In the case of WE, the amount of electricity necessary to sustain the reformer is higher than that generated by the fuel cell therefore the system is dependent on an external electricity supply (assumed to come from the grid) to produce the amount of hydrogen required.

The CPJ system is the most attractive as CO₂ emissions have been removed completely and energy generation costs for the HQ C_s case are more than 4 times better than that for SMR. In summary CPJ outperforms the current commercial SMR and is substantially better than WE.

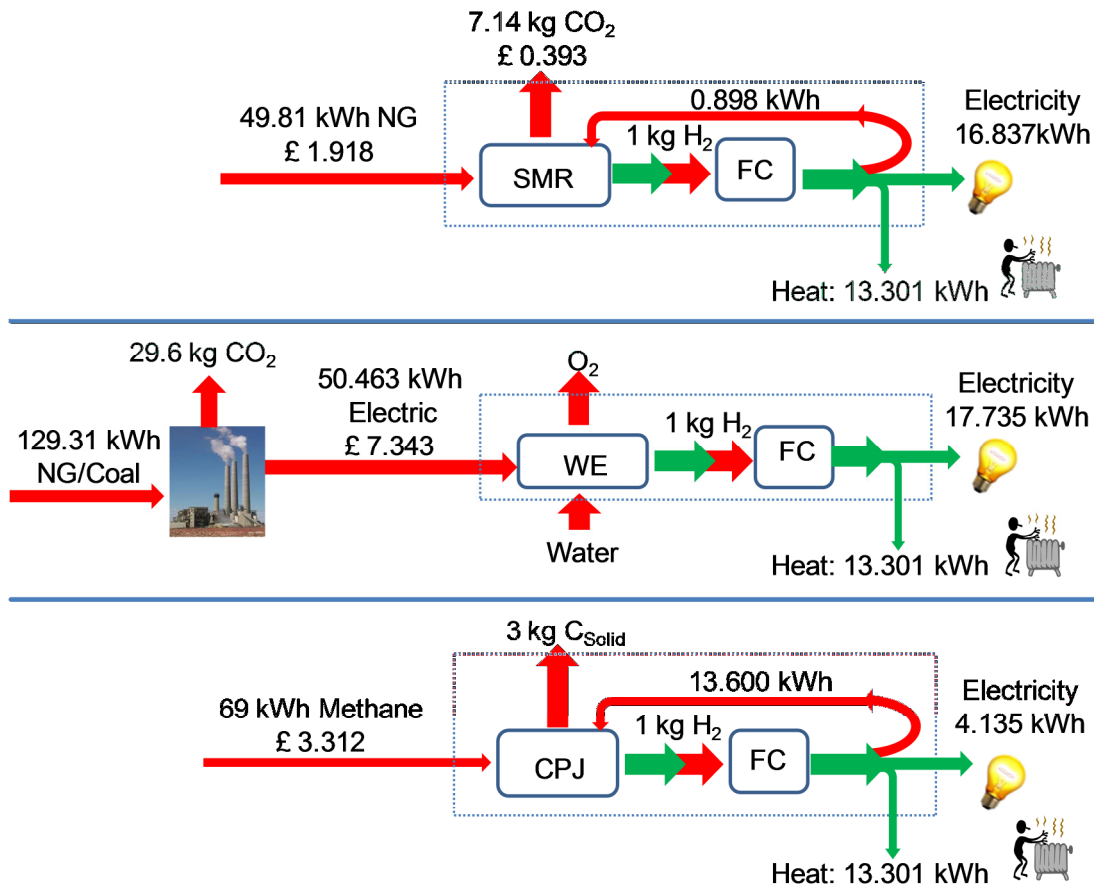


Figure 9.6: Summary of the system analysis with integrated FC-CHP system.

Table 9.10: Summary of the system analysis with integrated FC-CHP system.

	SMR	WE	CPJ		
			No C _s credit	LQ C _s	HQ C _s
Energy Conversion Efficiency	77.7	78.1	47.7	47.7	47.7
Overall System Efficiency	60.5	24	25	25	25
Energy Cost (£/kWh)	0.077	0.237	0.190	0.156	0.018
CO₂ emissions (kg CO₂/kg H₂)	7.14	29.6	0	0	0

9.6. Conclusions

In the UK the national grid operates at a high overall efficiency of 67 % for the supply of domestic electricity and heat. However, modern society concerns for CO₂ emissions strengthen from day to day globally and new developments in the energy sector are necessary to achieve the ambitious environmental goals set by the government. Even with the anticipated use of CCS technology, emissions from the heat generation at smaller scales cannot be eliminated.

Hydrogen shows a high potential as an energy carrier, especially when used to drive a fuel cell. Fuel cell technology is highly efficient, emissions free and capable of providing both electricity and heat. Steam methane reforming (SMR) is a well developed and commercialised method of hydrogen generation from methane and is used as a baseline in this work. Water electrolysis (WE) is at the research and development stage, and hence was also chosen to be compared with the non-thermal plasma decomposition method (cold plasma jet, CPJ) proposed. Under all scenarios analysed, CPJ was shown to be more competitive than WE in terms of hydrogen cost and CO₂ emissions. Indeed, the combination CPJ with a FC-CHP system can eliminate emissions altogether. CPJ also produces solid carbon, potentially of considerable value and means CPJ technology closely competes economically with commercialised SMR technology in terms of hydrogen generation costs. Especially if high quality carbon is produced, CPJ integrated with a FC-CHP system is not only emission free, but substantially out-competes SMR based on the cost of energy. This is a most attractive prospect, considering plasma technology is still at the R&D stage.

According to Bartels et al. (2010) the approximate cost of large scale hydrogen production using SMR was 2.48 – 3.17 US \$/kg of hydrogen in 2007 (equivalent to £1.6 – 2.05 at exchange rate of \$1 = £0.6464). For commercial large scale WE the cost was estimated to be in excess of 8 US \$/kg (Balat, 2008) (equivalent to £5.17). As expected, small scale hydrogen generation using both SMR and WE is a more costly process than for large scale generation. However, it is also necessary to consider the extra costs involved in implementing a new hydrogen infrastructure for transport, and storage for supplying domestic districts with hydrogen for FC-CHP. Further, the emissions from a large scale SMR plant have been estimated to be 13.7

kg CO₂ per kg of hydrogen (Muradov et al., 2005), while the small scale commercial SMR unit in this study only generates 7.67 kg CO₂ per kg hydrogen in total. An important conclusion is that CO₂ emissions for distributed hydrogen generation via SMR cannot be prevented, at least not in the foreseeable future.

Overall, from the above it is clear that distributed hydrogen generation could become very competitive, with the CPJ method showing a high potential for economic and clean energy generation. An important final point is this: given that the CPJ system, unlike the SMR and WE systems, is free of CO_x emissions so is therefore not sensitive to future political and technological uncertainties in CO₂ related costing.

Chapter 10: Conclusions and Recommendations

10.1. Conclusions

10.1.1. Hexadecane Cracking

Hexadecane cracking has not been achieved for a corona discharge under the conditions tested (given in Appendix B) due to the absence of the chosen plasma gas interaction with the liquid hexadecane. The following conclusions can be obtained based on the observations and analysis in the current study:

1. Argon is not a suitable plasma forming gas for liquid to gas interaction and other reactive gasses such as methane are necessary for cracking of heavy hydrocarbons in a liquid state.
2. Higher currents (maximum of 5 mA tested in this work) are necessary for liquid and plasma gas interaction and hence cracking of the hydrocarbons.

10.1.2. Methane decomposition

The experimental results for methane decomposition under a corona discharge are summarized below.

1. Higher discharge powers and longer residence time favour the conversion of methane and the production of hydrogen.
2. Energy conversion efficiency is mainly governed by hydrogen selectivity, due to its high calorific value.
3. Hydrogen selectivity is affected by the generation of other compounds, especially acetylene and ethene at discharge powers above 18 W and residence times above 2 min.
4. In the present work, acetylene has been the major by-product for methane decomposition experiments.
5. Hydrogen generation is favoured at higher inter-electrode distances.
6. Positive corona discharge polarity was preferable in terms of higher hydrogen production.
7. Energy conversion efficiency of 22 % has been achieved (above the aimed value of 20 %) with hydrogen selectivity of 56 % and methane conversion of 31 %, at 15

mm inter electrode distance, positive corona discharge, 19 W discharge power and 3 min residence time.

8. From the energy efficiency point of view, corona discharges are a promising approach for hydrogen generation by plasma assisted methane decomposition.

10.1.3. Propane decomposition

The experimental results for propane decomposition under a corona discharge are summarized below.

1. Higher discharge powers and longer residence time favour the conversion of propane and the production of hydrogen.
2. Energy conversion efficiency is mainly governed by hydrogen selectivity, due to its high calorific value.
3. Hydrogen selectivity is affected by the generation of other compounds, most of which also increase with residence time and total discharge energy.
4. Hydrogen generation increases with higher inter-electrode distances.
5. Hydrogen production is mainly governed by the total discharge energy, regardless of the inter-electrode distance.
6. Hydrogen selectivity of 33 % was achieved (above the aim of 14 %) with propane conversion of 48 % and energy conversion efficiency of 11 %, at 15 mm inter-electrode distance, positive corona discharge, 35 W discharge power and 303 s residence time.

10.1.4. Comparing methane and propane results

Two key conclusions can be drawn when comparing methane and propane decomposition results:

1. There is a high similarity between the chemical mechanisms for methane and propane decomposition under a corona discharge. In general, all of the parameters studied had identical trends and patterns on both methane and propane conversions, as well as hydrogen selectivity and production and energy conversion efficiencies.
2. Corona discharges show a higher ability for methane conversion when compared to propane. At 120 s residence time and approximately 19 W discharge power (2.4 kJ total), hydrogen selectivity and energy efficiency were both approximately double

for methane (47 % and 19.41 % respectively) when compared to propane (23 % and 9.52 % respectively).

10.2. Recommendations

10.2.1. Hexadecane cracking

Based on the current experimental facilities, the following task is strongly recommended to achieve hexadecane cracking:

1. A spray system of the liquid hexadecane could be designed instead of the expensive vaporization process.

The following tasks could be considered also to achieve hexadecane cracking, but as mentioned previously they have not been considered in this work due to high energy penalties:

1. Methane has been shown in the literature to be an effective additional gas for liquid hydrocarbon cracking and could be used as a plasma forming gas instead of argon.
2. Higher currents could be tested to achieve the liquid and gas interaction as described previously.
3. The liquid hexadecane can be vaporized for a better contact with the plasma gas.

10.2.2. Methane and propane decomposition

Based on the current experimental facilities the following is strongly recommended for methane and propane decomposition experiments within the current system:

1. Different gas composition ratios of argon and methane or propane need to be tested to determine the optimal ratio for the overall production rate of hydrogen and energy efficiency.
2. It is recommended to test different power supply systems such as AC and pulses, these have been reported in the literature to be very effective for partial oxidation reactions from energy efficiency point of view.

3. It would be highly beneficial for the future prototype development to test a mixture of different gaseous hydrocarbons, for example waste gasses from the oil refining processes.
4. The generated carbon should be classified under different plasma conditions to assess its commercial value.

10.3. Future Work

From Chapter 9 important conclusions can be drawn:

1. CO₂ emissions for distributed hydrogen generation via SMR cannot be prevented, at least not in the foreseeable future.
2. Distributed hydrogen generation could become very competitive, with the CPJ method showing a high potential for economic and clean energy generation.
3. Given that the CPJ system, unlike the SMR and WE systems, is emission-free in terms of the atmosphere, it is not sensitive to future political and technological uncertainties and decision changing in CO₂ -related costing.

In terms of future work, further system analyses could include a feasibility study for applying the FC-CHP system to meet the daily loads for domestic electricity and heat usage in the UK as a whole. Experimental work necessary includes the development of a flow non-thermal plasma reactor, with the aim of reducing the consumption of electrical power and enhance the overall efficiency. An example of the proposed flow system is shown in Figure 10.1. Different electrode configurations and designs should be tested to optimise hydrogen production and ensure effective solid carbon removal.

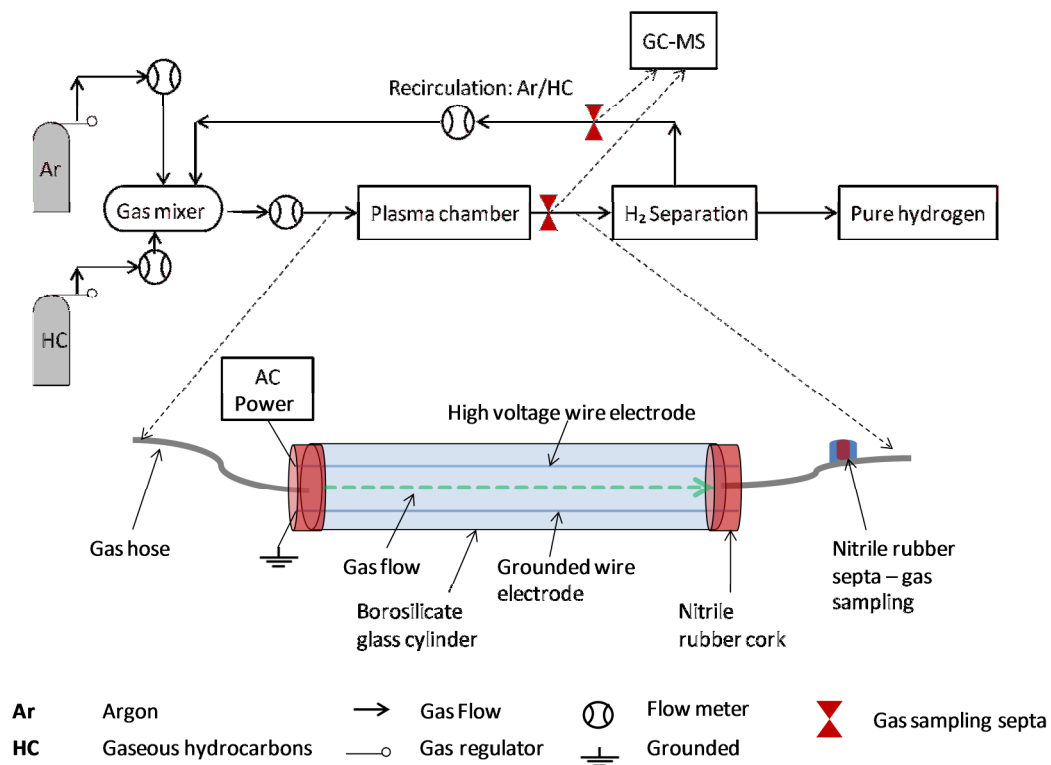


Figure 10.1: Laboratory scale flow system design for gaseous hydrocarbon decomposition to generate CO_x free hydrogen.

References

- Abbas, H. F., and Daud, W. M. A. W. (2009). Thermocatalytic decomposition of methane for hydrogen production using activated carbon catalyst: Regeneration and characterization studies. *Int. J. Hydrogen Energy*, vol. 34, p. 8034.
- Abbas, H. F., and Daud, W. M. A. W. (2009a). Deactivation of palm shell-based activated carbon catalyst used for hydrogen production by thermocatalytic decomposition of methane. *Int. J. Hydrogen Energy*, vol. 34, p. 6231.
- Abbas, H. F., and Daud, W. M. A. W. (2010). Hydrogen production by methane decomposition: A review. *Int. J. Hydrogen Energy*, vol. 35, p. 1160.
- Ahmed, S., Aitani, A., Rahman, F., Al-Dawood, A., Al-Muhaish, F. (2009). Decomposition of hydrocarbons to hydrogen and carbon. *Appl. Catal. A: General*, vol. 359, p. 1.
- Ahmed, S., Krumpelt, M. (2001). Hydrogen from hydrocarbon fuels for fuel cells. *Int. J. Hydrogen Energy*, vol. 26, p. 291.
- Aki, H., Taniguchi, Y., Tamura, I., Kegasa, A., Hayakawa, H., Ishikawa, Y., Yamamoto, S., Sugimoto, I. (2012). Fuel cells and energy networks of electricity, heat, and hydrogen: A demonstration in hydrogen-fuelled apartments. *Int. J. Hydrogen Energy*, vol. 37, p. 1204.
- Akischev, Y. S., Dem'yanov, A. V., Karal'nik, A. E., Monich, A. E., Trushkin, N. I. (2003). Comparison of the AC barrier corona with DC positive and negative coronas and barrier discharges. *Plasma Phys. Rep.*, vol. 29, p. 82.
- Akischev, Y., Goosens, O., Callebaut, T., Leys C., Napartovich, A., Trushkin, N. (2001a). The influence of electrode geometry and gas flow on corona-to-glow and glow-to-spark threshold currents in air. *J. Phys. D: Appl. Phys.*, vol. 34, p. 2875.
- Akischev, Y., Grushin, M. E., Deryugin, A. A. (1999). Self-oscillations of a positive corona in nitrogen. *J. Phys. D: Appl. Phys.*, vol. 32, p. 2399.
- Akischev, Y., Grushin, M. E., Karal'nik, V. B., Trushkin, N. I. (2001b). Pulse mode of a negative corona in Nitrogen: I. Experiment. *Plasma Phys. Reports*, vol. 27, p. 520.
- Akischev, Y., Grushin, M. E., Karal'nik, V. B., Trushkin, N. I. (2001c). Pulse mode of a negative corona in Nitrogen: II. Numerical calculations. *Plasma Phys. Reports*, vol. 27, p. 532.

Aleknaviciute, I., Karayiannis, T. G., Collins, M.W., Xanthos, C. (2010). Plasma-assisted decomposition of gaseous propane to produce CO_x free hydrogen. *Int. J. Low-Carbon Technol.*, doi: 10.1093/ijlct/cts015.

Aleksandrov, A., Bazelyan, E. M., Gorunov, A. Y., Kochetov, I. V. (1999). A non-thermal mechanism of spark breakdown in Ar. *J. Phys. D: Appl. Phys.*, vol. 32, p. 2636.

Aleksandrov, A., Bazelyan, E. M., Novitskii, G. A. (2001). The effects of small O₂ addition on the properties of a long positive streamer in Ar. *J. Phys. D: Appl. Phys.*, vol. 34, p. 1374.

Alibaba (<http://www.alibaba.com/showroom/granular-activated-carbon.html>)

Al-Traboulsi, M., Sjogersten, S., Colls, J., Steven, M., Craigon, J., Black, C. (2012). Potential impact of CO₂ leakage from carbon capture and storage (CCS) systems on growth and yield in spring field bean. *Environmental and Experimental Botany*, vol. 80, p. 43.

Amin, A., M., Croiset, E., Epling, W. (2011). Review of methane catalytic cracking for hydrogen production. *Int. J. Hydrogen Energy*, vol. 36, p. 2904.

Antano, D. S., Staack, D. A., Fridman, A., Farak, B. (2009). Atmospheric pressure DC corona: operating regimes and applications. *Plasma Sources Sci. Technol.*, vol. 18, p. 1.

Atrazhev, V. M., Atrazhev, V. V., Bonifaci, N., Denat, A., Kochetov, I. V., Napartovich, A. P. (2003). Cathode sheath formation of corona discharges in dense gaseous and liquid Argon. *Proc. of 30th EPS Conf. on Contr. Fusion and Plasma Phys.*, St. Petersburg, ECA, vol. 27A, 0 – 1.5D.

Balat, M. (2008). Potential importance of hydrogen as a future solution to environmental and transportation problems. *Int. J. Hydrogen Energy*, vol. 33, p. 4013.

Bardos, L., and Barankova, H. (2009). Plasma properties at atmospheric and low pressures. *Vacuum*, vol. 83, p. 522.

Barelli, L., Bidini, G., Gallorini, F., Ottaviano, A. (2012). Dynamic analysis of PEMFFC-based CHP systems for domestic application. *Applied Energy*, vol. 91, p. 13.

Bartels, J. R., Pate, M. B., Olson, N. K. (2010). An economic survey of hydrogen production from conventional and alternative energy sources. *Int. J. Hydrogen Energy*, vol. 35, p. 8371.

Baxi Innotech. Specification booklet for Gamma 1 model. (<http://www.baxi-innotech.de/index.php?id=26&lang=1>).

Benocci, R., and Mauri, L. (2004). I-V characteristics and photocurrents of a He corona discharge under flow conditions. *J. Phys. D: Appl. Phys.*, vol. 37, p. 709.

Benocci, R., Urbano, M., Mauri, L. (2006). Study of a positive corona discharge in argon at different pressures. *Eur. Phys. J. D.*, vol. 35, p. 122.

Besser, R. S. and Lindner, P. J. (2010). Microplasma reforming of hydrocarbons for fuel cell power. *J. Power Sources*, doi: 10.1016/j.jpowersour.2010.11.135.

Biniwale, R. B., Mizuno, A., Ichikawa, M. (2004). Hydrogen production by reforming of isooctane using spray-pulsed injection and effect of non-thermal plasma. *Applied Catalysis A: General*, vol. 276, p. 169.

Bockris, J. O'M. (2002). the origin of ideas on hydrogen economy and its solution to the decay of the environment. *Int. J. Hydrogen Energy*, vol. 27, p. 731.

Bogaerts, A., Neyts, E., Gijbels, R., Mullen, J. V. D. (2002). Gas discharge plasmas and their applications. *Spectrochimica Acta. Part B*: vol. 57, p. 609.

Bonifaci, N., Denat, A., Atrazhev, V. (1997). Ionization phenomena in high-density gaseous and liquid argon in corona. *J. Phys, D: Appl. Phys.*, vol. 30, p. 2717.

Bozorgzadeh, H. R., Aziznia, A., Seyed-Matin, N., Baghalha, M., Jalili, A. H. (2009). Carbon dioxide reforming of methane via DC corona streamer discharge. 19th ISPC, Germany.

Brame, J. S. S., and King, J. G. (1967). *Fuel: solid, liquid and gaseous*. Fifth Edition. London: Edward Arnold., p. 240 – 244.

Bromberg L., Cohn D.R., Rabinovich A., Surma J. E., Virden J. (1999b), Compact plasmatron-boosted hydrogen generation technology for vehicular applications. *Int. J. Hydrogen Energy*, vol. 24, p. 341.

Bromberg, L., Cohn, D. R., Hadidi, K., Heywood, J., Rabinovich, A. (2005). Plasmatron fuel reformer development and internal combustion engine vehicle applications. DEER, Coronado CA, PSFC-JA-05-22.

Bromberg, L., Cohn, D.R., Rabinovich, A., Alexeev, N. (1999a). Plasma catalytic reforming of methane. *Int. J. Hydrogen Energy*, vol. 24, p. 1131.

Bromberg, L., Cohn, D.R., Rabinovich, A., Alexeev, N., Samokhin, A., Ramprasad, R., Tamhankar, S. (2000). System optimization and cost analysis of plasma catalytic reforming of natural gas. *Int. J. Hydrogen Energy*, vol. 25, p. 1157.

Bromberg, L., Hadidi, K., Cohn, D. R. (2006). Experimental investigation of plasma assisted reforming of propane. MIT Plasma Science and Fusion Centre, PSFC/JA-05-15.

Brown, J. E., Hendry, C. N., Harborne, P. (2007). An emerging market in fuel cells? Residential combined heat and power in four countries. *Energy Policy*, vol. 35, p. 2173.

Bruggeman, P., Liu, J., Degroote, J., Kong, M. C., Vierendeels, J., Leys, C. (2008b). DC excited discharges in atmospheric pressure air in point-to-water electrode systems. *J. Phys. D: Appl. Phys.*, vol 41, doi: 10.1088/0022-3727/41/21/215201.

Bruggeman, P., Ribežl, E., Degroote, J., Vierendeels, J., Leys, C. (2008a). Plasma characteristics and electrical breakdown between metal and water electrodes. *J. Optoelectronics and Advanced Materials*, vol. 10, p. 1964.

Bruggeman, P., Ribežl, E., Maslani, A., Dgroote, J., Malesevic, A., Rego, R., Vierendeels, J., Leys, C. (2008c). Characteristics of atmospheric pressure air discharges with liquid cathode and a metal anode. *Plasma Sources Sci. Technol.*, vol. 17, doi: 10.1088/0963-0252/17/2/025012.

Bush, P. V., and Snyder, T. R. (1987). Laboratory analyses of corona discharges. *J. Electrostatics*, vol. 19, p. 83.

Calo, E., Giannini, A., Monteleone, G. (2010). Small stationary reformers for H₂ production from hydrocarbons. *Int. J. Hydrogen Energy*, vol. 35, p. 9828.

Capezzuto, P., Cramarossa, F., D'Agostino, R., Molinari, E. (1978). Cracking and oxidation of methane under electrical discharge in the presence of carbon dioxide, water vapour and oxygen. *Combustion and Flame*, vol. 33, p. 251.

Carrey, F. A., and Sundberg, R. J. (1937). *Advanced organic chemistry. Part A: structure and mechanisms*. New York: Plenum Press, p. 2-3.

Černák, M., and Hosokawa, T. (1989). The first trichel pulse of negative corona discharge in N₂ with small admixture of SF₆. *Czech. J. Phys. B*, vol. 39, p. 1032.

Černák, M., and Hosokawa, T. (1991). Complex form of current pulses in negative corona discharge. *Phys. Rev. A*, vol. 43, p. 1107.

Chang, J-S., Lawless, P.A., Yamamoto, T. (1991). Corona discharge process. *IEEE Trans. Plasma Sci.*, vol. 19, p. 1152.

Chao, Y., Huang, C-T., Lee, H-M, Chang, M-B. (2008). Hydrogen production via partial oxidation of methane with plasma-assisted catalysis. *Int. J. Hydrogen Energy*, vol. 33, p. 664.

Chen, H. L., Lee, H. M., Chen, S. H., Chao, Y., Chang, M. B. (2008). Review of plasma catalysis on hydrocarbon reforming for hydrogen production – Interaction, integration, and prospects. *Applied Catalysis B: Environmental*, vol. 85, p. 1.

Chen, J., and Davidson, J. H. (2003). Ozone production in the negative DC Corona: The dependence of discharge polarity. *Plasma Chem. Plasma Processing*, vol. 23, p. 501.

Chen, Q., Dai, W., Tao, X., Yu, H., Dai, X., Yin, Y. (2006). CO₂ reforming of CH₄ by atmospheric pressure abnormal glow plasma. *Plasma Science and Technology*, vol. 8, p. 181.

Cheng, D-G., Zhu, X., Ben, Y., He, F., Cui, L., Liu, C-J. (2006). Carbon dioxide reforming of methane over Ni/Al₂O₃ treated with glow discharge plasma. *Catal. Today*, vol. 115, p. 205.

Cheng, H-M., Yang, Q-H., Liu, C. (2001). Hydrogen storage in carbon nanotubes. *Carbon*, vol. 39, p. 1447.

Cho, W., Kim, Y. C., Kim, S-S. (2010). Conversion of natural gas to C₂ product, hydrogen and carbon black using a catalytic plasma reactions. *J. Ind. Eng. Chem.*, vol. 16, p. 20.

Chun, Y. N., and Song, H. O. (2008). Syngas production using gliding arc plasma. *Energy Sources, Part A*, vol. 30, p. 1202.

Chun, Y. N., Kim, S. W., Song, H. O. (2004). Steam plasma reforming of biogas by non-thermal pulsed discharge. *Korean J. Chem. Eng.*, vol. 21, p. 670.

Chun, Y. N., Yang, Y. C., Yoshikawa, K. (2009). Hydrogen generation from biogas reforming using gliding arc plasma-catalyst reformer. *Catal. Today*, vol. 148, p. 283.

Conrads, H., and Schmidt, M. (2000). Plasma generation and plasma sources. *Plasma Sources Sci. Technol.*, vol. 9, p. 441.

Cormier J. M., and Rusu L. (2001). Syngas production via methane steam reforming with oxygen: plasma reactors versus chemical reactors. *J. Phys. D: Appl. Phys.*, vol. 34, p. 2798.

Czernichowski, A., Czernichowski, M., Czernichowski, P. (2003). Glid Arc-assisted reforming of carbonaceous feedstocks into synthesis gas. Detailed study on propane. ISPC 16, Taormina.

Czernichowski, A., Czernichowski, M., Wesolowska, K. (2003). Glidarc-assisted production of synthesis gas from rapeseed oil. 1st European Hydrogen Energy Conference, Grenoble, France. CP1, p. 67.

Czernichowski, P. (2000). Device with plasma from mobile electric discharges and its applications to convert carbon matter. PCT Patent WO 00/13786

Da Silva, C. F., Ishikawa, S., Alves, Jr. C., Marninelli, A. E. (2006). Production of hydrogen from methane using pulsed plasma and simultaneous storage to titanium sheet. *Int. J. Hydrogen Energy*, vol. 31, p. 49.

DECC - Department of Energy and Climate Change. (2011). Digest of UK energy statistics 2011. ISBN 9780115155277.

DECC - Department of Energy and Climate Change. (2012). 2010 UK greenhouse gas emissions, final figures. (http://www.decc.gov.uk/en/content/cms/statistics/climate_stats/gg_emissions/uk_emissions/2010_final/2010_final.aspx).

DECC - Department of Energy and Climate Change. (2012a). Digest of UK energy statistics 2012. ISBN 9780115155284.

DECC. (2011a). A brief guide to the carbon valuation methodology for UK policy appraisal.

DECC. (2012a). CCS Roadmap: Supporting deployment of carbon capture and storage in the UK. April, 2012 release.

Deminsky, M., Jivotov, V., Potapkin, B., Rusanov, Y. (2002). Plasma Assisted Production of hydrogen from hydrocarbons. *Pure Appl. Chem.*, vol. 74 p. 413.

Diguang, Z., and Dexuan, X. (1990). Analysis of the current for negative point-to-plane corona discharge in air. *J. Electrostatics*, vol. 25, p. 221.

Dinelli, G., Civitano, L., Rea, M. (1990). Industrial experiments on pulse corona simultaneous removal of NO_x and SO₂ from flue gas. *IEEE Trans. Industry Appl.*, vol. 26, p. 535.

DOE. (1998). Energy and Environmental Profile of the U.S. Petroleum Refining Industry. Prepared by Energetics, Inc. Columbia, Maryland.

DOEHP. (2006). Distributed hydrogen production from natural gas. NREL/BK-150-40382.

Dorian, J. P., Franseen, H. T., Simbeck, D. R., MD. (2006). Global challenges in energy. *Energy Policy*, vol. 34, p. 1984.

Doucet, G., Etievant, C., Puyenchet, C., Grigoriev, S., Millet, P. (2009). Hydrogen based PEM auxiliary power unit. *Int. J. Hydrogen Energy*, vol. 34, p. 4983.

Du, C., Li, H., Zhang, L., Wang, J., Huang, D., Xiao, M., Cai, J., Chen, Y., Yan, Y., Xiong, Y., Xiong, Y. (2012). Hydrogen production by steam-oxidative reforming of bio-ethanol assisted by Laval nozzle arc discharge. *Int. J. Hydrogen Energy*, vol. 37, p. 8318.

Dufour, J., Galvez, J. L., Serrano, D. P., Moreno, J., Martinez, G. (2010). Life Cycle Assessment of hydrogen production by methane decomposition using carbonaceous catalysts. *Int. J. Hydrogen Energy*, vol. 35, p. 1205.

Dufour, J., Serrano, D. P., Galvez, J. L., Moreno, J., Garcia, C. (2009). Life Cycle Assessment of processes for hydrogen production. Environmental feasibility and reduction of greenhouse gas emissions. *Int. J. Hydrogen Energy*, vol. 34, p. 1370.

EC. (2003). Hydrogen energy and fuel cells: A vision of our future. European Commission, EUR 20719 EN.

EC. (2003a). World energy, technology and climate policy outlook 2030. European commission, EUR 20366.

EC. Hydrogen energy and fuel cells: A vision of our future. European Commission 2003; EUR 20719 EN.

Edwards, P. P., Kuznetsov, V. L., David, W. I. F., Brandon, N. P. (2008). Hydrogen and fuel cells: towards a sustainable energy future. *Energy Policy*, vol. 36, p. 4356.

EECCC (Element Energy for the Committee on Climate Change). 2010. Potential for the application of CCS to UK industry and natural gas power generation. (http://downloads.theccc.org.uk/s3.amazonaws.com/0610/pr_supporting_research_element_Energy_CCS_on_gas_and_industry.pdf).

EIA, US DOE. (2011). Analysis of impacts of a clean energy standard.

Eichwald, O., Ducasse, O., Dubois, D., Abahazem, A., Merbahi, N., Benhenni, M., Yousfi, M. (2008). Experimental analysis and modelling of positive streamer in air: towards an estimation of O and N radical production. *J. Phys. D: Appl. Phys.*, vol. 41, p. 11.

Europe's Energy Portal (<http://www.energy.eu/#Domestic-Elec>).

Faria, W. L. S., Dieguez, L. C., Schmal, M. (2008). Autothermal reforming of propane for hydrogen production over Pd/CeO₂/Al₂O₃ catalyst. *Appl. Catal. B: Env.*, vol. 85, p. 77.

Farouk, T., Farouk, B., Gutsol, A., Fridman, A. (2008). Atmospheric pressure methane-hydrogen dc micro-glow discharge for thin film deposition, *J. Phys. D: Appl. Phys.*, vol. 41, 175202 [doi:10.1088/0022-3727/41/17/175202](https://doi.org/10.1088/0022-3727/41/17/175202).

Fieser, L. F., and Fieser, M. (1961). *Advanced organic chemistry*. New York: Reinhold Publishing Corporation, p. 12-14.

Fridman, A. (2008). *Plasma Chemistry*. Cambridge: Cambridge University Press.

Fridman, A., Chirokov, A., Gutsol, A. (1999). Gliding arc gas discharge. *Progress in Energy and Combustion Science*, vol. 25, p. 211.

Fridman, A., Chirokov, A., Gutsol, A. (2005). Non-thermal atmospheric pressure discharges. *J. Phys. D: Appl. Phys.*, vol. 38, p. R1.

Fu, C., and Gundersen, T. (2012). Carbon capture and storage in the power industry: challenges and opportunities. *Energy Procedia*, vol. 16, p. 1806.

Fuel Cell Today (2011). The fuel cell today industry review 2011. p. 40. (<http://fuelcelltoday.com/analysis/industry-review/2011/the-industry-review-2011>).

Fuel Cells Bulletin (2005). First UK domestic fuel cell cogen installation. Issue 10, p. 6.

Fulcheri, L., and Schwob, Y. (1995). From methane to hydrogen, carbon black and water. *Int. J. Hydrogen Energy*, vol. 20, p 197.

Gallon, H. J., Tu, X., Twigg, M. V., Whitehead, J. C. (2011). Plasma-assisted methane reduction of NiO catalyst-Low temperature activation of methane and formation of carbon nanofibres. *Appl. Catal. B: Env.*, vol. 106, p. 616.

Ghorbanzadeh, A. M., Lotfalipour, R., Rezaei, S. (2009). Carbon dioxide reforming of methane at near room temperature in low energy pulsed plasma. *Int. J. Hydrogen Energy*, vol. 34, p. 293.

Giddey, S., Badwal, S.P.S., Kulkarni, A., Munnings, C. (2012). A comprehensive review of direct carbon fuel cell technology. *Progress in Energy and Combustion Science*, vol. 38, p. 360.

Glaser, B., Lechman, J., Zech, W. (2002). Ameliorating physical and chemical properties of highly weathered soils in the tropics with charcoal – a review. *Biol. Fertil. Soils*, vol. 35, p. 219.

Goldman, M., Goldman, A., Sigmond, R. S. (1985). The corona discharge, its properties and specific uses. *Pure and Appl. Chem.*, vol. 57, p. 1353.

Goldstein, R. F., and Waddams, A. L. (1967). The petroleum chemicals industry. 3rd edition. London: E. & F. SPON LTD, Chapter 1.

Gordon, C. L., Lobban, L. L., Mallinson, R. G. (2003). Ethylene production using a Pd and Ag-Pd-Y-zeolite catalyst in a DC plasma reactor. *Catal. Today*, vol. 84, p. 51.

Gorska, A., Krawczyk, K., Jodzis, S., Schmidt-Szalowski, K. (2011). Non-oxidative methane coupling using CU/ZnO/Al₂O₃ catalyst in DBD. *Fuel*, vol. 90, p. 1946.

Gough, C., Mander, S., Haszeldine, S. (2010). A roadmap for carbon capture and storage in the UK. *Int. J. Greenhouse Gas Control*, vol. 4, p. 1.

Gould, R. F. (1971). Origin and refining of petroleum. Washington D.C.: American Chemical Society.

Gurnett, D. A., and Bhattacharjee, A. (2005). Introduction to plasma physics. Cambridge: Cambridge University Press, p. 1-3.

Hammer, T. (1999). Application of plasma technology in environmental techniques. *Contrib. Plasma Phys.*, vol. 39, p. 441.

Hammer, T., Kappes, T., Baldauf, M. (2004). Plasma Catalytic hybrid processes: gas discharge initiation and plasma activation of catalytic processes. *Catal. Today*, vol. 89, p. 5.

Hartmann, W., Römheld, M., Rohde, K-D. (2007). All-solid-state power modulator for pulsed corona plasma reactors. *IEEE Trans. Dielectrics and Electrical Insulation*, vol. 14, p. 858.

Hayashi, D., Hoeben, W. F. L. M., Dooms, G., Veldhuizen, E. M., Rutgers, W. R., Kroesen, G. M. W. (2000). Influence on gaseous atmosphere on corona-induced degradation of aqueous phenol. *J. Phys. D: Appl. Phys.*, vol. 33, p. 2769.

Heintze, M., and Pietruszka, B. (2004). Plasma catalytic conversion of methane into syngas: the combined effect of discharge activation and catalysis. *Catal. Today*, vol. 89, p. 21.

Herrera, A. V. H., Curbelo, M. A. G., Borges, J. H., Delgado, M. A. R. (2012). Carbon nanotubes in separation science: A review. *Analytica Chimica Acta*, vol. 734, p. 1.

Hites, R. A. (2007). Elements of environmental chemistry. New Jersey: John Wiley and Sons Inc. P. 9 – 10. ISBN: 978-0-471-99815-0.

Hoeben, W. F. L. M., Veldhuizen, E. M., Rutgers, W. R., Kroesen, G. M. W. (1999). Gas phase corona discharges for oxidation of phenol in an aqueous solution. J. Phys. D: Appl. Phys., vol. 32, p. L133.

Holladay, J.D., Hu, J., King, D. L., Wang, W. (2009). An overview of hydrogen production technologies. Catalysis Today, vol. 139, p 244.

Hollahan, J. R., and Bell, A. T. (1974). Techniques and applications of plasma chemistry. Canada: John Wiley & Sons, Inc., p.1.

Hornig, R-F., Lai, M-P., Chang, Y-P., Yur, J-P., Hsieh, S-F. (2009). Plasma-assisted catalytic reforming of propane and assessment of its applicability on vehicles. Int. J Hydrogen Energy, vol. 34, p. 6280.

Huang, A., Xia, G., Wang, J., Suib, S. L., Hyashi, Y., Matsumoto, H. (2000). CO₂ reforming of CH₄ by atmospheric pressure arc discharge plasmas. J. Catalysis, vol. 189, p 349.

Hwang, N. K., Lee, D. H., Cha, M. S., Song, Y-H. (2007). Pathways of methane decomposition in plasma process by arc jet. 18th International Symposium on Plasma Chemistry, Japan (symposium proceedings).

Hydrogen Analysis Resource Centre, US DOE: (http://hydrogen.pnl.gov/cocoon/morf/hydrogen/site_specific/fuel_heating_calculator?canprint=false).

Hydrogenics HyPM datasheet. (<http://www.hydrogenics.com/fuel/stationary>).

IEA. (2009). World energy outlook. International Energy Agency. ISBN: 97892 64 06130 9.

IEA. (2011). Cost and performance of carbon dioxide capture and storage from power generation.

Intardo, A. (2008). Hydrogen production from methane in a dielectric barrier discharge using oxide zinc and chromium as catalysts. J. Chinese Institute Chem. Eng., vol. 39, p. 23.

Intardo, A., Choi, J-W., Lee, H., Song, H. K. (2006). Effect of additive gases on methane conversion using gliding arc discharge. Energy, vol. 31, p. 2986.

IPHE. (2010). Hydrogen and fuel cell global commercialization & development update. International Partnership for hydrogen and fuel cells in the economy.

Itadi, A. N. A. S. (2006). Co-generation of synthesis gas and C₂₊ hydrocarbons from methane and carbon dioxide in a hybrid catalytic plasma reactor: A Review. *Fuel*, vol. 85, p. 577.

Italiano, G., Delia, A., Espro, C., Bonura, G., Frusteri, F. (2010). Methane decomposition over Co thin layer supported catalysts to produce hydrogen for fuel cells. *Int. J. Hydrogen Energy*, vol. 35, p. 11568.

Ivy, J. (2004). Summary of Electrolytic Hydrogen Production. Milestone Completion Report: National Renewable Energy Report. NREL/MP-560-36734.

Jarzebski, S., and Chojnowski, M. (1974). Influence of shapes of corona electrodes on density of emission currents in electrostatic dust collectors. *Atmospheric Environment*, vol. 8, p. 29.

Jasinski, M., Dors, M., Mizeraczyk, J. (2008). Production of hydrogen via methane reforming using atmospheric microwave pressure plasma. *J. Power Sources*, vol. 181, p. 41.

Jaworek, A., and Krupa, A. (1995a). Electrical characteristics of multipoint-to-plane corona discharge reactor. 17th Symp. Plasma Physics and Technology, 13 – 16 June, Prague, p. 326.

Jaworek, A., and Krupa, A. (1995b). Electrical characteristics of a corona discharge reactor of multipoint-to-plane geometry. *Czech. J. Phys.*, vol. 45, p. 1035.

Jaworek, A., and Krupa, A. (1996). Corona discharge from a multipoint electrode in flowing air. *J. Electrostatics*, vol. 38, p. 187.

Jibril, B. Y., and Atta, A. Y. (2011). Activated carbon incorporated with first-row transition metals as catalysts in hydrogen production from propane. *Int. J. Hydrogen Energy*, vol. 36, p. 5951.

Jones, D. S. J., and Pujado, P. R. (2006). *Handbook of petroleum processing*. Netherlands: Springer.

Kado, S., K., Skine, Y., Fujimoto, Y. (1999). Direct synthesis of acetylene from methane by direct current pulse discharge. *Chem. Comm.*, p. 2485.

Kado, S., Skine, Y., Muto, N., Nozaki, T., Okazaki, K. (2003a). Application of non-thermal plasmas to natural gas utilization. 16th ISPC, Taormina.

Kado, S., Urasaki, K., Skine, Y. (2001a). Direct conversion of methane into valuable products with DC pulse discharge. 15th ISPC, Orleans.

Kado, S., Urasaki, K., Skine, Y., Fujimoto, Y. (2001). Low temperature reforming of methane to synthesis gas with direct current pulse discharge method. *Chem. Comm.*, p. 415. Doi: 10.1039/b008922m.

Kado, S., Urasaki, K., Skine, Y., Fujimoto, Y. (2003). Direct Conversion of methane to acetylene or syngas at room temperature using non-equilibrium pulsed discharge. *Fuel*, vol. 82, p. 1377.

Kalra, C. S., Cho, Y. I., Gutsol, A. F., Fridman, A. A., Rufael, T. S. (2005a). Gliding arc in tornado using a reverse vortex flow. *Review of Scientific Instruments*, vol. 76, p. 025110-1.

Kalra, C. S., Gutsol, A. F., Fridman, A. A. (2005). Gliding arc discharges as a source of intermediate plasma for methane partial oxidation. *IEEE Trans. Plasma Sci.*, vol. 33, p. 32.

Katayama, K., Fukada, S., Nishikawa, M. (2010). Direct decomposition of methane using helium RF plasma. *Fusion Engineering and Design*, vol. 85, p. 1381.

Khani, M. R., Barzoki, S. H. R., Yaghmaee, M. S., Hosseini, S. I., Shariat, M., Shokri, B., Fakhari, A. R., Nojavan, S., Tabani, H., Ghaedian, M. (2011). Investigation of cracking by cylindrical dielectric barrier discharge reactor on the n-hexadecane as a model compound. *IEEE Trans. Plasma Sci.*, vol. 39, p 1807.

Kim, K. S., Seo, J. H., Nam, J. S., Ju, W. T., Hong, S. H. (2005). Production of hydrogen and carbon black by methane decomposition using DC-RF hybrid thermal plasma. *IEEE Trans. Plasma Sci.* vol. 33, p. 813.

Kim, S. C., and Chun, Y. N. (2008). Production of hydrogen by partial oxidation with thermal plasma. *Renewable Energy*, vol. 33, p. 1564.

Knox, B. E., and Palmer, H. B. (1961). Bond dissociation energies in small hydrocarbon molecules. *Chem. Rev.*, vol. 61, p. 247.

Kong, P. C. (1995). Reactive plasma upgrade of squalane – a heavy oil stimulant. *International Association for Bridge and Structural Engineering Symposium*, San Francisco, 23 – 25 Aug., p. 607.

Kong, P. C. (1997). Method for cracking hydrocarbon compositions using a submerged reactive plasma system. U.S. Patent 5,626,726.

Kong, P. C., Nelson, L. O., Detering, B. A. (2005). Non-thermal plasma systems and methods for natural gas and heavy hydrocarbon co-conversion. U. S. Patent 6,896,854 B2.

Kong, P. C., Nelson, L. O., Detering, B. A. (2009). Methods for natural gas and heavy hydrocarbon co-conversion. U.S. Patent 7,494,574 B2.

Koorneef, J., Ramirez, A., Turkenburg, W., Faaij, A. (2012). The environmental and risk assessment of CO₂ capture, transport and storage – An evaluation of the knowledge base. *Progress in Energy and Combustion Science*, vol. 38, p. 62.

Kotz, J. C., Treichel, P. R., Townsend, J. R. (2009). Chemistry and chemical reactivity. 8th Edition, Belmont: Brooks/Cole, p. 518. ISBN: 13:978-0-8400-4828-8.

Kunhardt, E. E. (2000). Generation of large-volume, atmospheric-pressure, non-equilibrium plasmas. *IEEE Trans. Plasma Sci.*, vol. 28, p. 189.

Kusakabe, K., Fukuda, K., Taneda, M., Takahashi, O. (2009). Steam reforming of propane in a zirconia membrane reactor with Rh-supported Ce_{0.15}Zr_{0.85}O₂ catalyst. *Asia-Pac. J. Chem. Eng.*, vol. 4, p. 246.

Laan, M., Paris, P., Repän, V. (1997). Triggering of negative corona. *J. Phys. IV. France*, vol. 7 -C4, p. 259.

Langmuir, (1928). Oscillations in ionized gases. *Proc. Nat. Acad. Sci. U.S.*, vol. 14, p. 628, ([doi:10.1073/pnas.14.8.627](https://doi.org/10.1073/pnas.14.8.627)).

Larkin, D. W., Lobban, L. L., Mallinson, R. G. (2001). The direct partial oxidation of methane to organic oxygenates using a dielectric barrier discharge reactor as a catalytic reactor analogue. *Catal. Today*, vol. 71, p. 199.

Laurencelle, F., Chahine, R., Hamelin, J., Agbossou, K., Fournier, M., Bose, T. K., Laperriere, A. (2001). Characterization of a Ballard MK5-E Proton Exchange Membrane Fuel Cell Stack. *Fuel Cells*, vol. 1 (1), p. 66.

Ledjeff-Hey, K., Kalk, T., Mahlendorf, F., Niemzig, O., Trautman, A., Roes, J. (2004) portable PEFC generator with propane as fuel. *J. Power Sources*, vol. 86, p. 166.

Lee, D. H., Kim, K-T., Cha, M-S., Song, Y-H. (2010). Plasma-controlled chemistry in plasma reforming of methane. *Int. J. Hydrogen Energy*, vol. 35, p. 10967.

Lee, H-J., Lim, Y-S., Park, N-C., Kim, Y-C. (2009). Catalytic autothermal reforming of propane over the noble metal-doped hydrotalcite-type catalysts. *Chem. Eng. J.*, vol. 146, p. 295.

Li ,X-S., Zhu, A-M., Wang, K-J., Xu, Y., Song, Z-M. (2004). Methane conversion to C₂ hydrocarbons and hydrogen in atmospheric non-thermal plasmas generated by different electric discharge techniques. *Catal. Today*, vol. 98, p. 617.

Li, D., Li, X., Bai, M., Tao, X., Shang, S., Dai, X., Yin, Y. (2009a). CO₂ reforming of CH₄ by atmospheric pressure glow discharge: A high conversion ability. *J. Fuel. Chem. Technol.*, vol. 34, p. 308.

Li, M-W., Liu, C-P., Xu, Y-L., Xu, G-H., Zhang, F-C., Wang, Y-Q. (2006). Effects of catalysts in carbon dioxide reforming of methane via corona plasma reactors. *Energy and Fuels*, vol. 20, p. 1033.

Li, X., Bai, M-G., Tao, X-M., Shang, S-Y., Yin, Y-X., Dai, X-Y. (2010). Carbon dioxide reforming of methane to synthesis gas by an atmospheric pressure plasma jet. *J. Fuel. Chem. Technol.*, vol. 38, p. 195.

Li, X., Tao, X., Yin, Y. (2009b). An atmospheric-pressure glow-discharge plasma jet and its applications. *IEEE Trans. Plasma Chem.*, vol. 37, p. 759.

Li, Y., Li, D., Wang, G. (2011). Methane decomposition to CO_x-free hydrogen and nano-carbon material on group 8-10 base metal catalysts: A review. *Catal. Today*, vol. 162, p. 1.

Li, Y., Zhang, B., Tang, X., Xu, Y., Shen, W. (2006a). Hydrogen production from methane decomposition over Ni/CeO₂ catalysts. *Catal. Comm.*, vol. 7, p. 380.

Lie, L., Bin, W., Chi, Y., Chengkang, W. (2006). Characteristics of gliding arc discharge plasma. *Plasma Sci. Technol.*, vol. 8, p. 653.

Lin, J-C. M., Yan, Z-A., Wang, S-K. (2010). Technological development of a PEMFC-based CHP system. *ESD, Thailand*.

Ling, W., Tan, Y-S., Han, Y-Z., Zhao, J-T., Wu, J., Zhang, D. (2011). Hydrogen production by methane cracking over different coal chars. *Fuel*, vol. 90, p. 3473.

Liu, C., Marafee, A., Mallinson, R., Lobban, L. (1997). Methane conversion to higher hydrocarbons in a corona discharge over metal oxide catalysts with OH groups. *Appl. Catal. A: General*, vol. 164, p. 21.

Liu, C-J., Mallinson, R., Lobban, L. (1998). Non-oxidative methane conversion to acetylene over zeolite in a low temperature plasma. *J. Catal.*, vol. 179, p. 334.

Liu, C-J., Mallinson, R., Lobban, L. (1999). Comparative investigations on plasma catalytic methane conversion to higher hydrocarbons over zeolites. *Appl. Catal. A: General*, vol. 178, p. 17.

Long, H., Shang, S., Tao, X., Yin, Y., Dai, X. (2008). CO₂ reforming of CH₄ by combination of cold plasma jet and Ni/ γ -Al₂O₃ catalyst. *Int. J. Hydrogen Energy*, vol. 33, p. 5510.

Lowke, J. J., and Morrow, R. (1994). The theory of electric corona including the role of plasma chemistry. *Pure and Appl. Chem.*, vol. 66, p. 1287.

Luche, J., Aubury, O., Khacef, A., Cormier, J-M. (2009). Syngas production from methane oxidation using a non-thermal plasma: Experiments and kinetic modelling. *Chemical Engineering Journal*, vol. 149, p. 35.

Lukeš, P., Člupek, M., Babický, V., Šunka, P. (2004). Ozone formation by gaseous corona discharge generated above aqueous solution. *Czech. J. Phys.*, vol. 54, p. C908.

March, J. (1992). *Advanced organic chemistry: Reactions, mechanisms and structure*. Fourth Edition. John Wiley and Sons, p. 186.

Mekhilef, S., Saidur, R., Safari, A. (2011). Comparative study of different fuel cell technologies. *Renew. Sustain. Energy Rev.* Doi: 10.1016/j.rser.2011.09.020.

Meng, X., Xu, C., Gao, J., Liu, Z. (2008). Influence of feed properties and reaction conditions on catalytic pyrolysis of gas oils and heavy oils. *Fuel*, vol. 87, p. 2463.

Merbahi, N., Eichwald, O., Dubois, D., Abahazem, A., Yousfi, M. (2007). Positive point-to-plane corona discharge in air: electrical and optical analysis. 28 ICPIG, July, Prague, Czech Republic, topic 10, p. 963.

Mierlo, J. V., Maggetto, G., Lataire, Ph. (2006). Which energy source for road transport in the future? A comparison of battery, hybrid and fuel cell vehicles. *Energy Conversion and Management*, vol. 47, p. 2748.

Mishra, L. N., Shibata, K., Ito, H., Yugani, N., Nishida, Y. (2007). Characteristics of methane destruction using a pulsed corona discharge at atmospheric pressure. *J. Plasma Fusion Res. Series*, vol. 6, p. 760.

Mishra, L. N., Shibata, K., Ito, H., Yugani, N., Nishida, Y. (2007). Characterization of pulsed discharge plasma at atmospheric pressure. *Surface and Coatings Technol.*, vol. 201, p. 6101.

Mitchell, C. M., Kenis, P. J. A. (2006). Ceramic microreactors for on-site hydrogen production from high temperature steam reforming of propane. *Lab Chip*, vol. 6, p. 1328.

Mlotek, M., Sentek, J., Krawczyk, K., Schmidt-Szalowski, K. (2009). The hybrid plasma-catalytic process for non-oxidative methane coupling to ethylene and ethane. *Appl. Catal. A: General*, vol. 366, p. 232.

Monahan, J., Powell, J. C. (2011). A comparison of the energy and carbon implications of new systems of energy provision in new build housing in the UK. *Energy Policy*, vol. 39, p. 290.

Muradov, N. Z., and Veziroğlu, T. N. (2005). From hydrocarbon to hydrogen-carbon to hydrogen economy. *Int. J. Hydrogen Energy*, vol. 30, p. 225.

Muradov, N., Chen, Z., Smith, F. (2005a). Fossil hydrogen with reduced CO₂ emission: modelling thermocatalytic decomposition of methane in a fluidized bed of carbon particles. *Int. J. Hydrogen Energy*, vol. 30, p. 1149.

Mutaf-Yardimici, O. (1998). Employing plasma as catalyst in hydrogen production. *Int. J. Hydrogen Energy*, vol. 23, p. 1109.

NAHB Research Centre. (2001). Review of residential electrical energy use data. (<http://www.toolbase.org/PDF/CaseStudies/ResElectricalEnergyUseData.pdf>).

Nair, S. A., Nozaki, T., Okazaki, K. (2007). Methane oxidative conversion pathways in a dielectric barrier discharge reactor – investigation of a gas phase mechanism. *Chem. Eng. J.*, vol. 132, p. 85.

Neef, H-J. (2009). International overview of hydrogen and fuel cells. *Energy*, vol. 34, p. 327.

Nehra, V., Kumar, A., Dwivedi, H. K. (2008). Atmospheric non-thermal plasma sources. *Int. J. Eng.*, vol. 2, p. 53.

Neishem, S. J., and Ertsveg, I. S. (2007). Efficiencies and indicators defined to promote combined heat and power. *Energy Conversion and Management*, vol. 48, p. 1004.

Ni, H., Lan, Y., Cheng, C., Meng, Y., Wang, X. (2011). Reforming of methane and carbon dioxide by DC water plasma at atmospheric pressure. *Int. J. Hydrogen Energy*, vol. 36, p. 12869.

Nikiforov, A. Y., and Leys, C. (2006). Breakdown process and corona to spark transition between metal and liquid electrodes. *Czech. J. Phys.*, vol. 56, p. 952.

Nuvera Fuel Cell Avanti datasheet. (<http://www.nuvera.com/products/avanti.php>).

Onovwiona, H. I., and Ugursal, V. I. (2006). Residential cogeneration systems: review of the current technology. *Renewable and Sustainable Energy Reviews*, vol. 10, p. 389.

Orinakova, R. and Orinak, A. (2011). Recent applications of carbon nanotubes in hydrogen production and storage. *Fuel*, vol. 90, p. 3123.

Ostermark, U. (1995). Characterization of volatile hydrocarbons emitted to air from a cat-cracking refinery. *Chemosphere*, vol. 30, p. 1813.

Patino, P., Pérez, Y., Caetano, M. (2005). Coupling and reforming of methane by means of low pressure radio-frequency plasmas. *Fuel*, vol. 84, p. 2008.

Paulmier, T., and Fulcheri, L. (2005). Use of non-thermal plasma for hydrocarbon reforming. *Chemical Engineering Journal*, vol. 106, p. 59.

Pena, M. A., Gómez, J. P., Fierro, J. L. G. (1996). New catalytic routes for syngas and hydrogen production. *Appl. Catal. A: General*, vol. 144, p. 7.

Petipas, G., Rollier, J-D., Darmon, A., Gonzalez-Aguilar, J., Metkemeijer, R., Fulcheri, L. (2007). A comparative study of non-thermal plasma assisted reforming technologies. *Int. J. Hydrogen Energy*, vol. 32, p. 2848.

Peyrous, R., and Millot, R-M. (1981). Ozone production in oxygen by corona discharges in a point-to-plane gap subjected to a chopped DC positive voltage. *J. Phys. D: Appl. Phys.*, vol. 14, p. 2237.

Pham, M. H., Goujard, V., Tatibouët, J. M., Batiot-Dupeyrat, C. (2011). Activation of methane and carbon dioxide in a dielectric-barrier discharge-plasma reactor to produce hydrocarbons – Influence of $\text{La}_2\text{O}_3/\gamma\text{-Al}_2\text{O}_3$ catalyst. *Catal. Today*, vol. 171, p. 67.

Pietruszka, B., and Heintze, M. (2004). Methane conversion at low temperature: the combined application of catalysis and non-equilibrium plasma. *Catal. Today*, vol. 90, p. 151.

Pietruszka, B., Anklam, K., Heintze, M. (2004). Plasma assisted partial oxidation of methane to synthesis gas in a dielectric barrier discharge. *Appl. Catal. A: General*, vol. 261, p. 19.

Pinilla, J. L., Suelves, I., Lazaro, M. J., Moliner, R., Palacios, J. M. (2010). Parametric study of the decomposition of methane using a $\text{NiCu}/\text{Al}_2\text{O}_3$ catalyst in a fluidized bed reactor. *Int. J. Hydrogen Energy*, vol. 35, p. 9801.

Pires, J. C. M., Martins, F. G., Alvin-Ferraz, M. C. M., Simoes, M. (2011). Recent developments on carbon capture and storage: An overview. *Chemical Engineering Research and Design*, vol. 89, p. 1446.

Prieto, G., Okumoto, M., Shimano, K-I. (1999). Heavy oil conversion by plasma chemical reactors. *IEEE, Industry Applications Conference, 34th IAS Annual meeting*, vol. 2, p. 1144, 10.1109/IAS.1999.801648.

Rafiq, M. H., and Hustad, J. E. (2011). Biosyngas production by autothermal reforming of waste cooking oil with propane using a plasma-assisted gliding arc reactor. *Int. J. Hydrogen Energy*, vol. 36, p. 8221.

Raizer, Y. P. (1991). *Gas discharge physics*. Springer, Berlin, Heidelberg, New York.

Rakib, M. A., Grace, J. R., Lim, C. J., Elnashaie, S. S. E. H., Ghiashi, B. (2010). Steam reforming of propane in a fluidized bed membrane reactor for hydrogen production. *Int. J. Hydrogen Energy*, vol. 35, p. 6276.

Raseev, S. (2003). *Thermal and catalytic processes in petroleum refining*, Marcel Dekker, Inc.

Rastler, D. (2008). EPRI Hydrogen Briefing to DOE. Electric power Research institute. (http://www1.eere.energy.gov/hydrogenandfuelcells/production/electro_processes.html).

Rueangjitt, N., Akarawitoo, C., Sreethawong, T., Chavadej, S. (2007). Reforming of CO₂-containing natural gas using an AC gliding arc system: effect of gas components in natural gas. *Plasma Chem. Plasma Proces.*, vol. 27, p. 559.

Rueangjitt, N., Akarawitoo, C., Sreethawong, T., Ouraipryvan, P., Chamnanmanoontham, J., Chavadej, S. (2009a). Biogas reforming with/without partial oxidation in a multi-stage AC gliding arc discharge system. 19th ISPC, Germany.

Rueangjitt, N., Sreethawong, T., Chavadej, S., Sekiguchi, H. (2009). Plasma-catalytic reforming of methane in AC microsized gliding arc discharge: Effects of input power, reactor thickness and catalyst existence. *Chemical Engineering J.*, vol. 155, p. 874.

Ryan, M. (2011). A perspective on hydrogen and smart grids. *Fuel Cell Today, Analyst Views*, October. (<http://www.fuelcelltoday.com/analysis/analyst-views/2011/11-10-12-a-perspective-on-hydrogen-and-smart-grids>).

Schadel, B. T., Duisberg, M., Deutshmann, O. (2009). Steam reforming of methane, ethane, propane, butane and natural gas over rhodium-based catalyst. *Catal. Today*, vol. 142, p. 42.

Schoots, K., Ferioli, G. J., Kramer, G. J., Zwaan, B. C. C. (2008). Learning curves for hydrogen production technology: An assessment of observed cost reductions. *Int. J. Hydrogen Energy*, vol. 33, p. 2630.

Schoots, K., Kramer, G. J., Zwaan, B. C. C. (2010). Technology learning for fuel cells: An assessment of past and potential cost reductions. *Energy Policy*, vol. 38, p. 2887.

Schram, D. C. (2002). Plasma processing and plasma chemistry. *Pure Appl. Chem.*, vol. 74, p. 369.

Sekine, Y., Urasaki, K., Kado, S., Asai, S., Matsukata, M., Kikuchi, E. (2003). Steam reforming of hydrocarbons and alcohols using non-equilibrium pulsed discharge. 16th ISPC, Taormina.

Sentek, J. (2010). Plasma-catalytic methane conversion with carbon dioxide in dielectric barrier discharges. *Appl. Catal. B: Environmental*, vol. 94, p. 19.

Silberova, B., Venvik, H. J., Holmen, A. (2005a). Production of hydrogen by short contact time partial oxidation and oxidative steam reforming of propane. *Catal. Today*, vol. 99, p. 69.

Silberova, B., Venvik, H. J., Walmsley, J. C., Holmen, A. (2005). Small-scale hydrogen production from propane. *Catal. Today*, vol. 100, p. 457.

Simanzhenkov, V., and Idem R. (2003). *Crude oil chemistry*. Marcel Dekker, Inc., p. 40-41.

Slovetskii, D. I. (2006). Plasma-chemical processes in petroleum chemistry (Review). *Petroleum Chemistry*, vol. 46, p. 295.

Sobacchi, M. G. (2002). Experimental assessment of a combined plasma/catalytic system for hydrogen production via partial oxidation of hydrocarbon fuels. *Int. J. Hydrogen Energy*, vol. 27, p. 635.

Solovyev, E. A., Kuvshinov, D. G., Ermakov, D. Y., Kuvshinov, G. G. (2009). Production of hydrogen and nanofibrous carbon by selective catalytic decomposition of propane. *Int. J. Hydrogen Energy*, vol. 34, p. 1310.

Song, H. K., Choi, J-W., Yue, S-H., Lee, H., Na, B-K. (2004). Synthesis gas production via dielectric barrier discharge over Ni/ γ -Al₂O₃ catalyst. *Catal. Today*, vol. 89, p. 27.682

Speight, J. G. (2006). *The Chemistry and Technology of Petroleum*, Fourth Edition, CRC Press.

Sreethawong, T., Chavadej, S., Rueangjitt, N. (2007a). Reforming of CO₂-containing natural gas using an AC gliding arc system: Effects of applied voltage and frequency. 18th ISPC, Japan.

Sreethawong, T., Thakonpatthanakun, P., Chavadej, S. (2007). Partial oxidation of methane with air for synthesis gas production in a multistage gliding arc discharge system. *Int. J. Hydrogen Energy*, vol. 32, p. 1067.

Suarasan, I., Ghizdavu, L., Budu, S., Dascalescu, L. (2002). Experimental characterization of multi-point corona discharge devices for direct ozonation of liquids. *J. Electrostatics*, vol. 54, p. 207.

Suelves, I., Lazaro, M. J., Moliner, R., Corbella, B. M., Palacios, J. M. (2005). Hydrogen production by thermo catalytic decomposition of methane on Ni-based catalysts: influence of operating conditions on catalyst deactivation and carbon characteristics. *Int. J. Hydrogen Energy*, vol. 30, p. 1555.

Sugasawa, M., Terasawa, T., Futamura, S. (2010). Effects of initial water content on steam reforming of aliphatic hydrocarbons with nonthermal plasma. *J. Electrostatics*, vol. 68, p. 212.

Supat, K., Kruapong, A., Chavadej, S., Lobban, L. L., Mallinson, R. G. (2003). Synthesis gas production from partial oxidation of methane with air in AC electric gas discharge. *Energ. Fuel*, vol. 17, p. 474.

Swaty, T. E. (2005). Global refining industry trends: the present and future. *Hydrocarbon Processing*, vol. 84, p. 35.

Synnogy Ltd. (2009). UK fuel cell capabilities. Fuel cells UK, Clean Energy now. (www.fuelcellsuk.org).

Takahashi, N., Goldman, A., Goldman, M., Rault, J. (2000). Surface modification of LDPE by a DC corona discharge generated in a point-to-grid system: the influence of geometric parameters of the system on modification power. *J. Electrostatics*, vol. 50, p. 49.

Tamosiunas, A., Grigaitiene, V., Valatkevicius, P., Valincius, V. (2012). Syngas production from hydrocarbon-containing gas in ambient of water vapour plasma. *Catal. Today*, vol. 196, p. 81.

Tao, X., Bai, M., Li, X., Long, H., Shang, S., Yin, Y., Dai, X. (2011). CH₄ - CO₂ reforming by plasma – challenges and opportunities. *Progress in Energy and Combustion science*, vol. 37, p. 113.

Tao, X., Bai, M., Wu, Q., Huang, Z., Yin, Y., Dai, X. (2009). CO₂ reforming of CH₄ by binode thermal plasma. *Int. J. Hydrogen Energy*, vol. 34, p. 9373.

Tao, X., Qi, F., Dai, X. (2008). CO₂ reforming of CH₄ by combination of thermal plasma and catalyst. *Int. J. Hydrogen Energy*, vol. 33, p. 1262.

Tendero, C., Tixier, C., Tristant, P., Desmaison, J., Leprince, P. (2006). Atmospheric pressure plasmas: A review. *Spectrochimica Acta. Part B*: vol. 61, p. 2.

Thanh, L. G. (1985). Negative corona in a multiple interacting point-to-plane gap in air. *IEEE Trans. Ind. Appl.*, vol. 1A – 21, p. 518.

Thomson, J. J. (1897). Cathode Rays. *Philosophical Magazine*, vol. 44, p. 293. (<http://web.lemoyne.edu/~GIUNTA/thomson1897.html>).

Tokoro, T., Kato, T., Tanaka, Y., Kato, K., Negishi, A., Nozaki, K. (2011). Feasibility of distributed carbon capture and storage (DCCS). *Energy Conversion and Management*, vol. 52, p. 2509.

Trichel, G. W. (1938). Mechanism of a negative point-to-plane corona near onset. *Phys. Rev.*, vol. 54, p. 1078.

Trichel, G. W. (1939). The mechanism of the positive point-to-plane corona in air at atmospheric pressure. *Phys. Rev.*, vol. 55, p. 382.

Tsai, C-H., and Chen, K-T. (2009). Production of hydrogen and nano carbon powders from direct plasmalysis of methane. *Int. J. Hydrogen Energy*, vol. 34, p.833.

Tsai, C-H., Hsien, T-H., Shin, M., Huang, Y-J., Wei, T-C. (2005). Partial oxidation of methane to synthesis gas by a microwave plasma torch. *Env. Energy Eng.*, vol. 51, p.2853.

Tseng, P., Lee, J., Friley, P. (2005). A hydrogen economy: opportunities and challenges. *Energy*, vol. 30, p. 2703.

Uhm, H. S. (1998). Influence of chamber temperature on properties of the corona discharge system. *Physics of Plasmas*, vol. 6, p. 623.

Utgikar, V. P., Vijaykumar, J., Thyagarajan, K. (2011). Refinement of motivity factor in comparison of transportation fuels. *Int. J. Hydrogen Energy*, vol. 36, p. 3302.

Veldhuizen, E. M., and Rutgers, W. R. (2001). Corona discharges: fundamentals and diagnostics. *Proceedings: frontiers in Low Temp. Plasma Diagn. IV*, Rolduc, The Netherlands, p. 40.

Veldhuizen, E. M., Rutgers, W. R., Ebert, U. (2002). Branching of a streamer type corona discharge. *Proceedings of the XIV International Conference on Gas discharges and Applications*, Liverpool, UK.

Veldhuizen, E. M., Zhou, L. M., Rutgers, W. R. (1998). Combined effects of pulse discharge removal of NO, SO₂, and NH₃ from Flue gas. *Plasma Chem. Plasma Processing*, vol. 18, p. 91.

Venturelli, L., Santangelo, P. E., Tartarini, P. (2009). Fuel cell and traditional technologies. Part II: Experimental study on dynamic behaviour of PEMFC in stationary power generation. *Appl. Thermal Eng.*, vol. 29, p. 3469.

Veziroglu, A., and Macario, R. (2011). Fuel cell vehicles: State of the art with economic and environmental concerns. *Int. J. Hydrogen Energy*, vol. 36, p. 25.

Villacampa, J. I., Royo, C., Romeo, E., Montoya, J. A., Del Angel, P., Monzon, A. (2003). Catalytic decomposition of methane over Ni-AL₂O₃ coprecipitated catalysts: Reaction and regeneration studies. *Catal. A: General*, vol. 252, p. 363.

Wang Y., Shah, N., Huffman, G. P. (2005). Simultaneous production of hydrogen and carbon nanostructures by decomposition of propane and cyclohexane over alumina supported binary catalysts. *Catal. Today*, vol. 99, p. 359.

Wang, G. (2011). Advanced vehicles: costs, energy use, and macroeconomic impacts. *Journal of Power Sources*, vol. 196, p. 530.

Wang, Q., Shi, H., Yan, B., Jin, Y., Cheng, Y. (2011a). Steam enhanced carbon dioxide reforming of methane in DBD plasma reactor. *Int. J. Hydrogen Energy*, vol. 36, p. 8301.

Wang, X., Wang, N., Wang L. (2011). Hydrogen production by sorption enhanced steam reforming of propane: A thermodynamic investigation. *Int. J. Hydrogen Energy*, vol. 36, p. 466.

Wang, X., Wang, N., Zhao, J., Wang L. (2010a). Thermodynamic analysis of propane and steam reforming for synthesis gas or hydrogen production. *Int. J. Hydrogen Energy*, vol. 35, p. 12800.

Wang, Y., Yan, B-H., Jin, Y., Chen, Y. (2009). Investigating dry reforming of methane in a dielectric barrier discharge reactor. *Plasma Chem. Plasma Process.* vol. 29, p. 217.

Wang, Y-F., Tsai, C-H., Chang, W-Y., Kuo, Y-M. (2010). Methane steam reforming for producing hydrogen in an atmospheric-pressure microwave plasma reactor. *Int. J. Hydrogen Energy*, vol. 35, p. 135.

Wing, J. (2011). Hydrogen in centralised power generation. *Fuel Cell Today, Analyst views*, September. (<http://fuelcelltoday.com/analysis/analyst-views/2011/11-09-14-hydrogen-in-centralised-power-generation>).

Xing, Y., Liu, Z., Couttenye, R. A., Willis, W. S., Suib, S. L., Fanson, P. T., Hirata, H., Ibe, M. (2007). Generation of hydrogen and light hydrocarbons for automotive exhaust purification: Conversion of n-hexane in a PACT (plasma and catalysis integrated technologies) reactor. *J. Catal.*, vol. 250, p. 67.

Xing, Y., Liu, Z., Couttenye, R. A., Willis, W. S., Suib, S. L., Fanson, P. T., Hirata, H., Ibe, M. (2008). Processing of hydrocarbons in an AC discharge non-thermal plasma reactor: An approach to generate reducing agents for on-board automotive exhaust gas cleaning. *J. Catal.*, vol. 253, p. 28.

Xu, Z., Baowei, W., Yongwei, L., Genhui, X. (2009). Conversion of methane by steam reforming using dielectric barrier discharge. *Chi. J. Chem. Eng.*, vol. 17, p. 625.

Yang, Y. (2002). Methane conversion and reforming by non-thermal plasma on pins. *Industrial and Chemical Engineering Research*, vol. 41, p. 5918.

Yang, Y. (2003). Direct non-oxidative methane conversion by non-thermal plasma: experimental study. *Plasma Chem. Plasma Process.*, vol. 23, p. 283.

Yang, Y-C., Lee, B-J., Chun, Y-N. (2009). Characteristics of methane reforming using gliding arc reactor. *Energy*, vol. 34, p. 172.

Yao, S. L., Suzuki, E., Meng, N., Nakayama, A. (2002). A high-efficiency reactor for the pulsed plasma conversion of methane. *Plasma Chemistry and Plasma Processing*, vol. 22, p. 225.

Yao, S., Nakayama, A., Suzuki, E. (2001). Acetylene and hydrogen from pulsed plasma conversion of methane. *Catal. Today*, vol. 71, p.219.

Yao, S., Nakayama, A., Suzuki, E. (2001a). Methane conversion using a high-frequency pulsed plasma: Discharge Features. *AIChE J.*, vol. 47, p. 419.

Yao, S., Nakayama, A., Suzuki, E. (2001b). Methane conversion using a high-frequency pulsed plasma: important factors. *AIChE J.*, vol. 47, p. 413.

Yi, Y., Rao, A. D., Brouwer, J., Samuelsen, G. S. (2005). Fuel flexibility study of an integrated 25kW SOFC reformer system. *J. Power Sources*, vol. 144, p. 67.

Yu, M., Zhai, L. Y., Zhou, Q., Li, C. P., Zhang, X. L. (2012). Ionic liquid as novel catalysts for methane conversion under a DC discharge plasma. *Appl. Catal. A: Gen.* Doi: 10.1016/j.apcata.2012.01.010.

Yu, Q., Kong, M., Liu, T., Fei, J., Zheng, X. (2011). Non-thermal plasma assisted CO₂ reforming of propane over Ni/Y-Al₂O₃ catalyst. *Catal. Comm.*, vol. 12, p. 1318.

Zeng, G., Tian, Y., Li, Y. (2010). Thermodynamic analysis of hydrogen production for fuel cell via oxidative steam reforming of propane. *Int. J. Hydrogen Energy*, vol. 35, p. 6726.

ZEP (European Technology Platform for Zero Emissions Fossil Fuel Power Plants). The cost of CO₂ capture, transport and storage.

Zhu, J., Zhang, D., King, K. D. (2001). Reforming of CH₄ by partial oxidation: thermodynamic and kinetic analysis. *Fuel*, vol. 80, p. 899.

Appendix A

Fuel cell technology and commercialization

A1: Fuel cell technology

Fuel cell designs differ mainly in the chemical characteristics of the electrolyte, but all operate with the same basic principle (Mekhilef et al., 2011):



Fuel cells have four main parts, namely anode, cathode, electrolyte and the external circuit. At the anode, hydrogen is oxidised into protons and electrons (Mekhilef et al., 2011):



At the anode oxygen is reduced to oxide species and reacts to form water (Mekhilef et al., 2011):



Depending on the electrolyte, either protons or oxide ions are transported through an ion-conductor electron-insulating electrolyte whilst electrons travel through an external circuit to deliver electric power, see Figure A.1. The characteristics of summary of different types of fuel cells and their applications are summarised in Table A.1.

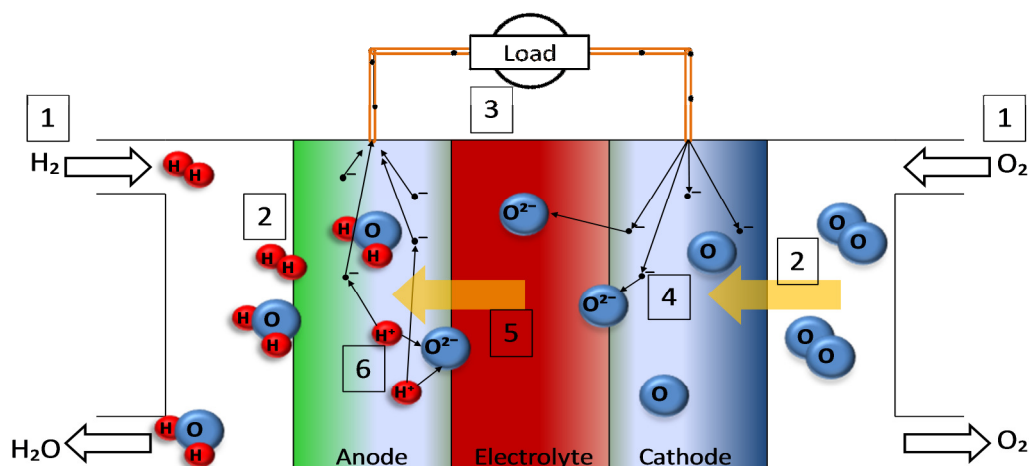


Figure A.1: Shows an example of an SOFC fuel cell, where only negative ions can pass through the electrolyte: 1) The input of hydrogen and oxygen into the fuel cell; 2) Hydrogen is oxidised to protons and electrons at the anode, oxygen diffuses to the cathode; 3) Electrons transport through the external circuit due to charge difference from anode to cathode generating electricity; 4) Electrons reduce oxygen to negative ions; 5) Negative oxygen ions pass through the electrolyte; 6) Oxygen ions combine with protons to generate water.

Table A.1: Types of fuel cells.

Fuel Cell	Fuel ¹	Operational temperature ¹ (°C)	Electrical Efficiency ¹ (%)	Power range ¹ (kW)	Applications ²
Proton Exchange Membrane (PEMFC)	Hydrogen	50 - 100	40 - 55	0.01 – 250	Stationary Mobile Portable
Alkaline (AFC)	Hydrogen	60 - 90	50 - 70	0.1 - 50	Submarines Spacecraft
Phosphoric Acid (PAFC)	Hydrogen	200	40 – 45	50 - 1000	Stationary
Solid Oxide (SOFC)	Hydrogen Natural gas (Tolerate impurities)	1000	40 - 72	0.5 - 2000	Stationary
Molten Carbonite (MCFC)	Hydrogen	650	50 - 60	200 – 100,000	Stationary
Direct Methanol (DMFC)	Methanol	30 – 130	40	0.001 - 1000	Mobile Portable

¹ Edwards et al. (2008)

²Schoots et al. (2010)

A2: Commercialization of fuel cells and the hydrogen infrastructure: not if, but when and where...

In this section the question of commercialization is addressed, and has already been noted that the future prospect of this is taken for granted. The timelines for, and the worldwide nature of the research leading to commercial use are now described.

In 2003, the European Commission (EC, 2003) stated that hydrogen and fuel cells are firmly established as strategic technologies that can meet the following objectives: (i) Maintaining economic prosperity and quality of life, and (ii) Achieving a sustainable energy system that meets the conflicting demands of increased energy supply and security, whilst maintaining cost-competitiveness, reducing climate change, and improving air quality. In 2003 the EC also announced a European hydrogen vision that by 2050 a hydrogen orientated economy would be globally implemented (EC, 2003). At present, fuel cell vehicles are still in the research and development stage, with the focus on durability and efficiency for real life applications. This indicates that the step to commercialization is close (Veziroglu and Macario, 2011). The view of manufacturers is that the transition to general use of fuel cell vehicles will take approximately 55 years, the timeline being as follows (Veziroglu and Macario, 2011):

- design of a market competitive fuel cell vehicle about 15 years
- penetration of up to 35% of new vehicle production about 25 years
- penetration up to 35% of fleet-miles driven about 20 years

In 2006 a group of EU high-level hydrogen specialists forecast the following timeline for the hydrogen and fuel cells area (Mierlo et al., 2006):

- up to 2020: technological research and demonstration fleets and infrastructure
- 2020-2030: implementation of large demonstration fleet and infrastructure together with the start of real economic use
- 2030 onwards: market development

Turning to research and development, in 2010, the **International Partnership for the Hydrogen Economy** (IPHE) reported on the state of the art for fuel cell developments worldwide (IPHE, 2010), some examples are given in Table A.2.

The *FuelCellToday* Newsletter is a rich source of information that follows and reports on any industry activities and is freely available on the internet. The 13 April 2011 Newsletter reported 'one of the most successful deployments of fuel cell products yet is the Japanese Ene-Farm project'. Around 14,000 micro combined heat and power (m-CHP) systems delivered to domestic customers in Japan so far, with more sales to come (FuelCellToday, 2011). Amongst other developments, FuelCellToday have reported the Callux project, Germany's biggest field trial. This is run by the German Ministry for Transport, Construction and Urban Development (BMVBS) with nine industrial partners including energy suppliers (EnBW, E.ON Ruhrgas, EWE, MVV Energie and VNG) and system manufacturers (Baxi Innotech, Hexis and Vaillant). The Vaillant and Hexis systems are both SOFC-based, producing 1 kW electricity and 2 kW heat with overall efficiencies above 90%, whereas the Baxi Innotech Gamma 1.0 uses a low-temperature PEM, giving 1 kW electricity and 1.7 kW heat with a total efficiency of 85%. The systems are all designed for connection to the existing gas pipeline. Callux aims to have around 800 of these products installed in selected private homes by 2012, with the full test programme running until 2015 (FuelCellToday, 2011).

Worldwide policies and programmes are being undertaken for hydrogen production and its use in fuel cells, notably in Germany, Japan, Europe, US, Australia, UK, South Korea and Denmark (IPHE, 2010). Demonstration projects continue to validate hydrogen and fuel cell technologies world-wide. These have engendered the aspirations of many automakers and governmental agencies to introduce fuel cell vehicles, together with a hydrogen re-fuelling infrastructure, by 2015.

Table A.2: Summary of the state of the art of the fuel cell deployment worldwide (IPHE, 2010).

Application	Country	State of art
Power generation and grid support	Korea	Posco Power plant: 24 MW fuel cells; Samsung: 4.8 MW fuel cells.
	Italy	16 MW hydrogen fuelled combined cycle plant in operation with 46% efficiency.
	Canada	Hybrid fuel cell plant in operation providing electricity for approximately 1700 homes.
Transportation and hydrogen infrastructure	Germany	Hydrogen Mobility initiative to develop hydrogen infrastructure by 2012-2015, aim to produce and sell 100,000 fuel cell and battery vehicles annually. 2008 – 2010: 47 fuel cell vehicles and 4 buses demonstrated.
	Japan	2010: 60 registered fuel cell vehicles and 14 stations operating. Plan to build 1,000 stations and 2 million fuel cell vehicles by 2025
	US	2010: over 50 fuelling stations present, industries demonstrating 152 fuel cell vehicles and 24 hydrogen stations, achieving 75,000 miles of work durability of the fuel cells.
	UK	2010: 2 hydrogen fuelling stations operating in Birmingham and Loughborough, 30 fleet small urban fuel cell vehicles, 20 fuel cell hybrid taxis, 5 fuel cell busses.
	China	196 fuel cell vehicle fleet being demonstrated.
	Canada	20 hydrogen fuel cell buses have commenced operation.
Combined heat and power	Japan	5000 residential fuel cell units installed as a government initiative.
	US	Major companies (Coco-Cola, Price Chopper) have installed large systems of up to 400 kW for their properties.
Back-up and remote power generation	India	Wireless IT Services Ltd. (major telecom in India) contracted to purchase of 200 GenSys fuel cell systems for grid towers.
	US	Sprint and AT&T are deploying fuel cells for back-up power at cell phone towers, with, 24 fuel cells deployed in 2010 September.
	Germany	5 fuel cell back-up systems installed in telecommunication industry.
	Australia	Ergon Energy is demonstrating fuel cell systems for remote energy.
Material handling and equipment	US	Fuel cell forklifts in use at Coca-Cola and Sysco; commercialization of 276 fuel cell forklifts. Department of defence demonstrating 40 fuel cell powered forklifts and an indoor hydrogen re-fuelling facility in Pennsylvania.
	Canada	Wallmart has invested in 75 fuel cell forklifts.
Energy storage	Canada	Excess of peak electricity is converted and stored as hydrogen via an electrolyser; in Bella Coola diesel consumption has decrease by an estimated 200,000 L/year and 600 tonnes GHG/year.
	Germany	Hydrogen produced from wind power is used in energy storage.

Appendix B

Chapter 5 Hexadecane cracking under corona discharge: Conditions tested

1) Positive corona discharge in air

Table B.1: Experimental conditions for power input variation at inter-electrode distance 10 mm, sample amount 5 ml and residence time 15 min.

Sample Code	Polarity	Gas mixture	Pressure	Run time (min)	Sample amount (ml)	D (mm)	Applied V (kV)	Power input (W)	Corona Current (mA)
L1	+	Air	Atm	15	5	10	12	0.36	0.03
L2	+	Air	Atm	15	5	10	13	0.52	0.04
L3	+	Air	Atm	15	5	10	14	50.50	3.61
L4	+	Air	Atm	15	5	10	15	59.80	3.99
L5	+	Air	Atm	15	5	10	16	68.90	4.31
L6	+	Air	Atm	15	5	10	17	78.81	4.64
L7	+	Air	Atm	15	5	10	18	88.13	4.90

Table B.2: Experimental conditions for power input variation at inter-electrode distance 15 mm, sample amount 5 ml and residence time 15 min.

Sample code	Polarity	Gas mixture	Pressure	Run time (min)	Sample amount (ml)	D (mm)	Applied V (kV)	Power input (W)	Corona Current (mA)
L21	+	Air	Atm	15	5	15	14	0.42	0.03
L22	+	Air	Atm	15	5	15	16	63.79	4.01
L23	+	Air	Atm	15	5	15	18	86.51	4.79

Table B.3: Experimental conditions for power input variation at inter-electrode distance 20 mm, sample amount 5 ml and residence time 15 min.

Sample code	Polarity	Gas mixture	Pressure	Run time (min)	Sample amount (ml)	D (mm)	Applied V (kV)	Power input (W)	Corona Current (mA)
L33	+	Air	Atm	15	5	20	18	83.45	4.64
L34	+	Air	Atm	15	5	20	19	93.03	4.90

Table B.4: Experimental conditions for sample amount variation at power input of 86 W, inter-electrode distance 15 mm and residence time 15 min.

Sample code	Polarity	Gas mixture	Pressure	Run time (min)	Sample amount (ml)	D (mm)	Applied V (kV)	Power input (W)	Corona Current (mA)
L43	+	Air	Atm	15	2	15	18	86.33	4.80
L44	+	Air	Atm	15	5	15	18	85.97	4.78
L45	+	Air	Atm	15	10	15	18	85.97	4.78

Table B.5: Experimental conditions for residence time variation at power input of 86 W, inter-electrode distance 15 mm and sample amount 5 ml.

Sample code	Polarity	Gas mixture	Pressure	Run time (min)	Sample amount (ml)	D (mm)	Applied V (kV)	Power input (W)	Corona Current (mA)
L40	+	Air	Atm	15	5	15	18	86.51	4.81
L41	+	Air	Atm	60	5	15	18	86.15	4.79
L42	+	Air	Atm	90	5	15	18	86.15	4.79

2) Positive corona discharge in argon

Table B.6: Experimental conditions for power input variation at inter-electrode distance 10 mm, sample amount 5 ml and residence time 15 min.

Sample code	Polarity	Gas mixture	Pressure	Run time (min)	Sample amount (ml)	D (mm)	Applied V (kV)	Power input (W)	Corona Current (mA)
L8	+	Ar	Atm	15	5	10	6	9.05	1.51
L9	+	Ar	Atm	15	5	10	7	12.52	1.79
L10	+	Ar	Atm	15	5	10	8	16.15	2.02
L11	+	Ar	Atm	15	5	10	9	21.31	2.37
L12	+	Ar	Atm	15	5	10	12	38.49	3.21
L13	+	Ar	Atm	15	5	10	14	53.85	3.85
L14	+	Ar	Atm	15	5	10	16	71.14	4.45
L15	+	Ar	Atm	15	5	10	17	81.70	4.81

Table B.7: Experimental conditions for power input variation at inter-electrode distance 15 mm, sample amount 5 ml and residence time 15 min.

Sample code	Polarity	Gas mixture	Pressure	Run time (min)	Sample amount (ml)	D (mm)	Applied V (kV)	Power input (W)	Corona Current (mA)
L24	+	Ar	Atm	15	5	15	6	10.19	1.70
L25	+	Ar	Atm	15	5	15	8	17.74	2.22
L26	+	Ar	Atm	15	5	15	10	27.88	2.79
L27	+	Ar	Atm	15	5	15	12	42.80	3.57
L28	+	Ar	Atm	15	5	15	14	57.91	4.14
L29	+	Ar	Atm	15	5	15	16	77.21	4.83

Table B.8: Experimental conditions for power input variation at inter-electrode distance 20 mm, sample amount 5 ml and residence time 15 min.

Sample code	Polarity	Gas mixture	Pressure	Run time (min)	Sample amount (ml)	D (mm)	Applied V (kV)	Power input (W)	Corona Current (mA)
L35	+	Ar	Atm	15	5	20	14	57.21	4.09
L36	+	Ar	Atm	15	5	20	16	75.13	4.70
L37	+	Ar	Atm	15	5	20	17	83.23	4.90

Table B.9: Experimental conditions for sample amount variation at power input 77 W, inter-electrode distance 15 mm and residence time 15 min.

Sample code	Polarity	Gas mixture	Pressure	Run time (min)	Sample amount (ml)	D (mm)	Applied V (kV)	Power input (W)	Corona Current (mA)
L52	+	Ar	Atm	15	2	15	16	76.73	4.80
L53	+	Ar	Atm	15	5	15	16	77.05	4.82
L54	+	Ar	Atm	15	10	15	16	76.57	4.79

Table B.10: Experimental conditions for residence time variation at power input 77 W, inter-electrode distance 15 mm and sample amount 5ml.

Sample code	Polarity	Gas mixture	Pressure	Run time (min)	Sample amount (ml)	D (mm)	Applied V (kV)	Power input (W)	Corona Current (mA)
L49	+	Ar	Atm	15	5	15	16	77.05	4.82
L50	+	Ar	Atm	60	5	15	16	76.73	4.80
L51	+	Ar	Atm	90	5	15	16	77.05	4.82

3) Positive corona discharge in air and argon mixture

Table B.11: Experimental conditions for power input variation at inter-electrode distance 10 mm, sample amount 5 ml and residence time 15 min.

Sample code	Polarity	Gas mixture	Pressure	Run time (min)	Sample amount (ml)	D (mm)	Applied V (kV)	Power input (W)	Corona Current (mA)
L16	+	1:4 Ar:Air	Atm	15	5	10	10	3.10	0.31
L17	+	1:4 Ar:Air	Atm	15	5	10	12	37.65	3.14
L18	+	1:4 Ar:Air	Atm	15	5	10	14	55.81	3.99
L19	+	1:4 Ar:Air	Atm	15	5	10	16	73.85	4.62
L20	+	1:4 Ar:Air	Atm	15	5	10	17	81.70	4.81

Table B.12: Experimental conditions for power input variation at inter-electrode distance 15 mm, sample amount 5 ml and residence time 15 min.

Sample code	Polarity	Gas mixture	Pressure	Run time (min)	Sample amount (ml)	D (mm)	Applied V (kV)	Power input (W)	Corona Current (mA)
L30	+	1:4 Ar:Air	Atm	15	5	15	16	67.62	4.23
L31	+	1:4 Ar:Air	Atm	15	5	15	17	76.60	4.51
L32	+	1:4 Ar:Air	Atm	15	5	15	18	86.51	4.81

Table B.13: Experimental conditions for power input variation at inter-electrode distance 20 mm, sample amount 5 ml and residence time 15 min.

Sample code	Polarity	Gas mixture	Pressure	Run time (min)	Sample amount (ml)	D (mm)	Applied V (kV)	Power input (W)	Corona Current (mA)
L38	+	1:4 Ar:Air	Atm	15	5	20	18	84.53	4.70
L39	+	1:4 Ar:Air	Atm	15	5	20	19	93.03	4.90

Table B.14: Experimental conditions for sample amount variation at power input 86 W, inter-electrode distance 15 mm and residence time 15 min.

Sample code	Polarity	Gas mixture	Pressure	Run time (min)	Sample amount (ml)	D (mm)	Applied V (kV)	Power input (W)	Corona Current (mA)
L55	+	1:4 Ar:Air	Atm	15	2	15	18	87.23	4.85
L56	+	1:4 Ar:Air	Atm	15	5	15	18	86.51	4.81
L57	+	1:4 Ar:Air	Atm	15	10	15	18	85.97	4.78

Table B.15: Experimental conditions for residence time variation at power input 86 W, inter-electrode distance 15 mm and sample amount 5ml.

Sample code	Polarity	Gas mixture	Pressure	Run time (min)	Sample amount (ml)	D (mm)	Applied V (kV)	Power input (W)	Corona Current (mA)
L52	+	1:4 Ar:Air	Atm	15	5	15	18	86.15	4.79
L53	+	1:4 Ar:Air	Atm	60	5	15	18	86.51	4.81
L54	+	1:4 Ar:Air	Atm	90	5	15	18	86.51	4.81

4) Negative corona discharge in air

Table B.16: Experimental conditions for power input variation at inter-electrode distance 10 mm, sample amount 5 ml and residence time 15 min.

Sample code	Polarity	Gas mixture	Pressure	Run time (min)	Sample amount (ml)	D (mm)	Applied V (kV)	Power input (W)	Corona Current (mA)
L85	-	Air	Atm	15	5	10	16	2.24	0.14
L86	-	Air	Atm	15	5	10	18	3.24	0.18
L87	-	Air	Atm	15	5	10	20	4.40	0.22

Table B.17: Experimental conditions for power input variation at inter-electrode distance 15 mm, sample amount 5 ml and residence time 15 min.

Sample code	Polarity	Gas mixture	Pressure	Run time (min)	Sample amount (ml)	D (mm)	Applied V (kV)	Power input (W)	Corona Current (mA)
L81	-	Air	Atm	15	5	15	16	1.44	0.09
L82	-	Air	Atm	15	5	15	20	3.00	0.15
L83	-	Air	Atm	15	5	15	24	5.28	0.22
L84	-	Air	Atm	15	5	15	26	7.02	0.27

Table B.18: Experimental conditions for power input variation at inter-electrode distance 20 mm, sample amount 5 ml and residence time 15 min.

Sample code	Polarity	Gas mixture	Pressure	Run time (min)	Sample amount (ml)	D (mm)	Applied V (kV)	Power input (W)	Corona Current (mA)
L58	-	Air	Atm	15	5	20	14	0.56	0.04
L59	-	Air	Atm	15	5	20	16	0.96	0.06
L60	-	Air	Atm	15	5	20	18	1.44	0.08
L61	-	Air	Atm	15	5	20	20	2.00	0.1
L62	-	Air	Atm	15	5	20	22	2.86	0.13
L63	-	Air	Atm	15	5	20	24	3.60	0.15
L64	-	Air	Atm	15	5	20	26	4.68	0.18

5) Negative corona discharge in argon

Table B.19: Experimental conditions for power input variation at inter-electrode distance 10 mm, sample amount 5 ml and residence time 15 min.

Sample code	Polarity	Gas mixture	Pressure	Run time (min)	Sample amount (ml)	D (mm)	Applied V (kV)	Power input (W)	Corona Current (mA)
L91	-	Ar	Atm	15	5	10	10	28.47	2.85
L92	-	Ar	Atm	15	5	10	12	40.16	3.35
L93	-	Ar	Atm	15	5	10	15	68.19	4.55

Table B. 20: Experimental conditions for power input variation at inter-electrode distance 15 mm, sample amount 5 ml and residence time 15 min.

Sample code	Polarity	Gas mixture	Pressure	Run time (min)	Sample amount (ml)	D (mm)	Applied V (kV)	Power input (W)	Corona Current (mA)
L88	-	Ar	Atm	15	5	15	12	42.56	3.55
L89	-	Ar	Atm	15	5	15	14	56.09	4.01
L90	-	Ar	Atm	15	5	15	16	74.49	4.66

Table B. 21: Experimental conditions for power input variation at inter-electrode distance 20 mm, sample amount 5 ml and residence time 20 min.

Sample code	Polarity	Gas mixture	Pressure	Run time (min)	Sample amount (ml)	D (mm)	Applied V (kV)	Power input (W)	Corona Current (mA)
L65	-	Ar	Atm	15	5	20	10	22.98	2.3
L66	-	Ar	Atm	15	5	20	12	34.53	2.88
L67	-	Ar	Atm	15	5	20	14	51.90	3.71
L68	-	Ar	Atm	15	5	20	16	64.91	4.06

6) Negative corona discharge is air and argon mixture

Table B.22: Experimental conditions for power input variation at inter-electrode distance 10 mm, sample amount 5 ml and residence time 15 min.

Sample code	Polarity	Gas mixture	Pressure	Run time (min)	Sample amount (ml)	D (mm)	Applied V (kV)	Power input (W)	Corona Current (mA)
L77	-	Ar:Air 1:4	Atm	15	5	10	10	25.48	2.55
L78	-	Ar:Air 1:4	Atm	15	5	10	12	39.33	3.28
L79	-	Ar:Air 1:4	Atm	15	5	10	14	54.55	3.90
L80	-	Ar:Air 1:4	Atm	15	5	10	16	72.74	4.55

Table B.23: Experimental conditions for power input variation at inter-electrode distance 15 mm, sample amount 5 ml and residence time 15 min.

Sample code	Polarity	Gas mixture	Pressure	Run time (min)	Sample amount (ml)	D (mm)	Applied V (kV)	Power input (W)	Corona Current (mA)
L73	-	Ar:Air 1:4	Atm	15	5	15	10	23.48	2.35
L74	-	Ar:Air 1:4	Atm	15	5	15	14	52.74	3.77
L75	-	Ar:Air 1:4	Atm	15	5	15	16	69.54	4.35
L76	-	Ar:Air 1:4	Atm	15	5	15	17	80.00	4.71

Table B.24: Experimental conditions for power input variation at inter-electrode distance 20 mm, sample amount 5 ml and residence time 15 min.

Sample code	Polarity	Gas mixture	Pressure	Run time (min)	Sample amount (ml)	D (mm)	Applied V (kV)	Power input (W)	Corona Current (mA)
L69	-	Ar:Air 1:4	Atm	15	5	20	12	32.98	2.75
L70	-	Ar:Air 1:4	Atm	15	5	20	14	49.66	3.55
L71	-	Ar:Air 1:4	Atm	15	5	20	16	65.71	4.11
L72	-	Ar:Air 1:4	Atm	15	5	20	17.5	81.31	4.65

Curriculum Vitae

Personal Profile

Motivated chemical engineer, with previous work experience demonstrating strong laboratory and communication skills. Valuable experience working in a high pressure, time critical environment to deliver results above and beyond expectations as an organic chemistry analyst and during PhD research.

Key Skills Profile

- Extensive **laboratory** experience gained through experiments and research undertaken during my degree, work at i2 Analytical and PhD.
 - **Experienced** in operation, maintenance and method development for hydrocarbon determination using **GC-MS** instrumentation.
 - Strong **data handling and analysis** skills, using custom reports, AIS LIMS, excel, ChemStation and MassLab programmes during work as an organic analyst and PhD.
 - Confident **communicator** illustrated through dealing with clients during my work as a translator and organic analyst.
 - Proficient at presenting ideas clearly and creatively using **power point presentations** when engaging large audiences at conferences during my PhD with two 1st and 2nd oral presentation prize awards at yearly ResCon competitions.
 - Strong organizational and time management skills were a key for **high quality and delivery** of my work as an organic chemistry analyst at a commercial company, and in the timely completion of my PhD.
-

Education

Sept 09 – Mar 13 **PhD Chemical Engineering** **Brunel University**

Extensive research into plasma and hydrocarbon chemistry. Involved a thorough study of the UK National Grid systems for domestic energy supply and fuel cell applications, with the aim towards the development of sustainable, clean and economically viable domestic energy supply.

MSc level modules:

- Environmental Risk Assessment
- Life Cycle Approach
- Sustainable Development
- Financial Management

Laboratory

- Design and construction of a non-thermal plasma unit for decomposition of hydrocarbons.
- Development of accurate, safe and efficient experimental procedures.
- Method development and daily use of the GC-MS instrumentation for gaseous and liquid sample testing.

Sept 2004 – Jun 08 **First BSc (Hons) Biochemistry** **Brunel University**

Key Modules

- Chemistry
- Advanced Biochemistry
- Mathematics
- Genetics

Laboratory assignments: learning objectives gained through accurate execution of laboratory procedures and the ability to learn the correct use of laboratory instrumentation.

Employment History

Jun 2006 – Sept 2007 **Industrial Placement** **i2 Analytical**

- Full training on health and safety in the laboratory, under COSHH regulations.
- Laboratory work for liquid and solid sample extraction to determine organic compounds by GC-MS analysis, and metals by ICP-OES on a daily basis.
- Accurate execution of the laboratory procedures in a time critical environment was crucial for correct results analysis and reporting to the clients.

Sept 2007 – Jun 2008 **Part-time organic analyst** **i2 Analytical**

- Progressed from laboratory assistant to organic analyst; gained expertise to operate GC-MS for sample analysis; as well as maintenance of GC column, the MS source and head space sampler.
- Became skilled at data analysis on a daily basis using ChemStation program for VOC, PAH, TPH, SVOC and PCB methods; and exporting large amounts of data using custom reports and AIS LIMS programs.

Jun 2008 – Sept 2009 **Organic chemistry analyst, full-time** **i2 Analytical**

- Further development within the position with increased responsibilities of quality and delivery of work.
 - Accurate and precise record keeping procedures, using excel, were required to maintain the high standards needed for UKAS accreditation.
 - Representing i2 I have travelled to Ukraine and Poland to coordinate many successful projects.
 - I found working in a commercial environment that because of the financial cost of missing deadlines I showed that I can be innovative, adaptable, and proactive when working in a team or when given individual responsibility.
-

Part Time Employment

Jun 2005 – Jun 2006 **Section Supervisor** **Waitrose Superstore**

Managed the stock control and presentation of the dried goods section, and led a team to deliver the high standards expected by Waitrose. Strong communication skills were necessary to ensure customer satisfaction at all times.

Feb 2000 – Jun 2004 **Translator** **Earls Court**

English/Russian translator dealing with large audiences, developed strong communication and presentation skills.

Jun 2001 – Sep 2001 **Admin Assistant** **NovaTel Systems**

Strengthened organizational and communication skills; responsibilities included arranging events, meetings and conferences, dealing with client enquiries, document filling and daily use of Word and Excel.

Publications from the work covered in this thesis

Journals

Aleknaviciute, I., Karayiannis, T. G., Collins, M. W., Xanthos, C. (2013). Plasma Assisted Decomposition of Gaseous Hydrocarbons to Produce CO_x Free Hydrogen. *International Journal of Low Carbon Technologies*, vol. 8, p.197.

Aleknaviciute, I., Karayiannis, T. G., Collins, M. W., Xanthos, C. (2013). Non-thermal plasma reactor for decomposition of propane to generate CO_x free hydrogen. *Journal of Clean Energy Technologies*, vol. 1, p. 105.

Aleknaviciute, I., Karayiannis, T. G., Collins, M. W., Xanthos, C. Methane decomposition under a corona discharge to generate CO_x free hydrogen (2013). *Int. J. Energy*, vol. 59, p. 432.

Aleknaviciute, I., Karayiannis, T. G., Collins, M. W., Xanthos, C. Towards a clean and sustainable distributed energy: The potential of integrated PEMFC-CHP. Submitted to *International Journal of Low Carbon Technologies* 2014.

Peer-Reviewed Conferences

Aleknaviciute, I., Collins, M. W., Karayiannis, T. G. (2010). Hydrocarbon Cracking and the use of non-thermal plasmas: concise review of crude oils and plasmas. *UIT 28th Heat Transfer Congress, Bresica*. ISBN: 0978-88-89252-14-7.

Aleknaviciute, I., Collins, M. W., Karayiannis, T. G. (2010). Hydrocarbon Cracking and the use of non-thermal plasmas: corona discharge and its applications. *UIT 28th Heat Transfer Congress, Bresica*. ISBN: 0978-88-89252-14-7.

Aleknaviciute, I., Karayiannis, T. G., Collins, M. W., Xanthos, C. (2011). Plasma Assisted Decomposition of Gaseous Hydrocarbons to Produce CO_x Free Hydrogen. *ICWEE, Sharjah, UAE*.

Aleknaviciute, I., Karayiannis, T. G., Collins, M. W. (2013). Non-thermal plasma reactor for decomposition of propane to generate CO_x free hydrogen. Italy, Rome: International Conference on Future Environment and Energy, 24-25 Feb, 2013.

Key note speech

Aleknaviciute, I., Karayiannis, T. G., Collins, M. W. (2013). Plasma use in the generation of hydrogen and applications in fuel cell CHP systems. UK-China Clean Energy Forum, February 18th.

Presentations and awards

Aleknaviciute, I., Karayiannis, T. G., Collins, M. W. (2010). Cracking of large hydrocarbon molecules using non-thermal plasma. SED Research Student Conference, Brunel University. 2nd Prize award for oral presentation.

Aleknaviciute, I., Karayiannis, T. G., Collins, M. W. (2011). Plasma assisted pyrolysis of gaseous hydrocarbons to produce CO_x free hydrogen. SED Research Student Conference, Brunel University. 1st Prize award for oral presentation.